Imperial College London

Fabrication and Characterization of Bismuth-based Environmental-friendly Materials for Solar Cell Application

Bowon Yoo

Department of Chemistry

Imperial College London

Submitted in fulfilment of the requirements for the degree of

Doctor of Philosophy

June 2020

Declaration

The work presented herein was performed under the supervision of Prof. Saif A. Haque at Imperial College London. Except where otherwise cited or referenced, I hereby declare that the work presented in this thesis are my own. This thesis has not been submitted in whole or in part for another degree of qualification at this or any other institution of higher learning.

Bowon Yoo

June 2020

Abstract

Lead-based perovskites, $APbX_3$, achieved over 23 % of efficiency within only 7 years after first their usage in solar cells. Although these lead-based perovskites have rapidly achieved the high efficiency, they have two intrinsic problems to be addressed to be commercialised; toxicity and instability. To address the problems of lead at the same time, new lead-free and air-stable materials such as inorganic materials including bismuth iodide and bismuth- or antimony-based perovskites are emerging. However, the efficiency of the solar cells employing these new materials is relatively low below 5%. This thesis explores these new materials especially bismuth-based perovskite and bismuth iodide inorganic material for their photoelectronic application with improved device performance.

An inorganic material, BiI_3 has suitable optical properties for photovoltaic application but due to the short carrier lifetime (180-240ps), it needs structure optimisation to achieve higher device performance. For this, *in-situ* processed BiSI interlayer was employed to enhance charge-carrier extraction before their recombination and it was monitored by transient absorption spectroscopy. Fabricated solar cell devices showed improved device performance with the BiSI interlayer.

Regarding bismuth or antimony-based perovskites, large binding energy, high defects and large bandgap are main issues to be addressed. Bismuth/antimony mixed perovskites were fabricated and investigated using a combined experimental and computational approach in a collaboration with the university of Bath. In the study, it was found that Sb mixing

reduces the binding energy and it leads to higher solar cell efficiency. By employing 2D bismuth perovskite, improved PLQY obtained and it might come from the reduced defect density.

In addition, nanocrystals (NCs) of bismuth or antimony-based perovskites were fabricated. These perovskites have high binding energy to overcome for the high-performance solar cell application, but this high binding energy can be helpful for high PLQY. Also, the reduced size to nanometre scale brings less defects in NCs and excitons are more prone to recombine radiatively. Therefore, NCs of Bi/Sb perovskite were fabricated to improve their optical property for opto-electronic application. The fabricated NCs were investigated by a range of characterisation techniques.

Acknowledgements

First, I would like to say I do appreciate to my supervisor Prof. Saif A. Haque for his guidance and advice for 4 years of study. He has been not only a good supervisor but also a friend to confide in. Whenever I had problems in my life, he showed me a way to go.

I spent 5 years including Mres and PhD courses in the group. I am very glad to be in this field leading group and to be with wonderful people in the group. Especially, I would like to thank past and present post-docs in the group, Irene, Jose and Xinxing for sharing their knowledge to me, training me in many equipment, and supervising me in the laboratories. I also remember Magda, Danyang and Hyejin who were undergraduate and postgraduate students and helped my research and gave me lots of insights.

The study would have been more difficult without Rob and Luis who were with me for whole 5-years in the group. I will remember the time we spent together forever. Special thanks to Ding Dong, my friend and now post-doc in the group. I am sure I would have given up this tough road if she was not in the group.

Another special thanks to Dr. Alex Aziz who collaborated with me for a year. He guided me in many aspects and his warm mind brought me to be this stage. I will never forget his help.

I would like to take this chance to thank my family for their love and support. With the help from my parents and my wife, I was able to start, continue and finish my study.

Last but not the least, I do believe it was not possible to spend 5 years like this without God's help. Thanks God.

Table of Contents

List of Figures

Figure 3-6. (a) UV–Vis absorption spectra of a BiI_3 film without In_2S_3 interlayer (blue circle) and BiI_3 films on an In_2S_3 layer annealed at different temperatures, 100°C (green triangles) and 200°C (orange squares) and Tauc plots for the films annealed at (b) 100°C (c) 200°C with an In_2S_3 layer.

Figure 3-7. (a) Transient absorption kinetics measured at 1,600 nm of BiI_3 films in different thin film structures and (b) transient absorption spectrum of an Al_2O_3/BiSI/BiI_3/spiro-OMeTAD thin film measured 10 μs after pulsed excitation and a steady-state absorption spectrum of spiro-OMeTAD chemically oxidised with $N(PhBr)_3SbCl_6$. The signals were normalised by the absorption of the film at 510 nm, which is the excitation wavelength.

Figure 3-8. Transient absorption kinetics measured at 1,600 nm for BiSI/BiI_3 films on different ETLs. The signals were normalised by the absorption of the film at 510 nm, which is the excitation wavelength.

Figure 3-9. Schematic illustration of the charge transfer processes in the investigated samples. The energy levels of BiSI and BiI_3 are based on literature data; CB of SnO_2: -4.5 eV, CB of BiSI: -4.5 eV, CB of BiI_3: -4.1 eV, VB of BiI_3: -5.9 eV, and HOMO of spiro-OMeTAD: -5.1 eV.

Figure 3-10. (a) Schematic device architecture of BiI_3-based solar cells fabricated with the above knowledge and (b) cross-sectional SEM image of a prepared solar cell device.

Figure 3-11. (a) JV traces of the assembled devices (dashed lines represent measurements in the dark) with different ETLs and (b) an external quantum efficiency spectrum from a device

with an ITO/c-SnO_2/BiSI/BiI_3/Spiro-OMeTAD/Au structure.

Figure 3-12. Histogram from 45 prepared solar cell devices with ITO/c-SnO_2/BiSI/BiI_3/Spiro-OMeTAD/Au structure.

Figure 3-13. The increase of PCE with oxidation time.

Figure 3-14. JV traces of the best performing solar cell with ITO/c-SnO_2/BiSI/BiI_3/Spiro-OMeTAD/Au structure.

Figure 3-15. (a) X-ray diffraction patterns of $MA_3Bi_2I_9$ on (a) mp-Al_2O_3 and (b) mp-Al_2O_3/BiSI substrates and references of $MA_3Bi_2I_9$ (black, code: 01-085-6013) and BiSI (red, code: 01-073-1171) and (b) UV-Vis absorption spectra of $MA_3Bi_2I_9$ on glass and glass/BiSI substrates.

Figure 3-16. (a) Transient absorption kinetics measured at 1,600 nm for $(MA)_3Bi_2I_9$ films on SnO_2 or SnO_2/BiSI ETLs. The signals were normalised by the film's absorption at 450 nm, which is the excitation wavelength. (b) JV traces of solar cell devices with $(MA)_3Bi_2I_9$ films with and without a BiSI interlayer.

Figure 3-17. Schematic drawing of thin film preparation including a BiSI inter-layer through the SVA method.

Figure 3-18. Absorption spectra of BiSI/BiI_3 thin films formed with and the without SVA method.

Figure 3-19. X-ray diffraction patterns of BiI_3 films on In_2S_3 (a) annealed and (b) solvent

vapour annealed at 300°C and references of BiI_3 (black, code: 01-076-1742) and BiSI (green, code: 01-073-1171) (a peak marked with * is from mo-TiO_2).

Figure 3-20. SEM images of BiI_3/In_2S_3 thin films annealed at 300°C (a) without SVA and (b) with SVA.

Figure 3-21. Time-resolved transient absorption spectrums of BiI_3 thin films in different concentrations and annealed in different atmospheres.

Figure 3-22. Current density–voltage (JV) curves of the fabricated solar cell devices with and without SVA.

Figure 4-1-1. Hexagonal 2 × 1 × 1 supercell of a possible configuration of $MA_3(BiSb)_2I_9$. Individual unit cells are marked with black lines. $M_2X_9^{3-}$ (M = Bi, Sb) clusters are dimer units comprising of pairs of face-sharing MX_6 octahedra. Inorganic octahedra are shown in brown (Sb) or green (Bi), iodine atoms are shown in purple. Unit cell information: a- 8.568 Å, b- 14.861 Å, c- 21.757 Å, β- 90.04°, space group: $P6_3/mmc$.

Figure 4-1-2. Preparation of bismuth-and-antimony mixed perovskite films on substrates.

Figure 4-1-3. (a) The X-ray diffraction pattern of $MA_3Bi_2I_9$ thin film on a glass substrate and a reference of $MA_3Bi_2I_9$ (code: 01-085-6013), (b) the diffraction patterns of $MA_3(Bi_{1-x}Sb_x)_2I_9$ films on glass substrates and (b) DFT calculated compositional dependence of the lattice parameters of $MA_3(Bi_{1-x}Sb_x)_2I_9$. The DFT was calculated by Dr. Alex Aziz.

Figure 4-1-4. SEM images of $MA_3(Bi_{1-x}Sb_x)_2I_9$ films prepared on glass substrates.

Figure 4-1-5. Experimentally obtained and computationally calculated bandgaps of $MA_3(Bi_{1-x}Sb_x)_2I_9$. The theoretical bandgaps were calculated by Dr. Alex Aziz and averaged over the three configurations with the highest probability.

Figure 4-1-6. (a)-(i) Tauc plots for $MA_3(Bi_{1-x}Sb_x)_2I_9$ thin films.

Figure 4-1-7. (a) The three lowest energy configurations of $MA_3(BiSb)_2I_9$ and (b) experimentally obtained PLQY values for $MA_3(Bi_{1-x}Sb_x)_2I_9$ thin films. The configurations were obtained by Dr. Alex Aziz. The selected excitation wavelength was 320 nm for the samples and photoluminescence between 340 nm and 620 nm was collected.

Figure 4-1-8. Absorption spectra of $MA_3(Bi_{1-x}Sb_x)_2I_9$ films prepared on glass substrates.

Figure 4-1-9. (a) Calculated effective mass and dielectric constant and (b) calculated binding energy of $MA_3(Bi_{1-x}Sb_x)_2I_9$. The effective mass, dielectric constant and binding energy were obtained by Dr. Alex Aziz.

Figure 4-1-10. (a) transient absorption kinetics measured at 1,000 nm for $MA_3Bi_2I_9$ and $MA_3Sb_2I_9$ thin films on glass substrates with P3HT and (b) transient absorption spectrum of a glass/$MA_3Bi_2I_9$/P3HT thin film measured 5 ms after pulsed excitation and a steady-state absorption spectrum of P3HT chemically oxidised with $N(PhBr)_3SbCl_6$. The signals were normalised by the absorption of the film at 450 nm, which is the excitation wavelength.

Figure 4-1-11. (a) Schematic illustration of the prepared device architecture with energy levels. The energy levels of bismuth perovskite and antimony perovskite (yellow dashed line) are based on related literature. (b) the calculated relative energy levels of $MA_3(Bi_{1-x}Sb_x)_2I_9$. The

relative energy levels were calculated by Dr. Alex Aziz.

Figure 4-1-12. (a) JV traces of the assembled devices (dashed lines represent measurements in the dark) in ITO/PEDOT:PSS/$MA_3(Bi_{1-x}Sb_x)_2I_9$/$PC_{70}BM$/Ag and (b) box plots of PCE of six best devices of each composition in $MA_3(Bi_{1-x}Sb_x)_2I_9$.

Figure 4-2-1. Preparation of 2D bismuth perovskite films on substrates.

Figure 4-2-2. The X-ray diffraction pattern of $PEA_3Bi_2I_9$ powder and fitted pattern. The diffraction pattern and fitted pattern were obtained by Martin Vickers, a senior research associate at University College London.

Figure 4-2-3. The crystal structure of $Rb_3Bi_2I_9$ ($P2_1/n$) as reported by Lehner *et al*.[9]

Figure 4-2-4. X-ray diffraction pattern of PEA, MA and PEA/MA mixed bismuth perovskite thin films on glass substrates.

Figure 4-2-5. SEM images of PEA and MA bismuth perovskite thin films on glass substrates.

Figure 4-2-6. UV–Vis and PL spectra of PEA and MA bismuth perovskite thin films on glass substrates.

Figure 4-2-7. Tauc plots from PEA and MA bismuth perovskite thin films.

Figure 4-2-8. TRPL from $PEA_3Bi_2Br_9$ and $MA_3Bi_2Br_9$ thin films on glass substrates. TRPL from $PEA_3Bi_2Br_9$ and $MA_3Bi_2Br_9$ thin films on glass substrates. The selected excitation wavelength was 282 nm for samples and probed at 450 nm and 468 nm for $PEA_3Bi_2Br_9$ and

$MA_3Bi_2Br_9$ respectively.

Figure 4-2-9. Transient absorption kinetics measured at 1,000 nm for $PEA_3Bi_2I_9$ thin films on different substrates and with different polymers. The signals were normalised by the absorption of the film at 450 nm, which is the excitation wavelength.

Figure 4-2-10. X-ray diffraction patterns of $PEA_3Bi_2I_9$ on (a) mp-Al_2O_3 and (b) mp-Al_2O_3/BiSI substrates and the reference of BiSI (blue, code: 01-073-1171).

Figure 4-2-11. Normalised absorption spectra of $PEA_3Bi_2I_9$ on glass and glass/BiSI substrates.

Figure 4-2-12. Transient absorption kinetics measured at 1,600 nm for $PEA_3Bi_2I_9$ thin films on c-SnO_2 with and without a BiSI interlayer. The signals were normalised by the absorption of the film at 450 nm, which is the excitation wavelength.

Figure 4-2-13. (a) Schematic device architecture of $PEA_3Bi_2I_9$-based solar cells fabricated with the BiSI interlayer and (b) JV traces of the assembled devices with and without the BiSI interlayer.

Figure 5-1. A LaMer plot showing the separation of nucleation and growth.

Figure 5-2. Preparation of bismuth-and-antimony mixed perovskite NCs.

Figure 5-3. (a) X-ray diffraction pattern of prepared $Cs_3Bi_2Br_9$ powder and (b) a reference of $Cs_3Bi_2Br_9$ (code: 01-070-0493).

Figure 5-4. Absorbance spectrum (solid line) and normalized PL spectrum (dashed line) of prepared $Cs_3Bi_2Br_9$ NCs. The selected excitation wavelength was 280 nm for PL measurement.

Figure 5-5. TRPL from $Cs_3Bi_2Br_9$ NCs (blue) and its the fitted line using Eq. 5-1 (red). The selected excitation wavelength was 282 nm and probed at 400 nm.

Figure 5-6. (a) TEM image of $Cs_3Bi_2Br_9$ NCs and (b) analysis of the size distribution.

Figure 5-7. Photo of prepared $Cs_3Bi_2X_9$ (where X is I, Br or Cl) precursor solutions, NC solutions before and after centrifuging (from top to bottom).

Figure 5-8. X-ray diffraction pattern of (a) prepared $Cs_3Bi_2I_9$ powder and a reference of $Cs_3Bi_2I_9$ (code: 01-073-0707), (b) prepared $Cs_3Bi_2Cl_9$ powder and a reference of $Cs_3Bi_2Cl_9$ (code: 01-084-1037) and (c) prepared $Cs_3Bi_2X_9$ powders (where X = I, Br, Cl).

Figure 5-9. UV–Vis (solid lines) and PL (dashed lines) spectra of $Cs_3Bi_2I_9$ (black), $Cs_3Bi_2Br_{4.5}I_{4.5}$ (red), $Cs_3Bi_2Br_9$ (blue), $Cs_3Bi_2Cl_{4.5}Br_{4.5}$ (orange) and $Cs_3Bi_2Cl_9$ (purple) NCs.

Figure 5-10. (a), (b), (c) and (d) TEM images of $Cs_3Bi_2X_9$ NCs and (e), (f), (g) and (h) their analysis of the size distribution.

Figure 5-11. Photo of prepared $Cs_3(Bi_{1-x}Sb_x)_2Br_9$ precursor solutions, NC solutions before and after centrifuging (from top to bottom).

Figure 5-12. X-ray diffraction patterns of prepared $Cs_3(Bi_{1-x}Sb_x)_2Br_9$ powders.

Figure 5-13. Normalised (a) UV–Vis and (b) PL spectra of $Cs_3(Bi_{1-x}Sb_x)_2Br_9$ NCs. The selected

excitation wavelength was 282 nm for PL measurement.

Figure 5-14. (a) TRPL from $Cs_3(Bi_{1-x}Sb_x)_2Br_9$ NCs and (b) the t_1 and t_2 values from the fitting. The selected excitation wavelength was 282 nm and probed at 400 nm.

Figure 5-15. Photo of prepared $Cs_3(Bi_{1-x}Sb_x)_2Br_9$ (where the Sb amount is small) precursor solutions, NC solutions before and after centrifuging (from top to bottom).

Figure 5-16. X-ray diffraction patterns of the prepared $Cs_3(Bi_{1-x}Sb_x)_2Br_9$ (where the Sb amount is small) powders.

Figure 5-17. Normalised UV–Vis and PL spectra of $Cs_3Bi_2Br_9$ NCs with (a) 0%, (b) 2.5%, (c) 5%, (d) 7.5% and (e) 10% Sb doping. The selected excitation wavelength was 282 nm for PL measurement

Figure 5-18. TRPL from $Cs_3(Bi_{1-x}Sb_x)_2Br_9$ (where the Sb amount is small) NCs and (b) the t_1 and t_2 values from the fitting. The selected excitation wavelength was 282 nm and probed at 400 nm.

List of Tables

Abbreviations

a-Si	Amorphous silicon
BA	Butylammonium
BCP	Bathocuproine
BE	Backscattered electron
CB	Conduction band
CB	Chlorobenzene
CdTe	Cadmium telluride
CIGS	Copper indium gallium selenide
CZTS	Copper zinc tin sulfide
CZTSe	Copper zinc tin selenide
DI-water	Deionised water
DMF	Dimethylformamide

DMSO	Dimethyl sulfoxide
DSC	Differential scanning calorimetry
DSSC	Dye-sensitized solar cells
ETL	Electron transport layer
ETM	Electron transport material
F8	Poly-(9,9-di-n-octylfluorenyl-2,7-diyl)
FA	Formamidinium
FAPI	Formamidinium lead triiodide
FE	Field emission
FTO	Fluorine doped tin oxide
FWHM	Full width at half maximum
HOMO	Highest occupied molecular orbital
HTL	Hole transport layer
HTM	Hole transport material
ICDD	International centre for diffraction data

Indium dimethylpentyl xanthate or Indium xanthate	Indium(III) O-2,2-dimethylpentan-3-yl dithiocarbonate
IPA	Isopropanol
ITO	Indium tin oxide
J_{SC}	Short-circuit current
LiTFSI	Lithium bis(trifluoromethylsulphonyl)imide
LUMO	Lowest unoccupied molecular orbital
MA	Methylammonium
MAPI	Methylammonium lead triiodide
mp	Mesoporous
NC	Nanocrystal
NREL	National renewable energy laboratory
OA	Oleic acid
OD	Optical density
OlAm	Oleylamine

OPV	Organic photovoltaic
P3HT	Poly(3-hexylthiophene-2,5-diyl)
PC70BM	[6,6]-Phenyl C_{71} butyric acid methyl ester, mixture of iso mers
PCE	Power conversion efficiency
PEA	Phenylethylammonium
PEDOT:PSS	Poly(3,4-ethylenedioxythiophene) polystyrene sulfonate
PLQY	Photoluminescence quantum yield
PMMA	Polymethylmethacrylate
PSC	Perovskite solar cell
PV	Photovoltaic
PTAA	Polytriarylamine
QD	Quantum dot
QDSC	Quantum dot solar cell
RA	Relative amplitude
SE	Secondary electron

Spiro-OMeTAD	2,2′,7,7′Tetrakis-(N,N-di-p-methoxyphenylamine)9,9′-spirobifluorene
SEM	Scanning electron microscopy
TAS	Transient absorption spectroscopy
TBP	Tert-butyl pyridine
TCSPC	Time-correlated singe photon counting
TGA	Thermogravimetry
TRPL	Time-resolved photoluminescence
UV	Ultraviolet
VB	Valence band
V_{OC}	Open-circuit voltage
XRD	X-ray Diffraction

Chapter 1: Introduction

1-1. General Overview

Renewable Energy Demand

Global energy demand has been increasing since the industrial revolution, and it is expected to continuously increase with population growth and the continuation of industrialisation.[1] Humans have been relying on fossil fuels, specifically coal, petroleum, and natural gas, for more than 400 years to meet their energy demands and they are still >80% dependent on these fossil fuels, which are non-renewable (Figure 1-1).[1-3] However, fossil fuels have serious limitations in their continued use such as their increasing scarcity and greenhouse gas emissions. Therefore, the need to develop different energy resources has been growing and humans are beginning to find alternative energy resources that are renewable to supply their needs for sustainable development while avoiding the dangerous consequences of climate change.[2] Sunlight, which is the most abundant energy source with power density 1,000 W/m^2 at the peak on the surface of the Earth, promises to be the one of the best long-term alternatives.[4, 5] Therefore, the installation of photovoltaics (PVs) that can convert this abundant solar energy to electrical energy has rapidly increased by nearly 320 times in the last 10 years, recording the generation of >500 GW in 2018 (Figure 1-2).[6] This electrical energy is the most widely used energy form in the world due to its high transmission efficiency and convenience to control.[7]

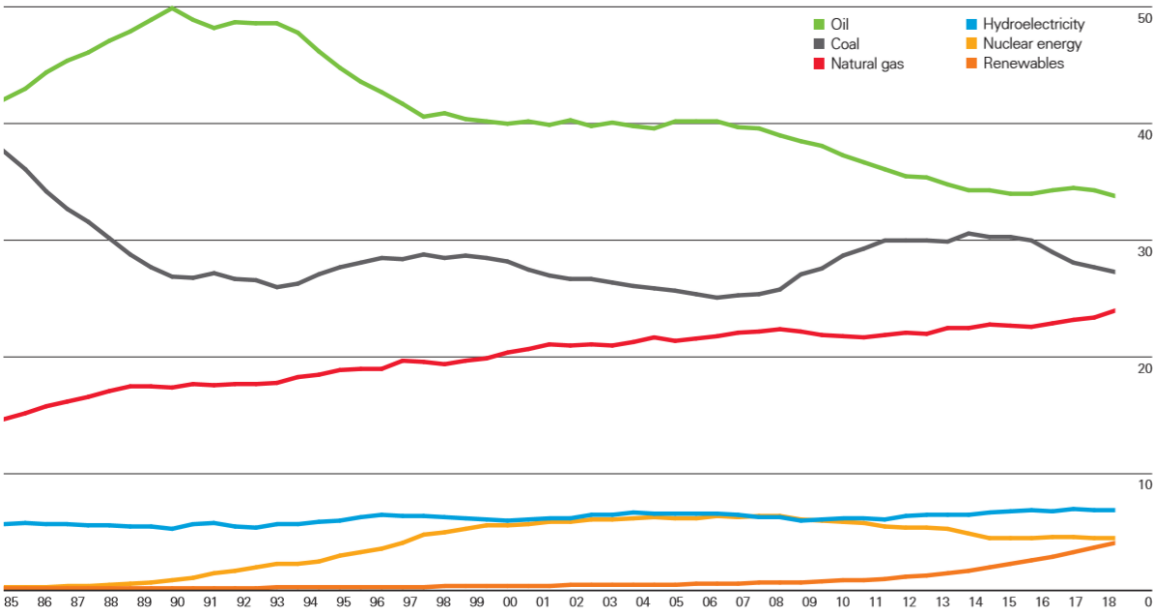

Figure 1-1. Energy consumption around the world for 1985–2018.[3]

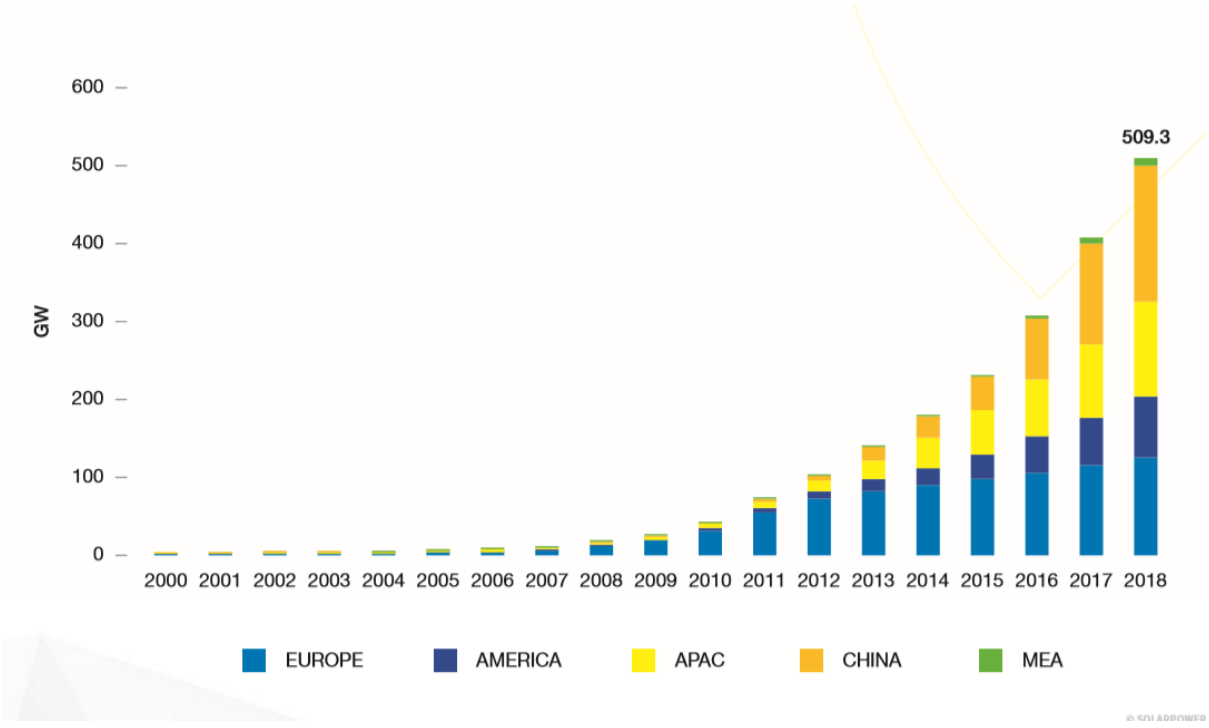

Figure 1-2. The capacity of the PV installed around the world in 2000–2018.[6]

Solar Cell Generation Development

The manufacturing cost of PVs has fallen steadily and continually since its invention, driven by continuous technological innovation and process improvements from $76.76/W in 1977 to $0.74/W in 2013 (Figure 1-3 (a)),[8] leading to the growth of PV installation. More than 60% of solar panel products are silicon-based first-generation solar cells, as shown in Figure 1-3 (b), because silicon is an abundant element on Earth (~26%) and environmentally safe. Notably, monocrystalline silicon-based solar cells give high efficiency >25%, which was maximised to 27.8% in 2018[9] and the solar panel market is dominated by first-generation silicon solar cells, which are those generally seen on rooftops.

Despite these advantages of first-generation solar cells, they have a huge barrier, namely the need for monocrystalline silicon ingots to produce proper wafers for high-efficiency PV. The process for creating monocrystalline silicon ingots needs massive amounts of energy, particularly when it is produced in bulk,[10] which accounts for about half of the total panel cost.[11] A significant portion of previously mentioned cost reductions came from 'economies-of-scale' benefits rather than system improvements.[12] In addition, the thickness is another drawback of silicon solar cells because first-generation solar cells need to be >1 μm thick.[13] Thus, the need for a cheaper system in terms of the energy in production and thinner devices for various applications has emerged.

To achieve systematic improvements to reduce the energy consumed during the manufacture of first-generation solar cells, second-generation solar cells appeared. Both first- and second-generation solar cells are based on p–n junction theory, but second-generation solar cells, which

are called 'thin-film solar cells' are much thinner, thus enabling their flexibility and lower weight. The first-generation solar cells employ an indirect bandgap semiconductor of silicon[14] and therefore need to be thick to absorb most of the sunlight. Thin-film solar cells employ direct bandgap absorbers that allow them to absorb sufficient light to generate electricity in several hundreds of nanometers.[15, 16]

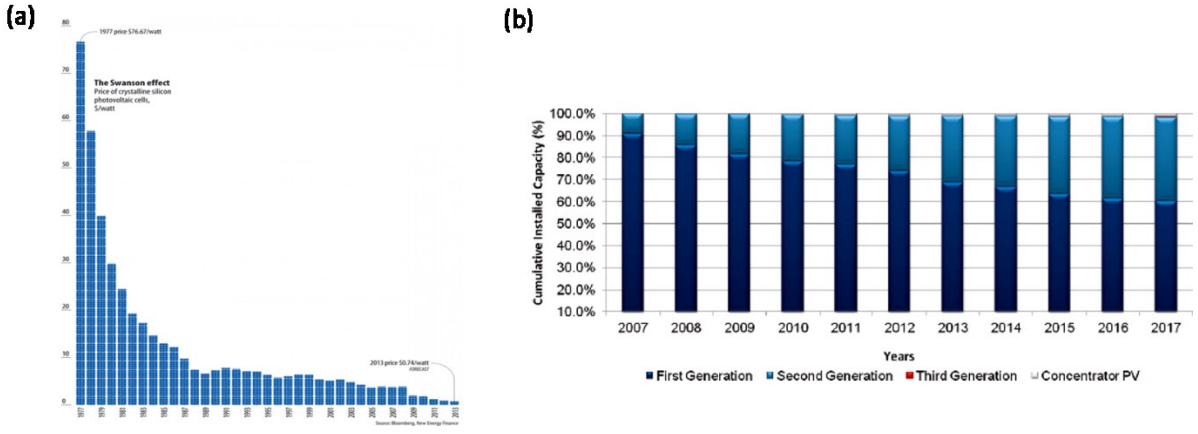

Figure 1-3. (a) The price history of PV solar cells for 1977–2012 and the forecast in 2013[8] and (b) market share for various photovoltaic (PV) technologies for 2007–2017[17].

Thin-film solar cells are mainly based on amorphous silicon (a-Si), cadmium telluride (CdTe), or copper indium gallium selenide (CIGS). Although all of these have the advantage of large-scale production with a vacuum deposition process, they present several unsolvable obstacles. Amorphous silicon solar cells show low efficiency and still require a high-cost process, CdTe solar cells contain the toxic heavy metal cadmium and the process of making quaternary CIGS cells is expensive. As a new alternative thin-film solar cell, copper zinc tin sulfide (CZTS) and copper zinc tin selenide (CZTSe) solar cells, which consist of cheap and non-toxic elements and use a low-cost manufacturing process have been developed and have shown recent

improvements in efficiency, but their efficiencies are not high enough for commercialisation.[18, 19] Even though thin-film solar cells have overcome some obstacles of first-generation solar cells, no type of cell presents a perfect alternative as each as certain barriers as mentioned above.

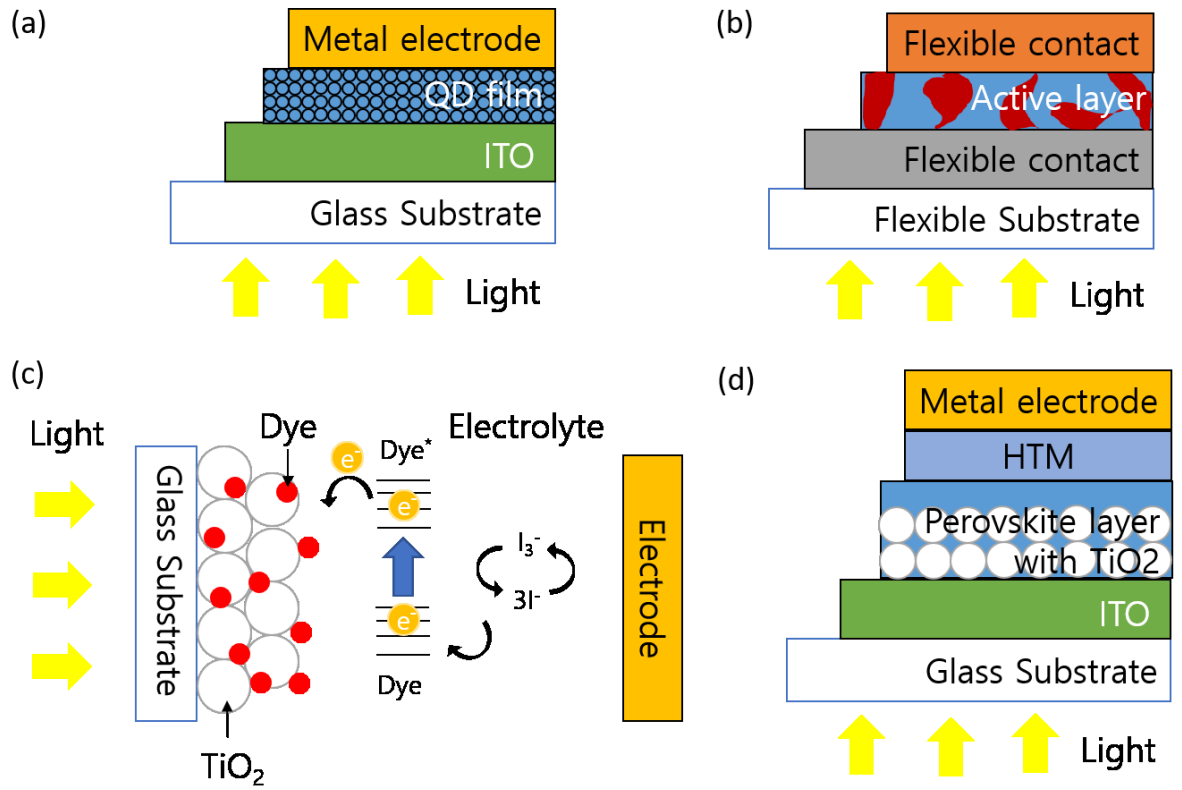

Figure 1-4. Schematic illustrations of 3rd generation solar cells: (a) QDCS, (b) OPV, (c) DSSC and (d) PSC.

For alternatives to first- and second-generation solar cells, many studies have been conducted on different types of PVs applied with different technologies. These third-generation solar cells include quantum dot solar cells (QDSCs), organic photovoltaics (OPVs), polymer solar cells, dye-sensitised solar cells (DSSCs), and perovskite solar cells (PSCs). They not only have the advantages of the second-generation solar cells but also enable large-scale production with a

solution process.[20-22]. In terms of QDSCs, they use quantum dots (QDs) as a light absorber, some of which have a size-dependent tuneable bandgap according to what materials they apply. They have the promise of multi-junction absorbance, which can theoretically lead to higher efficiency.[23] OPVs employ conductive organic molecules or polymers as light absorption and charge transfer materials, and are lightweight, flexible, transparent, and have a tuneable bandgap.[21] Regarding DSSCs, they are hybrid solar cells to which an inorganic electron-accepting nanoparticle such as TiO_2 is applied, which gives them a high surface area to organic dye sensitisers where charge carrier generation takes place.[24] Recently, PSCs that employ perovskites as light absorbers have become one of the most attractive PVs due to their solution process and low cost, showing rapid growth in efficiency over the last few years.

In summary, Figure 1-5 shows the efficiency improvements of various kinds of PVs since 1976 and the efficiencies are proven by the national renewable energy laboratory (NREL).[9] Despite these achievements in both efficiency and cost reduction and stability, they still do not supply the world's demands. Therefore, achieving higher efficiency, stability and lower cost are necessary.

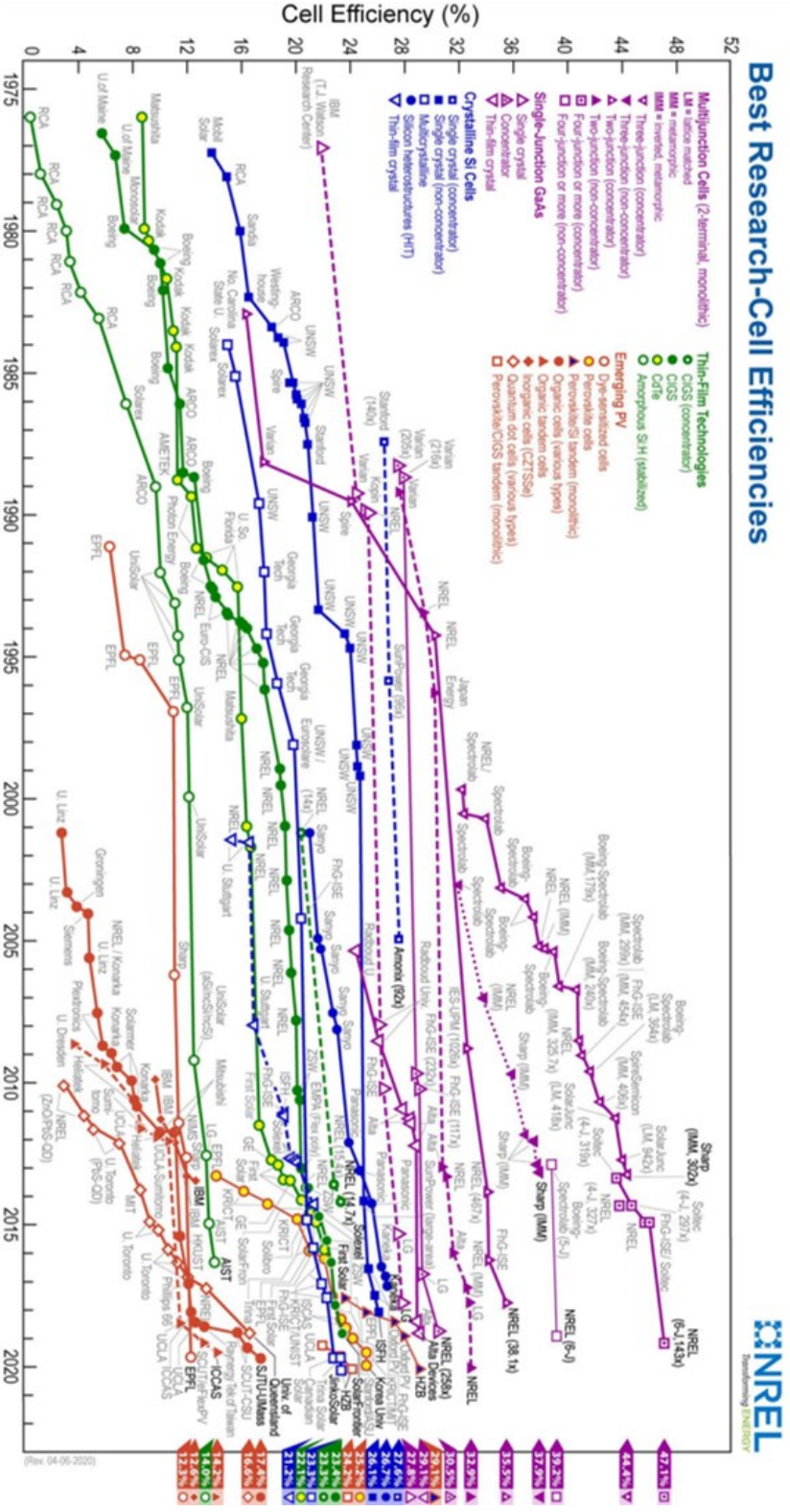

Figure 1-5. Best research-cell efficiencies by NREL.[9]

1-2. Perovskite Solar Cells

Characteristics of Perovskite Solar Cells

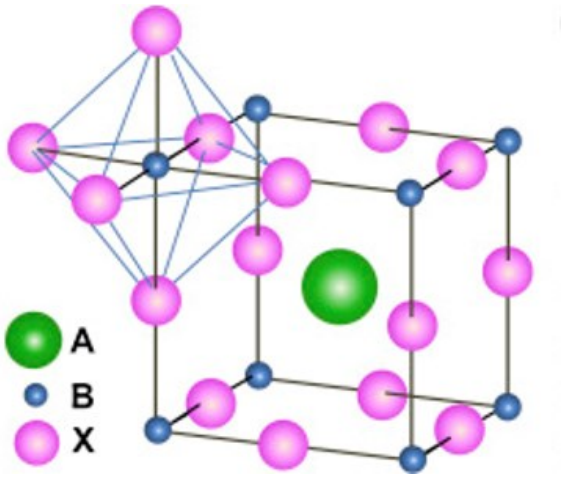

Figure 1-6. Schematic picture of ABX_3 perovskite.[25]

Perovskites have a crystal structure with the ABX_3 formula where A is a large cation, B is a small cation, and X is an anion (Figure 1-6). The larger cation A occupies a cubo-octahedral site linked with 12 X anions and the smaller cation B occupies in an octahedral site for better stability, shared with six X anions. In halide perovskites, X represents the halide ions F^-, Cl^-, Br^-, I^-, or mixed halide ions. There are two common perovskites, methylammonium (MA) lead triiodide (MAPI), formamidinium (FA) lead triiodide (FAPI). They have advantages in massive productions such as solution- or vapour-based processes and have a low cost as reviewed by Park.[25]

Lead-based perovskites have the following unique properties that make them suitable for electricity generation: (1) Long electron–hole diffusion lengths give generated charges a high

chance of being transferred to electrodes without recombination.[26] (2) High optical absorption enables the use of ultra-thin layers with high short-circuit current (Jsc).[27] (3) High open-circuit voltage (V_{OC}) (1.07 V) is available with a thin perovskite active layer (~300 nm).[28] (4) Free charge generation is predominant rather than exciton generation due to the low exciton binding energy (55 ± 20 meV).[29] (5) The tuneable bandgap can maximise the Shockley–Queisser limit[30]—the theoretical efficiency limit—at 31% without angular restriction.[31]

Evolution of Perovskite Solar Cell Structures

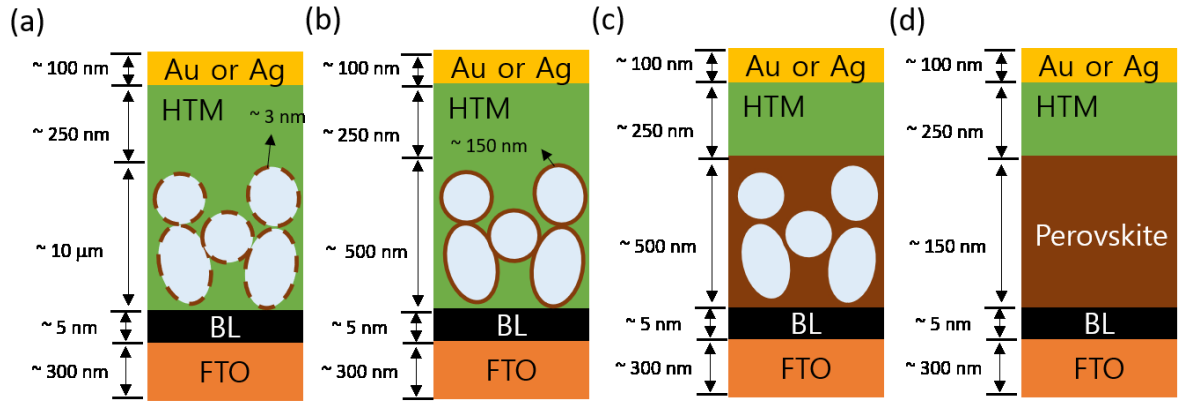

Figure 1-7. Evolution of perovskite solar cell structures: (a) DSSC concept, (b) meso-structure concept with an insulating scaffold, (c) pillared structure, and (d) planar heterojunction concept. The spheres represent TiO_2 in (a) and (c) and Al_2O_3 in (b). This figure is adapted from a reference[25].

MAPI, which is one of the most promising materials for a perovskite absorber, was first synthesised by Dieter Weber in 1972[32] and it has a tuneable optical bandgap between 2.46 eV and 1.6 eV with different halide content.[33, 34] Its first application in a PV device was reported in 2009 in a DSSC structure (Figure 1-7 (a)) where perovskite works as a dye on TiO_2 but it

showed low power conversion efficiency (PCE) of 3.8%.[35] After three years, 2–3 nm of perovskite was applied to QDSC as QD and generated 6.5% efficiency with post-annealing condition.[36] Then, Snaith's group achieved a remarkable efficiency rise to 10.9%.[37] They employed 2,2′,7,7′tetrakis-(N,N-di-p-methoxyphenylamine)9,9′-spirobifluorene (spiro-OMeTAD) as a hole transport material (HTM) and replaced the semi-conductive TiO_2 with insulating Al_2O_3 as illustrated in Figure 1-7 (b). In this structure, the holes generated in the perovskite active layer were more effectively extracted to spiro-OMeTAD than to the previously applied hole transport materials (HTMs) or redox electrolytes based on iodide/iodine, which resulted in high J_{SC} and V_{OC}. This new structure brought fresh insights into perovskite. Unlike DSSC, electron transfer to an electrode can occur win the perovskite layer without any semi-conductive scaffold with long electron diffusion length in MAPI..[26, 37] Therefore, a pillared structure in which the perovskite phase fills the pores of meso-porous TiO_2 pillars (Figure 1-7 (c)) and a planar pin heterojunction structure (Figure 1-7 (d)) were proposed and PCEs of 15.0%[38] and 15.4%[28] were achieved in the these structures, respectively. Then, these structures became the most common in PSCs. After that, rapid improvements in efficiency have occurred as a deeper understanding of the material has unfolded and rapid progress in processing conditions such as anti-solvent dripping, device architectures including an inverted structure[39] and precursor chemistries with triple- and quadruple-cation perovskites[40, 41] has been implemented, recently achieving up to 22.7%[9] PCE.

Two Intrinsic Problems

Despite the high efficiency and economic advantages of organic–inorganic hybrid PSCs for large-scale production, they have two serious limitations, their stability and toxicity. In terms

of stability, the causes of the degradation of lead halide perovskite in PV have been researched and revealed as temperature[42], moisture[43], ultraviolet (UV) light[44], and oxygen[45]. Various trials have been attempted to produce more-stable PSCs, such as encapsulating the cell[46], employing different electron transport materials (ETMs)[47-49], building with an inverted structure[39, 50], bromide-mixed perovskite[51], all-inorganic perovskite[52], perovskite with low-dimensionality[53] and creating triple- or quadruple-cation composition lead halide perovskite[40]. Although these trials have successfully extended the lifetime of the fabricated solar cells, another critical issue in lead-based perovskites is their toxicity. Lead perovskites decompose and partially dissolve in water; thus, they may contaminate and poison water sources. Lead poisoning seriously affects many organs and tissues,[54] and many countries have therefore banned the use of lead in commodities.[55] This intrinsic characteristic of lead is inevitable and there is one obvious solution to this problem, replacing the lead.

1-3. Lead-free Perovskite Solar Cells

Tin Perovskite Solar Cells

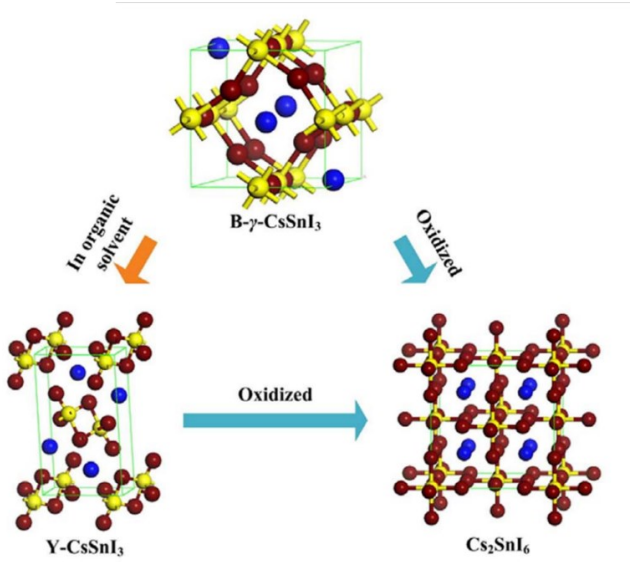

Figure 1-8. Schematic illustration of the oxidisation process from $CsSnI_3$ to Cs_2SnI_6.[56]

Expecting similar optical properties, tin, which is also in group 14 and has similar chemical properties, was suggested as an alternative to lead. The structural properties of tin halide perovskites were reported in 1974 and 1991[57] and its thin-film structure and optical properties were reported in 2010.[57-59] The first application of a tin halide perovskite in a solar cell structure was as a hole transport layer (HTL) in a DSSC.[60] Then, the application of tin halide perovskite as the active layer in a PSC emerged, initially to tune the bandgap of the lead halide perovskite by changing the ratio of lead and tin.[61] The development of tin-based perovskites are continually in progress, applying 2D structures and mixed cations or halides in perovskites, finding optimal solvents and anti-solvent treatments.[62-66] In recent studies, efficiency has been

growing by employing ETLs with well-matched band energies,[67, 68], new A-site cations,[69], new deposition methods,[70] and new additives[71], exceeding 13% of PCE.

Despite this development, tin-based perovskites also have an intrinsic problem that Sn^{2+} is easily oxidised to Sn^{4+}, and so $ASnX_3$ easily goes through oxidisation to A_2SnX_6 in air, as shown in Figure 1-8.[56] To prevent this oxidation, SnF_2, which provides extra Sn^{2+}, has become a common additive to tin halide perovskites to displace Sn^{4+}.[72, 73] Recent works shows the improvement in stability by introducing additives like an antioxidant, a polymer, and a bidentate ligand.[74-76]

Quasi-2D tin perovskites or 2D/3D-mixed perovskites are emerging as well. The quasi-2D structure has improved the stability of the tin-based perovskites.[63, 64] The quasi-2D structure can be obtained by employing a large cation at the A-site.[53] The 2D perovskite can be made when the organic A -site cation is large with a long chain because this long chain split the layers of the perovskite, forming $A_{n-1}B_nX_{3n+1}$, where n indicates the layer thickness of metal halide sheets, not ABX_3. Recent study revealed that shorter alkyl chain length of A-site cation promotes perpendicular crystal growth of 2D tin-based perovskite films, while longer chain of A-site cation leads parallel crystal growth.[77] This ordered orientation of 2D perovskites brought improved device efficiency as well.[78] The luminescence property can be enhanced by this 2D perovskite strategy because the longer and larger A-site cation passivates the perovskites.[79, 80]

However, although the progress in this tin-based perovskite field, the efficiency and the stability issues are not sufficiently addressed yet for commercialisation. Especially, tin-based perovskite is still much more unstable than lead-based perovskites. Thus, research into other

alternatives is still needed.

Stable Lead-free Perovskite Solar Cells

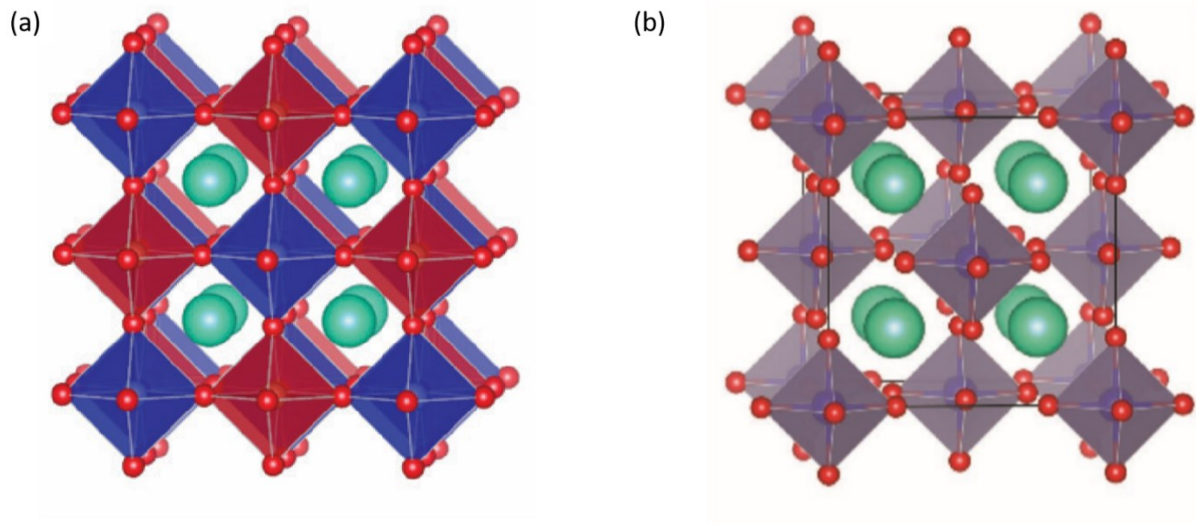

Figure 1-9. Schematic illustration of (a) double perovskite and (b) Sn^{4+} perovskite.[81, 82]

To overcome the stability and the toxicity problem of lead halide perovskites, stable lead-free perovskites including double perovskite, Sn^{4+} perovskite, bismuth-based perovskites and antimony-based perovskites are emerging.

After Slavney *et al*. reported the synthesis of the first halide double perovskite—$Cs_2AgBiBr_6$—in 2016,[83] several different types of double perovskites with silver and bismuth have been suggested with increased solar cell efficiency.[81, 84-87] They have long carrier lifetime, and therefore, there are high possibility of charge transfer to other layers before charge recombination, [83, 88] and one of these double perovskites achieved 4.3% of PCE, which is the highest among stable lead-free perovskites.[89] The development on this kind of materials is still ongoing with doping and component replacement, improving their optical properties.[90-92]

However, due to the inherent characteristics which is not suitable for solar cell application, for example, large indirect band gap, large charge carrier effective masses, low charge carrier transport capability, and poor sunlight absorption capability, other alternatives are still needed.[93, 94]

Already oxidised Sn^{4+} perovskite is another type of stable lead-free perovskite. In A_2SnX_6, Sn has a +4 oxidation state and thus does not lose its optical properties due to oxidation. The first application of this perovskite was also HTL in DSSC like the Sn^{2+} perovskite.[95] Despite the presence of isolated octahedral units due to vacancies, the closely packed iodide lattice provides significant room-temperature carrier mobility in Cs_2SnI_6 (310 $cm^2/V{\cdot}s$), which is the same order of magnitude as that of $CsSnI_3$.[95, 96] However, unlike Sn^{2+} perovskite, this type of perovskite has not yet been unable to achieve high efficiency due to its natural metallic conductivity, which comes from the high density of iodine vacancies and impurities in the material.[97]

Bismuth and Antimony Perovskites

Bismuth- and antimony-based perovskites are other emerging lead-free and stable perovskites. They have a $A_3B_2I_9$ structure, where A represents small cations and B represents the metal cations Bi or Sb. Unlike lead- or tin-based perovskites, these lead-free perovskites have octahedral halide coordination around the trivalent metal ions, forming $[Bi_2I_9]^{3-}$ or $[Sb_2I_9]^{3-}$ double octahedra that are surrounded by cations such as Cs^+ or MA^+ (Figure 1-10).[98, 99] These perovskites are also called 0D perovskites because the $[Bi_2I_9]^{3-}$ or $[Sb2I_9]^{3-}$ form the face-sharing double octahedra clusters rather than corner-sharing $[BiI_6]^-$ or $[SbI_6]^-$ octahedra.[99-101]

This term ‘0D’ does not mean that these materials are in quantum dots or small nano crystals (few nano size). This term is from the structure of the unit cell which includes $[Bi_2I_9]^{3-}$ or $[Sb_2I_9]^{3-}$ clusters, which are discrete molecular clusters. Additionally, they are not proper perovskites but perovskite analogues, which cannot form ABX_3 structure. Depending on the size of the small A-site cations, a 2D-layered perovskite structure is also available.[102]

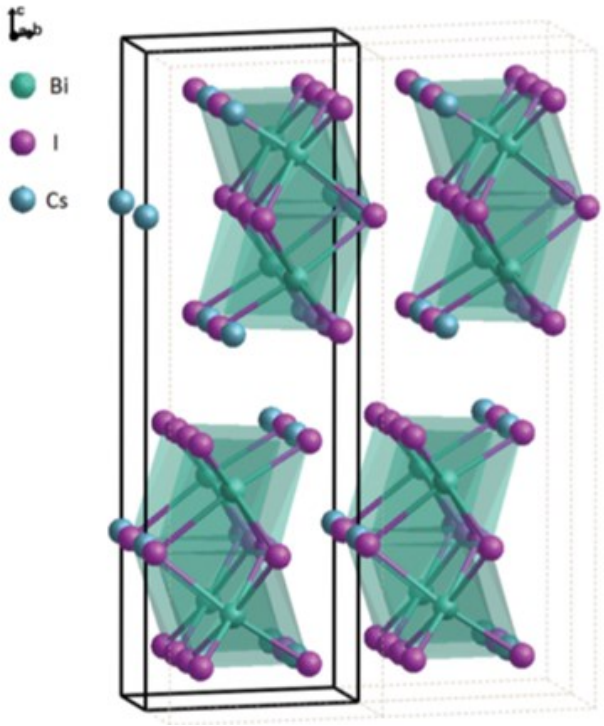

Figure 1-10. Schematic picture of the $Cs_3Bi_2I_9$ structure. The dark lines indicate the unit cell and the cyan octahedra indicate the $[Bi_2I_9]^{3-}$ octahedra.[100]

These materials are attracting interest in this field with low-toxic and stable characteristics and

also they have high enough absorption coefficient to make thin solar cell devices.[100] However, these materials has high Wannier–Mott exciton binding energy over 200 meV, which is higher than that of lead-based perovskites (25–50 meV), [29, 100, 103] and therefore, the charges generated in these materials forms not free charges but excitons. In addition, it was reported by Mathews et al. that there are the deep energy defects acting as recombination centres.[104]

Although the optical properties are not ideal for solar cell application, the efficiency of the solar cells employing these materials has been increasing from 1% to nearly 3% with the progress in device architecture and precursor chemistries as our understanding of the materials grows. Since the first application of bismuth-based perovskites as a solar cell absorber with 1.1% PCE by Park *et al*.[100], attempts have been made to improve their efficiency.[105-109] In a recent study employing two-step vapour-assisted processes brought remarkably improved efficiency to 3.2%.[110] In antimony-based perovskites, Hebig et al.[111] reported on a 0.49% planar solar cell with 0D $MA_3Sb_2I_9$ dimer. After this report, several antimony-based perovskites were reported with gradually increasing efficiency and a broadened understating of the materials.[99, 112, 113] High efficiency improvements were achieved in inverted n-i-p-type solar cells; in particular, using polymer hole transport material (HTM) instead of poly(3,4-ethylenedioxythiophene) polystyrene sulfonate (PEDOT:PSS) achieved the current efficiency record of 2.7%.[102, 114]

Recent works shows other applications for these 0D perovskites for various purposes. Bismuth-based perovskite is applicable for data storage in resistive switching memory devices with high reproducibility and reliability.[115] A photodetector with bismuth-based perovskite was also recently reported.[116] They also showed photocatalyst abilities for CO_2 reduction and pollutant degradation.[117, 118] Additionally, they can be used as a catalyst for C-H bond activation and ring-

opening reactions of various epoxides.[119, 120] Based on the material characteristics of these perovskites and their already reported applications, it seems that they can be used for more varied purposes. For this, it seems necessary to have a wider and deeper understanding of the understanding of these materials.

BiI_3: Stable Inorganic Solar Cells

All-inorganic metal-halides such as bismuth iodide (BiI_3) are potential candidates as light absorbers in solar cells.[121-123] Bismuth is one of the most popular elements for lead replacement as it exhibits chemical similarity and similar density.[124] Like lead, it has a $[Xe]^4f^{14}5d^{10}6s^2$ electronic configuration, which makes bismuth resistant to oxidation due to the presence of an inert $6s^2$ electron pair.[125] BiI_3 possesses a rhombohedral crystal structure (space group $R\bar{3}$)[126] with a layered 2D structure built from BiI_6 octahedra where the iodide atoms occupy a hexagonal close-packed lattice and the bismuth atoms occupy 2/3 of the octahedral sites between every second layer (Figure 1-11).[127]

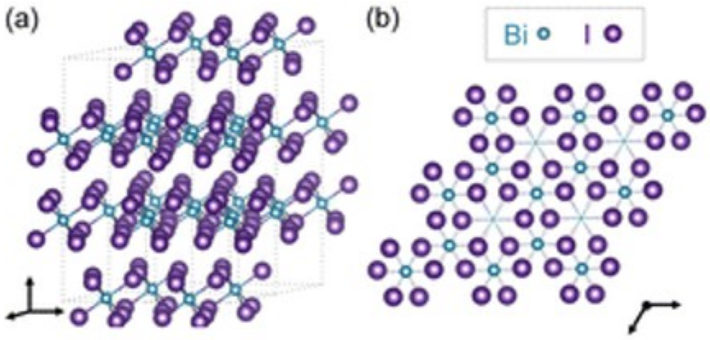

Figure 1-11. Crystal structure of BiI_3 showing the octahedrally coordinated Bi atoms.[131]

BiI_3 has been widely applied in X-ray detectors due to its large X-ray cross-section availability

that results from its large nuclear mass.[128] After the first applications of this material as a HTL in organic solar cells,[129] it has been attracting interest for photovoltaic (PV) applications due to its well-suited optical properties.[122, 130, 131] The bandgap (indirect) of BiI_3 is ~1.7 eV[122, 130, 131] and it has a high absorption coefficient of $>10^5$ cm^{-1} in the visible spectral region, which make this material attractive.[131] Another attractive feature of BiI_3 is that it can be solution-processed.[121, 122] In addition, its electron mobility was measured as 260 ± 50 $cm^2/V{\cdot}s$, which can be improved to 1,000 ± 200 $cm^2/V{\cdot}s$ by Sb doping.[128, 132] As such, BiI_3/organic HTM layers were used by Lehner *et al*., leading to a PCE of 0.35%.[122] Further improvements in device performance will inevitably require a better understanding of the material chemistry and optimising the components and device structures. Tiwari *et al.* showed that the performance of BiI_3 devices can be improved using a poly-(9,9-di-n-octylfluorenyl-2,7-diyl) (F8) hole transporting material instead of polytriarylamine (PTAA).[122, 123] Hamdeh *et al.* improved the PCE from 0.32% to 1% by annealing the as-deposited BiI_3 film under a solvent vapour environment.[121] Recently, anti-solvent treatment and an inverted structure were employed to the BiI_3 solar cells by Kang *et al*., and this new approach resulted in a 1.5% of PCE.[133] The device efficiency is increasing with these simple structural optimisation. Therefore, further effort to optimise structure of solar cells with bismuth iodide seems necessary to improve it.

Lead-based perovskites currently outperform all alternatives due to both lead's excellent properties and the huge research efforts on these materials. Despite the similarities in the electronic properties between the group-14 metals, tin-based perovskites have not yet become a perfect alternative because of their fast oxidation rate. Stable lead-free perovskites,

particularly bismuth-based perovskites and bismuth–iodine salts, are emerging and their device efficiencies are growing. I believe that lead-free halide perovskites and stable inorganic materials will take significant steps forward toward practical applications in photovoltaic areas with research to understand their physical properties.

1-4. The Basic Working Principles of Solar Cells

Semiconductors

On an atomic level, electrons exist in discrete quantum energy levels, or atomic orbitals. When a pair of atoms are combined to form a molecule, the molecular orbitals are rearranged, forming a pair of molecular orbitals with slightly higher and lower energy levels than the original levels as described in Figure 1-12 (a). When a very large number of atoms are combined in a solid, each atomic orbital is rearranged into very large number of energy levels. If the rearranged energy levels are so close that they are overlapped, they form continuous bands of energy (Figure 1-12 (b)).

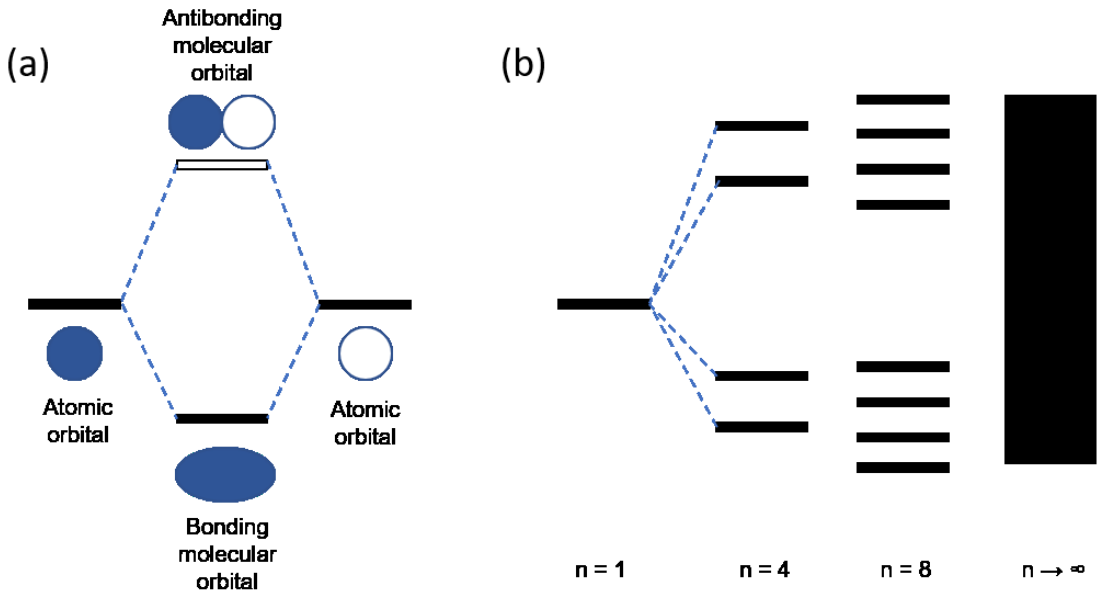

Figure 1-12. Schematic illustration to demonstrate (a) the formation of bonding and antibonding molecular orbitals for a diatomic system and (b) the formation of continuous bands from molecular orbitals.

These bands are occupied or nor occupied when the original molecular orbitals are occupied or not, respectively. The highest occupied band contains the valence electrons and it is called valence band (VB). The lowest unoccupied band is called conduction band (CB). When the valence band overlaps with the lowest unoccupied band in energy in a material, this material is called metal. In a metal, the empty states at similar energy level allow the electrons to be excited easily, and these electrons can act as transporters of heat or charges. Therefore, the metal can conduct the heat and electric current. When the valence band is completely full and separated from the next empty band by an energy gap, so called bandgap (ΔE_g), the solid is called a semiconductor or an insulator depending on the value of the bandgap. The electrons in this kind of materials require energy to overcome the band gap to be removed to the nearest unoccupied level, therefore these materials do not conduct hear or electricity easily.

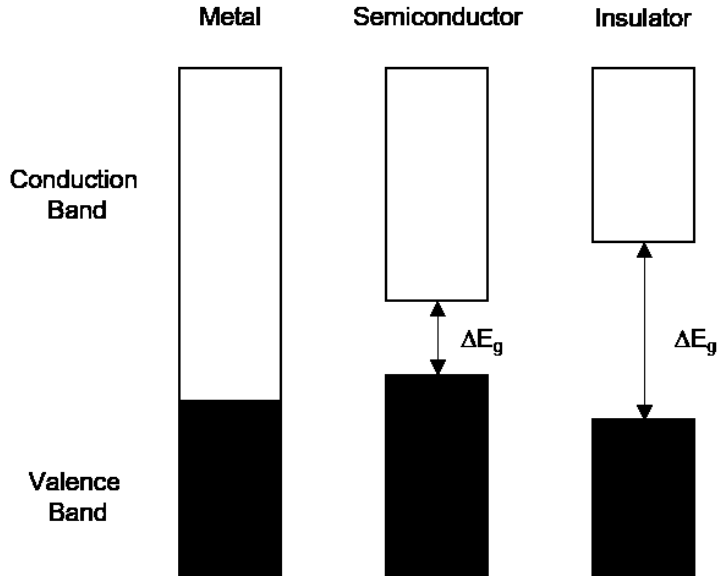

Figure 1-13. Schematic illustration of the band structure of a metal, a semiconductor and an insulator.

Semiconductors are distinguished these kinds of materials with bandgap between 0.5 eV and 3 eV (0.5 eV$\leq\Delta E_g \leq$3 eV). Semiconductors have a small conductivity in the dark because only a small number of valence electrons can have enough kinetic energy to overcome the bandgap at the room temperature. Insulators have wider band gap more than 3 eV ($\Delta E_g >$ 3eV). Therefore, conductivity at the room temperature is negligible. Materials with bandgap less than 0.5 eV ($\Delta E_g <$ 0.5 eV) can have a reasonably high conductivity at the room temperature, and therefore they are also called, semimetals.

Electrons in the semiconductors can get some kinetic energy from vibrations of the lattice and some of them are able to break free. The freed electrons which is excited to the conduction band are able to travel and transport charge or energy. Meanwhile, the vacancies, which are left after electrons are excited, are able to move and also can conduct. These semiconductors also can be conductive when they are exposed to the light of energy greater than their bandgap. When a photon is absorbed by an electron in a valence band, the electron becomes free from the lattice and promoted into the conduction band. This creates a vacancy in the valence band. These created free electron and hole by the light can conduct electricity, and it is called photoconductivity. Photovoltaic devices use these photoconductive semiconductors to convert solar energy into electricity and involve three processes.

Photovoltaics

In photovoltaic devices, the energy from photons is absorbed by a light absorber and then the electrons in the ground-state that absorb energy become excited, generating electron–hole pairs. Materials with a small dielectric constant have a relatively high electron–hole binding energy,

and so the electron–hole pairs generated by the photons to be bound are called excitons.[134] Obtaining free charge carriers in such materials requires a certain amount of energy to overcome the binding energy. Then, the free charges usually diffuse into an interface between the donor and acceptor materials and dissociate. In lead-based perovskite materials, their large dielectric constant leads to a low exciton binding energy (for MAPI, 55 ± 20 meV at room temperature) and while free charge carriers and weakly bound excitons coexist, the free charge carriers dominate.[29] The weekly bound perovskite excitons are also easily dissociated by thermal energy at room temperature. Finally, the charge carriers, electrons and holes, are collected by an external circuit. For more effective charge extraction/transfer, heterojunctions for the electron and hole transport layers are generally interposed between the electrode and perovskite layer. An effective solar cell device can be produced by transporting the generated charge carriers without loss through the recombination processes described below.

Photoexcitation

The generation of electron–hole pairs by light absorption is fundamental to the operation of a solar cell and an ideal solar cell absorber should be able to absorb sufficient sunlight to have high efficiency. Since light is both absorbed and reflected by the surface of a solar cell device and transmitted through the device, it cannot achieve complete absorption. While reflections can be reduced by introducing anti-reflection coatings, the transmittance relies on the light absorber.

When the photon energy (E) is less than the bandgap energy (E_g) ($E < E_g$), photons cannot excite the electrons from the valence band (VB) to the conduction band (CB). When a photon

has the energy equal to or larger than the bandgap energy ($E \geq E_g$), photons can excite the electrons, but excess energy is quickly lost and the carriers relax to the band edges. Although the photons have much more energy than the bandgap ($E > E_g$), the excess energy is lost, thus achieving the same result as ($E = E_g$).

Figure 1-14 shows a schematic of the optical absorption transitions of Si, which has an indirect bandgap, and GaAs, which has a direct bandgap. For materials like Si with indirect bandgap, the CB minimum and VB maximum aligns at different values of the wavevector (**k),** and therefore a photon with E_g is insufficient to create the electron–hole pair because the excitation of electrons across the fundamental bandgap requires a change in momentum. The extra momentum can be supplied by a phonon, which is a collective excitation, in a periodic or elastic arrangement of atoms in the material. The absorption coefficient (α) of this kind of material is relatively low, which leads to the devices having a thick light absorber to absorb sufficient light to generate charges. For efficient solar cells, the minority carrier diffusion length of the light absorber needs to exceed its absorption depth. Although Si has an indirect bandgap, it has a large recombination lifetime and large diffusion length, and so an efficient solar cell device can be produced with Si. In materials such as GaAs with a direct bandgap where the CB minimum and VB maximum occur at the same wavevector value, a photon with E_g creates an electron–hole pair. The materials with a direct bandgap generally have a high absorption coefficient, which means that the solar cell devices can be as thin as several hundreds of nanometers.[134]

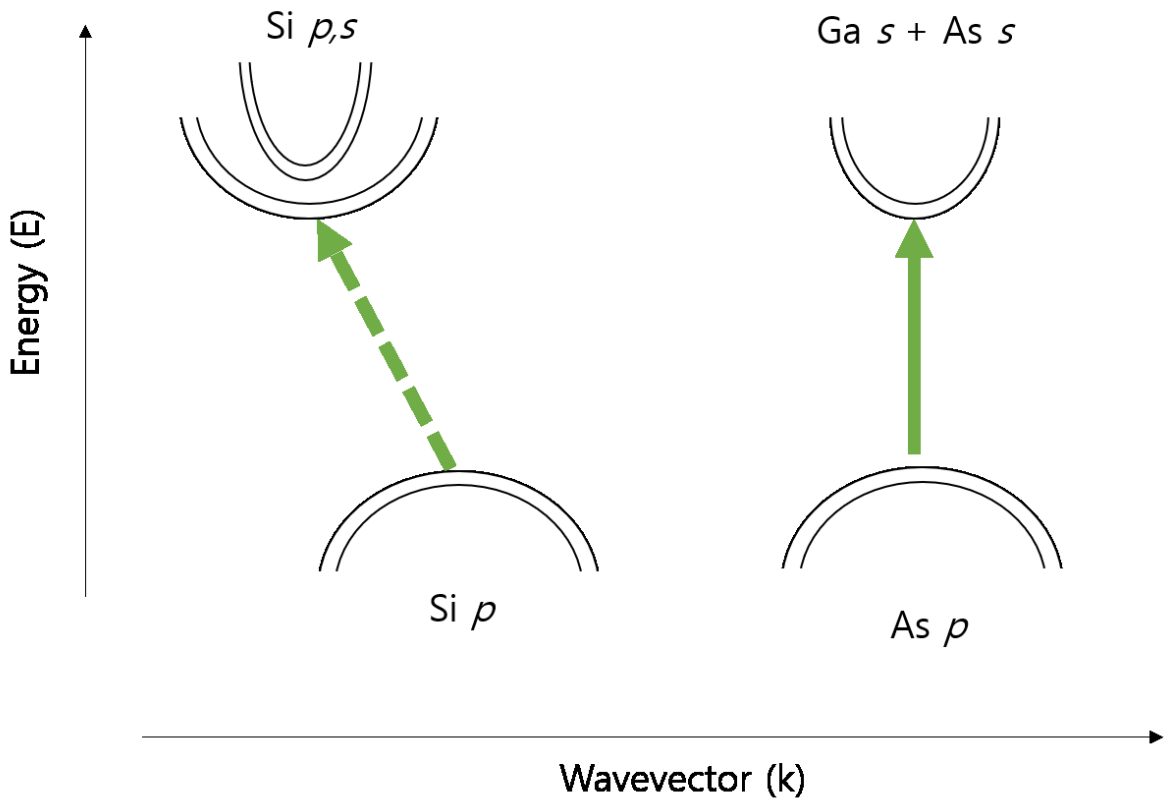

Figure 1-14. Schematic of the optical absorption transitions of a) Si and b) GaAs.

Charge-carrier Recombination

The absorption of photons causes electrons to move from the valence band (VB) to the conduction band (CB), forming electron–hole pairs. These electrons and holes recombine where these two carriers annihilate each other. Depending on whether the energy released by this recombination is emitted in the form of a photon or heat, recombination processes can be classified as either radiative recombination or non-radiative recombination. These recombination processes are undesirable in solar cell devices as they lose charge before they can be collected by the electrodes.

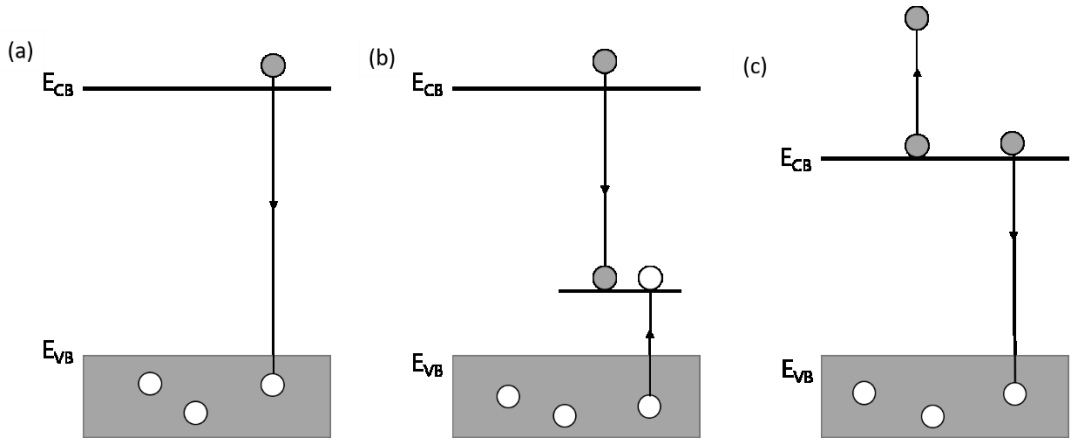

Figure 1-15. Recombination processes in solar cells: (a) radiative band-to-band, (2) non-radiative via a trap state and (3) Auger recombination. This figure is adapted from a reference[134].

Figure 1-15 illustrates different recombination pathways. The first recombination is free carrier band-to-band recombination, which is often referred to as radiative bimolecular recombination. This is the reverse process of photon absorption. In a direct bandgap material, when electrons have become relaxed to the valence band, they emit photons with energies equal to bandgap energy while the relaxation energy is partially shared with a phonon in a material with an indirect bandgap. The second recombination is the non-radiative recombination visa trap state. Impurities or defect states can form localised energy levels between the CB and VB of a semiconductor. This energy level can trap electrons and holes and they become relaxed through this energy level. The single-level trap recombination process relies on the position of the energy level of the trap state because when the energy level is very close to one of the band edges of CB or VB, it will not trap both electrons and holes. Meanwhile, if the energy level of the trap state is sufficiently far from the band edges, the charges can be easily trapped in this energy state. The third recombination is Auger recombination, which is another non-radiative recombination involving the interaction between three particles: two holes (or electrons) and

one electron (or hole). Electrons and holes directly recombine as a radiative recombination while the energy from the relaxation is delivered to another charge carrier and the excited electron or hole then rapidly relaxes and releases energy as phonons. All three recombination processes could happen simultaneously; therefore, the overall recombination rate is the sum of the rates of three processes.

In addition, the charge transferred to ETL or HTL can also go through a recombination processes as described above. If the thickness of ETL is longer than its carrier diffusion length, the transferred charge cannot transfer to the electrode. The transferred charge can recombine with the other charge remaining in the light absorber. When contact occurs between ETL and HTL due to pin-holes or cracks, the transferred holes and electrons are recombined at the spots.

Electron and Hole Collection Strategies

The devices' photocurrent is limited by the amount of charge extracted from the solar cell, whereas the photovoltage is dependent on the bandgap. Therefore, a small bandgap would increase the photocurrent as more electrons could be excited but lower the photovoltage. For efficient solar cell devices, as much generated charge should be transferred to the electrodes as possible to minimise the charge recombination.

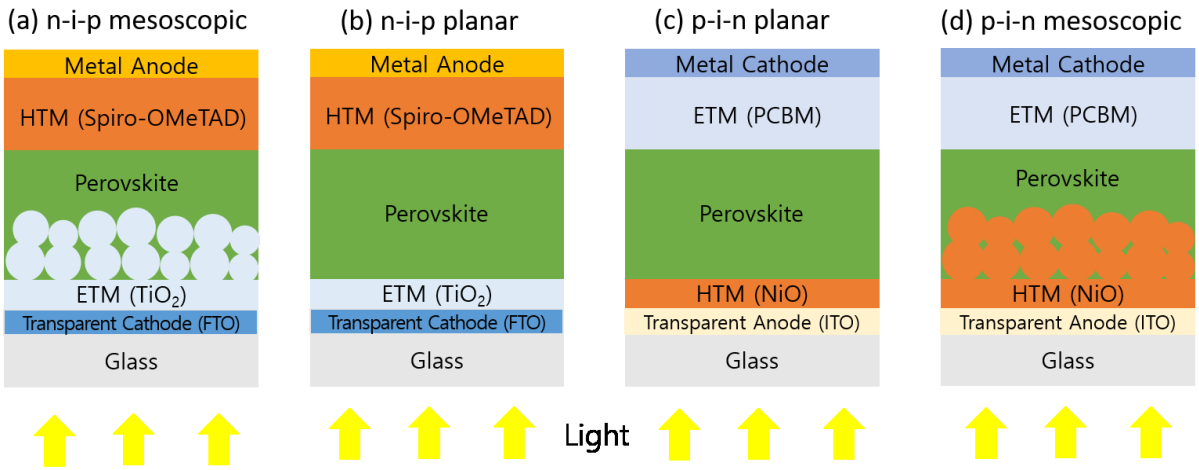

Figure1-16. Generic structures of perovskite solar cells: (a) conventional n-i-p mesoscopic, (b) conventional n-i-p planar, (c) inverted p-i-n planar and (d) inverted p-i-n mesoscopic structures.[135]

Figure 1-16 shows the four major device structures used for perovskite solar cells. Each structure consists of six basic components: a transparent electrode, a metallic electrode, a light absorber, an electron transport layer, a hole transport layer and a glass substrate. The two electrodes transfer the collected charges to the external circuit and two transport layers are necessary to improve the sensitivity of the charge collection for the respective electrodes.[136] The components of the solar cells can vary depending on the generation of the solar cells or the type of light absorber. The first two perovskite device structures are called 'conventional' device structures because they parallel DSSCs by employing nanocrystalline TiO_2 as the electron transport layer (ETL), but the light-harvesting dye and the liquid electrolyte were replaced with the halide perovskite and the solid-state hole transport layer, respectively. If the HTL is on top of the perovskite absorber and the ETL is below it, forming an p-i-n structure, it is called an 'inverted' structure.[137]

Figure 1-17 shows the schematic of the charge transfer processes in a conventional perovskite device. There are three desirable processes: (1) photo-excitation, (2) electron transfer to the ETM (TiO_2 or SnO_2) and (3) hole transfer to the HTM such as a spiro-OMTAD or Poly(3-hexylthiophene-2,5-diyl) (P3HT) and then the transferred charges goes to electrodes, generating electricity. However, there are four undesirable processes that block the charge transfer to the electrodes, (4) recombination of generated charges, (5, 6) charge back transfer at the interfaces and (7) charge back transfer between the ETM and HTM when there is contact between them.

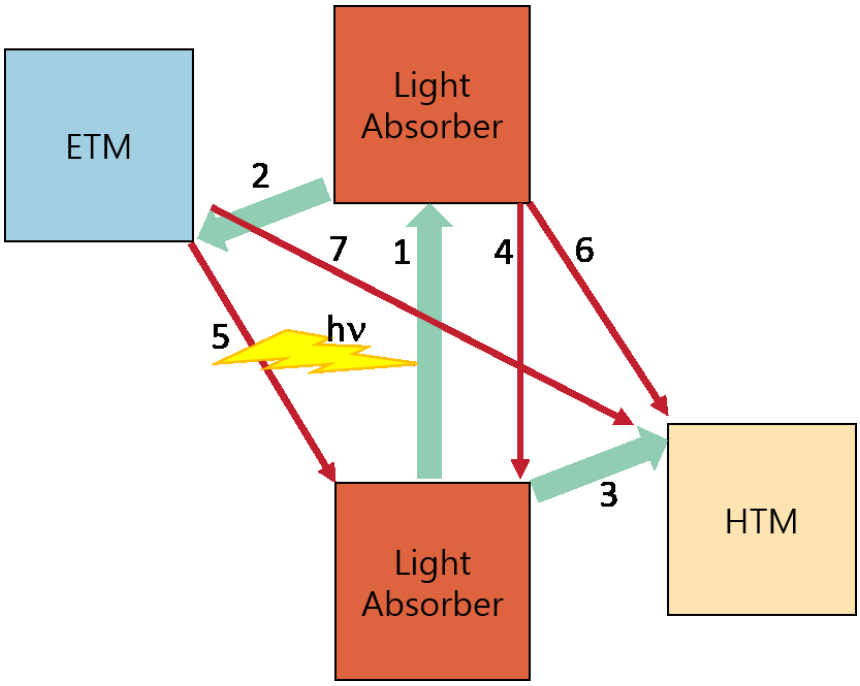

Figure 1-17. The schematic of the electron-transfer processes in a perovskite solar cell device. (1) photo-excitation, (2) electron transfer to the ETM, (3) hole transfer to the HTM, (4) recombination of generated charges, (5, 6) charge back transfer at the interfaces and (7) charge back transfer between the ETM and HTM.

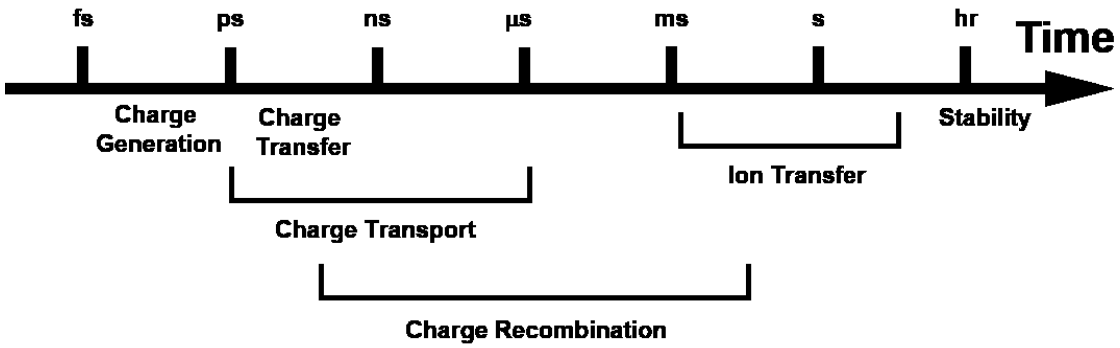

Figure 1-18. The timescale of the charge processes in a perovskite solar cell.

Figure 1-18 shows the timescale of the charge processes in a perovskite solar cell. The absorbed photons generate the exciton and subsequently, free charge carriers, in the timescale range of femtosecond to picosecond. Generally, electrons and holes are transported to ETL and HTL within several nanoseconds through the bulk by diffusion or drift and then usually extracted by the transfer materials within several microseconds.[134, 138-140]

1-5. Project Aims and Thesis Outline

The main motivation of this project is to contribute to efforts to manufacture devices with lead-free and air-stable materials, particularly bismuth-iodide- and bismuth-and-antimony-based perovskites. Achieving this requires a comprehensive understanding of not only the material itself but also the relationship between the processing parameters, film properties and device performance. Thus, this thesis focuses on understanding these materials by a range of characterisation techniques and then finding ways to improve their solar cell performance based on this understanding.

Specifically, this project uses steady-state and transient spectroscopic techniques to reveal the optoelectronic properties of bismuth iodide, x-ray diffraction techniques to obtain crystallographic information and electron microscopy to see the morphologies of the fabricated films. The experimental details of these techniques can be found in Chapter 2.

Chapter 3 focuses on finding a way to improve the charge separation and photovoltaic performance of bismuth iodide. This was achieved using an *in situ*-formed bismuth sulfide iodide interlayer between the light absorber and the ETL.

Chapter 4 presents two ways of improving the optoelectronic properties of bismuth-based perovskites. The first approach introduces a quasi-2D perovskite structure by changing the small A cation methylammonium (MA^+) to larger one, phenylethylammonium (PEA^+). The other approach is to mix bismuth and antimony in a perovskite structure, forming $(MA)_3(Bi_{1-x}Sb_x)2I_9$. They successfully improved the optoelectronic properties for the solar cell performance.

Chapter 5 introduces nanocrystals with bismuth- and antimony-based perovskite and their mixture. The fabrication of the nanocrystals and their characterisation can be found in this chapter.

Chapter 6 contains the conclusion and describes future work. It is believed that the insights from the studies in this thesis are also applicable to lead-free and air-stable materials and provides proper recommendations for future work.

1-6. References

1. S. Chu and A. Majumdar, *Nature*, 2012, **488**, 294-303.

2. World Energy Outlook 2018, https://www.iea.org/weo2018/fuels/, (accessed September, 23, 2019).

3. Statistical Review of World Energy, file:///C:/Users/ybw01/Dropbox/From%20office%20Compuer/Gradulation_Thesis/references/3_bp-stats-review-2019-full-report.pdf, (accessed September 23, 2019).

4. V. Smil, *Science, energy, ethics, and civilization*, Cambridge University Press, Cambridge, 2010.

5. D. J. MacKay, *Sustainable Energy - without the hot air*, UIT Cambridge Ltd Cambridge, 2009.

6. Global Market Outlook 2019-2023, file:///C:/Users/ybw01/Downloads/222.pdf, (accessed September 23, 2019).

7. V. K. Mehta and R. Mehta, *Principle of Power System*, S. Chand Publishing, New Delhi, 2005.

8. Sunny uplands: Alternative energy will no longer be alternative, https://www.economist.com/news/2012/11/21/sunny-uplands, (accessed September 23, 2019).

9. National Renewable Energy Laboratory. Research Cell Record Efficiency Chart, https://www.nrel.gov/pv/assets/pdfs/best-research-cell-efficiencies.20200406.pdf, (accessed 6 April, 2020).

10. B. S. Xakalashe and M. Tangstad, *Silicon processing: from quartz to crystalline silicon solar cells*, Southern African Institute of Mining and Metallurgy Johannesburg, 2011.

11. M. A. Green, *J. Mater. Sci.: Mater. Electron*, 2007, **18**, S15-S19.

12. A. Goodrich, P. Hacke, Q. Wang, B. Sopori, R. Margolis, T. L. James and M. Woodhouse, *Sol. Energy Mater. Sol. Cells*, 2013, **114**, 110-135.

13. T. Tiedje, E. Yablonovitch, G. D. Cody and B. G. Brooks, *IEEE Trans. Electron Devices*, 1984, **31**, 711-716.

14. K. Dovidenko, J. Cournoyer, D. Vernooy, B. Lita and F. Seymour, *Microsc. Microanal.*, 2010, **16**, 1344-1345.

15. D. H. Baek, S. B. Kim and D. K. Schroder, *J. Appl. Phys.*, 2008, **104**.

16. D. R. Wight, D. Bradley, G. Williams, M. Astles, S. J. C. Irvine and C. A. Jones, *J. Cryst. Growth*, 1982, **59**, 323-331.

17. D. o. E. a. P. S. National Research Council, National Materials and Manufacturing Board, Committee on Harnessing Light: Capitalizing on Optical Science Trends and Challenges for Future Research, *Optics and Photonics: Essential Technologies for Our Nation*, National Academies Press, Washington, D.C., 2013.

18. M. T. Winkler, W. Wang, O. Gunawan, H. J. Hovel, T. K. Todorov and D. B. Mitzi, *Energy Environ. Sci.*, 2014, **7**, 1029-1036.

19. W. Wang, M. T. Winkler, O. Gunawan, T. Gokmen, T. K. Todorov, Y. Zhu and D. B. Mitzi, *Advanced Energy Materials*, 2014, **4**.

20. P. C. Choubey, A. Oudhia and R. Dewangan, *Recent Research in Science and Technology*, 2012, **4**.

21. J. Nelson, *Materials Today*, 2011, **14**, 462-470.

22. G. Hodes, *Science*, 2013, **342**, 317-318.

23. G. H. Carey, A. L. Abdelhady, Z. J. Ning, S. M. Thon, O. M. Bakr and E. H. Sargent, *Chem. Rev.*, 2015, **115**, 12732-12763.

24. N. Tetreault and M. Gratzel, *Energy Environ. Sci.*, 2012, **5**, 8506-8516.

25. N. G. Park, *Materials Today*, 2015, **18**, 65-72.

26. S. D. Stranks, G. E. Eperon, G. Grancini, C. Menelaou, M. J. P. Alcocer, T. Leijtens, L. M. Herz, A. Petrozza and H. J. Snaith, *Science*, 2013, **342**, 341-344.

27. W.-J. Yin, T. Shi and Y. Yan, Adv. Mater., 2014, **26**, 4653.

28. M. Z. Liu, M. B. Johnston and H. J. Snaith, *Nature*, 2013, **501**, 395-398.

29. V. D'Innocenzo, G. Grancini, M. J. P. Alcocer, A. R. S. Kandada, S. D. Stranks, M. M. Lee, G. Lanzani, H. J. Snaith and A. Petrozza, *Nat. Commun.*, 2014, **5**, 3586.

30. W. Shockley and H. J. Queisser, *J. Appl. Phys.*, 1961, **32**, 510-519.

31. W. E. I. Sha, X. G. Ren, L. Z. Chen and W. C. H. Choy, *Appl. Phys. Lett.*, 2015, **106**, 221104.

32. D. Weber, *Z. Naturforsch. B*, 1978, **33**, 1443-1445.

33. M. A. Green, A. Ho-Baillie and H. J. Snaith, *Nat. Photonics*, 2014, **8**, 506-514.

34. K. T. Butler, J. M. Frost and A. Walsh, *Mater. Horiz.*, 2015, **2**, 228-231.

35. A. Kojima, K. Teshima, Y. Shirai and T. Miyasaka, *J. Am. Chem. Soc.*, 2009, **131**, 6050-6051.

36. J.-H. Im, C.-R. Lee, J.-W. Lee, S.-W. Park and N.-G. Park, *Nanoscale*, 2011, **3**, 4088-4093.

37. M. M. Lee, J. Teuscher, T. Miyasaka, T. N. Murakami and H. J. Snaith, *Science*, 2012, **338**, 643-647.

38. J. Burschka, N. Pellet, S.-J. Moon, R. Humphry-Baker, P. Gao, M. K. Nazeeruddin and M. Graetzel, *Nature*, 2013, **499**, 316-+.

39. C. G. Wu, C. H. Chiang, Z. L. Tseng, M. K. Nazeeruddin, A. Hagfeldt and M. Gratzel, *Energy Environ. Sci.*, 2015, **8**, 2725-2733.

40. M. Saliba, T. Matsui, J. Y. Seo, K. Domanski, J. P. Correa-Baena, M. K. Nazeeruddin, S. M. Zakeeruddin, W. Tress, A. Abate, A. Hagfeldt and M. Gratzel, *Energy Environ. Sci.*, 2016, **9**, 1989-1997.

41. M. Saliba, T. Matsui, K. Domanski, J. Y. Seo, A. Ummadisingu, S. M. Zakeeruddin, J. P. Correa-Baena, W. R. Tress, A. Abate, A. Hagfeldt and M. Gratzel, *Science*, 2016, **354**, 206-209.

42. B. Conings, J. Drijkoningen, N. Gauquelin, A. Babayigit, J. D'Haen, L. D'Olieslaeger, A. Ethirajan, J. Verbeeck, J. Manca, E. Mosconi, F. De Angelis and H. G. Boyen, *Adv. Energy Mater.*, 2015, **5**.

43. A. M. A. Leguy, Y. Hu, M. Campoy-Quiles, M. I. Alonso, O. J. Weber, P. Azarhoosh, M. van Schilfgaarde, M. T. Weller, T. Bein, J. Nelson, P. Docampo and P. R. F. Barnes, *Chem. Mater.*, 2015, **27**, 3397-3407.

44. T. Leijtens, R. Prasanna, A. Gold-Parker, M. F. Toney and M. D. McGehee, *ACS Energy Lett.*, 2017, **2**, 2159-2165.

45. N. Aristidou, I. Sanchez-Molina, T. Chotchuangchutchaval, M. Brown, L. Martinez, T. Rath and S. A. Haque, *Angew. Chem. Int.*, 2015, **54**, 8208-8212.

46. Y. Han, S. Meyer, Y. Dkhissi, K. Weber, J. M. Pringle, U. Bach, L. Spiccia and Y. B. Cheng, *J. Mater. Chem. A*, 2015, **3**, 8139-8147.

47. D. Liu and T. L. Kelly, *Nat. Photonics*, 2014, **8**, 133-138.

48. D. Q. Bi, G. Boschloo, S. Schwarzmuller, L. Yang, E. M. J. Johansson and A. Hagfeldt, *Nanoscale*, 2013, **5**, 11686-11691.

49. X. Liu, K. W. Tsai, Z. Zhu, Y. Sun, C. C. Chueh and A. K. Y. Jen, *Adv. Mater. Interfaces*, 2016, **3**.

50. Z. L. Zhu, Y. Bai, X. Liu, C. C. Chueh, S. H. Yang and A. K. Y. Jen, *Adv. Mater.*, 2016, **28**, 6478-6484.

51. N. J. Jeon, J. H. Noh, W. S. Yang, Y. C. Kim, S. Ryu, J. Seo and S. I. Seok, *Nature*, 2015, **517**, 476-480.

52. G. E. Eperon, G. M. Paterno, R. J. Sutton, A. Zampetti, A. A. Haghighirad, F. Cacialli and H. J. Snaith, *J. Mater. Chem. A*, 2015, **3**, 19688-19695.

53. I. C. Smith, E. T. Hoke, D. Solis-Ibarra, M. D. McGehee and H. I. Karunadasa, *Angew. Chem. Int.*, 2014, **53**, 11232-11235.

54. L. D. Grant, *Environmental Toxicants: Human Exposures and Their Health Effects*, Wiley, New Jersey, 3 edn., 2008.

55. M. Grätzel, *Nat. Mater.*, 2014, **13**, 838-842.

56. J. Zhang, C. H. Yu, L. L. Wang, Y. Z. Li, Y. H. Ren and K. Shum, *Sci. Rep.*, 2014, **4**.

57. K. Yamada, S. Funabiki, H. Horimoto, T. Matsui, T. Okuda and S. Ichiba, *Chem. Lett.*, 1991, **20**, 801-804.

58. D. E. Scaife, P. F. Weller and W. G. Fisher, *J. Solid State Chem.*, 1974, **9**, 308-314.

59. K. Shum, Z. Chen, J. Qureshi, C. L. Yu, J. J. Wang, W. Pfenninger, N. Vockic, J. Midgley and J. T. Kenney, *Appl. Phys. Lett.*, 2010, **96**.

60. I. Chung, B. Lee, J. Q. He, R. P. H. Chang and M. G. Kanatzidis, *Nature*, 2012, **485**, 486-494.

61. F. Hao, C. C. Stoumpos, R. P. H. Chang and M. G. Kanatzidis, *J. Am. Chem. Soc.*, 2014, **136**, 8094-8099.

62. N. K. Noel, S. D. Stranks, A. Abate, C. Wehrenfennig, S. Guarnera, A. A. Haghighirad, A. Sadhanala, G. E. Eperon, S. K. Pathak, M. B. Johnston, A. Petrozza, L. M. Herz and H. J. Snaith, *Energy Environ. Sci.*, 2014, **7**, 3061-3068.

63. L. Lanzetta, J. M. Marin-Beloqui, I. Sanchez-Molina, D. Ding and S. A. Haque, *ACS Energy Lett.*, 2017, **2**, 1662-1668.

64. S. Y. Shao, J. J. Dong, H. Duim, G. H. ten Brink, G. R. Blake, G. Portale and M. A. Loi, *Nano Energy*, 2019, **60**, 810-816.

65. X. H. Liu, K. Yan, D. W. Tan, X. Liang, H. M. Zhang and W. Huang, *ACS Energy Lett.*, 2018, **3**, 2701-2707.

66. F. Hao, C. C. Stoumpos, P. J. Guo, N. J. Zhou, T. J. Marks, R. P. H. Chang and M. G.

Kanatzidis, *J. Am. Chem. Soc.*, 2015, **137**, 11445-11452.

67. X. Jiang, F. Wang, Q. Wei, H. Li, Y. Shang, W. Zhou, C. Wang, P. Cheng, Q. Chen, L. Chen and Z. Ning, *Nat. Commun.* 2020, **11**, 1245.

68. M. Lee, D. Kim, Y. K. Lee, H. Koo, K. T. Lee and I. Chung, *ACS Appl. Energy Mater.*, 2020, 3, 6, 5581–5588.

69. K. Nishimura, M. A. Kamarudin, D. Hirotani, K. Hamada, Q. Shen, S. Iikubo, T. Minemoto, K. Yoshino and S. Hayase, *Nano Energy*, 2020, **74**, 104858.

70. V. M. Kiyek, Y. A. Birkhölzer, Y. Smirnov, M. Ledinsky, Z. Remes, J. Momand, B. J. Kooi, G. Koster, G. Rijnders and M. Morales-Masis, *Adv. Mater. Interfaces*, 2020, **n/a**, 2000162.

71. X. Meng, Y. Wang, J. Lin, X. Liu, X. He, J. Barbaud, T. Wu, T. Noda, X. Yang and L. Han, *Joule*, 2020, **4**, 902-912.

72. M. H. Kumar, S. Dharani, W. L. Leong, P. P. Boix, R. R. Prabhakar, T. Baikie, C. Shi, H. Ding, R. Ramesh, M. Asta, M. Graetzel, S. G. Mhaisalkar and N. Mathews, *Adv. Mater.*, 2014, **26**, 7122.

73. S. Gupta, T. Bendikov, G. Hodes and D. Cahen, *ACS Energy Lett.*, 2016, **1**, 1028-1033.

74. T. Wang, Q. Tai, X. Guo, J. Cao, C.-K. Liu, N. Wang, D. Shen, Y. Zhu, C.-S. Lee and F. Yan, *ACS Energy Lett.*, 2020, DOI: 10.1021/acsenergylett.0c00526, 1741-1749.

75. G. Liu, C. Liu, Z. Lin, J. Yang, Z. Huang, L. Tan and Y. Chen, *ACS Appl. Mater. Interfaces*, 2020, **12**, 14049-14056.

76. Z. Lin, C. Liu, G. Liu, J. Yang, X. Duan, L. Tan and Y. Chen, *Chem. Commun.*, 2020, **56**, 4007-4010.

77. F. Li, Y. Xie, Y. Hu, M. Long, Y. Zhang, J. Xu, M. Qin, X. Lu and M. Liu, *ACS Energy Lett.*, 2020, **5**, 1422-1429.

78. M. Li, W.-W. Zuo, Y.-G. Yang, M. H. Aldamasy, Q. Wang, S. H. T. Cruz, S.-L. Feng, M. Saliba, Z.-K. Wang and A. Abate, *ACS Energy Lett.*, 2020, DOI: 10.1021/acsenergylett.0c00782, 1923-1929.

79. J.-T. Lin, Y.-K. Hu, C.-H. Hou, C.-C. Liao, W.-T. Chuang, C.-W. Chiu, M.-K. Tsai, J.-J. Shyue and P.-T. Chou, *Small*, 2020, **16**, 2000903.

80. Z. Wang, F. Wang, B. Zhao, S. Qu, T. Hayat, A. Alsaedi, L. Sui, K. Yuan, J. Zhang, Z. Wei and Z. a. Tan, *J. Phys. Chem. Lett.*, 2020, **11**, 1120-1127.

81. F. X. Wei, Z. Y. Deng, S. J. Sun, N. T. P. Hartono, H. L. Seng, T. Buonassisi, P. D.

Bristowe and A. K. Cheetham, *Chem. Commun.*, 2019, **55**, 3721-3724.

82. Z. F. Tan, J. H. Li, C. Zhang, Z. Li, Q. S. Hu, Z. W. Xiao, T. Kamiya, H. Hosono, G. D. Niu, E. Lifshitz, Y. B. Cheng and J. Tang, *Adv. Funct. Mater.*, 2018, **28**.

83. A. H. Slavney, T. Hu, A. M. Lindenberg and H. I. Karunadasa, *J. Am. Chem. Soc.*, 2016, **138**, 2138-2141.

84. F. Igbari, R. Wang, Z. K. Wang, X. J. Ma, Q. Wang, K. L. Wang, Y. Zhang, L. S. Liao and Y. Yang, *Nano Letters*, 2019, **19**, 2066-2073.

85. A. Kulkarni, A. K. Jena, M. Ikegami and T. Miyasaka, *Chem. Commun.*, 2019, **55**, 4031-4034.

86. H. M. Zhu, M. B. Johansson and E. M. J. Johansson, *Chemsuschem*, 2018, **11**, 1114-1120.

87. S. Zhao, K. Yamamoto, S. S. Iikubo, S. Hayase and T. L. Ma, *J. Phys. Chem. Solids*, 2018, **117**, 117-121.

88. M. Delor, A. H. Slavney, N. R. Wolf, M. R. Filip, J. B. Neaton, H. I. Karunadasa and N. S. Ginsberg, *ACS Energy Lett.*, 2020, **5**, 1337-1345.

89. E. Greul, M. L. Petrus, A. Binek, P. Docampo and T. Bein, *J. Mater. Chem. A*, 2017, **5**, 19972-19981.

90. Y. Liu, X. Rong, M. Li, M. S. Molokeev, J. Zhao and Z. Xia, *Angew. Chem. Int. Ed.*, 2020, **n/a**.

91. N. Pai, J. Lu, M. Wang, A. S. R. Chesman, A. Seeber, P. V. Cherepanov, D. C. Senevirathna, T. R. Gengenbach, N. V. Medhekar, P. C. Andrews, U. Bach and A. N. Simonov, *J. Mater. Chem. A*, 2020, **8**, 2008-2020.

92. B. Yang, F. Hong, J. Chen, Y. Tang, L. Yang, Y. Sang, X. Xia, J. Guo, H. He, S. Yang, W. Deng and K. Han, *Angew. Chem. Int. Ed.*, 2019, **58**, 2278-2283.

93. X.-G. Zhao, D. Yang, J.-C. Ren, Y. Sun, Z. Xiao and L. Zhang, *Joule*, 2018, **2**, 1662-1673.

94. F. Igbari, Z.-K. Wang and L.-S. Liao, *Adv. Energy Mater.*, 2019, **9**, 1803150.

95. B. Lee, C. C. Stoumpos, N. Zhou, F. Hao, C. Malliakas, C.-Y. Yeh, T. J. Marks, M. G. Kanatzidis and R. P. H. Chang, *J. Am. Chem. Soc.*, 2014, **136**, 15379-15385.

96. I. Chung, J.-H. Song, J. Im, J. Androulakis, C. D. Malliakas, H. Li, A. J. Freeman, J. T. Kenney and M. G. Kanatzidis, *J. Am. Chem. Soc.*, 2012, **134**, 8579-8587.

97. W. H. Ning and F. Gao, *Adv. Mater.*, 2019, **31**.

98. K. M. McCall, C. C. Stoumpos, S. S. Kostina, M. G. Kanatzidis and B. W. Wessels, *Chem. Mater.*, 2017, **29**, 4129-4145.

99. M. Scholz, M. Morgenroth, K. Oum and T. Lenzer, *J. Phys. Chem. C*, 2018, **122**, 5854-5863.

100. B. W. Park, B. Philippe, X. Zhang, H. Rensmo, G. Boschloo and E. M. J. Johansson, *Adv. Mat.*, 2015, **27**, 6806-6813.

101. R. L. Z. Hoye, R. E. Brandt, A. Osherov, V. Stevanovic, S. D. Stranks, M. W. B. Wilson, H. Kim, A. J. Akey, J. D. Perkins, R. C. Kurchin, J. R. Poindexter, E. N. Wang, M. G. Bawendi, V. Bulovic and T. Buonassisi, *Chem. Eur. J.*, 2016, **22**, 2605-2610.

102. P. Karuppuswamy, K. M. Boopathi, A. Mohapatra, H. C. Chen, K. T. Wong, P. C. Wang and C. W. Chu, *Nano Energy*, 2018, **45**, 330-336.

103. M. Saba, M. Cadelano, D. Marongiu, F. Chen, V. Sarritzu, N. Sestu, C. Figus, M. Aresti, R. Piras, A. G. Lehmann, C. Cannas, A. Musinu, F. Quochi, A. Mura and G. Bongiovanni, *Nat. Commun.*, 2014, **5**.

104. B. Ghosh, S. Chakraborty, H. Wei, C. Guet, S. Li, S. Mhaisalkar and N. Mathews, *J. Phys. Chem. C*, 2017, **121**, 17062-17067.

105. X. Zhang, G. Wu, Z. Gu, B. Guo, W. Liu, S. Yang, T. Ye, C. Chen, W. Tu and H. Chen, *Nano Res.*, 2016, **9**, 2921-2930.

106. M. Lyu, J. H. Yun, M. Cai, Y. Jiao, P. V. Bernhardt, M. Zhang, Q. Wang, A. Du, H. Wang, G. Liu and L. Wang, *Nano Res.*, 2016, **9**, 692-702.

107. J. Shin, M. Kim, S. Jung, C. S. Kim, J. Park, A. Song, K. B. Chung, S. H. Jin, J. H. Lee and M. Song, *Nano Res.*, 2018, **11**, 6283-6293.

108. F. Bai, Y. H. Hu, Y. Q. Hu, T. Qiu, X. L. Miao and S. F. Zhang, *Sol. Energy Mater. Sol. Cells*, 2018, **184**, 15-21.

109. S. Oz, J.-C. Hebig, E. Jung, T. Singh, A. Lepcha, S. Olthof, J. Flohre, Y. Gao, R. German, P. H. M. van Loosdrecht, K. Meerholz, T. Kirchartz and S. Mathur, *Sol. Energy Mater Sol.*, 2016, **158**, 195-201.

110. S. M. Jain, D. Phuyal, M. L. Davies, M. Li, B. Philippe, C. De Castro, Z. Qiu, J. Kim, T. Watson, W. C. Tsoi, O. Karis, H. Rensmo, G. Boschloo, T. Edvinsson and J. R. Durrant, *Nano Energy*, 2018, **49**, 614-624.

111. J. C. Hebig, I. Kuhn, J. Flohre and T. Kirchartz, *ACS Energy Lett.*, 2016, **1**, 309-314.

112. P. C. Harikesh, H. K. Mulmudi, B. Ghosh, T. W. Goh, Y. T. Teng, K. Thirumal, M. Lockrey, K. Weber, T. M. Koh, S. Li, S. Mhaisalkar and N. Mathews, *Chem. Mater.*, 2016, **28**, 7496-7504.

113. F. Y. Jiang, D. W. Yang, Y. Y. Jiang, T. F. Liu, X. G. Zhao, Y. Ming, B. W. Luo, F. Qin, J. C. Fan, H. W. Han, L. J. Zhang and Y. H. Zhou, *J. Am. Chem. Soc.*, 2018, **140**, 1019-1027.

114. K. M. Boopathi, P. Karuppuswamy, A. Singh, C. Hanmandlu, L. Lin, S. A. Abbas, C. C. Chang, P. C. Wang, G. Li and C. W. Chu, *J. Mater. Chem. A*, 2017, **5**, 20843-20850.

115. B. Hwang and J.-S. Lee, *Nanoscale*, 2018, **10**, 8578-8584.

116. A. A. Hussain, A. K. Rana and M. Ranjan, *Nanoscale*, 2019, **11**, 1217-1227.

117. S. S. Bhosale, A. K. Kharade, E. Jokar, A. Fathi, S.-m. Chang and E. W.-G. Diau, *J. Am. Chem. Soc.*, 2019, **141**, 20434-20442.

118. B.-M. Bresolin, S. B. Hammouda and M. Sillanpää, *J. Photochem. Photobiol. A*, 2019, **376**, 116-126.

119. Y. Dai, C. Poidevin, C. Ochoa-Hernández, A. A. Auer and H. Tüysüz, *Angew. Chem. Int. Ed.*, 2020, **59**, 5788-5796.

120. Y. Dai and H. Tüysüz, *ChemSusChem*, 2019, **12**, 2587-2592.

121. U. H. Hamdeh, R. D. Nelson, B. J. Ryan, U. Bhattacharjee, J. W. Petrich and M. G. Panthani, *Chem. Mater.*, 2016, **28**, 6567-6574.

122. A. J. Lehner, D. H. Fabini, H. A. Evans, C. A. Hebert, S. R. Smock, J. Hu, H. B. Wang, J. W. Zwanziger, M. L. Chabinyc and R. Seshadri, *Chem. Mater.*, 2015, **27**, 7137-7148.

123. D. Tiwari, D. Alibhai and D. J. Fermin, *ACS Energy Lett.*, 2018, **3**, 1882-1886.

124. F. A. Cotton, G. Wilkinson, C. A. Murillo, M. Bochmann and R. Grimes, *Advanced Inorganic Chemistry*, Wiley, New York, 1999.

125. N. V. Sidgwick, *Electronic Theory of Valency*, H. Milford, Oxford, 1953.

126. D. Nason and L. Keller, *J. Cryst. Growth*, 1995, **156**, 221-226.

127. R. A. Mackay and W. Henderson, *Introduction to Modern Inorganic Chemisty*, CRC Press, 6 edn., 2002.

128. A. T. Lintereur, W. Qiu, J. C. Nino and J. Baciak, *Nuclear Instruments & Methods in Physics Research Section a-Accelerators Spectrometers Detectors and Associated Equipment*, 2011, **652**, 166-169.

129. K. M. Boopathi, S. Raman, R. Mohanraman, F. C. Chou, Y. Y. Chen, C. H. Lee, F. C. Chang and C. W. Chu, *Sol. Energy Mater. Sol. Cells*, 2014, **121**, 35-41.

130. N. J. Podraza, W. Qiu, B. B. Hinojosa, H. X. Xu, M. A. Motyka, S. R. Phillpot, J. E. Baciak, S. Trolier-McKinstry and J. C. Nino, *J. Appl. Phys.*, 2013, **114**.

131. R. E. Brandt, R. C. Kurchin, R. L. Z. Hoye, J. R. Poindexter, M. W. B. Wilson, S. Sulekar, F. Lenahan, P. X. T. Yen, V. Stevanovic, J. C. Nino, M. G. Bawendi and T. Buonassisi, *J. Phys. Chem. Lett.*, 2015, **6**, 4297-4302.

132. H. Han, M. Hong, S. S. Gokhale, S. B. Sinnott, K. Jordan, J. E. Baciak and J. C. Nino, *J. Phys. Chem. C,* 2014, **118**, 3244-3250.

133. J. Kang, S. Chen, X. Zhao, H. Yin, W. Zhang, M. Al-Mamun, P. Liu, Y. Wang and H. Zhao, *Nano Energy*, 2020, **73**, 104799.

134. J. Nelson, *The Physics of solar cells*, Imperial College Press, 2003.

135. Perovskites and Perovskite Solar Cells: An Introduction, https://www.ossila.com/pages/perovskites-and-perovskite-solar-cells-an-introduction, (accessed November 14, 2019).

136. Z. N. Song, S. C. Watthage, A. B. Phillips and M. J. Heben, *J. Photonics Energy*, 2016, **6**.

137. K. C. Wang, J. Y. Jeng, P. S. Shen, Y. C. Chang, E. W. G. Diau, C. H. Tsai, T. Y. Chao, H. C. Hsu, P. Y. Lin, P. Chen, T. F. Guo and T. C. Wen, *Sci. Rep.*, 2014, **4**.

138. G. C. Xing, N. Mathews, S. Y. Sun, S. S. Lim, Y. M. Lam, M. Gratzel, S. Mhaisalkar and T. C. Sum, *Science*, 2013, **342**, 344-347.

139. Z. G. Xiao, Q. F. Dong, C. Bi, Y. C. Shao, Y. B. Yuan and J. S. Huang, *Adv. Mater.*, 2014, **26**, 6503-6509.

140. J. J. Shi, Y. M. Li, Y. S. Li, D. M. Li, Y. H. Luo, H. J. Wu and Q. B. Meng, *Joule*, 2018, **2**, 879-901.

Chapter 2: Experimental Technique

2-1. Materials and Sample Fabrication

Materials

TiO_2 nanoparticle paste (30NR-D), phenylethylammonium iodide (PEAI) and Methylammonium iodide (MAI) were purchased from Dyesol Ltd. Antimony bromide, antimony iodide and caesium bromide were obtained from Alfa Aesar. $N(PhBr)_3SbCl_6$, bismuth bromide, bismuth iodide, mp-Al_2O_3 in isopropanol (20 wt%), tin chloride dihydrate, lithium bis(trifluoromethylsulphonyl)imide (LiTFSI), tert-butyl pyridine (TBP), acetonitrile, oleic acid, oleylamine, terpineol, titanium isopropoxide, 2-methyloxyethanol, poly (methyl methacrylate) (PMMA), Poly(3-hexylthiophene-2,5-diyl) (P3HT), ethanolamine and Bathocuproine (BCP) were purchased from Sigma Aldrich. Bismuth chloride, caesium chloride, caesium iodide, hydriodic acid, anhydrous dimethylformamide (DMF), dimethyl sulfoxide (DMSO) and anhydrous chlorobenzene (CB) were purchased from ACROS Organics™. poly(3,4-ethylenedioxythiophene) polystyrene sulfonate (PEDOT:PSS), [6,6]-Phenyl C_{71} butyric acid methyl ester, mixture of isomers ($PC_{70}BM$) and Spiro-OMeTAD were purchased from Heraeus Clevios GmbH, Ossila and Feiming Chemical Limited, respectively. Absolute ethanol, acetone, toluene and isopropanol (IPA) were purchased from VWR. All products were used directly without any further purification. Indium(III) O-2,2-dimethylpentan-3-yl dithiocarbonate (indium dimethylpentyl xanthate) was received from Thomas Rath, who is a previous postdoc in our group, and it was synthesised following a reported synthesis procedure.[1]

Sample Preparation

The more specific film, device fabrication and nanoparticle synthesis conditions will be introduced in each individual chapter. For the characterisation of the materials, thin films, nanoparticles and powders were required.

In general, thin films were prepared on glass substrates (VWR chemicals) that were cleaned using an ultrasonic bath treatment in deionised water (DI-water), acetone and isopropanol for 15 min each then dried with nitrogen blowing. For the deposition of a mesoporous (mp)-TiO_2 or mp-Al_2O_3 layer, a diluted TiO_2 paste or mp-Al_2O_3 was spin-coated on the cleaned glass substrates and then annealed first on a hot plate and then in a furnace. For the deposition of the compact (c)-TiO_2 or c-SnO_2 layer, a prepared precursor solution for each element was spin-coated and then annealed first on a hot plate and then in a furnace. The active layers were deposited directly on one of these prepared substrates or on the glass substrates. The hole transport material (HTM) or PMMA, which is an insulating polymer, was deposited on the prepared active layers when needed.

Commercial indium tin oxide (ITO) glass substrates were used for the device fabrication. The glass/ITO substrates were cleaned consecutively in ultrasound baths with soap, DI-water, acetone and isopropanol in order for 20 min each and then dried by N_2 blowing and heating in the oven. Then, the compact ETL, active layer, and HTL were prepared depending on the device structure through the same process as above. Finally, 100 nm of Ag as a backside electrode was thermally evaporated at a pressure not higher than 5×10^{-6} bar.

Nanoparticles were synthesised by slowly dropping a prepared precursor solution into an

antisolvent. The precursor solution was prepared by mixing bismuth halide or antimony halide with caesium halide in a 2:3 ratio in DMSO. After the dropped precursor solution reacted with the antisolvent, perovskite particles of various sizes were obtained in the solution. This solution was centrifuged to remove the larger particles and then the nanoparticles were prepared.

2-2. Steady-state UV-Vis Absorption Spectroscopy

Materials for a solar cell active layer absorb sunlight and generate charge carriers; therefore, knowing what range of radiation the material absorbs, which is a basic optical property, is necessary. Steady-state UV–Vis absorption spectroscopy is a very useful characterisation method to study the range of radiation absorption of photovoltaic materials.

For a liquid sample, a UV–Vis spectrometer can just measure the direct transmittance (%), which is the ratio of the light transmitted through the liquid sample. For the liquid sample, the sample's reflectance is neglected because the value is relatively small. Therefore, the sample's absorbance can be obtained using the Beer–Lambert Law:

$$\text{Absorbance} = \varepsilon\, c\, l = -\log\frac{I_t}{I_0} = -\log T \qquad \text{(Eq. 2-1)}$$

where ε is the molar absorption coefficient, c is the concentration of the liquid sample, l is the path length of the light, I_t is the intensity of the transmitted light, I_0 is the intensity of the original light, and T is the transmittance of the sample (see Figure 2-1). Note that there are other processes happening such as scatter, refraction and diffusion, but they are not considered for the absorbance calculation because their values are very small and could be reduced to their minimum by the spectrometer.

Meanwhile, the sample's reflectance must be considered for a film sample because its reflectance is non-negligible. Therefore, the absorption percentage rather than the absorbance is used for the film samples where the reflectance is non-negligible.

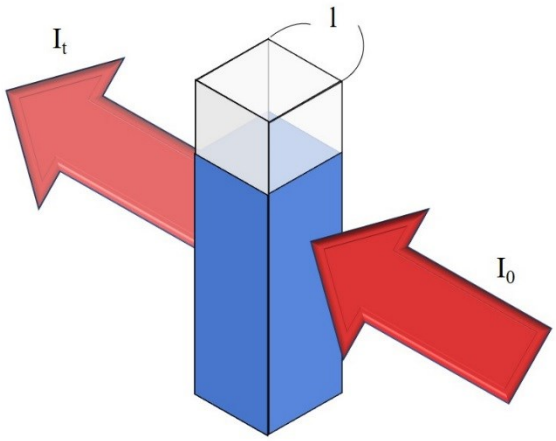

Figure 2-1. A schematic illustration of light passing through a liquid sample.

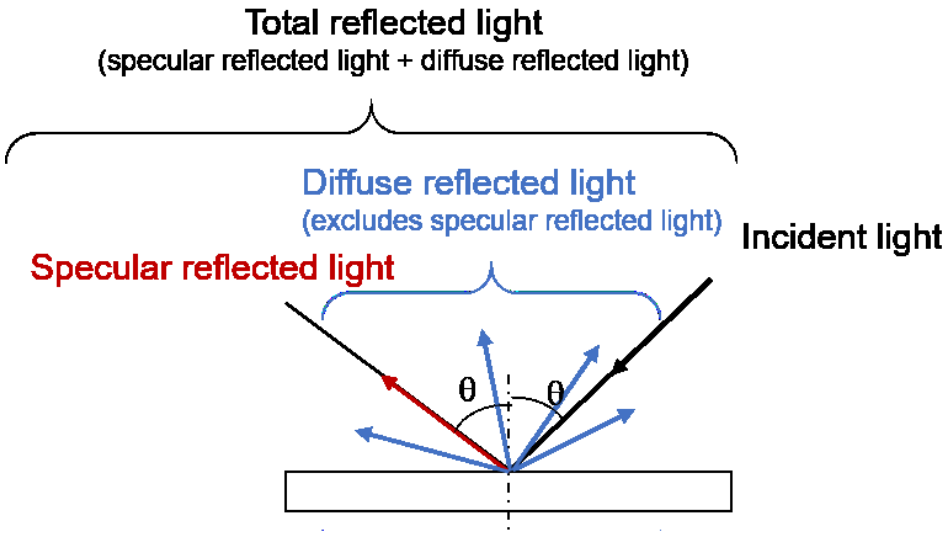

Figure 2-2. A schematic illustration of the types of reflected light.[2]

Reflectance can be measured by shining light (incident light) on a sample and measuring the light reflected from the sample. The reflected light consists of specular reflected light and diffuse reflected light and its combined is referred to as the total reflected light. Figure 2-2 shows a schematic illustration of these light types. The angle between the incident light and the

sample surface is called the incident angle, θ. The specular reflected light is that reflected symmetrically when the surface is smooth. The diffuse reflected light is the diffuse light reflected in all directions from rough surfaces such as paper and powder surfaces. The total reflected light is the total combination of the specular and diffuse reflected light.

The absorption percentage is the amount of light absorbed by the sample rather than transmitted or reflected. Therefore, the absorption can be obtained by the following equation:

$$\text{Absorption } (\%) = 100\ (\%) - T(\%) - R(\%) \qquad \text{(Eq. 2-2)}$$

where T is the transmittance and R is the total reflectance.

The obtained range of the radiation absorption gives information about the material including which wavelengths excite the sample for other spectroscopies including transient absorption spectroscopy and steady-state and transient photoluminescence. In this thesis, the steady-state UV–visible absorption spectroscopy was investigated using a Shimadzu 2600 spectrophotometer including an ISR-2600Plus integrating sphere attachment.

In addition, the absorption coefficient of a material can be determined using this UV–Vis spectroscopy and the equation:

$$\alpha = -\ln\left(\frac{\mathrm{T}}{(1-\mathrm{R})}\right)/d \qquad \text{(Eq. 2-3)}$$

, where α is absorption coefficient, T is transmittance, R is the reflectance, and d is the thickness of the sample. It is also important to know the absorption coefficient of a material because the optical band gap, which is the energy difference between the conduction band (CB) and the

valence band (VB) of the material, can be estimated by constructing a Tauc plot:

$$(\alpha h\nu)^n = A\left(h\nu - E_{opt}\right) \qquad \text{(Eq. 2-4.)}$$

where n = 2 for direct allowed transition and n = 0.5 for indirect allowed transition, h is Planck's constant, v is the speed of light, E_{opt} is the optical bandgap and A is a constant.[3, 4] By plotting $(\alpha h\nu)^n$ against hν and finding linear behaviour in a certain region, direct or indirect optical bandgap information can be given where the extrapolation of this straight line intercepts the hν-axis.

2-3. Transient Absorption Spectroscopy (TAS)

It is important to characterise fundamental processes of functioning devices, which include charge generation, separation, dissociation, and recombination. However, these processes occur in a few femtoseconds-to-microseconds and so ultra-fast techniques are necessary to understand them and different processes are observed at different time scales.[5–7] For example, the recombination of separated charge carriers on perovskite solar cells can be collected in microsecond timescale.[7] Transient absorption spectroscopy (TAS) is a very effective method with which to investigate those time-related processes, particularly non-emissive transient charge carriers that are generated by photo-excitation.

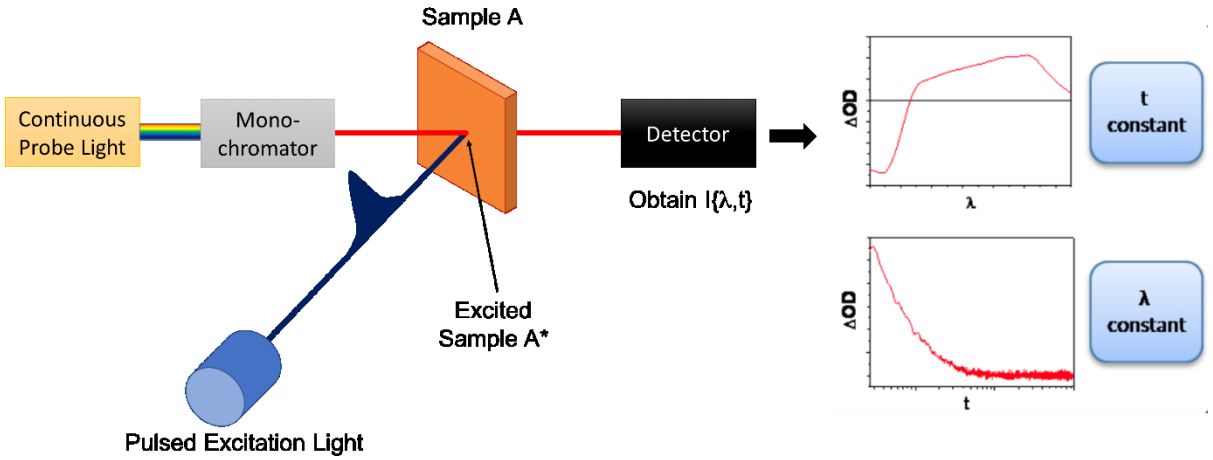

Figure 2-3. Schematic diagram showing the TAS setup used in this project.

As illustrated in Figure 2-3, for the TAS study, a sample is first excited by a pulsed excitation laser. The wavelength of the excitation laser is determined by the result from the steady-state absorption spectroscopy to promote the sample into its excited states with the laser. While the sample is being relaxed from its excited states, the absorbance of the excited states is monitored

by a constant probe light. Then, absorption signals are measured by a detector and processed by an oscilloscope as a difference between the absorption measured after and before the laser pulse, resulting in a difference in optical density (ΔOD). The ΔOD is mainly contributed by four processes: ground-state bleaching, stimulated emission, excited-state absorption and product absorption; the first two absorptions result in negative signals while the other two give positive signals.[8] These signals can be plotted vs. time at constant wavelength, or vs. the wavelength at a constant time point. The plot vs. wavelengths at a constant time point can give information about what is being observed and the plot vs. time at a constant wavelength can give the lifetime of what is observed.

In this thesis, I employed μs-TAS, which is TAS measurements carried out at the microsecond timescale. The films were excited in a nitrogen atmosphere by a pump light source (a dye laser from Photon Technology International Inc. GL-301 pumped by a Photon Technology International Inc. GL-3300 nitrogen laser; the laser excitation energy density was ~15 $\mu J \cdot cm^{-2}$). A probe light that was generated by a quartz halogen lamp (100 W; Bentham, IL 1) passed through the excited samples and electronic band-pass filters (Costronic Electronics) and the probe light was detected with light detectors (Si-photodiodes; Hamamatsu Photonics, S1722-01). The TAS signals were amplified by a digital oscilloscope (Tektronics, DPO3012) and collected and synchronised using a trigger signal of a pump laser pulse from a photodiode (Thorlabs Inc., DET210).

2-4. Steady-state Photoluminescence (PL) Spectroscopy

Photo-excited materials that absorbs the energy from the incident light can lose energy through different processes and relax to their ground state as explained in chapter 1-4. The possible emissive process is illustrated in Figure 2-4.

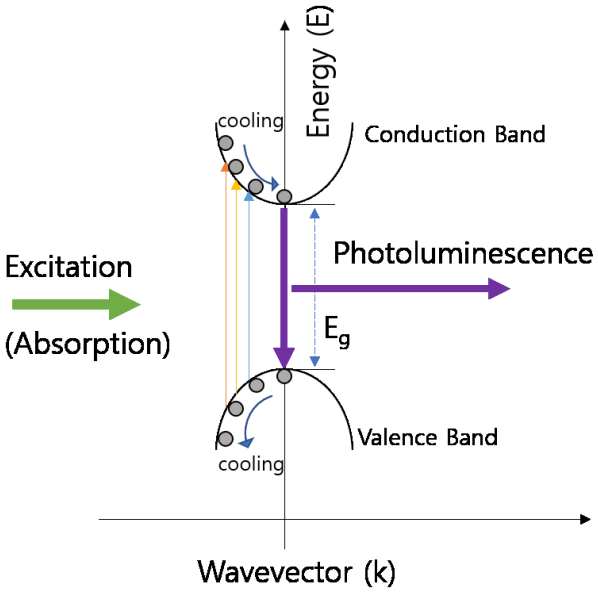

Figure 2-4. A schematic diagram of the photoluminescence process in direct-band-gap semi conductive materials.

In the case of direct gap material, both the CB minimum and the VB maximum appear at the centre of the region, where k = 0. When the absorbed UV- or visible-light energy exceeds the bandgap (Eg) of the material an electron–hole pair is generated, and the electron is excited to a higher conduction band and the hole is left in the valence band. Then, the excited electrons can lose their energy through vibrational relaxation (cooling in the figure 2-4). After that the electron can go through a radiative transition which is known as photoluminescence (PL). A

photoluminescence spectrum can show the change in fluorescence intensity as a function of the wavelength of the excitation light and can be measured using a spectrofluorometer. The wavelength of the emission monochromator is set to that of a known fluorescence emission by the sample and the wavelength of the excitation monochromator is scanned across the desired excitation range and the intensity of the fluorescence is recorded on the detector as a function of the excitation wavelength.

In this thesis, the standard steady-state emission spectra were obtained using a Fluorolog-3 instrument (Horiba Jobin Yvon) equipped with double-grating excitation, emission monochromators, and a 450 W Xe lamp as a light source. The excitation wavelength was chosen to promote the sample as a result of the steady-state UV–Vis. The emission spectra were corrected for the detector's spectral sensitivity using a calibration file of the detector response. The front-face illumination (30° with respect to the incident beam) was used for the film samples and right-angle illustration (90° with respect to the incident beam) was used for the liquid samples.

The photoluminescence quantum yield (PLQY) of a molecule or material is defined as the number of photons emitted as a fraction of the number of photons absorbed using Eq. 2-5:

$$\text{PLQY } (\phi_F) = \frac{number\ of\ photons\ emited}{number\ of\ photons\ absorbed} = \frac{k_f}{k_f + k_{nr} + k_t} \qquad \text{(Eq. 2-5)}$$

where K_f, K_{nr} and K_t are the rate coefficients of fluorescence, non-radiative recombination and energy transfer, respectively. This property of a fluorescent material is important for understanding its opto-electronic characteristics.

The integrating sphere method is a direct way to measure the PLQY. A sphere is coated with an entirely reflective surface such as barium sulfate-based materials or Spectralon® to capture all light going in and out of the sphere. From these two spectral measurements (sample and blank), PLQY can be calculated using Eq. 2-6:

$$\text{PLQY}\ (\%) = \left[\frac{A_{emission}}{A_{blank} - A_{sample}}\right] \quad \text{(Eq. 2-6)}$$

where $A_{emission}$ is the area under the perovskite emission peak, A_{blank} is the area under the excitation peak with a blank sample and A_{sample} is the area under the excitation peak with a perovskite sample. For this thesis, a Jobin Ybon Horiba Fluoromax-3 spectrofluorometer connected to a diffusely reflecting integrating sphere was employed to obtain PLQY.

2-5. Time-resolved Photoluminescence (TRPL) Spectroscopy

The photoluminescence lifetime is an intrinsic characteristic of luminescent materials and can provide information about the excited state dynamics. Time-resolved photoluminescence (TRPL) spectroscopy is one method to study the fast electronic recombination processes that result in the emission of photons, which normally occurs within the nanosecond timescale. This fluorescence lifetime can be influenced by the molecular environment resulting in quenching, changes in solvation or molecular rotation. Therefore, lifetime changes can provide information about the local chemical environment or insights into the reaction mechanisms.

Since the probability of detecting a single photon at a specific time after a low-intensity excitation pulse is proportional to the fluorescence intensity at that time, time-correlated singe photon counting (TCSPC) is a popular method of monitoring the fluorescence lifetime. It works by measuring the time between sample excitation by a laser pulse and the arrival of the emitted photon at the detector. A histogram of the fluorescence photon arrival times can be obtained based on successive excitation–collection cycles; this allows the reconstruction of the photoluminescence decay. Compared to other time-domain techniques, TCSPC has the advantages of great sensitivity, large dynamic range and high time resolution without needing a very stable high-power excitation source.

In this thesis, a Delta Flex system (Horiba Scientific) was used for the TCSPC measurements of the TRPL. The PL signal was collected using a single photon counting detector (PPD-650, Horiba scientific) and excitation source diode lasers (NanoLED N-02B, Horiba scientific) with the necessary wavelength, a <200 ps pulse duration and a 1 MHz repetition rate.

2-6. X-ray Diffraction (XRD)

Crystallographic properties were investigated using X-ray diffraction (XRD). Diffraction pattern appears to satisfy Braggs' law:

$$2d \sin \theta = n\lambda \qquad \text{(Eq. 2-7)}$$

where d is the inter-planar spacing, θ is the incident beam angle, and λ is wavelength of the incident beam. The diffraction pattern is brightest where n = 1, so Bragg's law usually becomes 2d sin θ = λ in conventional XRD. Many distinct peaks that correspond to different inter-planar spacing d are typically contained in a diffraction pattern from a crystal. Applying Miller indices (h, k, l) allows us to obtain the distance between planes (d_{hkl}) in the crystal. For crystals of low symmetry that contain more than several atoms per unit cell, indexing a diffraction pattern by hand becomes more difficult. A 'fingerprinting' approach has been used to overcome this difficulty. For each material, the observed inter-planar spacings for all observed diffraction peaks, their relative intensities, and their hkl indexing are included in a dataset. Software allows us to identify peaks in the experimental diffraction pattern and find candidate materials by searching the international centre for diffraction data (ICDD) database that maintains diffraction patterns of thousands of inorganic and organic materials. In this thesis, XRD was performed on a PANalytical X'Pert Pro MRD diffractometer using Ni filtered Cu Kα X-rays at 40 kV and 40 mA. The data were obtained in the 2θ range at 10°–60° and the powder samples were mounted in a top-loaded trough and rotated during data collection. The film samples on glass substrates were prepared following the same procedure as above.

2-7. Scanning electron microscopy (SEM)

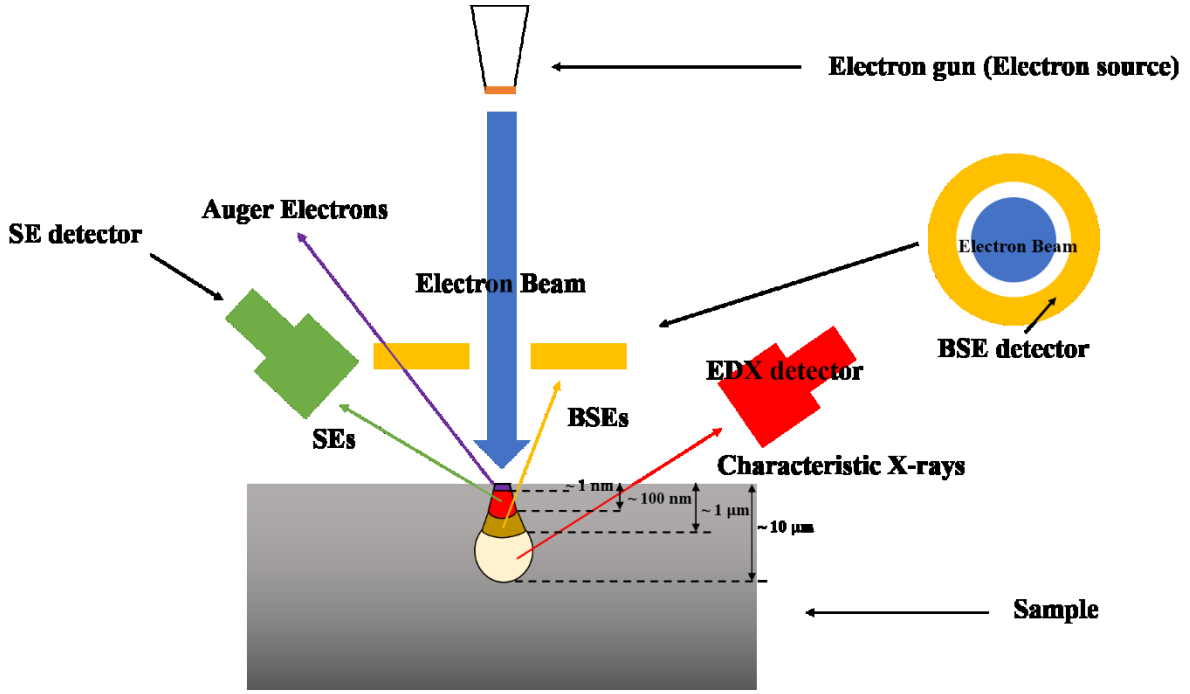

Figure 2-5. A schematic illustration of the image generation in SEM.

Figure 2-5 is a schematic illustration of SEM. The electron beam from the electron gun hits the sample's surface and then some electrons in the sample scatter out of the sample in three different ways: Auger electrons, secondary electrons (SEs) and backscattered electrons (BSEs). Auger electrons are generated near the surface, SEs come from a deeper region and BSEs come from a much deeper region from the sample surface. Additionally, x-rays are generated from the dippiest region of the interaction volume. These scattered electrons can be detected by detectors.

Since the SE detector is inclined and placed far from the main beam position, the amounts of SEs depend on the surface shape. If there is a cavity, most SEs are reabsorbed into the sample

rather than coming out as shown in Figure 2-5. Since there are fewer scattered electrons, its image looks dark. Whereas, the detector detects more SEs at a hill because the angle of incidence increases, thus more secondary electrons are scattered. Therefore, steep surfaces or sample edges appear brighter than flat surfaces in images.

In this thesis, SEM images of the prepared film samples were taken with a LEO Gemini 1525 high-resolution field emission SEM (Zeiss) that is equipped with Oxford Instruments INCA energy dispersive and wavelength dispersive X-ray spectrometers. Samples were placed on a conductive carbon tape and coated with a 10 nm chromium film (sputtered using a Q150T Turbo-Pumped Sputter Coater) prior to investigations.

2-8. Current–Voltage Characteristics

The power conversion efficiency (PCE) of the prepared devices were characterised using the current–voltage characteristics. Solar cell current-voltage characteristic curves (J-V curves) can be used to reveal the current-voltage (J-V) characteristics of a solar cell. The devices can be measured under dark and illumination conditions and they have different behaviours according to the conditions. Under dark condition, the solar cell devices behave as a diode, therefore so only forward bias is allowed and establish the current (I_D) while reverse bias is forbidden and cannot establish current. When the device is illuminated, charges are generated in the device and these charges are transferred and establish the current (I_L). This current, which is established by light is proportional to the light intensity. Here, I_L and I_D flow in the opposite direction and the equation of the current in a function of the voltage can be given by Shockley's equation as following,

$$I(V) = I_L - I_D = I_L - I_0(e^{qV/kT} - 1) \qquad \text{(Eq. 2-8)}$$

where I_L is the photogenerated current, I_D is the dark current, k is the Boltzmann constant, T is the absolute temperature of the p–n junction, and q is the magnitude of charge of an electron. To understand the current-voltage measurement results, an example of the J-V curves is given in Figure 2-6. There are five points in the figure, V_{OC}, J_{SC}, Maximum Power Point, V_{max} and J_{max}. When the solar cell is open-circuited, the amount of charge separation equals to the amount of charge recombination; therefore, the current is zero, and the voltage reaches the maximum value. The voltage at open-circuited condition is called open circuit voltage, V_{OC}. When the solar cell is short-circuited, which means that the positive and negative leads are

connected, there is no voltage across the circuit, and the current reaches its maximum value. The current at short-circuited condition is also known as short circuit current, J_{SC}.

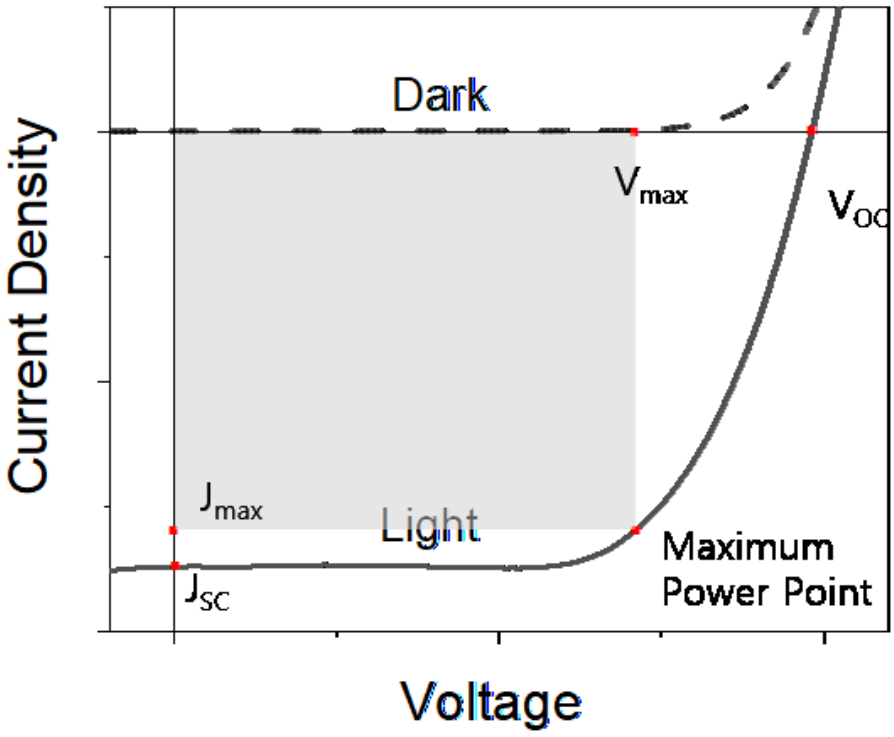

Figure 2-6. An example of current-voltage curves under dark (dashed line) and illuminated at 1 sun (solid line).

There is another point on the curve called maximum power point and at the point the device has the highest power output. The maximum power conversion efficiency (P_{max}) can be calculated using Eq. 2-9:

$$P_{max} = V_{OC} J_{SC} FF \qquad \text{(Eq. 2-9)}$$

where V_{OC} is the open-circuit voltage, J_{SC} is the short-circuit current density, FF is the fill factor.

FF is the ratio between the ideal performance of solar cells and the performance affected by various recombination losses. Therefore, the following equation becomes <1:

$$FF = \frac{V_{max} J_{max}}{V_{OC} J_{SC}} \qquad \text{(Eq. 2-10)}$$

where V_{max} is the maximum voltage and J_{max} is the maximum current density. The power conversion efficiency (PCE) can be determined by the ratio of P_{max} to the incident power P as below.

$$PCE = \frac{P_{max}}{P} = \frac{V_{OC} J_{SC} FF}{P} \qquad \text{(Eq. 2-11)}$$

The solar cell performance is heavily influenced by parasitic resistance which dissipates the power in the circuit. The most common resistances are series and shunt resistance (R_s and R_{sh}, respectively) as shown in Figure 2-7. R_s is mainly related to the movement of current inside the device and the resistance at interfaces between layers and R_{sh} is typically caused by manufacturing defects. These parasitic resistances are mostly affecting the fill factor. In an ideal solar cell, R_s is zero, leading to no voltage drop and R_{sh} should be infinite, limiting any alternative path for current flow. Increase in R_s and decrease in R_{sh} can reduce the fill factor and as a result, the device efficiency drops.

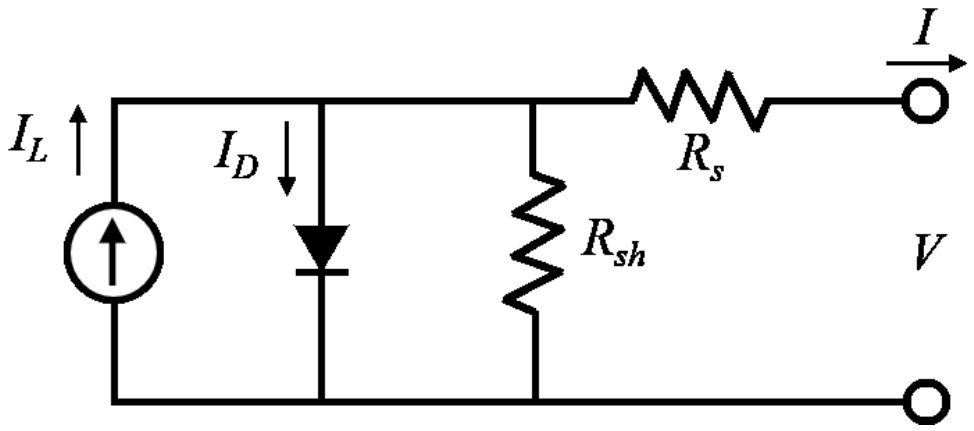

Figure 2-7. Equivalent circuit diagram of a solar cell with series and shunt resistance.

R_s can increase due to the ohmic losses which can be caused by the resistance of the material, the resistance between the material and the contact, and the resistance between the contacts themselves. The change in R_s has an impact near open-circuit voltage, but it does not affect open circuit voltage because the overall current flows through the solar cell, not through the series resistance. However, when R_s is high enough, the short-circuit current would be reduced. Regarding the shunt resistance, decrease in R_{sh} can be caused by current leakage across the p-n junction and between the contacts. The decreased R_{sh} would provide an alternative path for current flow, because it is in parallel with solar cell. This can bring the voltage drop.

In this thesis, the J–V characteristics of the fabricated solar cells with a 0.045 cm^{-2} area were recorded in dark conditions and under illumination (100 mW cm^{-2}) using a Keithley 2400 source meter with a 0.125 V s^{-1} scan rate. The samples were illuminated by a LCS-100TM solar simulator system with a 150 W xenon lamp equipped with an AM1.5 filter (ScienceTech) and calibrated with a standard silicon solar cell. The J-V hysteresis for BiI_3 and $MA_3Bi_2I_9$ were investigated by Kulkarni *et al.*[10] and Park *et al.*[11] respectively and showed negligible hysteresis

for both materials. Therefore, the hysteresis was not investigated in this thesis, but it can be investigated in the future.

2-9. External Quantum Efficiency

The external quantum efficiency (EQE) is also useful characteristic to investigate the solar cell and assess the device performance. EQE is also known as the incident photon conversion efficiency (IPCE), which is the ratio between the collected electrons by the solar cell to the total incident photons at a wavelength as below (Eq. 2-12).

$$EQE = \frac{number\ of\ collected\ electrons}{number\ of\ incident\ photons} \qquad \text{(Eq. 2-12)}$$

Once a photon is absorbed by the active layer, and a pair of electrons and holes will be generated. The generated electron-hole pairs will go through charge transfer, transport and recombination, and the remained electrons will be collected at the electrode as explained in chapter 1-4. Therefore, high EQE value means that a large number of electrons are remained after the processes. The integration of the area under the whole EQE spectrum should be equal to the J_{SC} measured from J-V characterisation under 1 sun.

This external quantum efficiency spectra were collected using Bentham Photovoltaic PVE300 system in this thesis.

2-10. References

1. T. Rath, M. Edler, W. Haas, A. Fischereder, S. Moscher, A. Schenk, R. Trattnig, M. Sezen, G. Mauthner, A. Pein, D. Meischler, K. Bartl, R. Saf, N. Bansal, S. A. Haque, F. Hofer, E. J. W. List and G. Trimmel, *Adv. Energy Mater.*, 2011, **1**, 1046-1050.

2. Solid Sample Reflectance Measurements, https://www.shimadzu.com/an/uv/support/fundamentals/reflectance_measurements.html, (accessed accessed September 16, 2019).

3. J. Tauc, *Mater. Res. Bull.*, 1970, **5**, 721-729.

4. E. A. Davis and N. F. Mott, *Philos. Mag. Lett.*, 1970, **22**, 903-922.

5. C. J. Brabec, G. Zerza, G. Cerullo, S. De Silvestri, S. Luzzati, J. C. Hummelen and S. Sariciftci, *Chem. Phys. Lett.*, 2001, **340**, 232-236.

6. G. C. Xing, N. Mathews, S. Y. Sun, S. S. Lim, Y. M. Lam, M. Gratzel, S. Mhaisalkar and T. C. Sum, *Science*, 2013, **342**, 344-347.

7. Q. Shen, Y. Ogomi, J. Chang, T. Toyoda, K. Fujiwara, K. Yoshino, K. Sato, K. Yamazaki, M. Akimoto, Y. Kuga, K. Katayama and S. Hayase, *J. Mater. Chem. A*, 2015, **3**, 9308-9316.

8. R. Berera, R. van Grondelle and J. T. M. Kennis, *Photosynthesis Research*, 2009, **101**, 105-118.

9. What is a Jablonski Diagram (Perrin-Jablonski Diagram)?, https://www.edinst.com/blog/jablonski-diagram/, (accessed accessed September 18, 2019).

10. A. Kulkarni, T. Singh, A. K. Jena, P. Pinpithak, M. Ikegami, and T. Miyasaka, *ACS Appl. Mater. Interfaces*, 2018, **10**, 9547–9554.

11. B. W. Park, B. Philippe, X. Zhang, H. Rensmo, G. Boschloo and E. M. J. Johansson, *Adv. Mater.*, 2015, **27**, 6806-6813.

Chapter 3: Improved Charge Separation and Photovoltaic Performance of BiI_3 Absorber Layers by Introducing an *in situ*-formed BiSI Interlayer

Abstract

Stable and non-toxic bismuth iodide (BiI_3) is emerging as a promising absorber material for solar cell applications because of its favourable optical properties such as a high absorption coefficient (10^5 cm^{-1}) in the visible region and narrow bandgap (1.7 eV). Although it has promising features, solar cells employing this material have only achieved power conversion efficiencies of 1% so far, which is distant from their theoretical efficiency limit of 28%. It is reasonable to suppose that the relatively low performance of BiI_3-based solar cells may originate from their very short carrier lifetimes (180–240 ps) in BiI_3, which makes the efficient separation of mobile charges a crucial factor for the improvement of this material's photovoltaic performance. For efficient charge separation, a bismuth sulfide iodide interlayer is inserted between the electron transport layer (ETL) and the bismuth iodide absorber. Herein, transient optical spectroscopy is employed to show that the use of a bismuth sulfide iodide interlayer promotes efficient charge separation. Based on this knowledge, BiI_3 solar cells with 1.21% power conversion efficiency were fabricated with a solar cell architecture comprised of ITO/SnO_2/BiSI/BiI_3/organic HTM.

3-1. Introduction

As discussed in Chapter 1, bismuth iodide is an emerging lead-free and stable material for photovoltaic applications with sufficiently narrow bandgap (1.7 eV) and high absorption coefficient to quickly improve device efficiency.[1–4] The improvement of the PCE from 0.32% to 1% through annealing the BiI_3 film under a solvent vapour environment by Hamdeh *et al*.[1] came from the formation of a BiOI layer that was shown to improve charge carrier transport in the active layer. However, the presence of this BiOI layer at the BiI_3/hole transporter heterojunction may impede interfacial charge transfer due to a mismatch in energy levels at this heterojunction. Moreover, the optimisation of interfacial electron and hole transfer at ETL/BiI_3/HTL heterojunctions is particularly important due to the relatively short lifetimes of generated excitons in BiI_3 films (180–240 ps), where BiI_3 shows excitonic behaviour with exciton binding energy of 160-180 meV.[5,6] This relatively short lifetime most likely results in the charges recombining before being transferred to the electrodes. Therefore, the optimising the supporting device architecture is crucial to extract photogenerated charges efficiently prior to their recombination within the BiI_3 material.

In this study, a BiSI layer was used at the ETL/BiI_3 interface that successfully improved the yield of the photoinduced charge separation and electron extraction in BiI_3 solar cells. This BiSI layer was processed by first introducing an indium sulfide film at the ETL/BiI_3 heterojunction, followed by annealing. Moreover, BiSI is an air-stable and low-toxicity material that has potential in PV applications.[7] Until now, very few studies have reported on BiSI-based solar cells and the PCEs obtained thus far are <1%.[8,9] This material has been theoretically determined to have a low conduction band of about -4.5 eV.[7,8] It is reasonable to

suppose that the low-lying conduction band of BiSI may assist in electron extraction from the BiI_3 layer and thus improve the solar cells' efficiency.

3-2. Method

Materials

TiO_2 nanoparticle paste (30NR-D) was purchased from Dyesol Ltd. $N(PhBr)_3SbCl_6$, BiI_3, lithium bis(trifluoromethylsulphonyl)imide (LiTFSI), mp-Al_2O_3 in isopropanol (20 wt%), tin chloride dihydrate, tert-butyl pyridine (TBP), acetonitrile, terpineol, titanium isopropoxide, 2-methyloxyethanol and ethanolamine were purchased from Sigma Aldrich. Anhydrous dimethylformamide (DMF) and anhydrous chlorobenzene were purchased from ACROS Organics™. Spiro-OMeTAD was acquired from Feiming Chemical Limited. Absolute ethanol, acetone and isopropanol (IPA) were purchased from VWR. All products were used directly without further purification. Indium(III) O-2,2-dimethylpentan-3-yl dithiocarbonate (indium dimethylpentyl xanthate) was prepared by Thomas Rath, who is a previous postdoc in the Haque group, following a previously reported synthesis procedure. [10]

Substrate preparation

Glass substrates (VWR Microscope Slides, BS7011, 1.0–1.2 mm) were used after cutting to the specified size (1.25 cm × 1.25 cm), washing and drying in a N_2-gas stream. The washing process included three consecutive steps: ultrasonic bath treatment in deionised water, acetone and isopropanol for 15 min each.

Compact TiO_2 film fabrication

A compact TiO_2 precursor solution containing titanium isopropoxide, ethanolamine and 2-methoxyethanol in a 70 µL:55 µL:1 ml ratio was spin-coated at 5,000 rpm with 2,000 rpm/s

acceleration for 30 s and then annealed in a furnace at 500°C for 45 min.

Mesoporous TiO_2 film fabrication

A mesoporous TiO_2 paste was prepared by diluting the Dyesol TiO_2 nanoparticle paste with terpineol in a 1:1.5 weight ratio. The diluted paste was then spin-coated at 5000 rpm with 2000 rpm/s acceleration for 30 s on the substrates. Then the films were annealed in a furnace at 500 °C for 45 min.

Compact SnO_2 film fabrication

The c-SnO_2 films were prepared by spin-coating a 0.3 M solution of tin chloride dihydrate in ethanol at 5,000 rpm with 2,000 rpm/s acceleration for 30 s followed by annealing in a furnace at 500 °C for 45 min.

BiI_3 film fabrication

A bismuth iodide solution was prepared by dissolving 200 mg of BiI_3 in 1 mL of anhydrous DMF. The solution was spin-coated at 2,000 rpm with 2,000 rpm/s acceleration for 30 s, followed by annealing at 100, 200 or 300°C on a hotplate for 20 min in a glovebox.

$MA_3Bi_2I_9$ film fabrication

A $MA_3Bi_2I_9$ precursor solution was prepared by dissolving 200 mg of BiI_3 and 80.87 mg of MAI in 1 mL of anhydrous DMF. The solution was spin-coated at 2,000 rpm with 2,000 rpm/s acceleration for 30 s, followed by annealing at 110°C on a hotplate for 20 min in a glovebox.

BiSI interlayer fabrication

The In_2S_3 interlayers were prepared by spin-coating a solution of indium dimethylpentyl xanthate in chlorobenzene (134 mg/ml) at 2,000 rpm with 2,000 rpm/s acceleration for 30 s. Afterwards, the films were annealed on a hotplate at 200°C for 15 min in a N_2-filled glovebox to form In_2S_3. On top of the In_2S_3 layer, the BiI_3 solution in DMF (200 mg/ml) was spin-coated at 2,000 rpm with 2,000 rpm/s acceleration for 30 s and then annealed on the hotplate over 200°C. For the film annealed at 200°C, an approximately 200 nm-thick film of a mixed BiSI/BiI_3 layer was formed. Figure 3-1 illustrates the whole process.

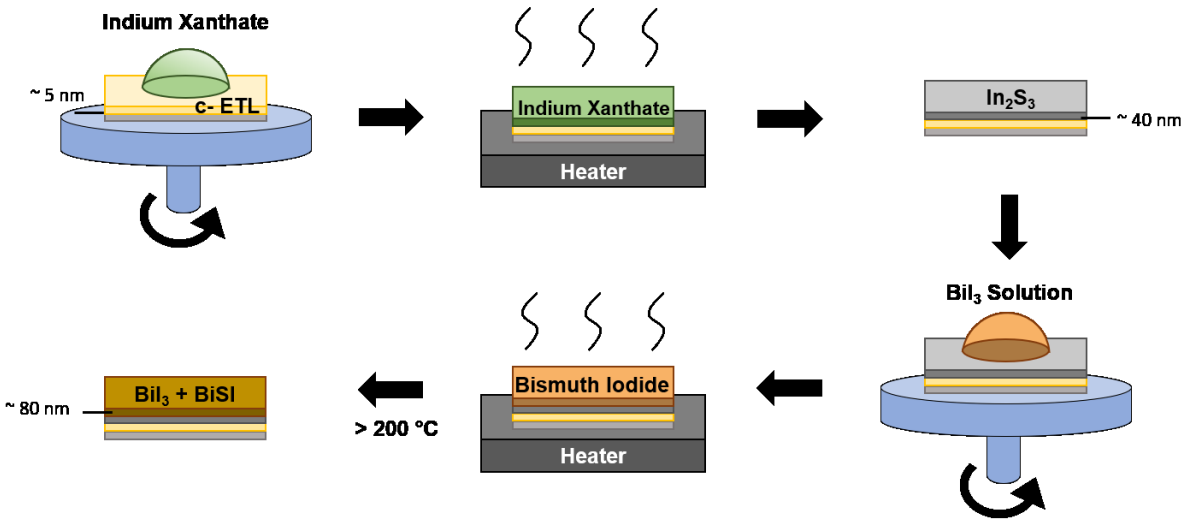

Figure 3-1. Preparation of thin-film samples of BiI_3 including a BiSI inter-layer.

Hole transport layer fabrication

The spiro-OMeTAD solution was prepared by dissolving 72.3 mg of spiro-OMeTAD in 1 ml

chlorobenzene and adding 17 µl of lithium LiTFSI solution in acetonitrile (520 mg/ml) and 28.8 µl of TBP. Afterwards, the solution was filtered through a PTFE syringe filter (0.2 µm) and deposited as a hole transport layer on top of the BiI_3 films by spin-coating at 2,000 rpm with 2,000 rpm/s acceleration for 30 s.

Solar Cell Fabrication

Commercial indium tin oxide-coated (ITO) glass substrates were used as a PV device with BiI_3. The glass/ITO substrates were cleaned consecutively in ultrasound baths with soap, deionised water, acetone and isopropanol in order for 20 min each and then dried by N_2 blowing and heating in an oven. The compact ETL, In_2S_3, BiI_3 active layer and HTL were prepared through the same process as described above. Finally, 100 nm of Ag as a backside electrode was thermally evaporated at ≤5E-6 mbar. The films were stored under ambient conditions without illumination for 14 days to oxidise spiro-OMeTAD.

For PV devices with $MA_3Bi_2I_9$, commercial fluorine-doped tin oxide (FTO) glass substrates were used. The glass substrates were cleaned consecutively in ultrasound baths with soap, deionised water, acetone and isopropanol in order for 20 min each and then dried by N_2 blowing and heating in an oven. The compact ETL, BiSI, bismuth perovskite active layer and HTL were prepared through the same process as above. Finally, 100 nm of Ag as a backside electrode was thermally evaporated at ≤5E-6 mbar.

Characterisation Techniques

SEM, XRD, thickness measurements, thermogravimetry (TGA), differential scanning

calorimetry (DSC), steady-state UV–Vis and transient absorption spectroscopy were carried out as described in Chapter 2. For thermal analysis on BiI_3, In_2S_3 and their mixture, TGA and DSC were conducted in a nitrogen atmosphere with a flow-rate of 50.0 ml/min and temperature variance from 25°C to 325°C at 30°C/min. These were conducted by Dr. Lisa D. Haigh, who is a technician in the Department of Chemistry.

3-3. Results & Discussion

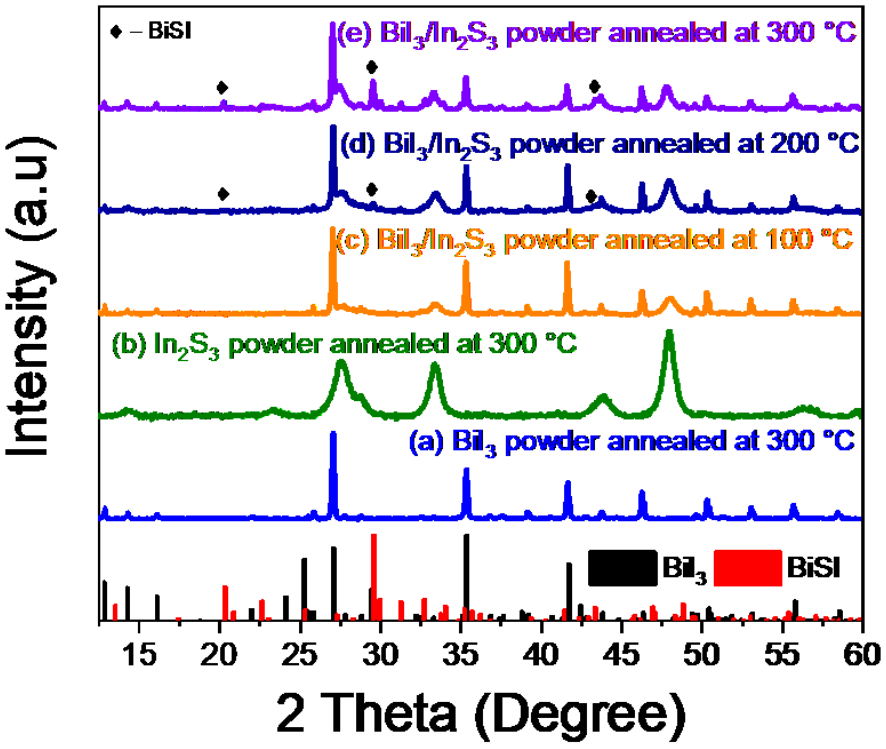

Figure 3-2. X-ray diffraction patterns of (a) BiI_3, (b) In_2S_3, (c), (d) and (e) BiI_3/In_2S_3 mixed powders annealed at different temperatures and references of BiI_3 (black, code: 01-076-1742) and BiSI (red, code: 01-073-1171).

To produce a BiSI interlayer between ETL and bismuth iodide, the *in situ* method was applied. Figure 3-2 shows the X-ray diffraction patterns from powders of BiI_3, In_2S_3 and their mixtures annealed at different temperatures. The powders were heated in a nitrogen-filled glovebox to prevent reactions with oxygen or moisture. As shown in the figure, no additional peak appeared when BiI_3 and In_2S_3 were annealed separately at 300°C. In addition, when their mixture was

annealed at 100°C, the XRD pattern only showed the patterns from In_2S_3 and BiI_3 without additional peaks. Meanwhile, when the mixture was annealed >200°C, it started having additional peaks that can be assigned to BiSI; these additional peaks become clearer with higher temperature annealing. This shows that there was a reaction between BiI_3 and In_2S_3, generating BiSI as a product when they were heated at high temperature. During its reaction there is possibility of generation of InSI but no XRD peaks were obtained. If amorphous InSI was generated, it is possible any XRD peaks are not obtained in the present study. It would be worth investigating it in the future.

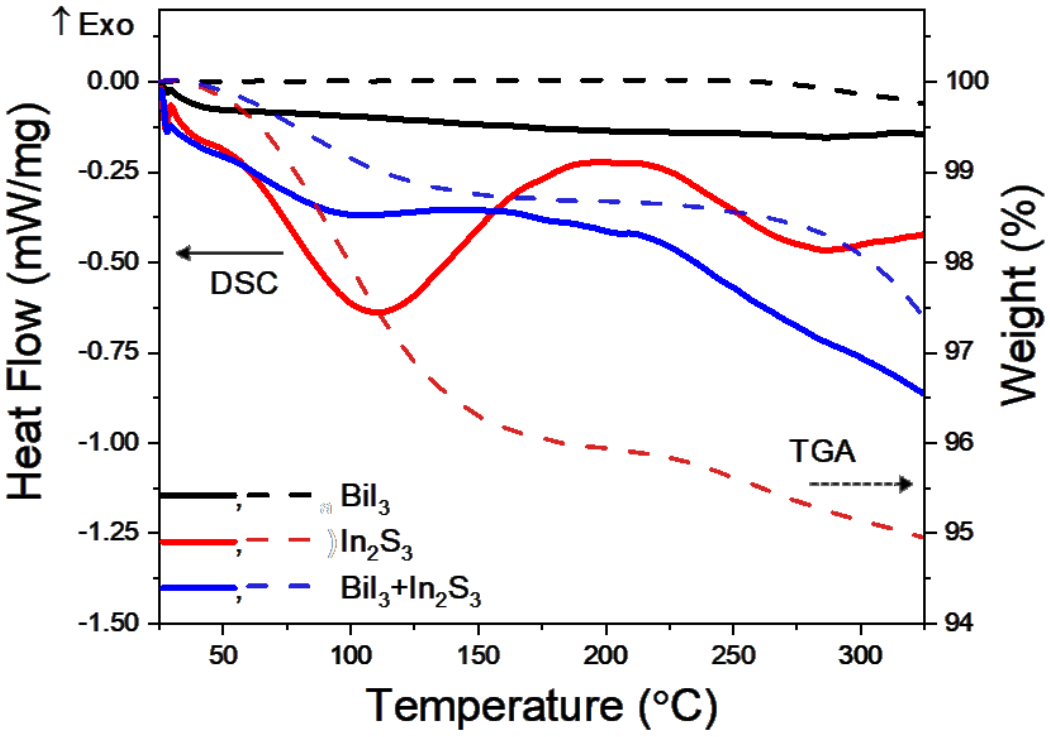

Figure 3-3. DSC (solid lines) and TGA (dashed lines) curves for BiI_3 and In_2S_3 powders and their mixture under N_2 atmosphere.

For further information regarding the temperature effect on the reaction between them, thermal analysis was conducted including differential scanning calorimetry (DSC) and thermal gravimetric analysis (TGA). The powders were heated under a nitrogen flow to prevent reactions with oxygen or moisture. Figure 3-3 shows the changes in the heat flow and the weight of BiI_3, In_2S_3, and their mixture during the temperature increases. In the 25–325°C temperature region, BiI_3 did not significantly change. In the case of In_2S_3, the first endothermic event occurred at 50–150°C, resulting in about 4% mass loss, which might have come from dehydration, specifically the loss of water remaining in the powder.[11] After dehydration, there was another endothermic event after 225°C, which is assumed to be the glass transition.[12] Meanwhile, the powder mixture went through a somewhat different process. It experienced dehydration at 50–150°C similar as In_2S_3. After 150°C, unlike the In_2S_3 powder, another endothermic event started but the weight was maintained until 225°C in the mixture. After that, there was sudden weight loss with more severe endothermic event. It seems that the endothermic event after 150°C was related to the reaction between BiI_3 and In_2S_3 that produced BiSI.

The peaks for BiSI were observable from the XRD pattern of the powder mixture (Figure 3-2 (d, e)) after being heated beyond 200°C. Therefore, it can be concluded that there was a reaction between BiI_3 and In_2S_3 after 150°C. In addition, the weight loss may come from the loss of iodine from BiI_3 and sulphur from In_2S_3 upon forming BiSI. With the knowledge from this analysis that the reaction starts at around 150°C and the mixture has a weight plateau until 225°C, the annealing temperature was chosen as 200°C.

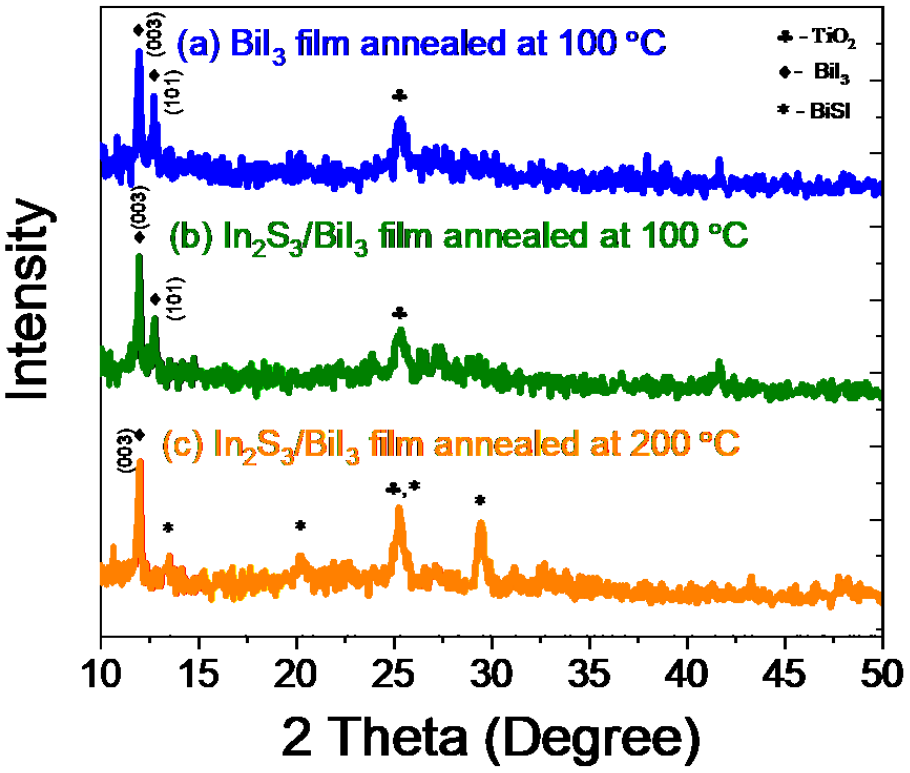

Figure 3-4. X-ray diffraction patterns of (a) a BiI_3 film annealed at 100 °C and BiI_3 films on In_2S_3 interlayers annealed at (b) 100 °C and (c) 200 °C, respectively.

Figure 3-4 presents the X-ray Diffraction (XRD) pattern of BiI_3 and In_2S_3/BiI_3 thin films annealed at different temperatures. It confirms the presence of BiSI in the sample annealed at 200°C. The XRD pattern of the BiI_3 film (Figure 3-4 (a)) and the In_2S_3/BiI_3 sample annealed at 100°C (Figure 3-4 (b)) show peak characteristics for BiI_3 (Figure 3-2). For these thin films, the preferred orientation is (003), indicating a crystalline growth along the c-axis. In contrast, the XRD pattern of the film annealed at 200°C (Figure 3-4 (c)) shows additional peaks. These additional peaks marked with stars can be assigned to the characteristic reflections of BiSI

(Figure 3-2). In the XRD pattern of the powder mixture and the In_2S_3/BiI_3 thin film, peaks for BiSI are clearly visible, thus providing further evidence for the formation of a BiSI film at the interface of the In_2S_3 and BiI_3 films during annealing.

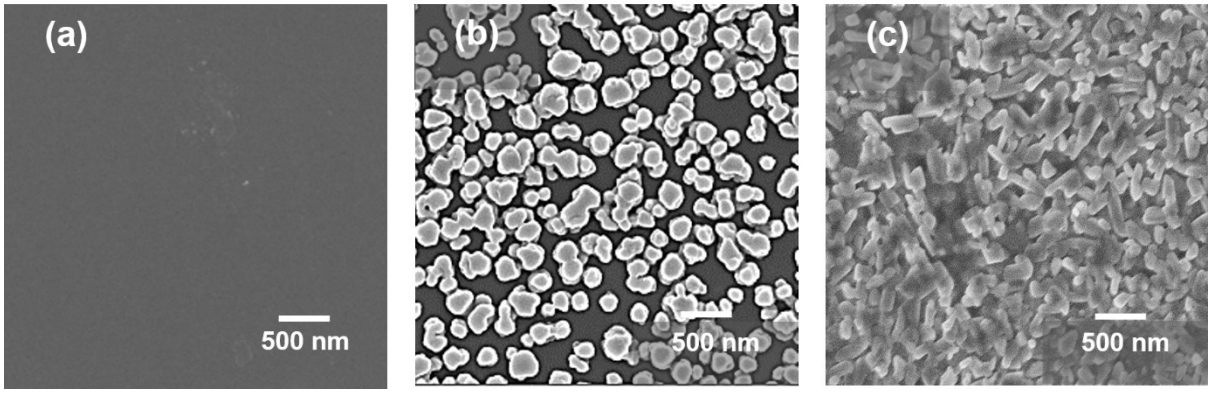

Figure 3-5. SEM images of (a) In_2S_3 as well as In_2S_3/BiI_3 thin films on c-TiO_2/glass substrates annealed at (b) 100 °C and (c) 200 °C.

Next, scanning electron microscopy (SEM) was used to study the morphology of the BiI_3-based photoactive layers. Figure 3-5 (a) shows an SEM image of a typical In_2S_3 layer prepared on a glass substrate. The In_2S_3 layer appears to be compact with uniform coverage. When a thin film of BiI_3 is spin-coated on the In_2S_3 layer and annealed at 100°C, BiI_3 crystals (approximately 200 nm in size) are observed but the surface coverage is relatively poor (see Figure 3-5 (b)). In contrast, the In_2S_3/BiI_3 layer annealed at 200°C, leads to the generation of elongated particles with uniform coverage (see Figure 3-5 (c)), which may have come from the generated BiSI.

Figure 3-6 (a) shows the absorption spectra of the BiSI/BiI_3 thin films. Upon annealing the In_2S_3/BiI_3 film at 200°C, the absorption onset is red-shifted. However, annealing the sample at the lower temperature of 100°C did not result in any change in the bandgap. This is most likely

due to the formation of BiSI at 200°C via the reaction between BiI_3 and In_2S_3 at the above-discussed interface. The Tauc method was applied to find a linear absorption edge (Figure 3-6 (b) and (c)). The direct bandgaps were determined as 1.74 and 1.60 eV and the indirect bandgaps were 1.75 and 1.62 eV for the BiI_3 (green curve) and sample annealed at 200°C (orange curve), and the observed bandgaps match well with those previously reported for BiI_3[4, 6, 13] and BiSI[7]. The BiI_3 sample has an absorption coefficient (α) $>10^5$ cm^{-1} above 1.9 eV (650 nm) that agrees with the published literature.[14] In contrast, the film comprising BiSI/BiI_3 exhibits an absorption coefficient $>10^5$ cm^{-1} above 1.75 eV (710 nm), which indicates that the layer can absorb a much larger fraction of the solar spectrum. From the Tauc plot, it is observed that there are direct bandgaps just below the indirect bandgaps for both materials. This seems to be the reason why they have strong absorption.

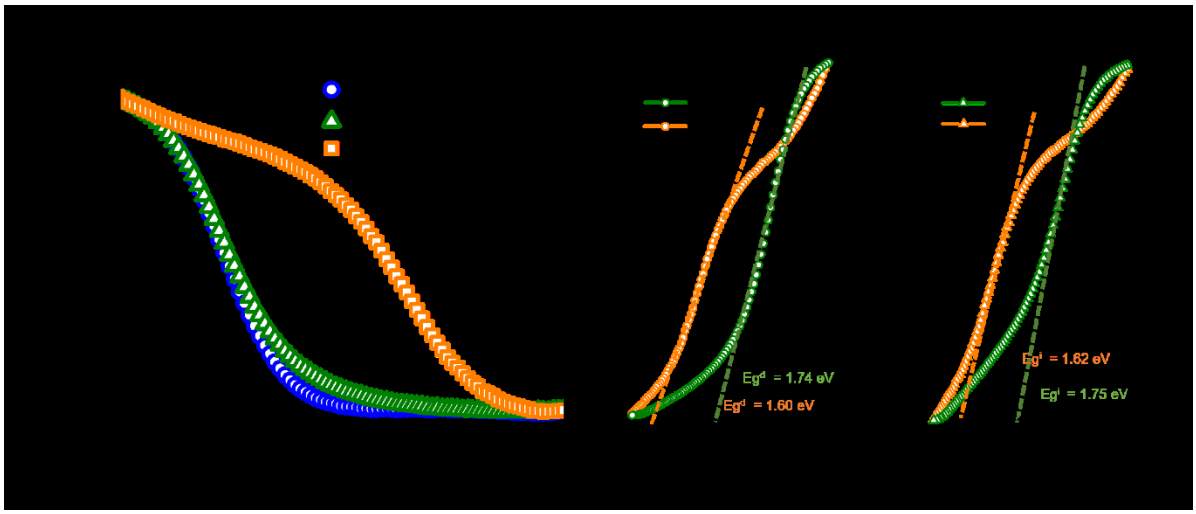

Figure 3-6. (a) UV–Vis absorption spectra of a BiI_3 film without In_2S_3 interlayer (blue circle) and BiI_3 films on an In_2S_3 layer annealed at different temperatures, 100 °C (green triangles) and 200°C (orange squares) and Tauc plots for the films annealed at (b) 100 °C (c) 200 °C with an In_2S_3 layer.

Next, transient absorption spectroscopy was used to study the effect of the BiSI layer on the yield of the photoinduced charge transfer at the metal oxide/BiSI/BiI_3/HTM heterojunction. For this purpose, microsecond-to-millisecond transient absorption spectroscopy was employed as described in the experimental section. The decays were not fitted because just to show the lifetime and the intensity differences. Regarding the implications of the signals, they have not been investigated yet. So, it would be investigated later to clear it out. However, where the signals come from is explained as below.

Figure 3-7 (a) (green curve); the yield of transfer is clearly negligible in the Al_2O_3/BiI_3/spiro-OMeTAD film. Here, Al_2O_3 was used to directly probe the hole transfer process; Al_2O_3 has a high conduction band edge that prohibits electron transfer from the BiI_3 absorber to the Al_2O_3. Moreover, in contrast, the presence of a BiSI layer leads to a significant increase in the yield of charge separation (compare the green and red curves in Figure 3-7 (a)). To confirm that the transient signal observed (the red curve in Figure 3-7 (a)) is due to the hole transfer from BiI_3 to spiro-OMeTAD, a control sample comprising Al_2O_3/BiI_3/poly (methyl methacrylate) (PMMA) was investigated; there is no hole or electron transfer to PMMA layer here because the highest occupied molecular orbital (HOMO) level of PMMA is lower than the VB of BiI_3 and BiSI and the lowest unoccupied molecular orbital (LUMO) level of PMMA is higher than the CB of BiI_3 and BiSI. The black trace in Figure 3-7 (a) clearly shows that no transient absorption signal is observed for this sample. A comparison of the charge separation yield in Al_2O_3/BiSI/BiI_3/HTM heated at 100°C and 200°C (compare the red and blue curves in Figure 3-7 (a)) support this conclusion, showing obvious differences. The higher yield of charge separation in Al_2O_3/BiSI/BiI_3/HTM relative to Al_2O_3/BiI_3/HTM is due to the presence of the

BiSI layer rather than any remaining In_2S_3 used to prepare BiSI.

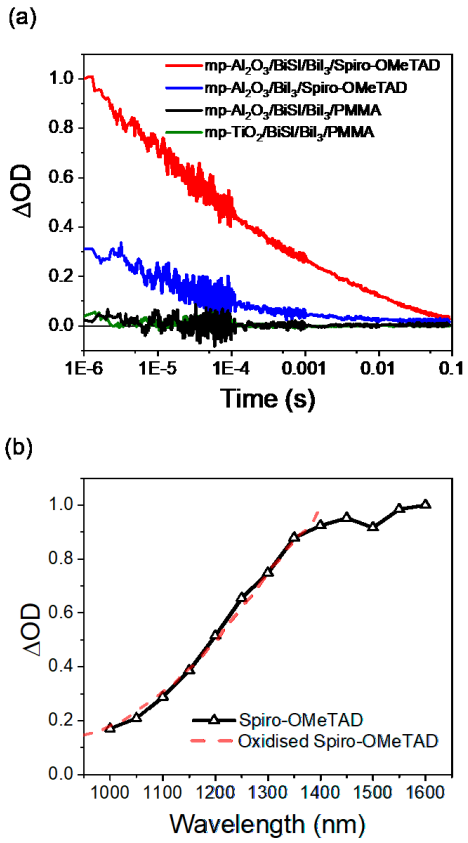

Figure 3-7. (a) Transient absorption kinetics measured at 1,600 nm of BiI_3 films in different thin film structures and (b) transient absorption spectrum of an Al_2O_3/BiSI/BiI_3/spiro-OMeTAD thin film measured 10 µs after pulsed excitation and a steady-state absorption spectrum of spiro-OMeTAD chemically oxidised with $N(PhBr)_3SbCl_6$. The signals were normalised by the absorption of the film at 510 nm, which is the excitation wavelength.

Figure 3-7 (b) presents a comparison of the transient absorption spectrum of the Al_2O_3/BiSI/BiI_3/HTM sample and the steady-state absorption spectrum of chemically oxidised spiro-OMeTAD.[15] Taken together, the data shown in Figures 3-7 (a) and (b) indicate that the

transient signal observed in Al_2O_3/BiSI/BiI_3/HTM following the excitation of BiI_3 is due to hole transfer.

Next, how the electron transport layer (ETL) influences the yield of charge separation was investigated. For this, we compared two commonly used metal oxides in hybrid solar cells, namely TiO_2 and SnO_2. Figure 3-8 shows the transient absorption decays obtained in TiO_2/BiSI/BiI_3/HTM and SnO_2/BiSI/BiI_3/HTM. The kinetics follows the charge recombination between the electrons in the metal-oxide semiconductor and holes in the spiro-OMeTAD. Moreover, they were obtained following 510 nm excitation and at a 1,600 nm probe wavelength.

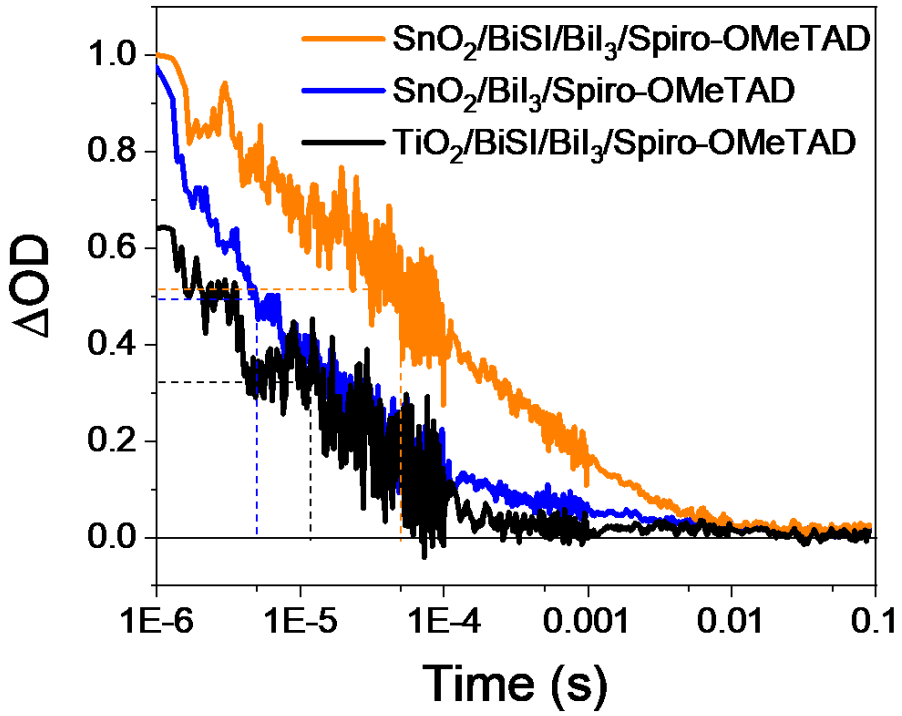

Figure 3-8. Transient absorption kinetics measured at 1,600 nm for BiSI/BiI_3 films on different ETLs. The signals were normalised by the absorption of the film at 510 nm, which is the

excitation wavelength.

Figure 3-8 clearly shows that the SnO_2-based sample exhibits a higher yield of charge separation compared to the TiO_2-based sample. This difference in charge separation yield likely stems from the more favourable interfacial energetics for electron transfer in the SnO_2-based sample due to the lower conduction band of SnO_2 relative to TiO_2. The SnO_2-based sample apparently exhibits a longer recombination lifetime ($\tau_{1/2} \fallingdotseq 80$ μs) compared to the TiO_2-based sample $\tau_{1/2} \fallingdotseq 12$ μs). When the decays from SnO_2/BiI_3/Spiro-OMeTAD and SnO_2/BiSI/BiI_3/Spiro-OMeTAD films are compared, they show similar amplitude but longer lifetime of polarons on Spiro-OMeTAD on the film with BiSI. First, it is also apparent that the use of the BiSI layer in the SnO_2-based samples slows the rate of recombination without affecting the yield. This may be due to the BiSI functioning as a recombination blocking layer. Similar behaviour has been reported when Al_2O_3 layers have been used to retard electron–hole recombination at dye/TiO_2 heterojunctions.[15] Second, they have similar amplitude and it may come from the similar conduction band energy levels of SnO_2, BiSI. They can have similar driving force to extract charges with similar energy levels but with BiSI, BiI_3 can stay in mixed structure due to the in-situ method and therefore, higher surface area between BiI_3 and BiSI can be made. This phenomenon seems to have an advantage here for photovoltaic application.

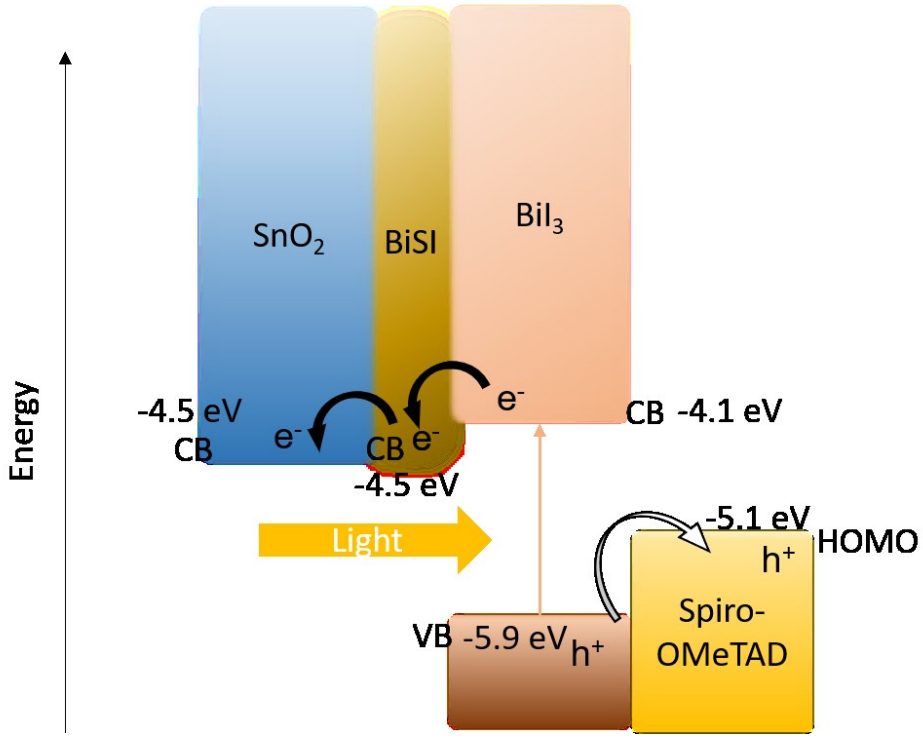

Figure 3-9. Schematic illustration of the charge transfer processes in the investigated samples. The energy levels of BiSI and BiI_3 are based on literature data; CB of SnO_2: -4.5 eV, CB of BiSI: -4.5 eV, CB of BiI_3: -4.1 eV, VB of BiI_3: -5.9 eV, and HOMO of spiro-OMeTAD: -5.1 eV.[4, 9]

Based on the transient absorption data presented above, a possible charge separation mechanism in the SnO_2/BiSI/BiI_3/HTM film can be proposed; this is summarised in Figure 3-9. Photon absorption by the BiI_3 layer leads to the formation of electrons and holes in the BiI_3. This is followed by electron transfer to BiSI and hole transfer to the spiro-OMeTAD phases. Electron transfer to BiSI is followed by further transfer of electrons to SnO_2 as a result of the favourable energy level alignment at the SnO_2/BiSI interface. BiI_3 is known to exhibit a fast electron–hole lifetime of ~200 ps[6]. Therefore, in the absence of the BiSI interlayer it is possible that electron and hole transfer to the metal oxide and HTM phases, respectively, directly

compete with the electron–hole recombination in the BiI_3 absorber, thereby leading to a low yield of hole transfer. The significantly lower yield of hole transfer observed in the Al_2O_3/BiI_3/spiro-OMeTAD film is consistent with this assertion.

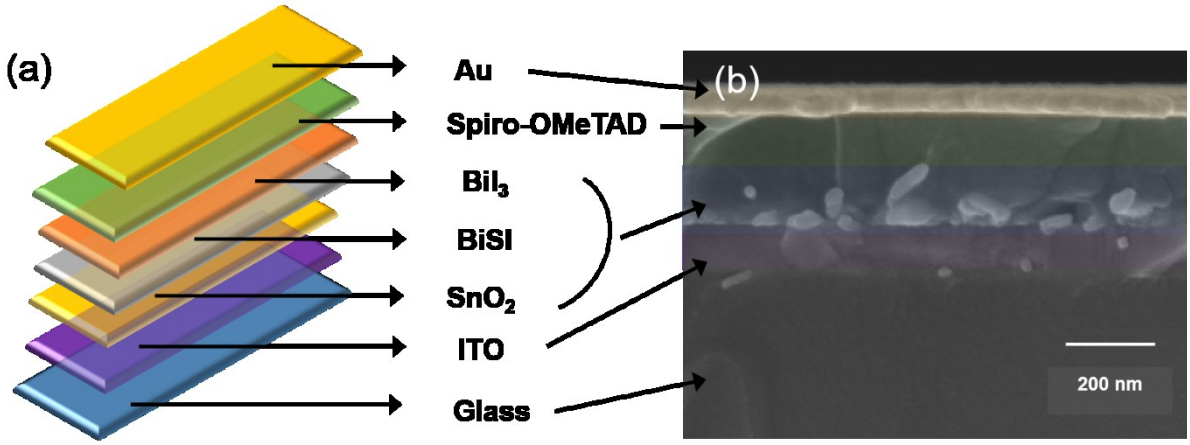

Figure 3-10. (a) Schematic device architecture of BiI_3-based solar cells fabricated with the above knowledge and (b) cross-sectional SEM image of a prepared solar cell device.

Solar cells were fabricated employing the $SnO_2/BiSI/BiI_3$/HTM films. Figure 3-10 (a) illustrates the structure of the fabricated solar cells and Figure 3-10 (b) shows its cross-sectional SEM image. The HTM (here, Spiro-OMeTAD) covers the rough surface of $BiSI/BiI_3$ mixture, efficiently collecting holes from them and preventing them from contacting the gold electrode directly.

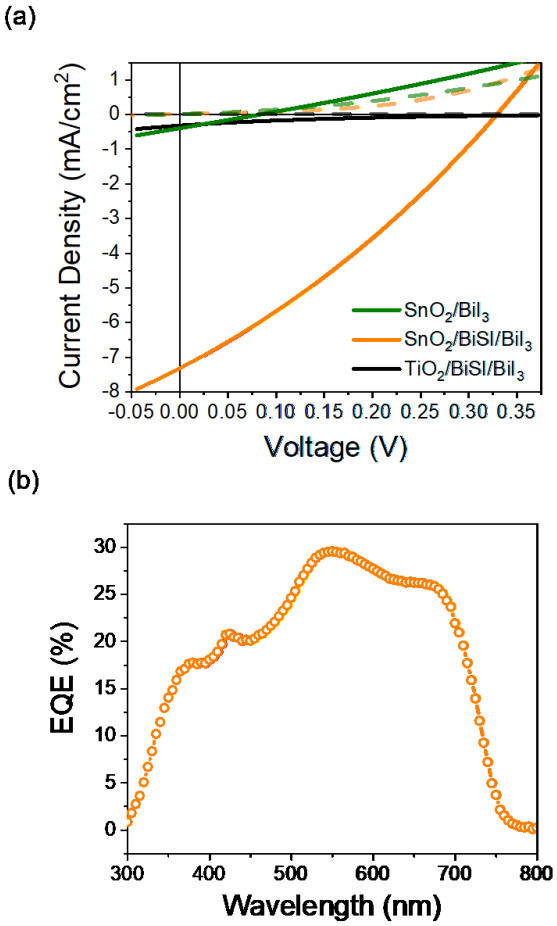

Figure 3-11. (a) JV traces of the assembled devices (dashed lines represent measurements in the dark) with different ETLs and (b) an external quantum efficiency spectrum from a device with an ITO/c-SnO_2/BiSI/BiI_3/Spiro-OMeTAD/Au structure.

Table 3-1. Summary of the photovoltaic performance of the solar cells prepared on different ETLs.

	V_{oc} (V)	J_{sc} (mA/cm^2)	FF	PCE (%)
SnO_2/BiI_3	0.08	0.40	0.25	0.01
$SnO_2/BiSI/BiI_3$	0.33	7.32	0.30	0.72
$TiO_2/BiSI/BiI_3$	0.49	0.32	0.12	0.02

Figure 3-11 (a) shows the JV characteristics of typical solar cells fabricated on SnO_2 and TiO_2. Table 3-1 gives the obtained photovoltaic parameters including J_{sc}, V_{oc}, FF and PCE. The device annealed at 100°C showed a relatively poor performance. This may result from the fast charge recombination in BiI_3 without charges being transferred to the ETL or HTL efficiently as discussed above. In the presence of a BiSI interlayer in the samples prepared on SnO_2 and annealed at 200°C, fast charge extraction from BiI_3 to BiSI is expected and so longer-lived charges can be extracted to the electrode showing higher V_{oc}, J_{sc} and PCE relative to the device without a BiSI interlayer. The device with TiO_2 also shows poor performance although there is BiSI interlayer. The energy mismatch between TiO_2 and BiSI means that the charge transfer from TiO_2 and BiSI is not favoured. Therefore, most extracted charges accumulate on BiSI and are recombined without being transferred. As a result, the device cannot perform well as shown in the figure. I note that this single calculated PCE can give error on the accuracy because the device efficiency can be affected by various conditions and the conditions can be affected during the device fabrication process. Therefore, it can give more accurate result to show the

result from large number of samples.

Figure 3-11 (b) is the EQE spectrum of a SnO_2-based solar cell annealed at 200°C that matches well with the absorption spectrum of the BiSI/BiI_3 film (see Figure 3-6 (a)), showing that the generated currency is from the light absorber.

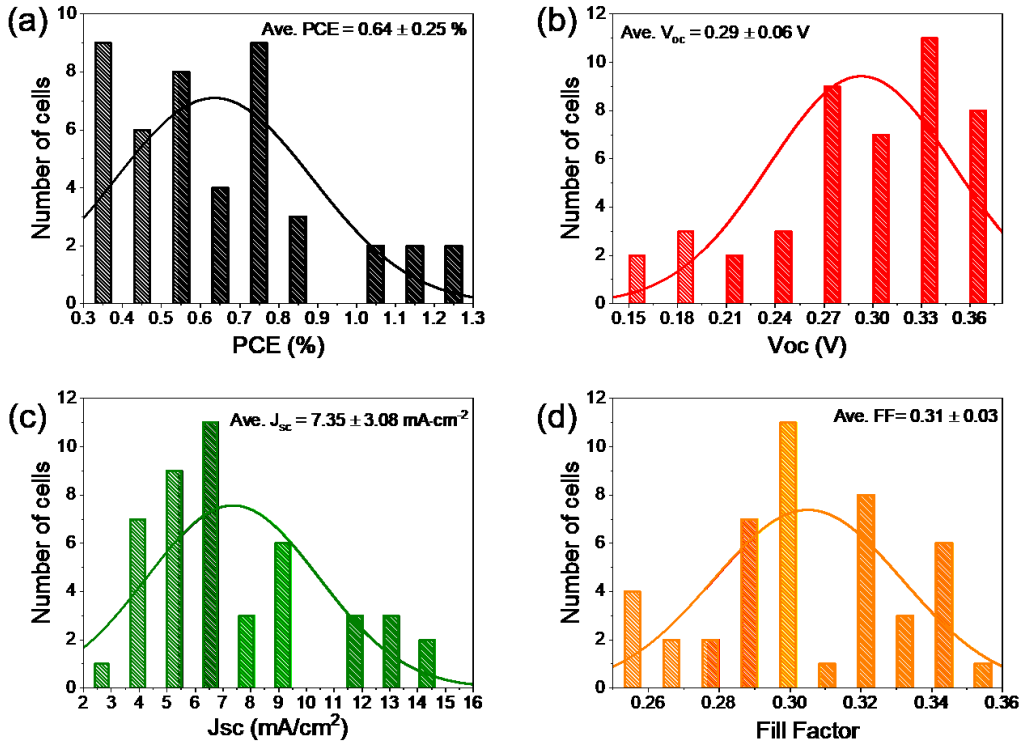

Figure 3-12. Histogram from 45 prepared solar cell devices with ITO/c-SnO_2/BiSI/BiI_3/Spiro-OMeTAD/Au structure.

Figure 3-12 shows the histogram obtained from 45 prepared solar cell devices in a structure of ITO/c-SnO2/BiSI/BiI3/Spiro-OMeTAD/Au. The average of PCE, V_{oc}, J_{sc} and FF are 0.64±0.25%, 0.29±0.06 V, 7.35±3.08 mA/cm^2 and 0.31±0.03, respectively. It is difficult to

maintain the film quality of BiSI and BiSI/BiI_3; the values have large distributions as seen in the figure. This might come from the thickness sensitivity of the BiSI layer. If the BiSI layer is too thick, it might be difficult to transfer charges to SnO_2; if the BiSI layer is too thin, it might be difficult to extract charges from BiI_3. The optimal thickness was not investigated because it generates a mixture of BiSI/BiI_3 rather than just a BiSI thin layer and so finding the exact thickness of the BiSI layer is difficult. It would be helpful to optimise the thickness by changing the concentration of indium dimethylpentyl xanthate and BiI_3.

The oxidised spiro-OMeTAD has improved conductivity of hole transport and enhanced charge transfer at the Au/Spiro-OMeTAD interface.[17, 18] Therefore, it is normal to oxidise spiro-OMeTAD to improve the performance. For this, the prepared devices were contained in a dark box before JV curve measurement for two weeks and this oxidation of spiro-OMeTAD improved their PCE, as shown in Figure 3-13. This result also proves that the BiI_3 is a stable material and it can maintain its ability for at least two weeks.

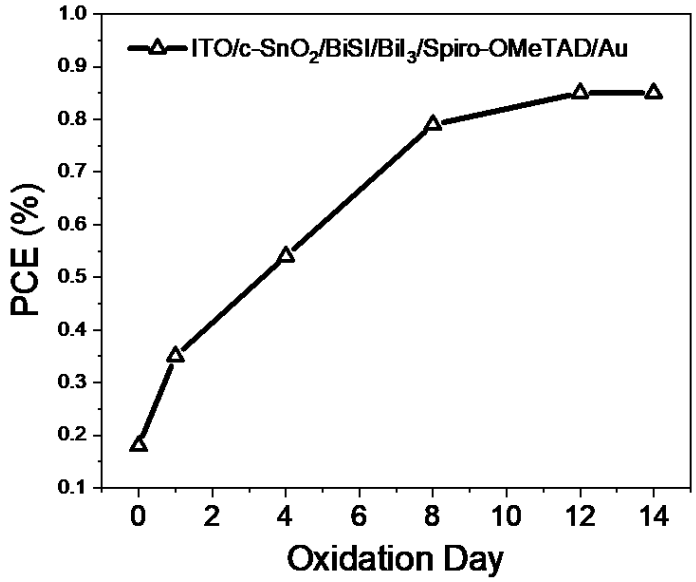

Figure 3-13. The increase of PCE with oxidation time.

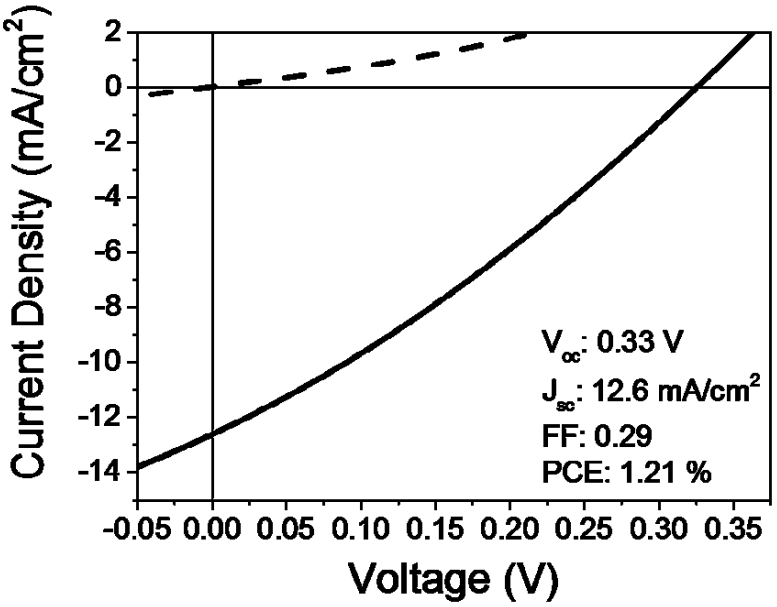

Figure 3-14. JV traces of the best performing solar cell with ITO/c-SnO_2/BiSI/BiI_3/Spiro-OMeTAD/Au structure.

Figure 3-14 is a JV curve from the champion solar cell with this architecture exhibiting a J_{SC} of 12.6 mA/cm² and a PCE of 1.21%. The highest PCE of 1.2% with BiI_3-based solar cell was reported by Tiwari *et al.* in 2018.[2] The best performing device from this work also showed a similar level of PCE that was achieved by integrating the BiSI interlayer. This significantly improved the yield of the hole transfer from the BiI_3 to spiro-OMeTAD. The improvement in the yield of the hole transfer is attributed to the BiSI layer acting as an electron acceptor and thus intercepting the photogenerated electron in the BiI_3 before it can decay back to its ground state. This subsequently allows the photogenerated hole in the BiI_3 to transfer to the organic HTM. Additionally, the device has low fill factor and low V_{OC} than expected. They may come from pinholes in the active layer (Figure 3-5). Although the morphology has been improved by BiSI formation, but there are still many pinholes. The ETM and HTM can meet at the pinholes and the transferred charges to ETM and HTM can recombine. It may have resulted in leakage in the dark current (dashed line) and low V_{OC} and low FF.

Application of the BiSI interlayer in $MA_3Bi_2I_9$

To confirm that the *in situ*-formed BiSI interlayer can be applied to solar cells based on different materials, methylammonium bismuth perovskite ($MA_3Bi_2I_9$) thin films were fabricated on a BiSI interlayer. To dissolve the remaining BiI_3 in the BiSI/BiI_3 mixture, a $MA_3Bi_2I_9$ precursor solution was loaded on the BiSI/BiI_3 layer for 25 s before spin-coating.

Figure 3-15 (a) shows the XRD patterns from the prepared $MA_3Bi_2I_9$ thin films. For the thicker layer to obtain clear patterns, mp-Al_2O_3 was used as scaffold. The blue pattern shows that the $MA_3Bi_2I_9$ layer is formed and matches the reference very well (01-085-6013). For this thin film, the preferred-orientation is (006), which indicates a crystalline growth along the c -axis. When comparing $MA_3Bi_2I_9$ with and without a BiSI layer (Figure 3-15 (a) blue and orange patterns, respectively), $MA_3Bi_2I_9$ on BiSI shows both $MA_3Bi_2I_9$ and BiSI peaks without additional peaks from other elements. In addition, peaks from $MA_3Bi_2I_9$ are the majority, showing that the $MA_3Bi_2I_9$ is thicker than the BiSI.

Figure 3-15 (b) is the UV–Vis spectra of $MA_3Bi_2I_9$ on glass (black symbol) and glass/BiSI (red symbol) substrates. For $MA_3Bi_2I_9$ on glass, the absorption starts to increase at around 600 nm (2.06 eV), which matches the reported bandgap of $MA_3Bi_2I_9$.[19, 20] Meanwhile, $MA_3Bi_2I_9$ on glass shows another absorption increase at around 750 nm (1.65 eV), which is a similar value to the BiSI Tauc plot above (Figure 3-6 (c)). From both data, we can conclude that $MA_3Bi_2I_9$ was formed on the BiSI interlayer without reacting with it.

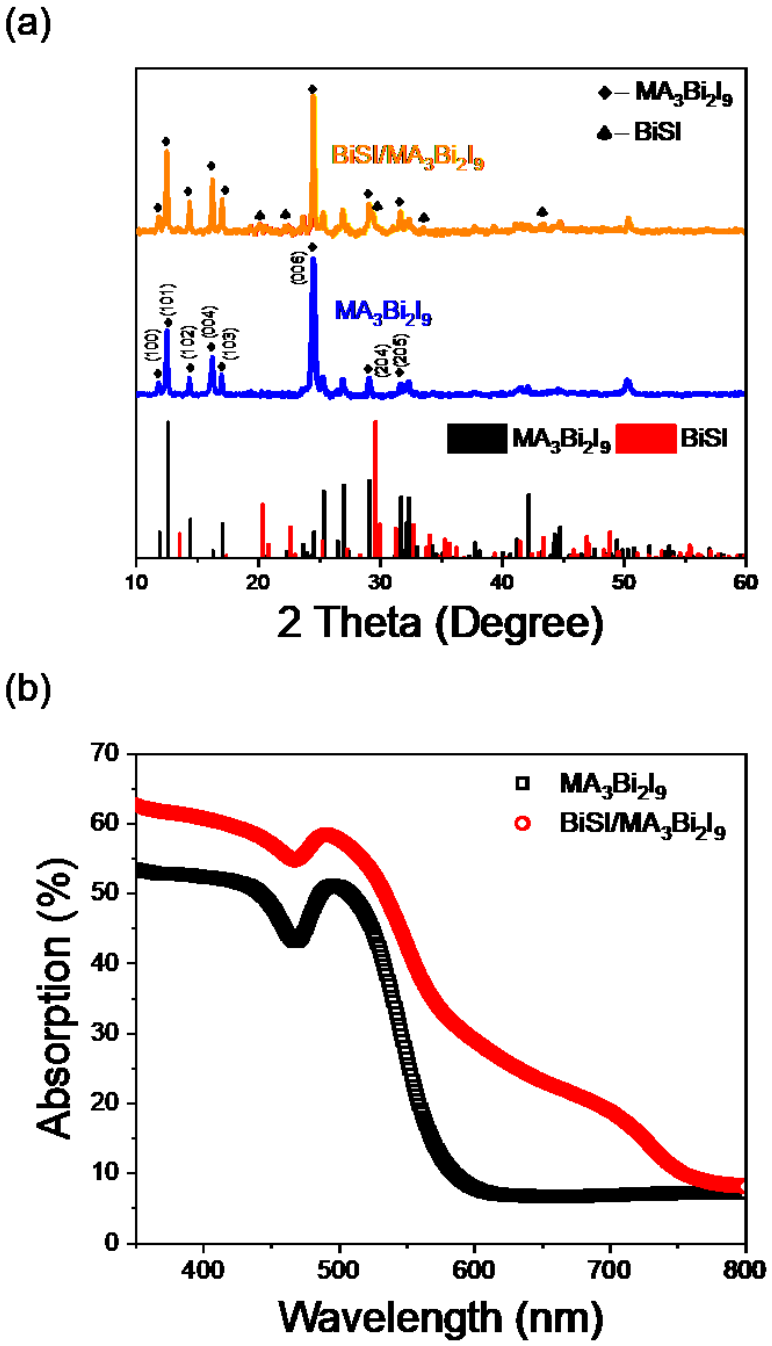

Figure 3-15. (a) X-ray diffraction patterns of $MA_3Bi_2I_9$ on (a) mp-Al_2O_3 and (b) mp-Al_2O_3/BiSI substrates and references of $MA_3Bi_2I_9$ (black, code: 01-085-6013) and BiSI (red, code: 01-073-1171) and (b) UV-Vis absorption spectra of $MA_3Bi_2I_9$ on glass and glass/BiSI

substrates.

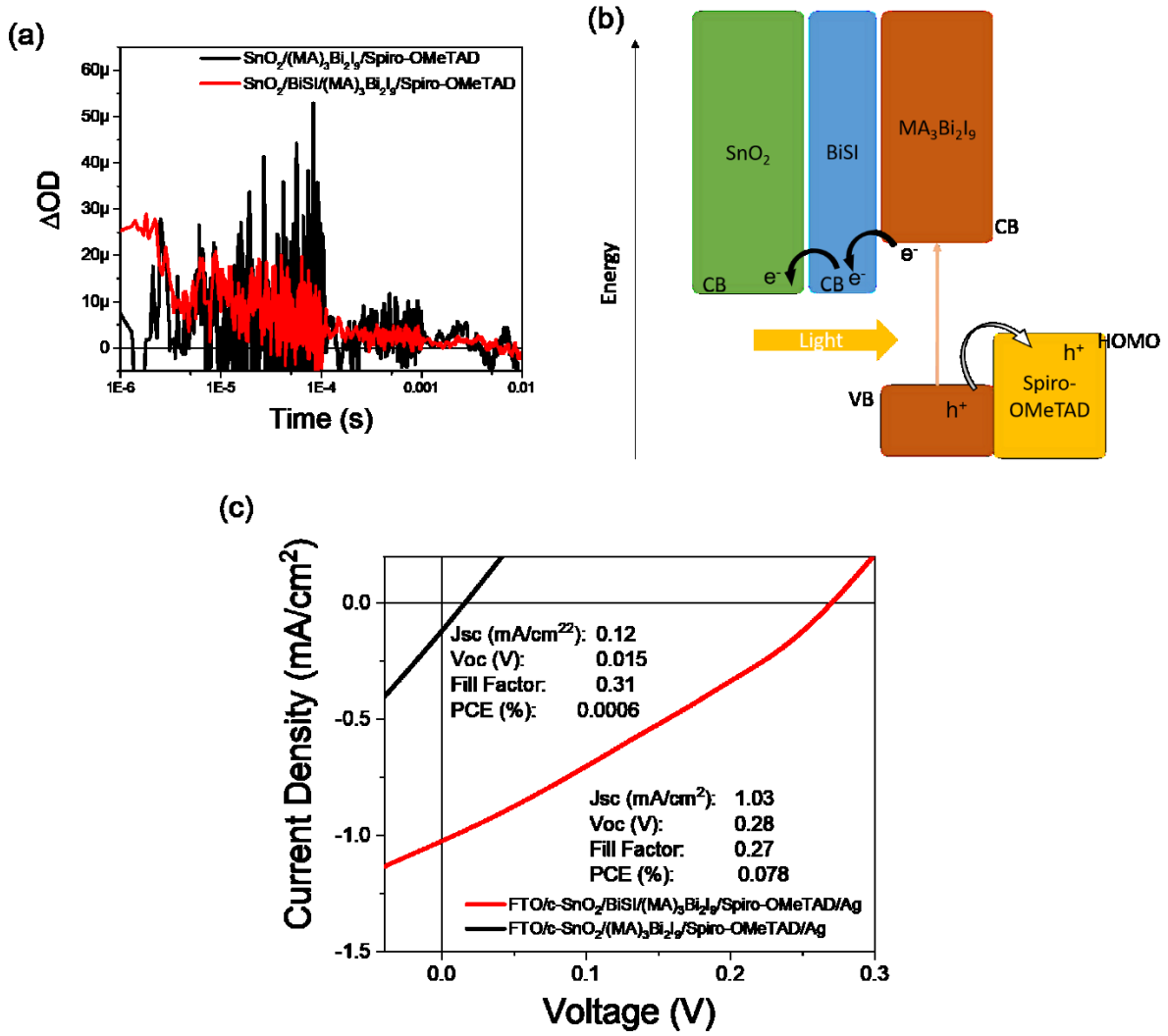

Figure 3-16. (a) Transient absorption kinetics measured at 1,600 nm for $(MA)_3Bi_2I_9$ films on SnO_2 or SnO_2/BiSI ETLs. The signals were normalised by the film's absorption at 450 nm, which is the excitation wavelength. (b) JV traces of solar cell devices with $(MA)_3Bi_2I_9$ films with and without a BiSI interlayer.

To observe the effect of the BiSI layer on the charge transfer on $MA_3Bi_2I_9$, microsecond-to-

millisecond TAS was employed. Figure 3-16 (a) shows the transient absorption kinetics from a $MA_3Bi_2I_9$ thin film with and without a BiSI layer covered by spiro-OMeTAD. The probe was at 1,600 nm where the polaron of spiro-OMeTAD can be easily observed. The signal is negligible for $MA_3Bi_2I_9$ without BiSI (black trace in Figure 3-16 (a)), meaning that while the charges were generated in $MA_3Bi_2I_9$, the generated holes could not live long due to the charge recombination between holes transferred to spiro-OMeTAD and the electrons remaining in $MA_3Bi_2I_9$. When BiSI was employed (red trace in Figure 3-16 (a)), the signal became more obvious compared to that without a BiSI layer. As described above with BiI_3, the BiSI layer extracted electrons more efficiently than the compact SnO_2 ETL, and so more holes could be transferred to spiro-OMeTAD and it was able to live longer due to the reduced recombination between electrons on $MA_3Bi_2I_9$ and holes on spiro-OMeTAD.

Figure 3-16 (b) helps illustrate this observation. With knowledge from TAS, solar cell devices with and without were fabricated and compared in Figure 3-16 (c). The solar cell without a BiSI layer (black trace in Figure 3-16 (c)) performed poorly. This might come from the unoptimised recipe for $MA_3Bi_2I_9$ with a BiSI layer (red trace in Figure 3-16 (c)), but the PCE was increased 100-fold even though this structure was not yet optimised.

Solvent Vapour Annealing (SVA)

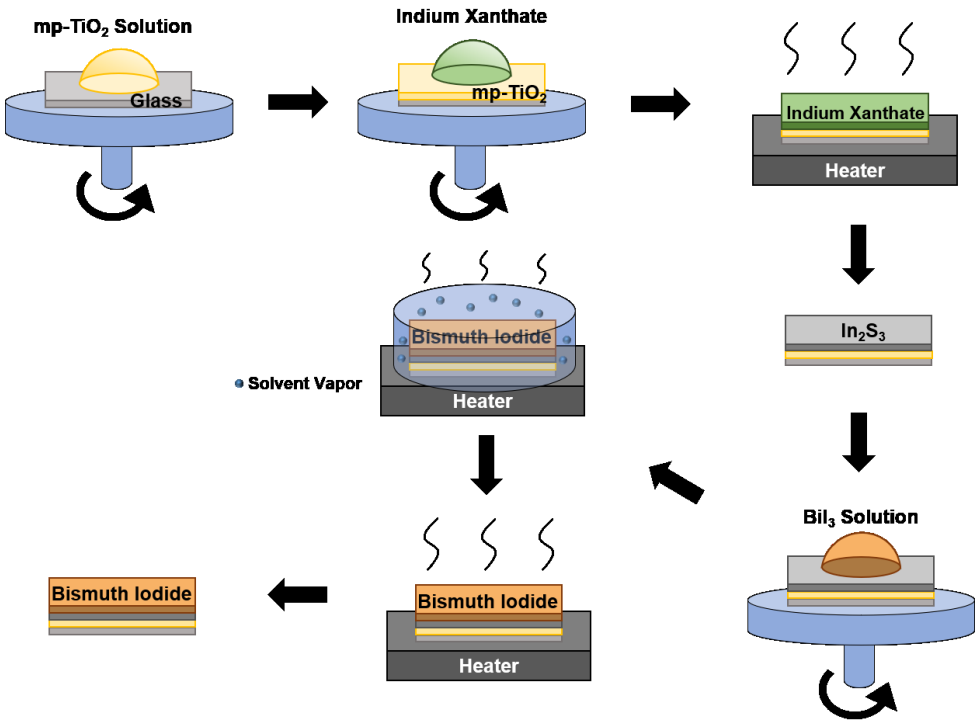

Figure 3-17. Schematic drawing of thin film preparation including a BiSI inter-layer through the SVA method.

Solvent Vapour Annealing (SVA) is a method normally used to improve film quality. Reportedly, this method helps increase the grain size and carrier diffusion lengths in lead-based perovskite.[21] Hamdeh *et al.*[1] applied this method to bismuth iodide and obtained larger grain sizes and polydispersity in grain sizes. This phenomenon led to improved film morphology and thus higher device efficiency. They suggested that while the SVA method has only a slight effect on the carrier lifetime, it leads to the increased carrier lifetime due to increased grain sizes and thicknesses, which reduces the grain boundaries.

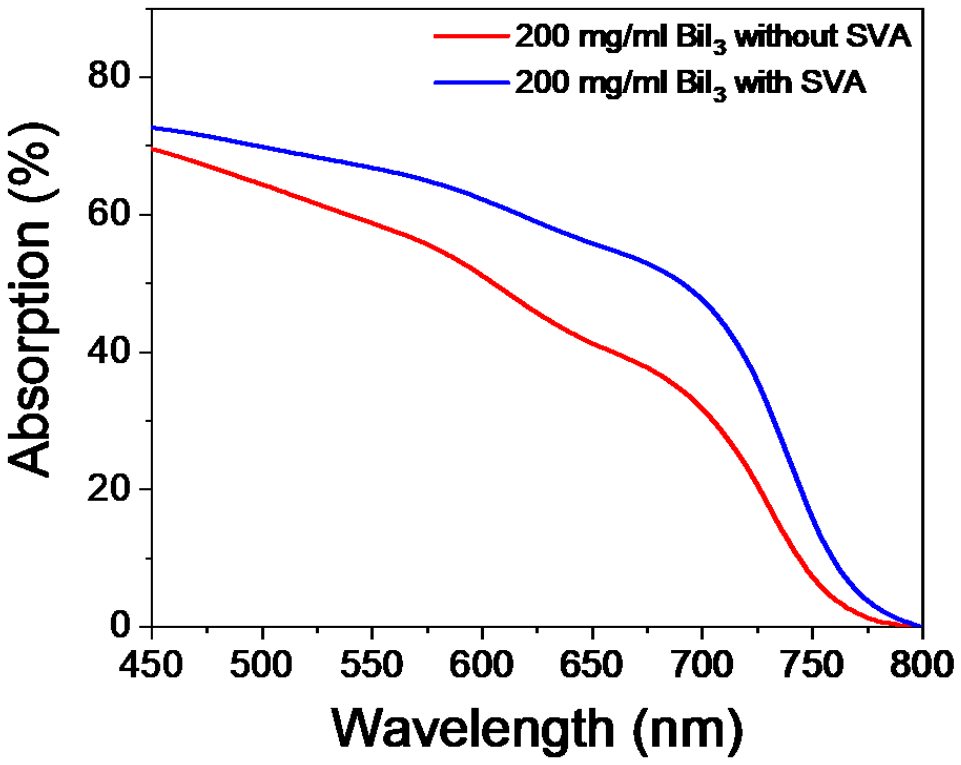

Figure 3-18. Absorption spectra of BiSI/BiI_3 thin films formed with and the without SVA method.

Expecting a similar effect for the system above, the SVA method was employed. Figure 3-17 shows how the SVA method was processed while the bismuth iodide layer was formed. This process is the same as that described in Chapter 3-2 (Figure 3-1), except dropping 100 µL of THF on the corner of the glass substrate covering the film with glassware when the annealing is being processed. Here, the annealing temperature was set to 300°C, because the experiment was conducted before temperature optimisation.

Thus, a darker film was obtained compared to those without SVA. Figure 3-18 clearly shows

this in the absorption spectra of the BiSI/BiI_3 thin films with and without the SVA method. When compared, the film with SVA method shows higher absorption and it might have come from thicker films as reported by Hamdeh *et al.*[1].

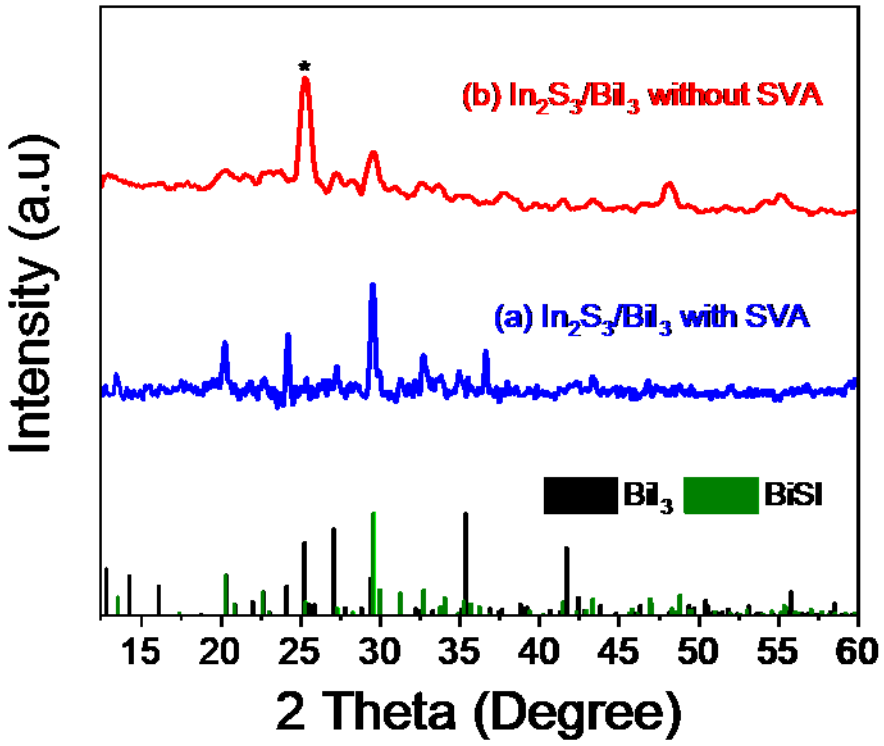

Figure 3-19. X-ray diffraction patterns of BiI_3 films on In_2S_3 (a) annealed and (b) solvent vapour annealed at 300°C and references of BiI_3 (black, code: 01-076-1742) and BiSI (green, code: 01-073-1171) (a peak marked with * is from mo-TiO_2).

XRD was obtained to determine whether the BiSI/BiI_3 has formed any other compound by the SVA method (Figure 3-19). The XRD patterns show only BiI_3 and BiSI in both films with and without the SVA method. The only difference is that the film through the SVA method shows

more obvious BiSI peaks, which has become the dominant pattern compared to the film without SVA. It seems that the SVA method brings a greater reaction between BiI_3 and In_2S_3, resulting in a larger amount of BiSI in the film. It matches with the UV–Vis spectra (Figure 3-18), showing higher absorption.

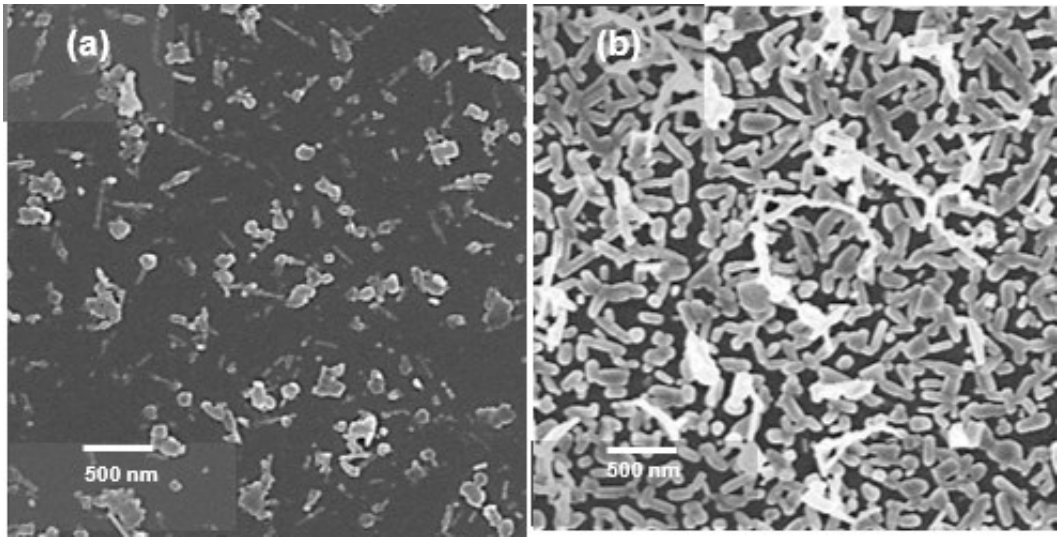

Figure 3-20. SEM images of BiI_3/In_2S_3 thin films annealed at 300 °C (a) without SVA and (b) with SVA.

Figure 3-20 shows SEM images from the films with and without the SVA method. The film without SVA shows the dominant In_2S_3 and just small domains of BiI_3 and BiSI. However, THF still gave inhomogeneous results, as can be seen in Figure 6 (d). Meanwhile, with SVA, a more compact layer was obtained with rod-like particles over the surface. This shows that the surface morphology can be improved by SVA as expected.

To study how this morphology and the BiI_3/BiSI thickness changes affect the charge mobility, TAS signals were collected as shown in Figure 3-21. It shows the collected TAS signals of

films with and without the SVA method. The films were covered with spiro-OMeTAD on top as the HTM. It shows the SVA method almost doubled the TAS signal, which means that the hole transfer from BiI_3 to HTM has increased. Additionally, as the concentration of BiI_3 solution increases, the TAS signal increases, indicating that more charges were generated, and thus more holes were transferred to the HTM.

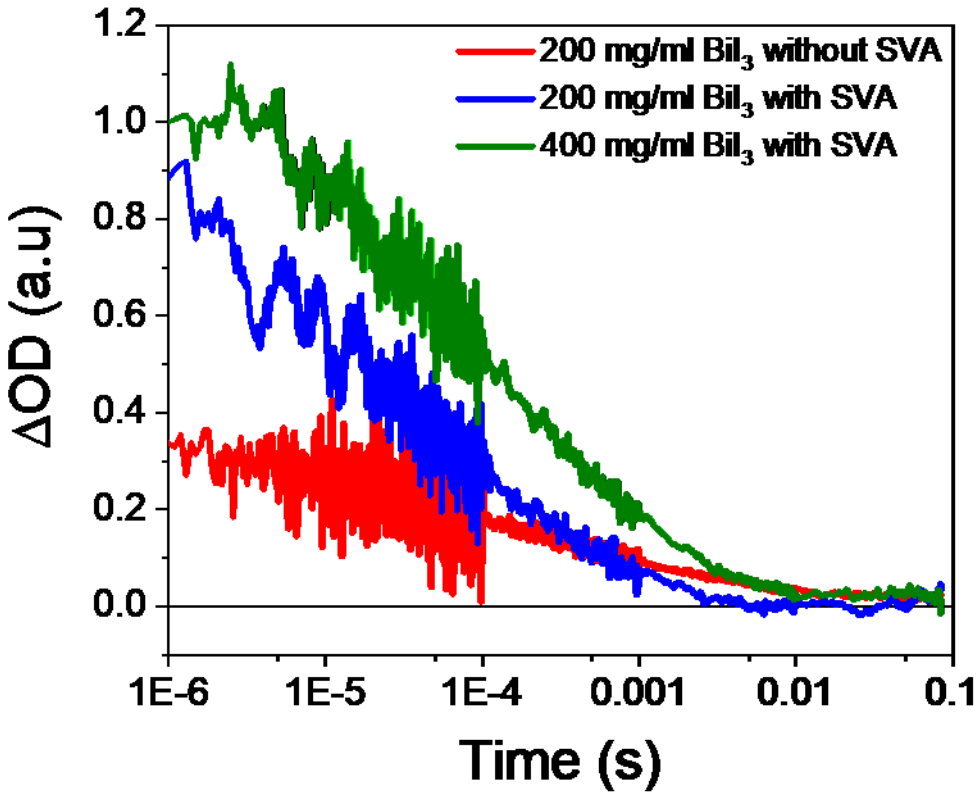

Figure 3-21. Time-resolved transient absorption spectrums of BiI_3 thin films in different concentrations and annealed in different atmospheres.

Solar cell devices were fabricated to investigate how the TAS results appear in real solar cell systems. The structure of the fabricated solar cell is the same as that above in Figure 3-10 (a).

Figure 3-22 shows the JV curves from fabricated solar cells. It was expected to have higher JSC because the TAS signals showed the improved charge transfer to HTM. However, against our expectation, the fabricated cells did not show significant difference in J_{SC}, V_{OC}, FF or PCE.

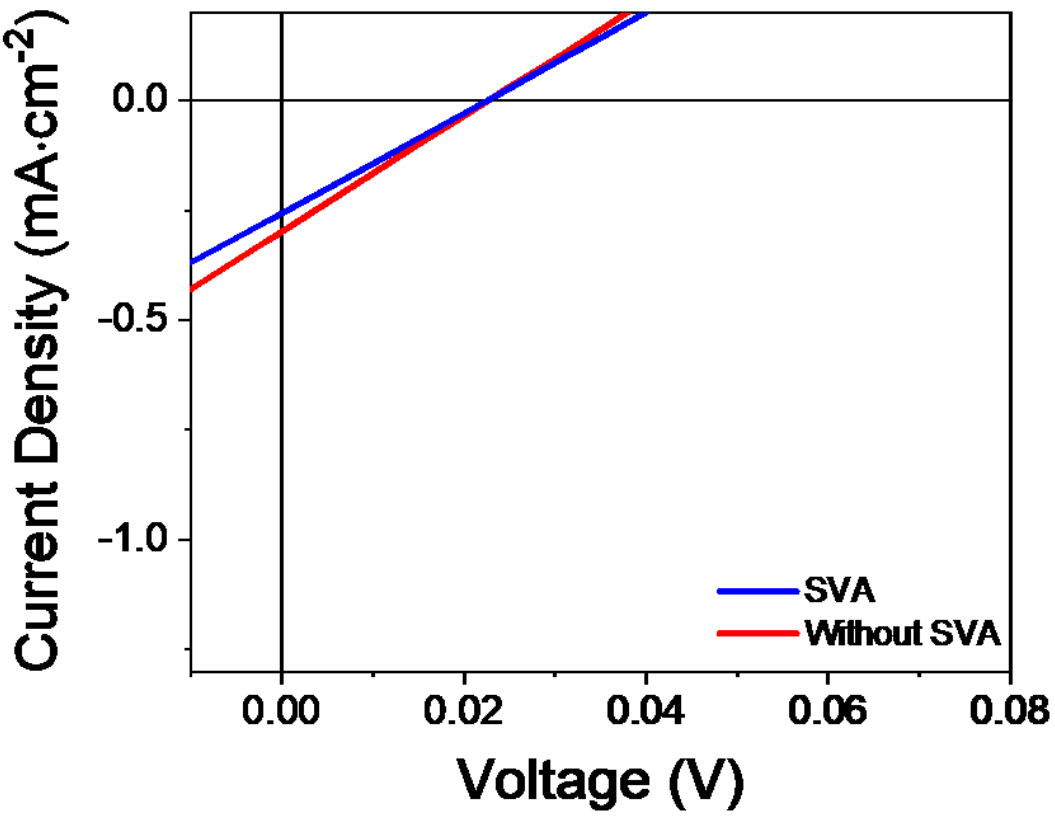

Figure 3-22. Current density–voltage (JV) curves of the fabricated solar cell devices with and without SVA.

This result shows that the thickness of BiSI is an important factor for device performance. When the BiSI layer is thick, the electrons in BiI_3 can be transferred easily and it helps the hole transfer to HTM, resulting in a higher TAS signal. However, in a device, electron transfer to

the electrode is also important. When the BiSI layer is thick, the electrons cannot be transferred to the ETM due to its low charge mobility nature.[9] Therefore, optimising the BiSI layer thickness is required for higher-performing devices. Compared with and without SVA method, through SVA method, it seems most of BiI_3 was converted to BiSI while some BiI_3 left without SVA method. This is clearly seen in XRD patterns, clear BiI_3 peaks observed in Figure 3-6 after annealing but no obvious BiI_3 peaks in Figure 3-19. The result in device was clear, without SVA method where BiI_3 left in the film showed much better device performance. Therefore, it might be possible to say that BiI_3 works as the active layer in this system. However, further investigation is needed in the future to clarify this. Energy-dispersive X-ray spectroscopy or mass spectroscopy can be useful for the investigation.

3-4. Conclusion

To conclude, a BiSI interlayer was generated *in situ* at the interface of the BiI_3 absorber layer and the ETL. Specifically, the BiSI layer was generated by the reaction between In_2S_3 and BiI_3 at 200°C. The formation of BiSI was confirmed by X-ray diffraction and UV–Vis spectroscopy. The integration of the BiSI interlayer in the following architecture: metal oxide/BiSI/BiI_3/spiro-OMeTAD was found to significantly improve the yield of hole transfer from the BiI_3 to spiro-OMeTAD. The improvement in the hole transfer yield is attributed to the BiSI layer acting as an electron acceptor and thus intercepting photogenerated electrons in the BiI_3 before it could decay back to the ground state. This subsequently allowed the photogenerated hole in the BiI_3 to transfer to the organic HTM. Moreover, a 1.21%-efficient photovoltaic cell was fabricated based on the following architecture: glass/ITO/SnO_2/BiSI/BiI_3/spiro-OMeTAD/Au. This structure was also applied to $MA_3Bi_2I_9$ and it successfully improved the charge transfer to HTM as shown with BiI_3. The PCE of the solar cell device was also significantly improved with the BiSI layer even though the device structure and the recipe were not yet optimised.

These devices reported herein employ planar junction SnO_2 layers. As such, we can expect to realise further enhancements in PCE using mesoporous metal oxide films and optimising the BiI_3 film morphology. Additionally, the thickness of the BiSI layer has not yet been optimised and if the optimal thickness can be found, there can be further improvement in the PCE of these devices.

3-5. References

1. U. H. Hamdeh, R. D. Nelson, B. J. Ryan, U. Bhattacharjee, J. W. Petrich and M. G. Panthani, *Chem. Mater.*, 2016, **28**, 6567-6574.

2. D. Tiwari, D. Alibhai and D. J. Fermin, *ACS Energy Lett.*, 2018, **3**, 1882-1886.

3. K. M. Boopathi, S. Raman, R. Mohanraman, F. C. Chou, Y. Y. Chen, C. H. Lee, F. C. Chang and C. W. Chu, *Sol. Energy Mater. Sol. Cells*, 2014, **121**, 35-41.

4. A. J. Lehner, D. H. Fabini, H. A. Evans, C. A. Hebert, S. R. Smock, J. Hu, H. B. Wang, J. W. Zwanziger, M. L. Chabinyc and R. Seshadri, *Chem. Mater.*, 2015, **27**, 7137-7148.

5. M. Scholz, K. Oum and T. Lenzer, *Phys. Chem. Chem. Phys.,* 2018, **20**, 10677-10685.

6. R. E. Brandt, R. C. Kurchin, R. L. Z. Hoye, J. R. Poindexter, M. W. B. Wilson, S. Sulekar, F. Lenahan, P. X. T. Yen, V. Stevanovic, J. C. Nino, M. G. Bawendi and T. Buonassisi, *J. Phys. Chem. Lett.*, 2015, **6**, 4297-4302.

7. A. M. Ganose, K. T. Butler, A. Walsh and D. O. Scanlon, *J. Mater. Chem. A*, 2016, **4**, 2060-2068.

8. N. T. Hahn, A. J. E. Rettie, S. K. Beal, R. R. Fullon and C. B. Mullins, *J. Phys. Chem. C*, 2012, **116**, 24878-24886.

9. N. T. Hahn, J. L. Self and C. B. Mullins, *J. Phys. Chem. Lett.*, 2012, **3**, 1571-1576.

10. T. Rath, M. Edler, W. Haas, A. Fischereder, S. Moscher, A. Schenk, R. Trattnig, M. Sezen, G. Mauthner, A. Pein, D. Meischler, K. Bartl, R. Saf, N. Bansal, S. A. Haque, F. Hofer, E. J. W. List and G. Trimmel, *Adv. Energy Mater.*, 2011, **1**, 1046-1050.

11. P. Miranda, L. P. Mercuri, J. R. Matos, M. F. Maduar and J. Zukerman-Schpector, *J. Therm. Anal. Calorim.*, 2005, **79**, 305-308.

12. P. N. Kumta, P. P. Phule and S. H. Risbud, *Mater. Lett.*, 1987, **5**, 401-404.

13. A. T. Lintereur, W. Qiu, J. C. Nino and J. Baciak, *Nucl. Instrum. Methods. Phys. Res. B*, 2011, **652**, 166-169.

14. A. Cuna, I. Aguiar, A. Gancharov, M. Perez and L. Fornaro, *Cryst. Res. Technol.*, 2004, **39**, 899-905.

15. F. T. F. O'Mahony, Y. H. Lee, C. Jellett, S. Dmitrov, D. T. J. Bryant, J. R. Durrant, B. C. O'Regan, M. Gräetzel, M. K. Nazeeruddin and S. A. Haque, *J. Mater. Chem. A*, 2015, **3**, 7219-7223.

16. E. Palomares, J. N. Clifford, S. A. Haque, T. Lutz and J. R. Durrant, *J. Am. Chem. Soc.*, 2003, **125**, 475-482.

17. S. Wang, W. Yuan and Y. S. Meng, *ACS Appl. Mater. Interfaces*, 2015, **7**, 24791-24798.

18. X. B. Wang, J. H. Wu, Y. Q. Yang, X. P. Liu, Q. Y. Guo, Z. Y. Song, G. D. Li, Z. Lan and M. L. Huang, *J. Mater. Chem. A*, 2019, **7**, 13256-13264.

19. M. Lyu, J. H. Yun, M. Cai, Y. Jiao, P. V. Bernhardt, M. Zhang, Q. Wang, A. Du, H. Wang, G. Liu and L. Wang, *Nano Res.*, 2016, **9**, 692-702.

20. B. W. Park, B. Philippe, X. Zhang, H. Rensmo, G. Boschloo and E. M. J. Johansson, *Adv. Mater.*, 2015, **27**, 6806-6813.

21. Z. Xiao, Q. Dong, C. Bi, Y. Shao, Y. Yuan and J. Huang, *Adv. Mater.*, 2014, **26**, 6503-6509.

Chapter 4: Overcoming the Intrinsic Problems of Bismuth-based Perovskites for Photovoltaic Applications

Abstract

As discussed above, stable lead-free perovskites are attracting interest from researchers in this field in the expectation of similar optoelectronic properties to lead-based perovskite but with high stability and low-toxicity; one of them is bismuth 0D perovskite. While they have achieved improved efficiency over the last few years, they have yet to achieve >4% PCE. The reason suggested for this efficiency limit is the high defects and high binding energy, which are their intrinsic properties.[1–4]

Two ways to overcome those concerns are suggested in this chapter. The first way is to mix bismuth and antimony in a 0D perovskite structure ($MA_3(Bi_{1-x}Sb_x)_2I_9$) and the other way is to introduce phenylethylammonium (PEA^+) to the small cation position, resulting in a 2D perovskite structure to bismuth perovskite. Both can successfully improve the optoelectronic properties for higher solar cell performance.

In the first part of this chapter, the opto-electronic properties of novel lead-free bismuth and antimony-based 0D perovskites $MA_3B_2I_9$ (B = Bi, Sb) are investigated. Complete miscibility was found across the solid-solution with a <1% change in the calculated lattice parameters. This miscibility extends to a full configurational disorder of Bi and Sb and a subsequent reduction in the experimentally observed PLQY. I would like to highlight the significance of the observed bandgap bowing to fine-tune the electronic structure for opto-electronic devices.

In addition, the substitution of Bi with the smaller Sb leads to lower calculated effective masses, and thus lower binding energies. As the binding energies measure the strength of the photoexcited electron and hole pairs, they play a crucial factor in electron–hole recombination processes. In this respect, there seems to be a shift from an excitonic regime to a non-excitonic regime.

In the second part of this chapter, a new 2D $(PEA)_3Bi_2I_9$ was prepared and the 2D structure was confirmed using XRD analysis. SEM showed the improved film morphology in 2D bismuth perovskite compared to the 0D one and it was found that charges lived longer in the 2D material according to TRPL. Finally, solar cells with this new material were fabricated and the efficiency was improved with the previously used structural optimisation.

The insights from this study are also applicable in other semiconductors such as silver, bismuth and antimony double perovskites, Sb/Bi sulfide and Sb/Bi triiodide.

4-1. Metal Cation Transmutation in Lead-free Perovskites

4-1-1. Introduction

The 0D $MA_3Bi_2I_9$ and $MA_3Sb_2I_9$ systems have recently been investigated for solar cell applications with efficiencies increasing from 0.5% to 3.2%, with the progression of device architectures and precursor chemistries.[1, 3, 5–15] However, some controversy remains over their structures in experiments, with $MA_3Bi_2I_9$ having been reported in both orthorhombic (space group: *Cmcm*)[16] and hexagonal phases (space group: $P6_3/mmc$).[1, 17, 18] Additionally, there has been some disagreement on the electronic structure of Bi/Sb end members with reported bandgaps in the range of 1.9–2.2 eV.[11, 15, 19, 20] Whilst these bandgaps may preclude them from becoming efficient solar cells,[21] the effect of mixing of Bi and Sb on the electronic properties has yet to be investigated and may provide a route to increasing the power conversion efficiencies by narrowing the bandgap. This follows previous work on lead/tin-based compounds where significant bandgap bowing was seen in mixed systems.[22–25]

In this chapter, the effect of mixing Bi and Sb on their atomistic structures, effective masses and exciton binding energies across a solid solution were investigated through a combination of *ab initio* simulations and experiments. All experimental work presented here was performed by myself and the computational work on $(MA)_3(Bi_{1-x}Sb_x)2I_9$ was performed by my postdoc collaborator Alex Aziz who is in Prof. Saiful's group at the University of Bath.

Recently, the Bi/Sb end members have been reported with binding energies in excess of 200 meV.[3, 6] This is significantly higher than lead-based perovskites, which have been reported at <50 meV.[18, 26, 27] Understanding the trend in these fundamental properties will have important

implications in the operation of devices, affecting the charge carrier mobilities and dissociation energies that are critical in the generation of free carriers from photoexcited electron–hole pairs.

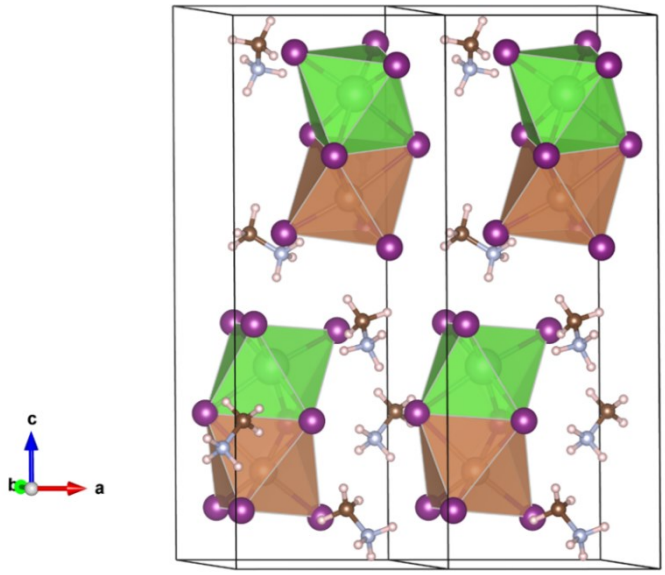

Figure 4-1-1. Hexagonal 2 × 1 × 1 supercell of a possible configuration of $MA_3(BiSb)_2I_9$. Individual unit cells are marked with black lines. $M_2X_9^{3-}$ (M = Bi, Sb) clusters are dimer units comprising of pairs of face-sharing MX_6 octahedra. Inorganic octahedra are shown in brown (Sb) or green (Bi), iodine atoms are shown in purple. Unit cell information: a- 8.568 Å, b- 14.861 Å, c- 21.757 Å, β- 90.04°, space group: $P6_3/mmc$.

4-1-2. Method

Materials

Methylammonium iodide (MAI) was purchased from Dyesol Ltd. BiI_3, SbI_3 and Bathocuproine (BCP) were purchased from Sigma Aldrich. PEDOT:PSS was purchased from Heraeus Clevios. GmbH and $PC_{70}BM$ were purchased from Ossila. Anhydrous dimethylformamide (DMF) and anhydrous chlorobenzene (CB) were purchased from ACROS Organics™. Absolute ethanol, acetone and isopropanol (IPA) were purchased from VWR. All products were used directly without any further purification.

Substrate preparation

Glass substrates (VWR Microscope Slides, BS7011, 1.0–1.2 mm) were used after cutting to the specified size (1.25 cm × 1.25 cm) and washing and drying in a N_2-gas stream. The washing process included three consecutive steps: ultrasonic bath treatment in deionised water and then acetone and isopropanol for 15 min each.

Perovskite layer fabrication

For the active layer, precursor solutions were prepared by dissolving 0.5 mmol BiI_3 or SbI_3 according to the different ratio and 0.75 mmol of MAI into DMF with HI additive (30 ml/ml). The prepared solutions were spin-coated at 6,000 rpm with 2,000 rpm/s acceleration for 40 s. During the spin-coating, CB (600 μL) quickly dropped to the centre of the substrates after 5 s. Annealing at 110°C on a hotplate for 20 min followed. This method follows the reported literature by Boopathi *et al*.[15] Figure 4-1-2 illustrates the whole process for the perovskite layer

fabrication.

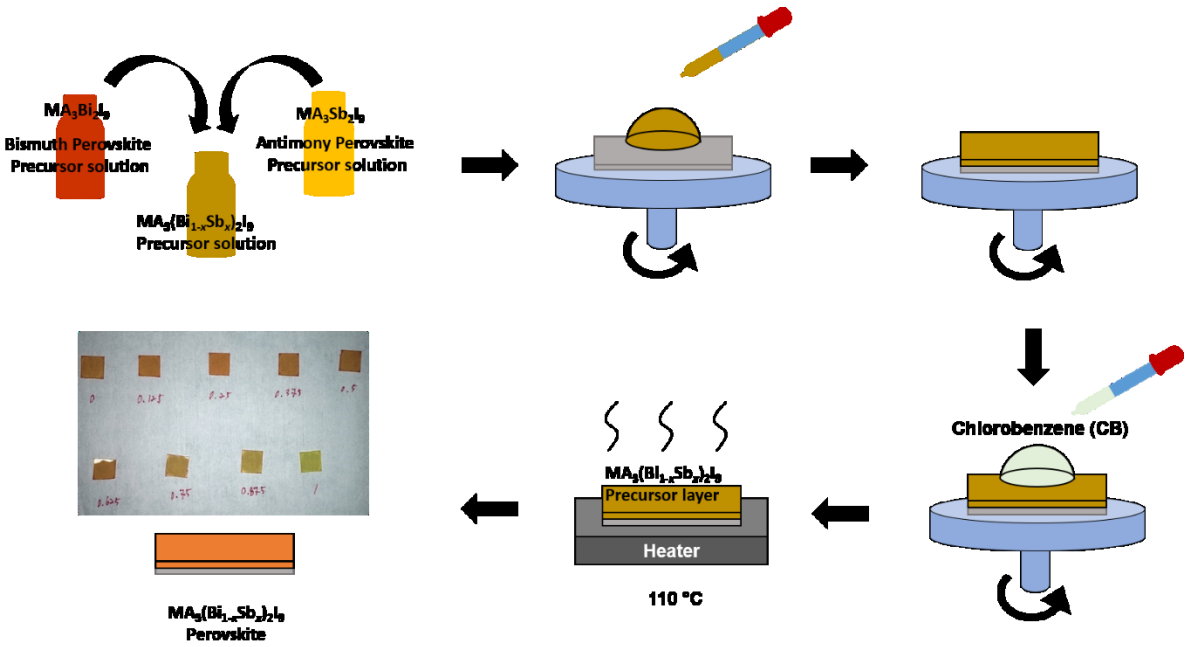

Figure 4-1-2. Preparation of bismuth-and-antimony mixed perovskite films on substrates.

Solar Cell Fabrication

Commercial ITO glass slides (Psiotec, 12 mm x 12 mm substrates, 15 Ohm/cm^2 with 8 mm wide stripe photomask) were used as substrates after washing with DI water, acetone and IPA by ultrasonic bath treatment. PEDOT:PSS was deposited onto ITO via spin-coating at 5,000 rpm for 30 s and then an $MA_3(Bi_{1-x}Sb_x)_2I_9$ active layer was prepared through the same process as above. $PC_{70}BM$ (20 mg/ml in CB) was deposited on top of the active layer at 2,000 rpm for 30 s. BCP was dissolved in anhydrous isopropanol (0.5 mg/ml) and applied via dynamic spin-coating at 5,000 rpm for 30 s. Each solution was filtered through a PTFE syringe filter (0.2 μm) before use. Finally, 100 nm of Ag as a backside electrode was thermally evaporated at ≤5E-6 mbar.

Characterisation Techniques

SEM, XRD, thickness measurements, steady-state PL, steady-state UV-Vis and transient absorption spectroscopy were carried out as described in Chapter 2.

4-1-3. Results & Discussion

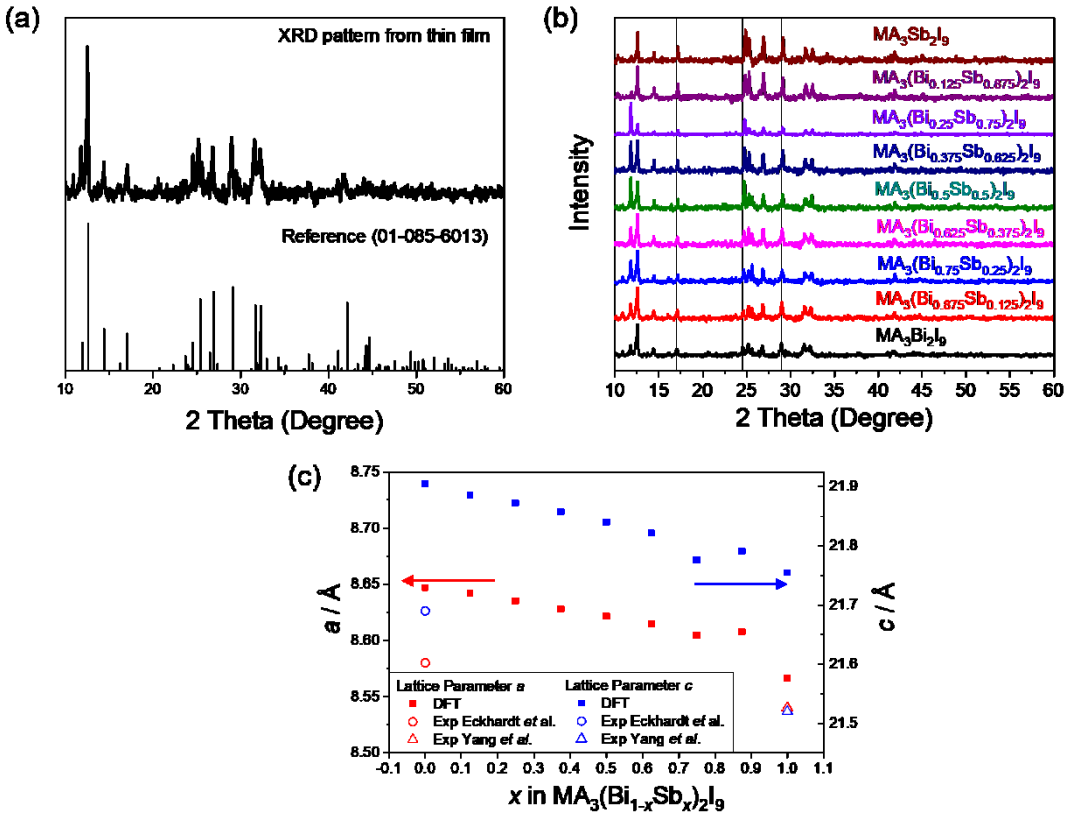

Figure 4-1-3. (a) The X-ray diffraction pattern of $MA_3Bi_2I_9$ thin film on a glass substrate and a reference of $MA_3Bi_2I_9$ (code: 01-085-6013), (b) the diffraction patterns of $MA_3(Bi_{1-x}Sb_x)_2I_9$ films on glass substrates and (b) DFT calculated compositional dependence of the lattice parameters of $MA_3(Bi_{1-x}Sb_x)_2I_9$. The DFT was calculated by Dr. Alex Aziz.

Figure 4-1-3 (a) shows the X-ray diffraction (XRD) patterns from prepared $MA_3Bi_2I_9$ thin film. The obtained pattern was compared to the reference (01-085-6013) and the XRD pattern matches with the reference except peaks at ~12° and 26°. This confirms that $MA_3Bi_2I_9$ thin film was successfully fabricated through the above method but with some remaining materials.

The impurity peaks might come from the remaining bismuth iodide (see Figure 3-2) which was not reacted during the annealing. Figure 4-1-4 (b) shows the XRD patterns of the $MA_3(Bi_{1-x}Sb_x)_2I_9$ films prepared on glass substrates. As Bi is replaced by Sb, no impurity peaks were observed, only a shift in the peaks to higher angles. This is consistent with experimental work on end members.[1, 14] For the Bi end member phase, the diffraction peaks seen at 17.03°, 24.56° and 28.98° were increased to 17.16°, 24.85° and 29.14°, respectively, for the Sb end member phase. This small change in the peak position indicates a small change in the lattice parameters and suggests complete mixing of the solid solution. To support this experimental characterisation of the crystal structures, calculations on $MA_3(Bi_{1-x}Sb_x)_2I_9$ were performed with help from the University of Bath. From the calculated results, it was found that across the solid solution, the substitution of Bi for Sb with a smaller atomic radius only lead to 0.9% and 0.7% decreases in the *a* and *c* lattice parameters, respectively. This is consistent with the XRD patterns that only show a small shift to higher 2θ angles as previously discussed. Both experimental and theoretical results confirm the absence of any large change in lattice parameters, which suggests that the solid solution would readily mix.

Figure 4-1-4 shows scanning electron microscopy (SEM) images from the prepared $MA_3(Bi_{1-x}Sb_x)_2I_9$ films on glass substrates. The nanoparticle size of the perovskites was roughly similar but decreased until the 37.5% Sb substitution in $MA_3(Bi_{1-x}Sb_x)_2I_9$ and then became somewhat larger (~50 nm) from the 50% Sb substitution to the end member. Interestingly, the as the amount of Sb increases in the material, the number and size of pinholes were reduced. Considering XRD patterns above (Figure 4-1-3 (b)), the impurity peaks were reduced with Sb substitution. It seems addition of Sb brings purer crystal formation reducing impurities,

resulting in lower pinholes in the film morphology.

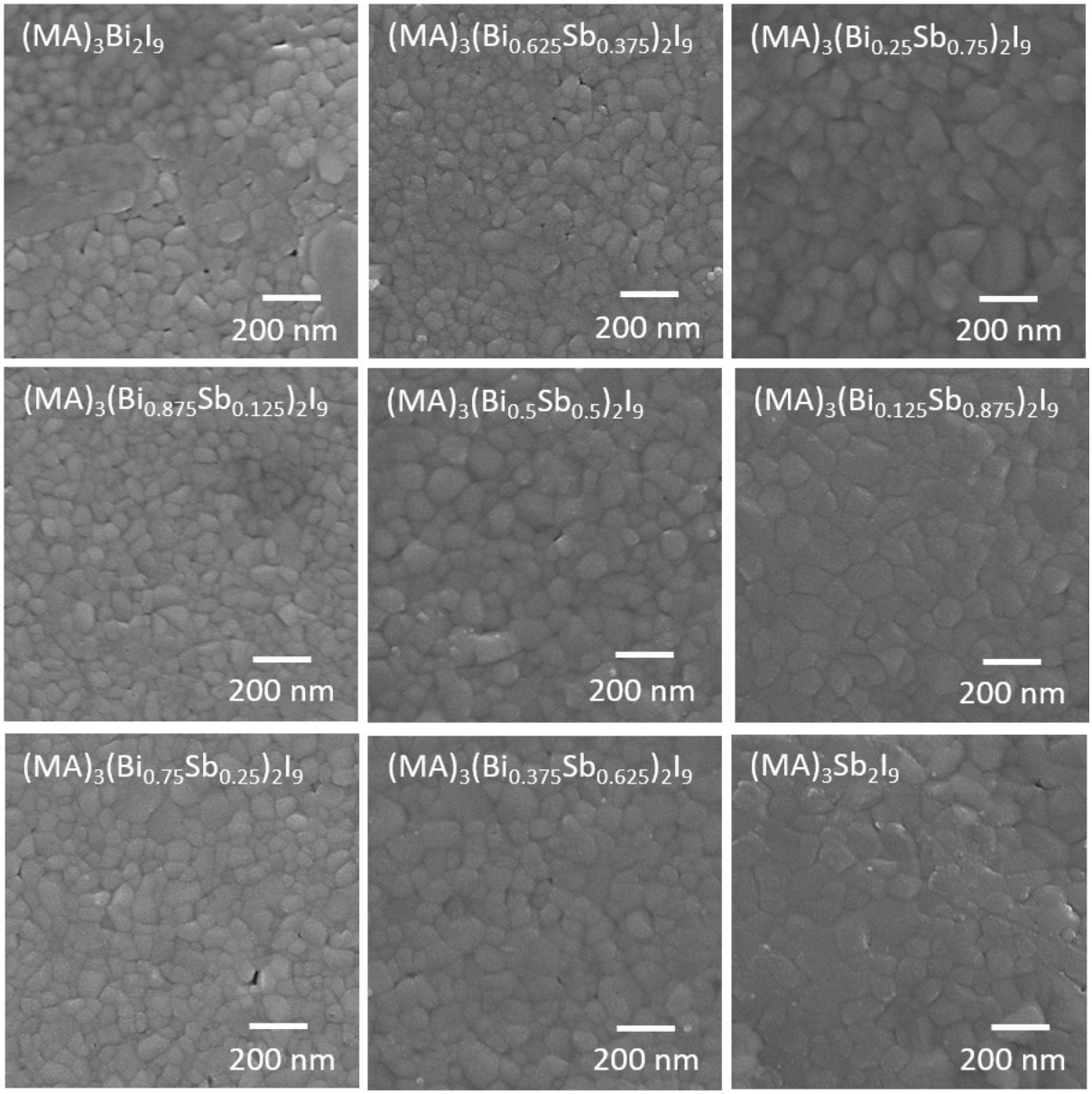

Figure 4-1-4. SEM images of $MA_3(Bi_{1-x}Sb_x)_2I_9$ films prepared on glass substrates.

Theory (average fitted)

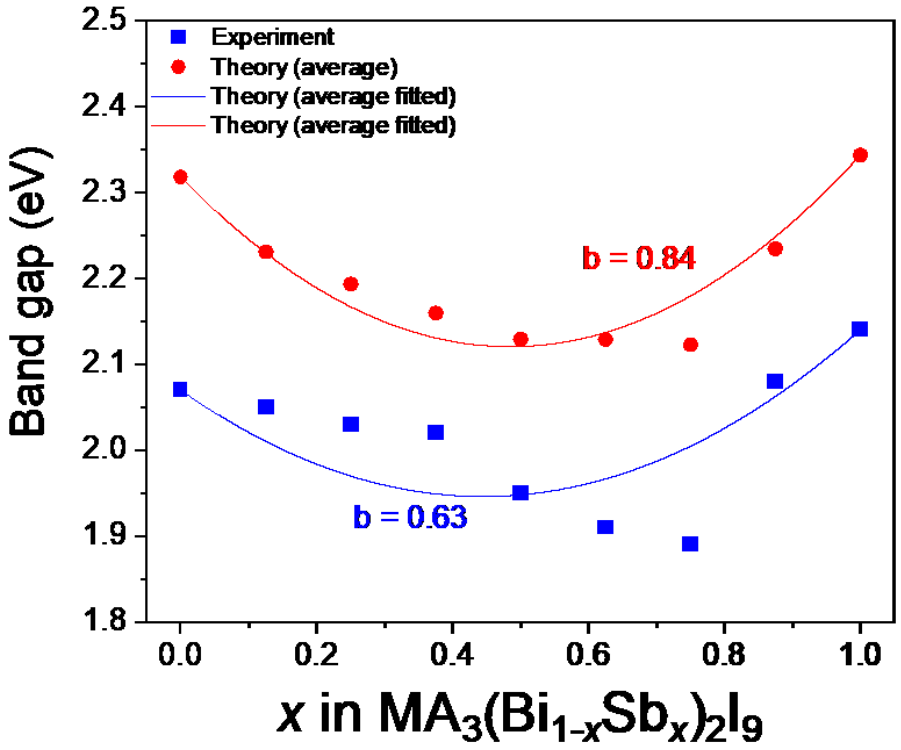

Figure 4-1-5. Experimentally obtained and computationally calculated bandgaps of $MA_3(Bi_{1-x}Sb_x)_2I_9$. The theoretical bandgaps were calculated by Dr. Alex Aziz and averaged over the three configurations with the highest probability.

Figure 4-1-5 shows the experimentally and computationally obtained bandgaps of $MA_3(Bi_{1-x}Sb_x)_2I_9$ and Figure 4-1-6 is Tauc plots from the fabricated $MA_3(Bi_{1-x}Sb_x)_2I_9$ thin films; they show how the experimental bandgaps were obtained for each mixed perovskite. To investigate the variation in the bandgap in $MA_3(Bi_{1-x}Sb_x)_2I_9$, the *ab initio* density functional theory (DFT) simulation with HSE06-SOC was employed with help from the University of Bath. Interestingly, the calculated bandgaps showed significant deviations from linearity across the solid solution. This deviation can be described by a parabolic bandgap curve:

$$E_g(x) = xE_g^{x=1} + (1-x)E_g^{x=0} - bx(1-x) \qquad \text{(Eq. 4-1-1)}$$

where $E_g^{x=1}$ and $E_g^{x=0}$ are the bandgaps of the end member phases and b is a single bowing parameter.

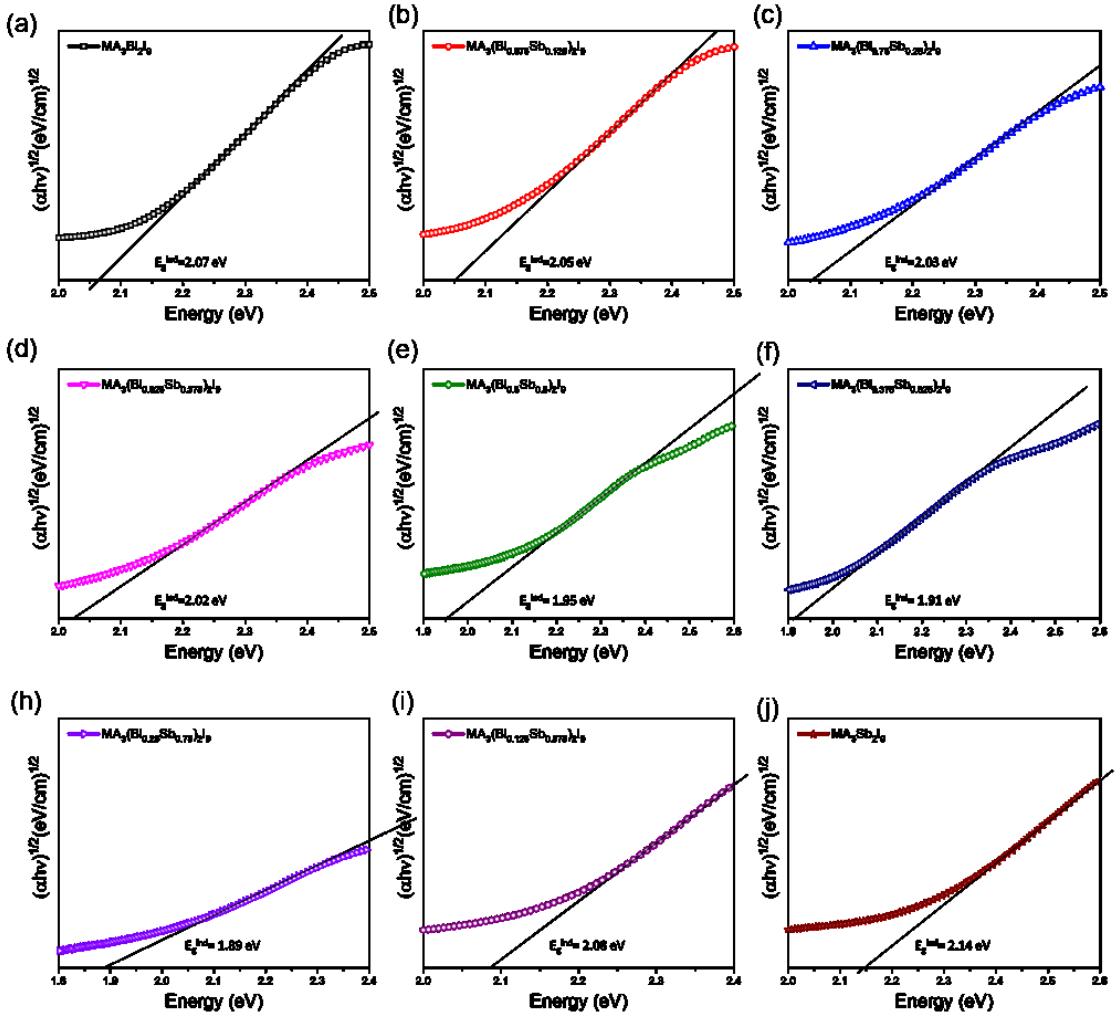

Figure 4-1-6. (a)-(i) Tauc plots for $MA_3(Bi_{1-x}Sb_x)_2I_9$ thin films.

This bowing effect was also reported in the archetypical alloy system $MA(Pb_{1-x}Sn_x)_2I_3$,[23–25] and it would be beneficial for solar-cell applications in both single-junction devices and tandem

devices where top cell materials require bandgaps in the range 1.7–1.9 eV.[23, 28] Goyal *et al.* suggested that bowing is chemical in nature and originates from differences in the energy mismatch between Pb and Sn *s* and *p* orbitals.[25] The results in this study also support this conclusion in $MA_3(Bi_{1-x}Sb_x)_2I_9$. Whilst SOC contributions have more significantly impacted the reduction in the bandgap in Bi-rich compositions, they do not account for the variation in the bandgap seen in different configurations in the 50:50 phase. The energy of the lowest three configurations differs by just 30 meV, yet their bandgaps differ by around ~0.3 eV (Figure 4-1-5). This might also result from differences in the energy alignment in the VBM that are dominated by Sb and Bi *p*-orbitals, which is the same as the Pb and Sn system. This bowing effect would be beneficial for fine-tuning and reducing the bandgap for solar-cell applications and their potential use in tandem devices.

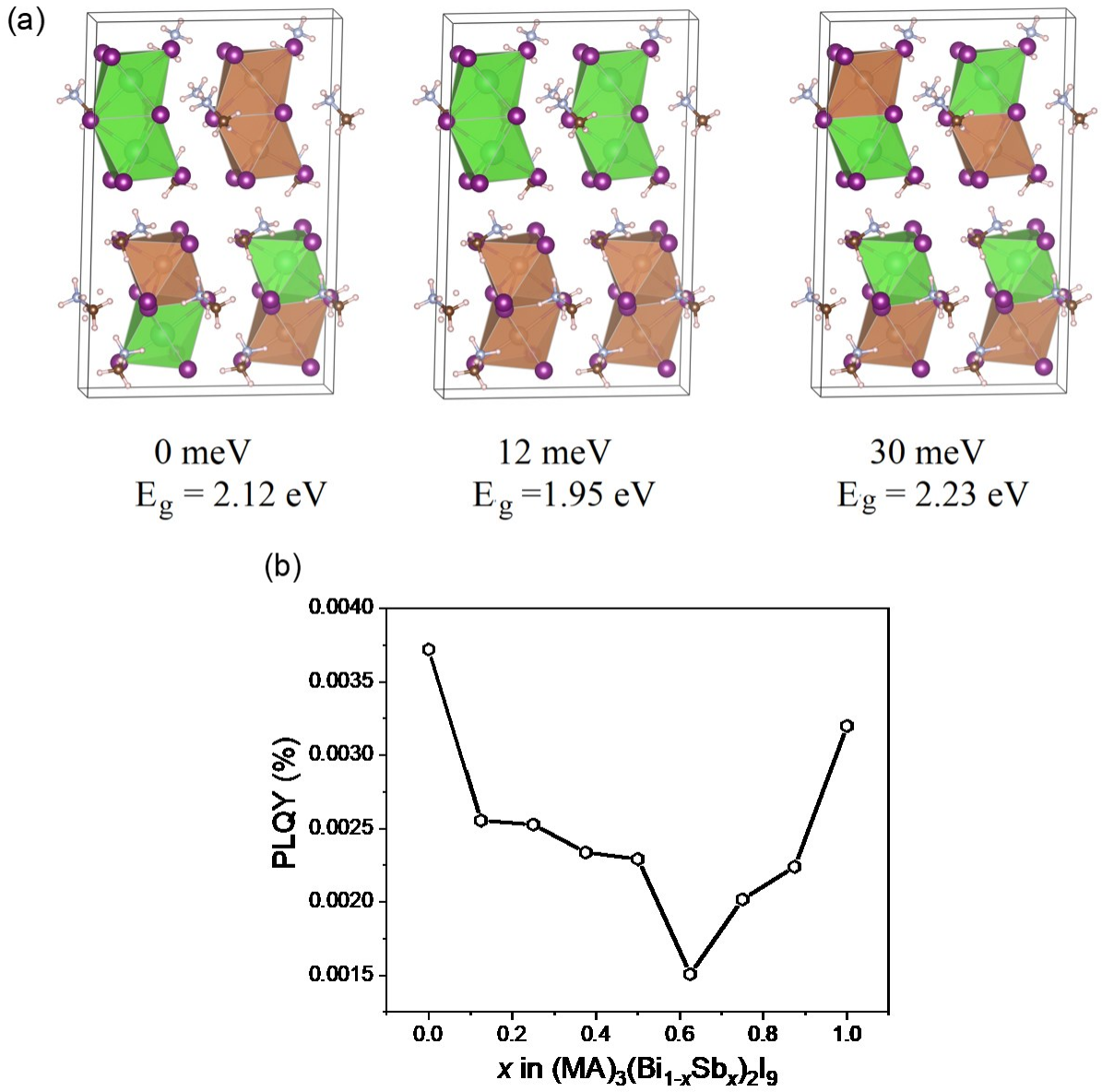

Figure 4-1-7. (a) The three lowest energy configurations of $MA_3(BiSb)_2I_9$ and (b) experimentally obtained PLQY values for $MA_3(Bi_{1-x}Sb_x)_2I_9$ thin films. The configurations were obtained by Dr. Alex Aziz. The selected excitation wavelength was 320 nm for the samples and photoluminescence between 340 nm and 620 nm was collected.

Table 4-1-1. Summary of PLQY for thin films of $MA_3(Bi_{1-x}Sb_x)_2I_9$.

***x* in Composition** $MA_3(Bi_{1-x}Sb_x)_2I_9$	PLQY (%)	***x* in Composition** $MA_3(Bi_{1-x}Sb_x)_2I_9$	PLQY (%)
0	0.0037	0.625	0.0015
0.125	0.0026	0.75	0.0020
0.25	0.0025	0.875	0.0022
0.375	0.0023	1	0.0032
0.5	0.0023		

Figure 4-1-7 (a) shows the complete disorder in this system. This disorder also influences the photoluminescence quantum yields (PLQY), which vary as a function of the composition in $MA_3(Bi_{1-x}Sb_x)_2I_9$. Increased disorder may introduce defect centres that can act as sites for non-radiative recombination within the films, leading to local changes in the photoluminescence intensity. We probed this by calculating the PLQY yields from experiments as a function of the composition in $MA_3(Bi_{1-x}Sb_x)_2I_9$ (Figure 4-1-7 (b)). The pure bismuth perovskite showed the highest PLQY and there was a reduction in PLQY upon Sb substitution until 62.5% Sb incorporation, where the PLQY started increasing (Table 4-1-1 lists the exact values). Note that while the low PLQY would result in significant experimental error, the trend remains clear

from the results and the low PLQY is inherent to this material, which has low PL intensities with short charge-carrier lifetimes.[1, 29]

Following photoexcitation, the negatively charged electrons and positively charged holes were only bound by columbic forces. The energy needed to overcome these interactions and generate free carriers is called the exciton binding energy and this is critical to the operation of any solar cell device. In archetypical halide perovskite $MAPbI_3$, exciton binding energies have been reported from as low as a few meV at room temperature to ~50 meV.[26, 30, 31] These values show that they almost have spontaneous free carrier generation. To gain an understanding of the exciton binding energies in $MA_3(Bi_{1-x}Sb_x)_2I_9$, we employ a combined experimental and theoretical approach.

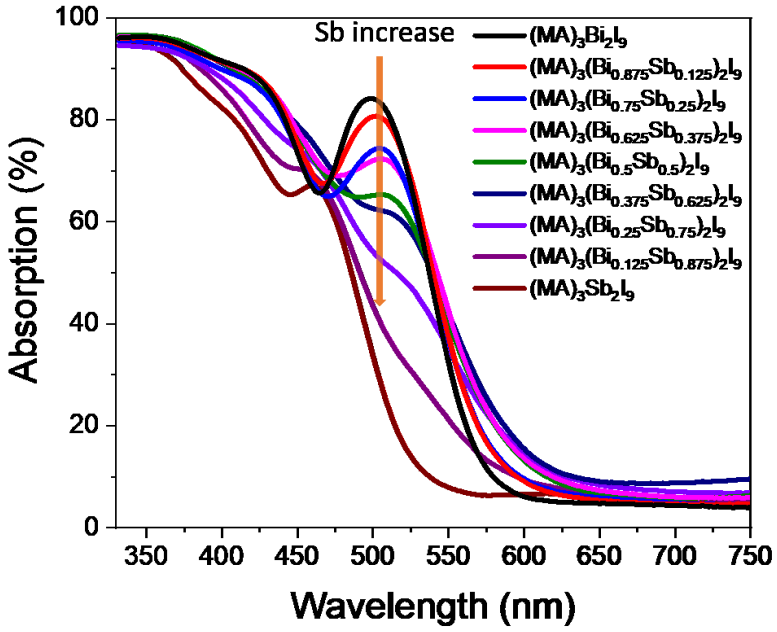

Figure 4-1-8. Absorption spectra of $MA_3(Bi_{1-x}Sb_x)_2I_9$ films prepared on glass substrates.

Figure 4-1-8 shows the absorption spectra of the thin films of $MA_3(Bi_{1-x}Sb_x)_2I_9$. In agreement with our results showing the bandgap bowing effect (Figure 4-1-8), we see a red-shift in the spectra as we moved from the end member phases to the mixed phase. The exciton peak at ~520 nm decreases as a function of Sb, leading to a lower density of excitons; this suggests lower binding energies in the Sb-phase. To confirm this assertion, the binding energies were calculated using the equation below with the Wannier exciton model:

$$E_{\mathrm{B}} = \frac{\mu e^4}{2(4\pi\hbar\varepsilon^{\infty})^2} \qquad \text{(Eq. 4-1-2)}$$

where μ is the reduced effective mass, *e* is the unit of charge, ε^{∞} is the high-frequency dielectric constant and ħ is the reduced Planck constant.[32–34]

Figure 4-1-9 shows the calculated effective mass, dielectric constant and binding energy of $MA_3(Bi_{1-x}Sb_x)_2I_9$. Following Eq. 4-1-2, the increase in the dielectric constant and decrease in the effective mass both led to reductions in the binding energy as a function of Sb in $MA_3(Bi_{1-x}Sb_x)_2I_9$. The major contributing factor in the reduction of the binding energy was the effective mass, which decreased by about a factor of two from the Bi- to Sb-phase, whereas the dielectric constant only increased by about 10%. This resulted in a reduction of the binding energy from 370 eV for $MA_3Bi_2I_9$ to 150 eV for $MA_3Sb_2I_9$. The values experimentally obtained from the literature of >300 meV[6] for bismuth perovskite and around 200 meV[3] for antimony perovskite are consistent with our results. These binding energies are over fourfold those reported for $MAPbI_3$.[26, 30, 31] Unlike lead-based perovskites that predominantly generate free charges, bismuth- or antimony-based perovskites form stable excitons inside clusters. This is also consistent with other reported studies that suggest that

the excitations are localised in $[Bi_2I_9]^{3-}$ or $[Sb_2I_9]^{3-}$ octahedral clusters.[2, 3] Even in the Sb-system where the lowest binding energy of ~150 meV can be found, this is still inhibitive to its implementation as a solar cell device. This is confirmed by the small yield obtained indicating a non-radiative recombination of localised excitons before charge separation can occur.[2, 3]

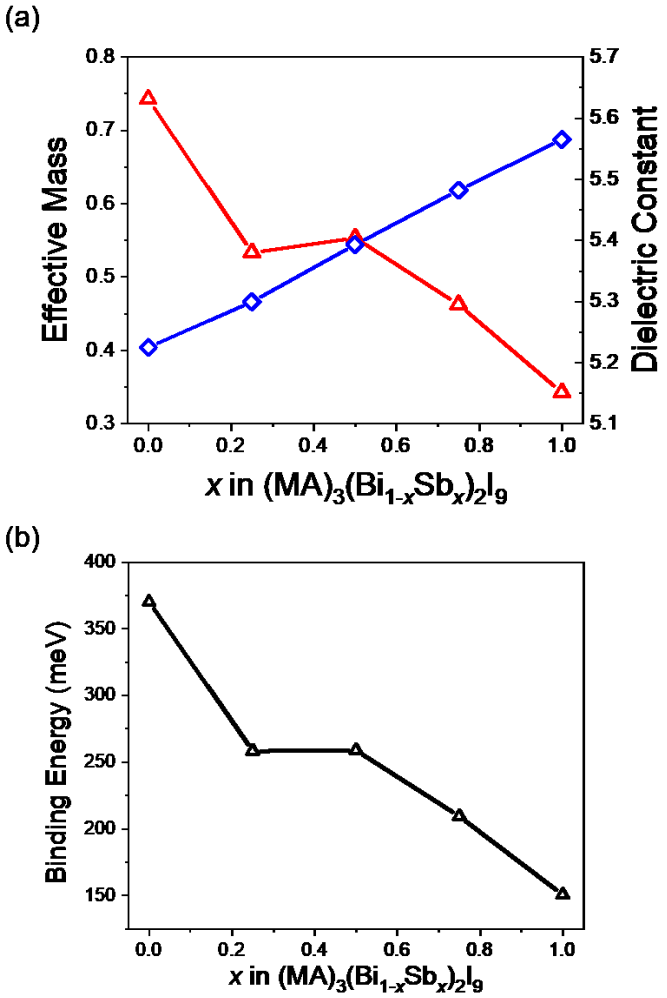

Figure 4-1-9. (a) Calculated effective mass and dielectric constant and (b) calculated binding energy of $MA_3(Bi_{1-x}Sb_x)_2I_9$. The effective mass, dielectric constant and binding energy were obtained by Dr. Alex Aziz.

To see the effect of the exciton binding energy reduction to the charge transfer, microsecond-to-millisecond transient absorption spectroscopy (TAS) was employed. The Bi/Sb end members' thin films were prepared on a glass substrate and P3HT were spin-coated on top of them. Figure 4-1-10 shows the decay of polarons generated on P3HT due to the charge transfer from the perovskites. From the decay, we can find that the charges from both $MA_3Bi_2I_9$ and $MA_3Sb_2I_9$ have long lifetimes >0.1 s. This long decay might come from the deep trapping of the charges. Comparing the intensity of the decay, that from $MA_3Sb_2I_9$ film (brown trace) had a higher intensity than that from $MA_3Bi_2I_9$ film (black trance). The decay was probed at 1,000 nm where the polaron of P3HT could be easily observed and Figure 4-1-10 (b) confirms that it is the polaron of P3HT because the spectra matches (not perfectly but generally) the chemically oxidised P3HT. There are several reasons the absorption has higher intensity: the absorption coefficient, concentration, thickness, following the Beer–Lambert Law (Eq 2-1.). Here, assuming that both films have the same thickness of P3HT from the same method, the concentration of polarons is the main factor in the difference. From this, it seems that a larger amount of holes was transferred from $MA_3Sb_2I_9$ than from $MA_3Bi_2I_9$. Note that $MA_3Sb_2I_9$ has a 0.3 eV higher valence band (VB) of -5.6 eV compared to $MA_3Bi_2I_9$, which has one at -5.9 eV. Therefore, $MA_3Sb_2I_9$ has a smaller driving force to transfer holes to P3HT than $MA_3Bi_2I_9$. Despite this, it showed a higher intensity signal, which shows that the binding energy has a critical effect.

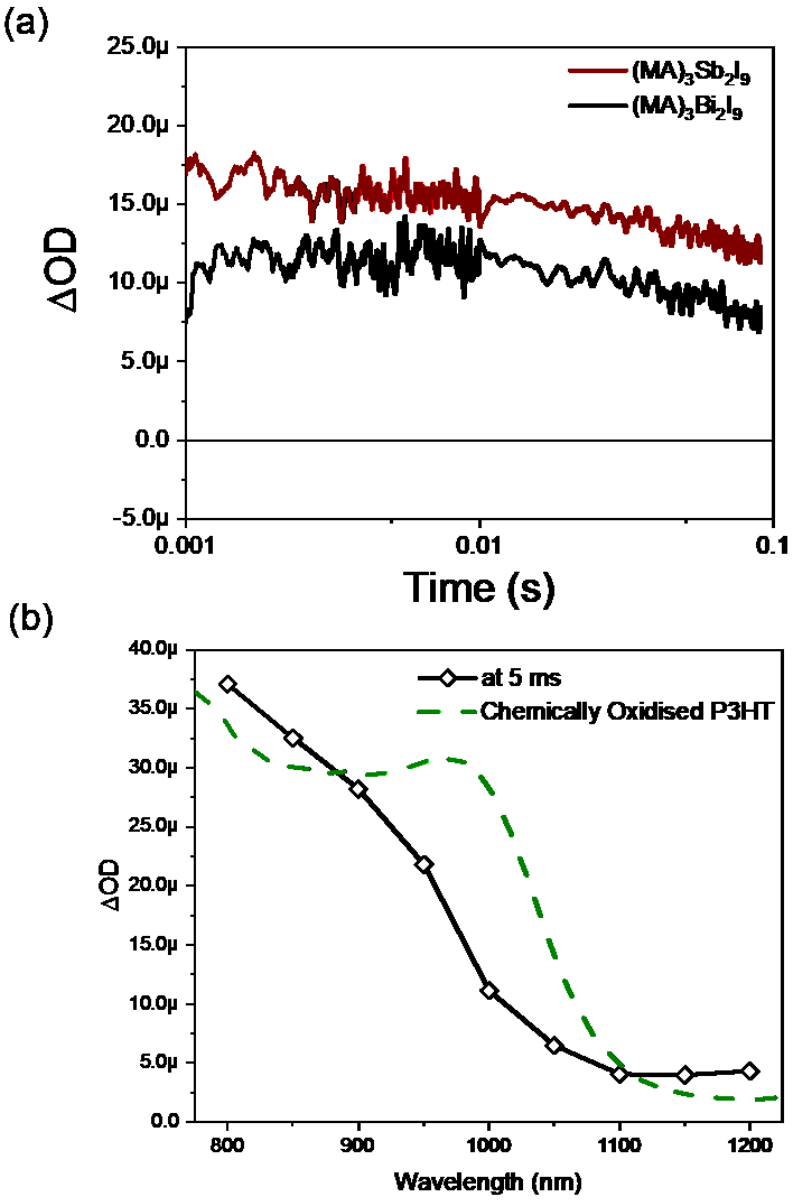

Figure 4-1-10. (a) transient absorption kinetics measured at 1,000 nm for $MA_3Bi_2I_9$ and $MA_3Sb_2I_9$ thin films on glass substrates with P3HT and (b) transient absorption spectrum of a glass/$MA_3Bi_2I_9$/P3HT thin film measured 5 ms after pulsed excitation and a steady-state absorption spectrum of P3HT chemically oxidised with $N(PhBr)_3SbCl_6$. The signals were normalised by the absorption of the film at 450 nm, which is the excitation wavelength.

Next, solar cells were fabricated to investigate the effect the discussed physical properties have on the device performance in $MA_3(Bi_{1-x}Sb_x)_2I_9$. The structure of the fabricated solar cells with their relevant energy levels are shown in Figure 4-1-11 (a).

For a device to perform as a solar cell, its architecture must have the right energy levels. For holes to be transported, the energy level of the VBM photoactive layer must be lower than that of the hole transport layer. For electron transport, the CBM of the photoactive layer must be higher in terms of energy than the electron transport layer. To probe this, the energy levels for $MA_3(Bi_{1-x}Sb_x)_2I_9$ were calculated with help from the University of Bath (Figure 4-1-11 (b)) and it was found that both the VBM and CBM increase by ~0.3 eV as a function of Sb. We see an almost linear increase in the VBM but a more parabolic trend in the CBM. These changes lead to the previously discussed bandgap bowing effect and are consistent with experimentally reported values.[6, 15] The shift to high energies with Sb-substitution for Bi (indicated by the dotted line in Figure 4-1-11 (a)), is well within the acceptable range for the device structure. The VBM of the perovskite is lower than the hole transport layer in PEDOT:PSS and the CBM of the perovskite is higher than that of the electron transport layer $PC_{70}BM$. These changes in band alignment will likely cancel each other out as the energy level difference between CB of perovskite and $PC_{70}BM$ increases while the energy level difference between the VB of perovskite and PEDOT:PSS decreases.

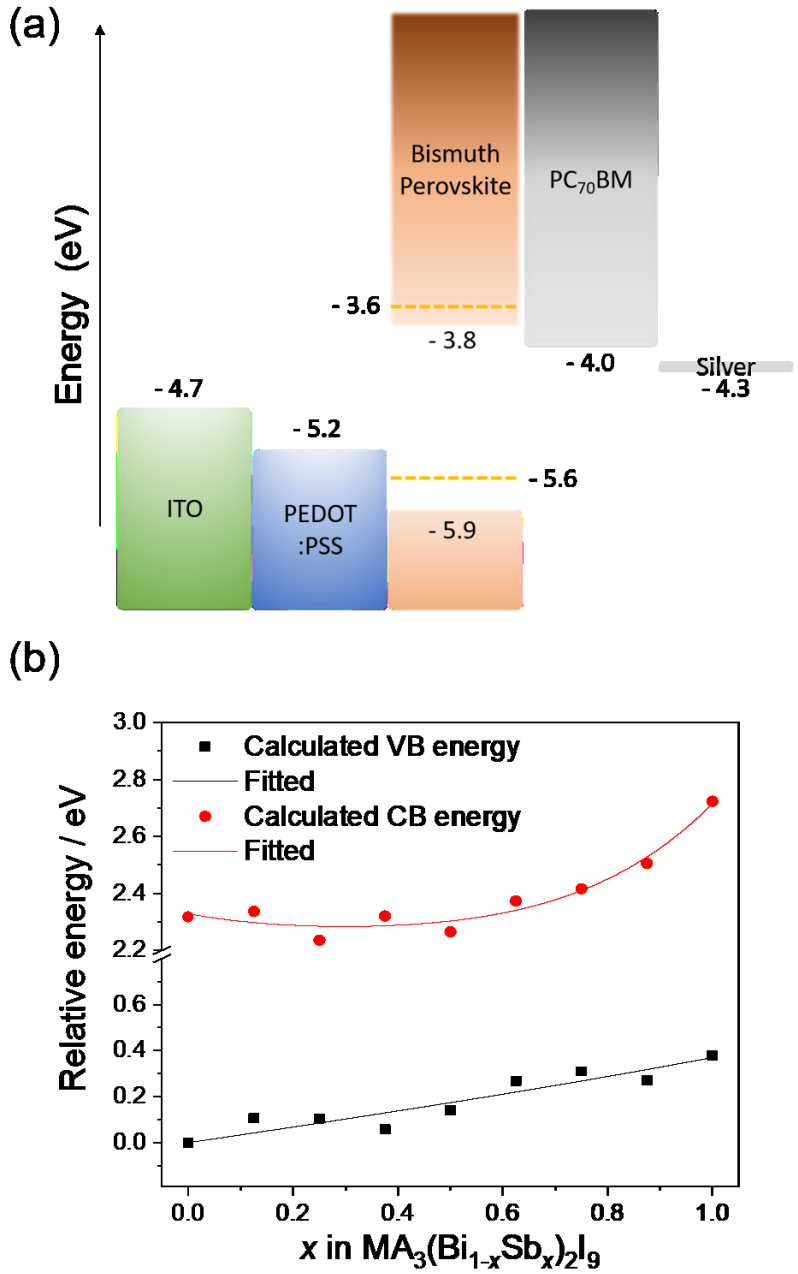

Figure 4-1-11. (a) Schematic illustration of the prepared device architecture with energy levels. The energy levels of bismuth perovskite and antimony perovskite (yellow dashed line) are based on related literature.[6, 15] (b) the calculated relative energy levels of $MA_3(Bi_{1-x}Sb_x)_2I_9$. The relative energy levels were calculated by Dr. Alex Aziz.

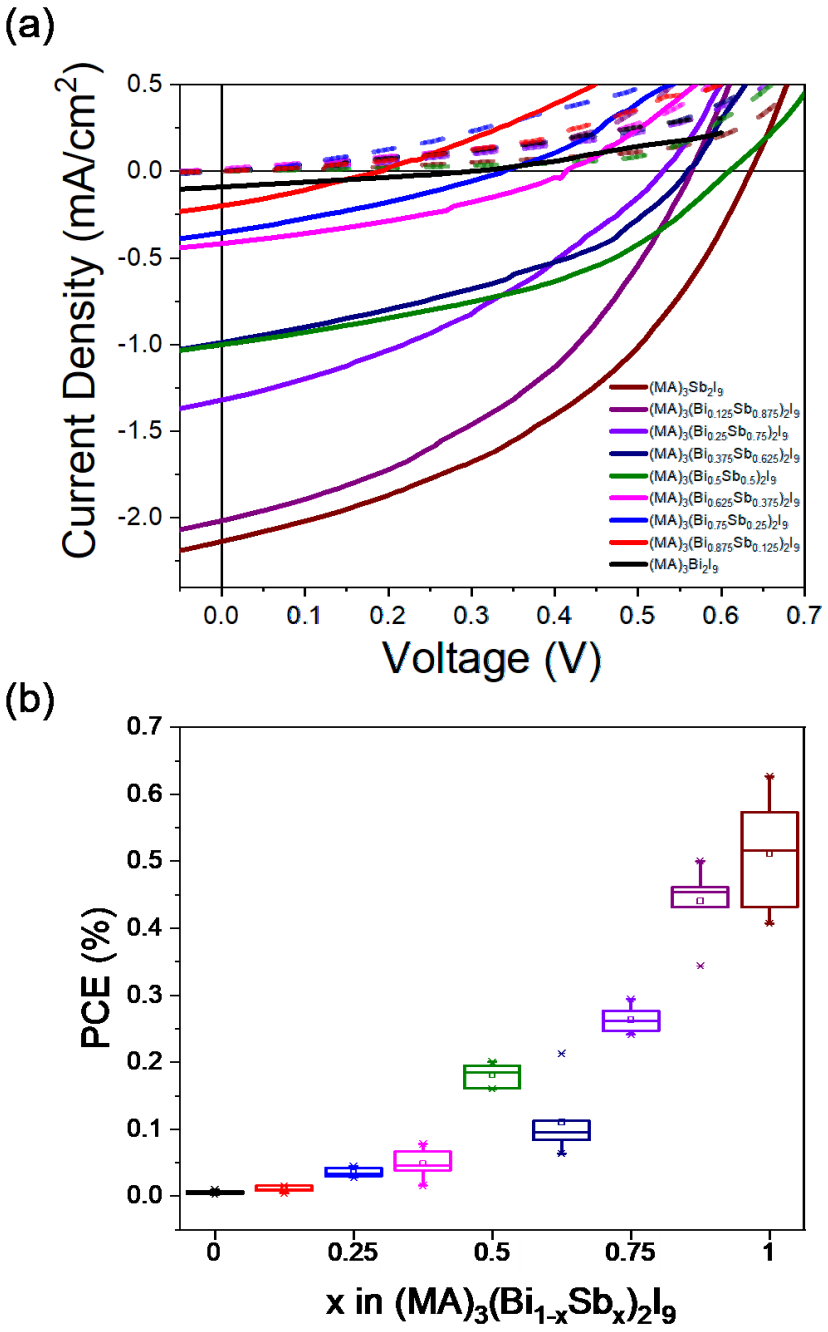

Figure 4-1-12. (a) JV traces of the assembled devices (dashed lines represent measurements in the dark) in ITO/PEDOT:PSS/$MA_3(Bi_{1-x}Sb_x)_2I_9$/$PC_{70}BM$/Ag and (b) box plots of PCE of six best devices of each composition in $MA_3(Bi_{1-x}Sb_x)_2I_9$.

Table 4-1-2. Summary of the photovoltaic performance of the solar cells with $MA_3(Bi_{1-x}Sb_x)_2I_9$ as the active layer presented in Figure 4-1-12 (a). The averaged values from six device cells are in brackets with the mean and standard deviation.

X in Composition $MA_3(Bi_{1-x}Sb_x)_2I_9$	Jsc (mA/cm^2)	Voc (V)	FF	PCE (%)
1	2.06 (2.13 ± 0.08)	0.66 (0.62 ± 0.05)	0.30 (0.39 ± 0.05)	0.41 (0.51 ± 0.09)
0.875	2.01 (1.97 ± 0.25)	0.56 (0.56 ± 0.04)	0.40 (0.40 ± 0.02)	0.46 (0.44 ± 0.05)
0.75	1.32 (1.42 ± 0.14)	0.53 (0.50 ± 0.07)	0.35 (0.38 ± 0.03)	0.25 (0.26 ± 0.02)
0.625	0.99 (0.72 ± 0.16)	0.56 (0.38 ± 0.13)	0.39 (0.34 ± 0.04)	0.21 (0.11 ± 0.05)
0.5	1.00 (0.90 ± 0.07)	0.61 (0.54 ± 0.04)	0.42 (0.38 ± 0.02)	0.25 (0.18 ± 0.02)
0.375	0.44 (0.45 ± 0.07)	0.50 (0.30 ± 0.12)	0.36 (0.34 ± 0.05)	0.08 (0.05 ± 0.02)
0.25	0.35 (0.33 ± 0.03)	0.34 (0.35 ± 0.08)	0.30 (0.30 ± 0.01)	0.04 (0.04 ± 0.01)
0.125	0.20 (0.21 ± 0.02)	0.19 (0.16 ± 0.08)	0.29 (0.34 ± 0.07)	0.01 (0.011 ± 0.004)
0	0.09 (0.10 ± 0.01)	0.30 (0.17 ± 0.12)	0.27 (0.34 ± 0.08)	0.007 (0.005 ± 0.003)

Figure 4-1-12 (a) shows the JV traces from the fabricated solar cells with $MA_3(Bi_{1-x}Sb_x)_2I_9$ in the above structure. Table 4-1-2 presents the obtained photovoltaic parameters including J_{sc}, V_{oc}, FF and PCE. From the JV traces and averaged parameters, it can be found that the J_{sc} increases linearly from 0.10 ± 0.01 mA/cm^2 to 2.13 ± 0.08 mA/cm^2 as the Sb contents increase in $MA_3(Bi_{1-x}Sb_x)_2I_9$. The increased current seems to be from the increased charges transferred by the binding energy reduction with Sb substitution. Box plots of the power conversion efficiencies (PCE) were plotted for the system (Figure 4-1-12 (b)) to assess the devices'

efficiency. The average values of J_{sc}, V_{oc}, FF and PCE with a distribution can be found in Table 4-1-2 in the brackets. From the box plots, a clear increase in PCE is seen as Sb is substituted for Bi in $MA_3(Bi_{1-x}Sb_x)_2I_9$ where the averaged PCE increases from 0.005 ± 0.003% to 0.51 ± 0.09% with Sb substitution. Although the determined efficiencies are low, a clear increase in PCE is seen as a function of the Sb in $MA_3(Bi_{1-x}Sb_x)_2I_9$. When the JV curve from the device with Sb perovskite is compared to the JV curve in chapter 3 (Figure 3-14), this device has lower current but higher V_{OC}. This might come from the better morphology without pinholes (Figure 4-1-4). As a result, the dark current did not show any obvious leakage not like the device with bismuth iodide. The devices with bismuth perovskites were proven to be stable for a month by Park *et al.*.[1]

In this work, several properties are investigated such as the bandgap, configurational disorder, effective mass, binding energy and band alignment, which are all related to device performance. I would like to suggest that the key parameter for device performance is the effective mass and its direct effect on the binding energy of the excitons in this $MA_3(Bi_{1-x}Sb_x)_2I_9$ system. The high binding energy found in this system deters the facilitation of exciton ionisation, thus lowering the yield of free carriers.[2, 3] The lower binding energies on Sb substitution were found and this leads to lower energies required to dissociate the excitons into free carriers although the binding energies are still too high to obtain PCEs that match those seen for the $MAPbI_3$-based perovskites.

4-2. 2D Bismuth Perovskites

4-2-1. Introduction

Perovskites with low dimensionality and excellent stability have also attracted widespread attention in recent years, resulting in rich properties for multifunctional devices.[35–37] The ionic radii, ionic valences, and coordination types of A, B and X in a 3D ABX_3 structure are the three key factors affecting the perovskite structure. Significant changes in these three key factors will result in low-D perovskites; replacing A, B or X ions affects the ionic radii and the hetero-valence ion substitution of B ions synergistically affects the three factors. In particular, by replacing the cation A with larger organic cation such as butylammonium (BA) or phenylethylammonium (PEA), the 3D lead-based perovskites ABX_3 can be sliced into a 2D structure with the general formula A_2BX_4.[1] They achieved improved stability by building a protective organic ligand layer out of the perovskite made of PEA or BA,[38,39] and reduced the defect density, leading to a higher photoluminescence quantum yield (PLQY).[40] It proves that the physical properties are strongly related to their structural dimensions.

The A-site substitution in $A_3B_2X_9$ brought in a new 2D type of perovskite derivative. $Cs_3Sb_2I_9$ is known to have two different structures, the 0D dimer form that can be prepared by a simple solution process and the 2D corrugated layers of polyanions form that can be prepared through SbI_3 vapour annealing. This 2D $Cs_3Sb_2I_9$ film had enhanced stability in ambient air, thus providing a decent platform for optoelectronic applications.[41] In addition, it has been demonstrated that Cl-incorporated 2D $MA_3Sb_2Cl_xI_{9-x}$ shows better absorption, higher carrier mobilities and higher efficiency in solar cells than 0D $MA_3Sb_2I_9$, where the inclusion of

methylammonium chloride into the precursor solutions can suppress the formation of an undesired 0D $MA_3Sb_2I_9$ dimer-phase.[13] $Rb_3Bi_2I_9$ is a 2D bismuth perovskite with direct bandgap and higher defect tolerance than the 0D bismuth halide phases.[42] Although it has good optical properties for photovoltaic applications, solar cell devices with this material have not yet been reported.

In this study, another 2D bismuth perovskite—$(PEA)_3Bi_2I_9$—was prepared by the solution process and its crystallographic and optical properties were characterised and compared with 3D $(MA)_3Bi_2I_9$. As a result, an improved film morphology and PLQY was obtained from 2D bismuth perovskite.

4-2-2. Method

Materials

Methylammonium iodide (MAI) and phenylethylammonium iodide (PEAI) were purchased from Dyesol Ltd.; BiI_3 and tin chloride dihydrate were purchased from Sigma Aldrich; spiro-OMeTAD was acquired from Feiming Chemical Limited; anhydrous dimethylformamide (DMF) and anhydrous chlorobenzene (CB) were purchased from ACROS Organics™; Absolute ethanol, acetone and isopropanol (IPA) were purchased from VWR; TiO_2 nanoparticle paste (30NR-D) was purchased from Dyesol Ltd.

Substrate preparation

Glass substrates (VWR Microscope Slides, BS7011, 1.0–1.2 mm) were used after cutting into pieces of the specified size (1.25 cm × 1.25 cm), washing and drying in a N_2-gas stream. The washing process included three consecutive steps: ultrasonic bath treatment in deionised water, acetone and isopropanol for 15 min each.

Compact SnO_2 film fabrication

The c-SnO_2 films were prepared by spin-coating a 0.3 M solution of tin chloride dihydrate in ethanol at 5,000 rpm with 2,000 rpm/s acceleration for 30 s followed by annealing in a furnace at 500°C for 45 min.

BiSI interlayer fabrication

A BiSI interlayer was prepared as described in Chapter 3. The In_2S_3 interlayers were prepared

by spin-coating a solution of indium dimethylpentyl xanthate in chlorobenzene (134 mg/ml) at 2,000 rpm with 2,000 rpm/s acceleration for 30 s. Afterwards, the films were annealed on a hotplate at 200°C for 15 min in a N_2-filled glovebox to form In_2S_3. On top of the In_2S_3 layer, a BiI_3 solution in DMF (200 mg/ml) was spin-coated at 2,000 rpm with 2,000 rpm/s acceleration for 30 s, then annealed on the hotplate at 200°C.

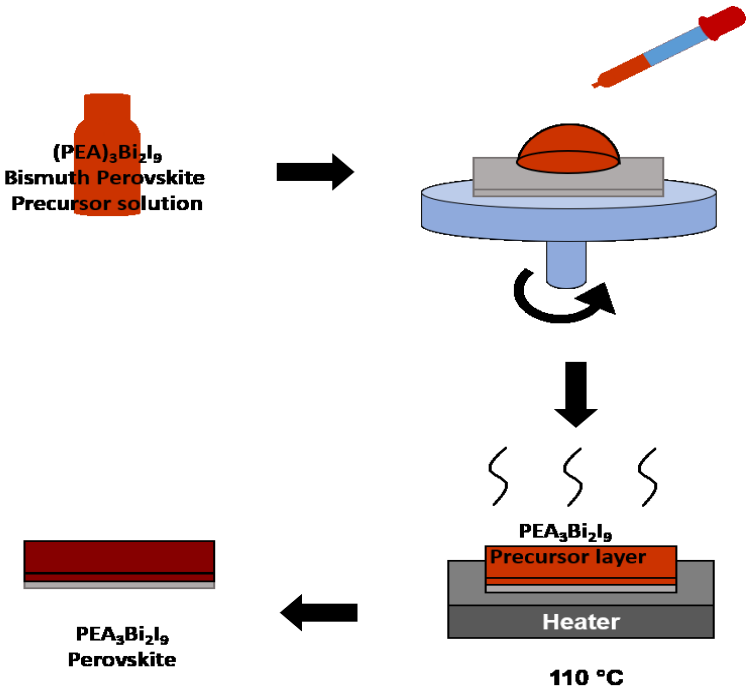

Figure 4-2-1. Preparation of 2D bismuth perovskite films on substrates.

Perovskite layer fabrication

For the active layer, bismuth perovskite precursor solutions were prepared by dissolving 200 mg of BiI_3 and 80.87 mg of MAI into DMF and 200 mg of BiI_3 and 126.74 mg of PEAI into DMF for 0D and 2D perovskite, respectively. The prepared solutions were spin-coated at 2,000 rpm with 2,000 rpm/s acceleration for 30 s, followed by annealing at 110°C on a hotplate for

20 min. Figure 4-2-1 shows the whole process for the perovskite layer fabrication.

Hole transport layer fabrication

The spiro-OMeTAD solution was prepared by dissolving 72.3 mg of spiro-OMeTAD in 1 ml chlorobenzene without any additives. Afterwards, the solution was filtered through a PTFE syringe filter (0.2 μm) and deposited as a hole transport layer on top of the bismuth perovskite films by spin-coating at 2,000 rpm with 2,000 rpm/s acceleration for 30 s.

Solar Cell Fabrication

For PV devices, commercial fluorine-doped tin oxide (FTO) glass substrates were used. The glass/FTO substrates were cleaned consecutively in ultrasound baths with soap, deionised water, acetone and isopropanol in order for 20 min each and then dried by blowing with N_2 and heating in an oven. The compact ETL, BiSI, bismuth perovskite active layer and HTL were prepared through the same process as above. Finally, 100 nm of Ag as a backside electrode was thermally evaporated at ≤5E-6 mbar.

Characterisation Techniques

SEM, XRD, thickness measurements, steady-state PL, steady-state UV–Vis, transient absorption spectroscopy (TAS) and time-resolved photoluminescence (TRPL) were carried out as described in Chapter 2.

4-2-3. Results & Discussion

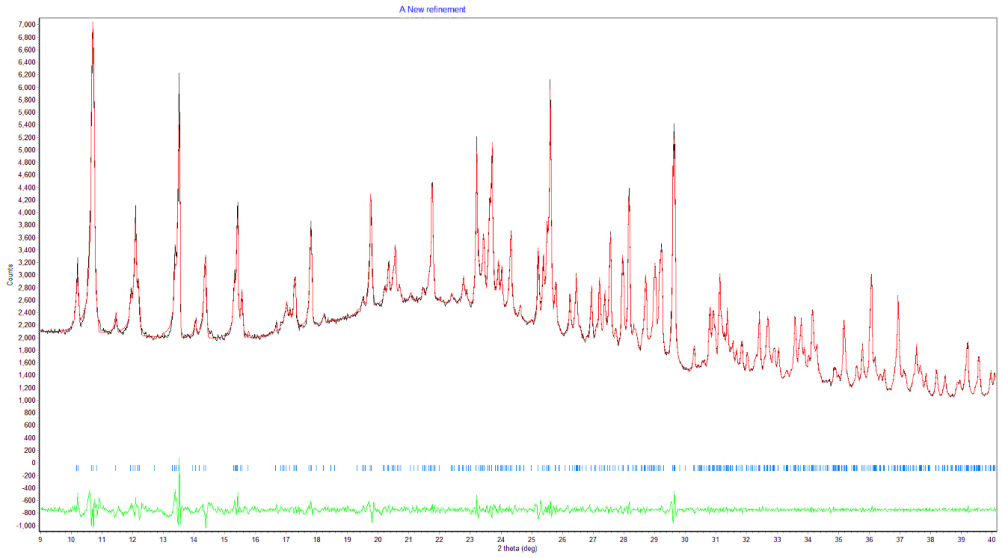

Figure 4-2-2. The X-ray diffraction pattern of $PEA_3Bi_2I_9$ powder and fitted pattern. The diffraction pattern and fitted pattern were obtained by Martin Vickers, a senior research associate at University College London.

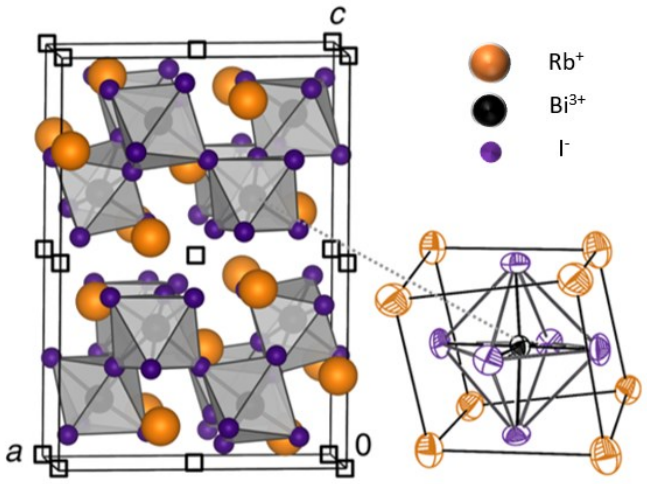

Figure 4-2-3. The crystal structure of $Rb_3Bi_2I_9$ ($P2_1/n$) as reported by Lehner *et al*.[42]

The crystal structure of $PEA_3Bi_2I_9$ was examined by X-ray Diffraction (XRD). The unit-cell dimensions were delivered from $PEA_3Bi_2I_9$ powder by fitting with a Le Bail fit using Rietica. Figure 4-2-2 shows the XRD pattern from $PEA_3Bi_2I_9$ powder and its fitting from a Le Bail fit using Rietica and Table 4-2-1 contains the unit-cell information from the fitting.

Table 4-2-1. Crystallographic parameters of $PEA_3Bi_2I_9$.

formula	$PEA_3Bi_2I_9$
sample	powder
crystal system	monoclinic
Space group	$P2_1/n$
unit cell (Å, degree)	
a	23.346
b	26.200
c	8.858
β	100.067

From the unit cell information, $PEA_3Bi_2I_9$ is in a monoclinic system and the space group of $P2_1/n$ is in the same crystal system and space group as $Rb_3Bi_2I_9$, as reported by Lehner *et al*.[42] From the report, $Rb_3Bi_2I_9$ contains corrugated layers of corner-connected BiI_6 octahedra and the ordered cubic close packing of Rb and I occur in such a manner that all BiI_6 octahedra are coordinated by eight Rb atoms in the arrangement of a distorted cube while every third M layer of the perovskite aristotype in [001] is depleted (Figure 4-2-3).[42] $PEA_3Bi_2I_9$ should have the

same crystal structure but it has longer lattice parameter and larger beta degree due to the larger atomic radius of PEA^+ compared to Rb^+. From this result, it can be said that the 2D-structured bismuth-based perovskite $PEA_3Bi_2I_9$ was successfully obtained.

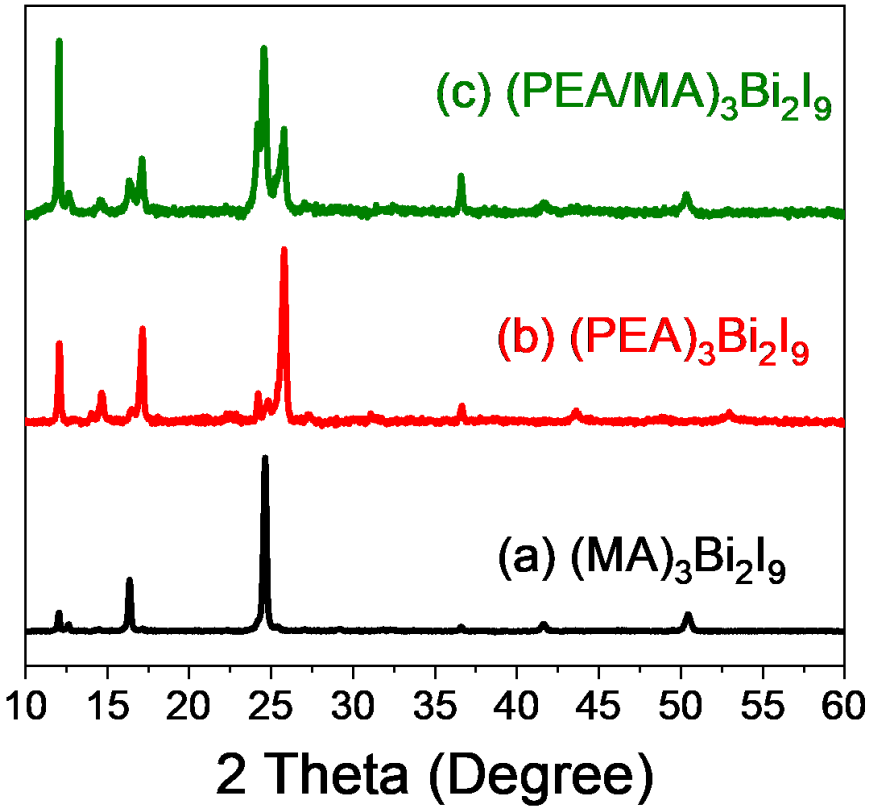

Figure 4-2-4. X-ray diffraction pattern of PEA, MA and PEA/MA mixed bismuth perovskite thin films on glass substrates.

Figure 4-2-4 shows the XRD patterns from $PEA_3Bi_2I_9$, $MA_3Bi_2I_9$ and $(PEA_{0.5}MA_{0.5})_3Bi_2I_9$. When the patterns are compared, interestingly, the pattern from $(PEA_{0.5}MA_{0.5})_3Bi_2I_9$ has separate patterns from both $PEA_3Bi_2I_9$ and $MA_3Bi_2I_9$. This means that although the precursor

solution can be made of PEA or MA, the crystal has two different phases, which are pure $PEA_3Bi_2I_9$ and $MA_3Bi_2I_9$. The relative peak intensities are different from Figure 4-2-2. The preferred orientation in the thin film results in a larger amount of diffraction at certain points. Therefore, thin film XRD patterns usually have less peaks than powder or single crystal XRD patterns. The morphology of the prepared films was investigated by scanning electron microscopy (SEM). Figure 4-2-5 shows SEM images of $PEA_3Bi_2I_9$, $PEA_3Bi_2Br_9$, $MA_3Bi_2I_9$ and $MA_3Bi_2Br_9$. The precursor solution had the same molar concentration to prepare these films. When the films from MA containing perovskite (Figures 4-2-5 (a) and (c)) and PEA containing perovskite (Figures 4-2-4 (b) and (d)) are compared, images from MA perovskites have several large pin-holes and vertically oriented perovskites images while images from PEA perovskites lack pinholes but have compact and smooth films.

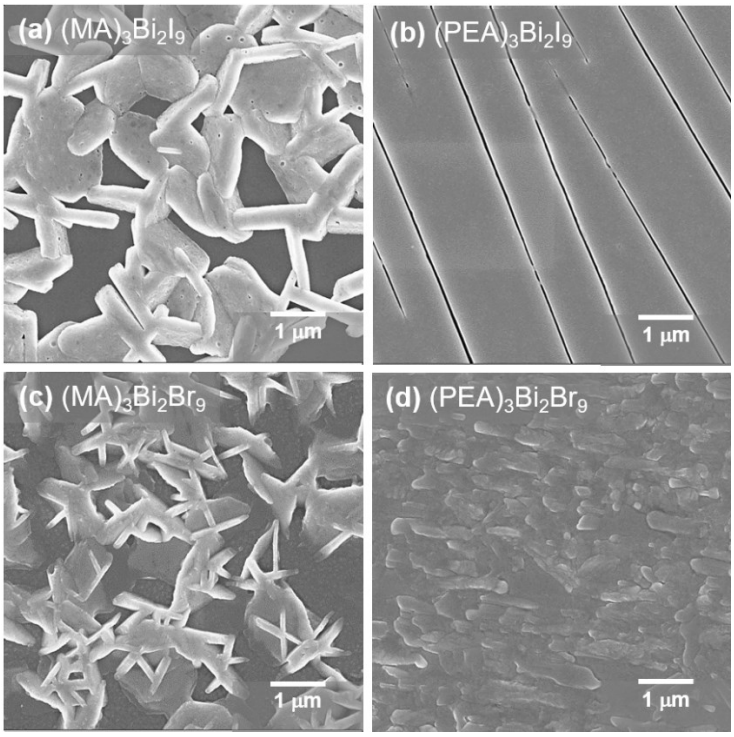

Figure 4-2-5. SEM images of PEA and MA bismuth perovskite thin films on glass substrates.

Improving the morphology of bismuth-based perovskite is a key solution to improving the efficiency of solar cells due to its poor film morphology.[1,6] While smooth films were obtained with anti-solvent treatment in the above chapter, the film formation with this treatment has poor reproducibility.[43] However, with $PEA_3Bi_2I_9$, it is much easier to make a smooth film that is beneficial for efficient solar cell fabrication. Therefore, improvements to the PCE of bismuth-based perovskite can be expected when such a material is fabricated in a solar cell device.

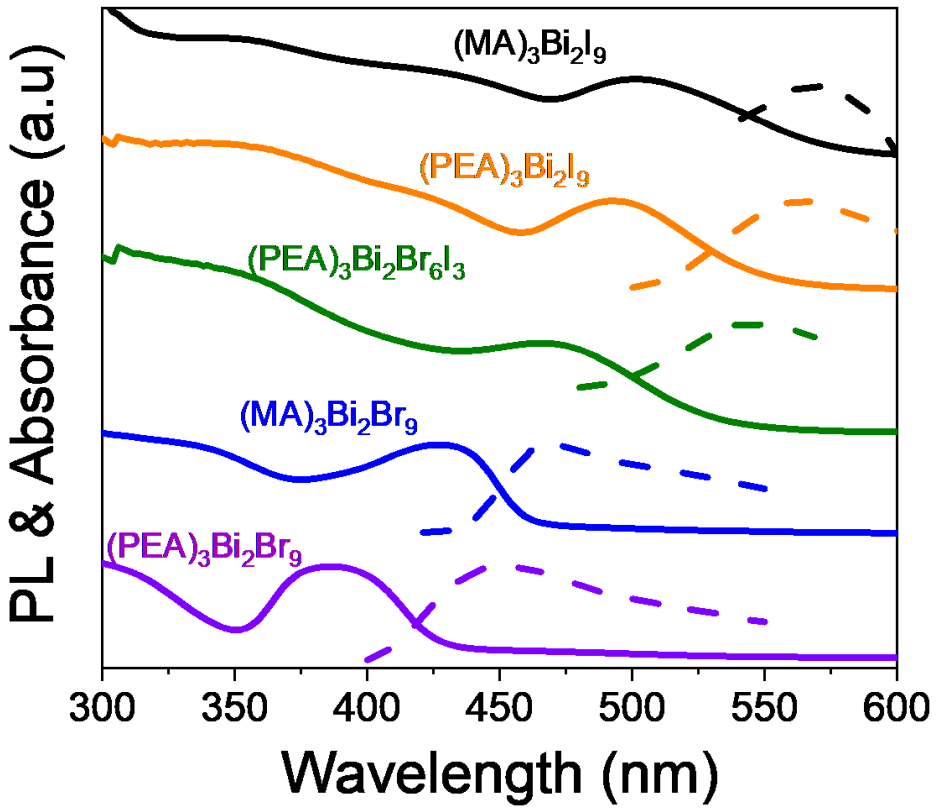

Figure 4-2-6. UV-Vis and PL spectra of PEA and MA bismuth perovskite thin films on glass substrates.

Steady-state UV–Vis and PL were employed to characterise the optical properties. Figure 4-2-6 shows both the UV–Vis and PL spectra from prepared bismuth-based perovskites. When bromide replaces iodine in $PEA_3Bi_2I_9$, there is an obvious peak shift to higher energy, which can also be seen in lead- and tin-based perovskites.[37,44] When comparing the spectra from $PEA_3Bi_2I_9$ and $MA_3Bi_2I_9$ and from $PEA_3Bi_2Br_9$ and $MA_3Bi_2Br_9$, blue-shifted spectra and sharper absorption bands and more obvious exciton bumps can be observed in PEA-containing perovskites. In particular, sharper absorption bands are attributable to the excitonic behaviour of these materials.

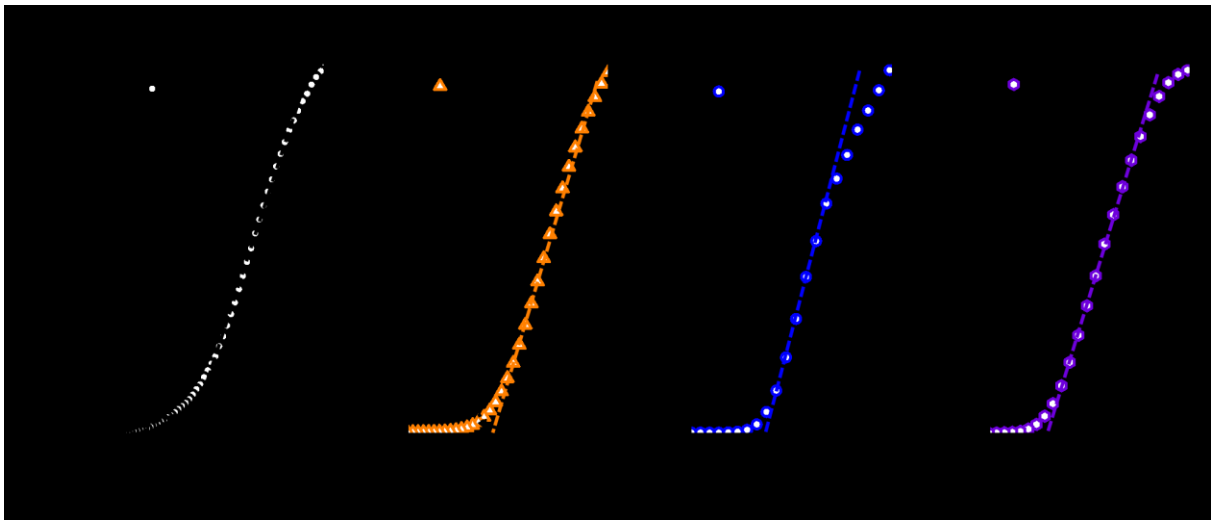

Figure 4-2-7. Tauc plots from PEA and MA bismuth perovskite thin films.

The optical bandgaps of $MA_3Bi_2I_9$, $PEA_3Bi_2I_9$, $MA_3Bi_2Br_9$ and $PEA_3Bi_2Br_9$ films were estimated as ~2.15, ~2.33, ~2.74 and ~3.00 eV, respectively (Figure 4-2-7). Note that the optical bandgap of perovskites increases when reducing the material's dimensionality from 0D (MA) to 2D (PEA) as shown in the UV–Vis spectra. We attribute this to a quantum size effect, as has been reported elsewhere for similar perovskite materials.[37] Interestingly, when

perovskites with MA and PEA are compared, PEA bismuth iodide/bromide perovskites have steeper gradient in the Tauc plot. This is related to the Urbach tail. Exponential tail appears in the poor crystalline, the disordered and amorphous materials. When the Tauc plot has lower gradient, the material has higher Urbach energy, meaning the crystallinity is poor. By replacing MA to PEA, this Urbach energy has been decreased, showing better crystallinity in the material.

Time-resolved PL decays of $MA_3Bi_2Br_9$ and $PEA_3Bi_2Br_9$ are shown in Figure 4-2-8. It is notable that the replacement of MA with PEA leads to longer decay lifetimes ($\tau_{1/3} \fallingdotseq 0.21$ ns from $MA_3Bi_2Br_9$ and 0.82 ns from $PEA_3Bi_2Br_9$). The observation of a longer time in $PEA_3Bi_2Br_9$ relative to $MA_3Bi_2Br_9$ is consistent with a higher PLQY in the 2D material. This agrees with the directly measured PLQY values ($PEA_3Bi_2Br_9$: 0.48%; $MA_3Bi_2Br_9$: 0.18%; Table 4-2-2). The better PLQY of $PEA_3Bi_2Br_9$ compared to that of $MA_3Bi_2Br_9$ is consistent with the increased excitonic character of $PEA_3Bi_2Br_9$ as shown in the UV spectra. In addition, the decreased defect density can be one reason for the increased PLQY.[40,42]

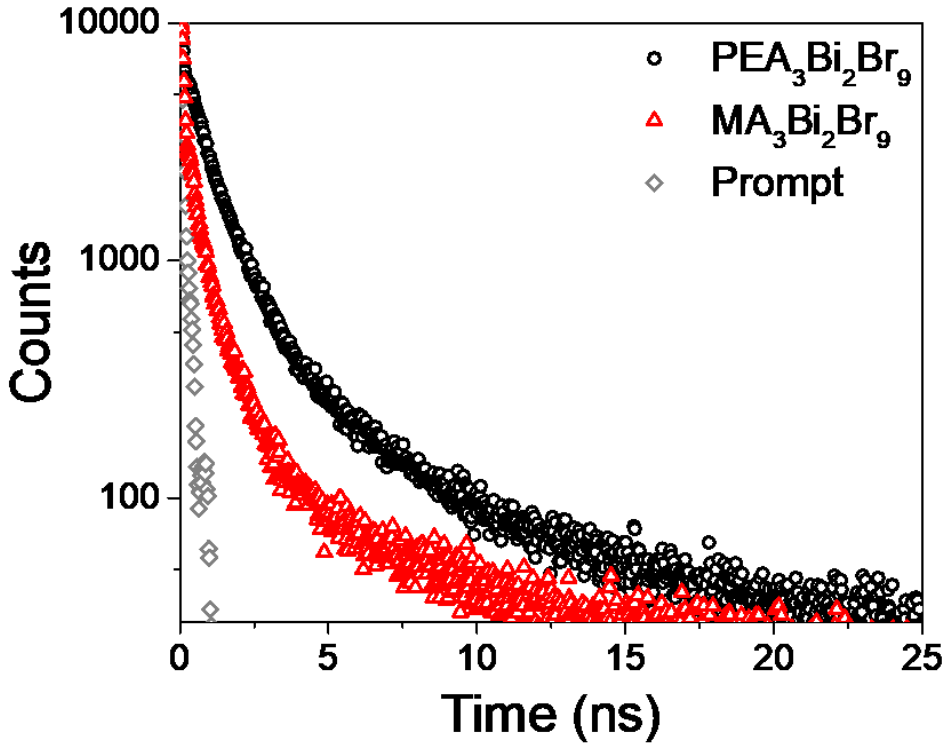

Figure 4-2-8. TRPL from $PEA_3Bi_2Br_9$ and $MA_3Bi_2Br_9$ thin films on glass substrates. The selected excitation wavelength was 282 nm for samples and probed at 450 nm and 468 nm for $PEA_3Bi_2Br_9$ and $MA_3Bi_2Br_9$ respectively.

Next, the microsecond-to-millisecond transient absorption spectroscopy (TAS) was used to study the transfer of generated charges in $PEA_3Bi_2I_9$ thin films at the metal oxide/ $PEA_3Bi_2I_9$/HTM heterojunction. Figure 4-2-9 shows the charge decay probed at 1,000 nm where the polaron of P3HT can be easily observed. All three $PEA_3Bi_2I_9$ films with different metal oxide and HTM layers show that no absorption was observed at this timescale. It is understandable that the film with PMMA has no decay because PMMA has a low HOMO level and high LUMO level, so there is no charge transfer to PMMA.

Table 4-2-2. PLQY values, emission peak position and full width at half maximum (FWHM) values of $PEA_3Bi_2Br_9$, $MA_3Bi_2Br_9$, $PEA_3Bi_2I_9$ and $MA_3Bi_2I_9$. The selected excitation wavelength was 320 nm for samples with bromide and 338 nm for samples with iodine respectively. The photoluminescence between 340 nm and 620 nm for bromide samples and between 500 nm and 600 nm for iodine samples was collected.

	PLQY (%)	Emission Peak (nm)	FWHM (nm)
$(PEA)_3Bi_2Br_9$	0.48	448	116
$(MA)_3Bi_2Br_9$	0.18	467	100
$(PEA)_3Bi_2I_9$	0.02	563	90
$(MA)_3Bi_2I_9$	0.01	570	60

However, films with P3HT, which has a sufficiently high HOME level where it can accept holes from the perovskite, also lacks obvious absorption. This means there was either no or too small charge transferred to HTM or the charges were recombined too quickly. The first reason seems more sensible because $PEA_3Bi_2I_9$ has more excitonic behaviour, as can be seen in Figure 4-2-6. If no holes can be transferred to HTM, the solar cell with this material cannot work. The *in situ* processed BiSI layer was employed to resolve this problem.

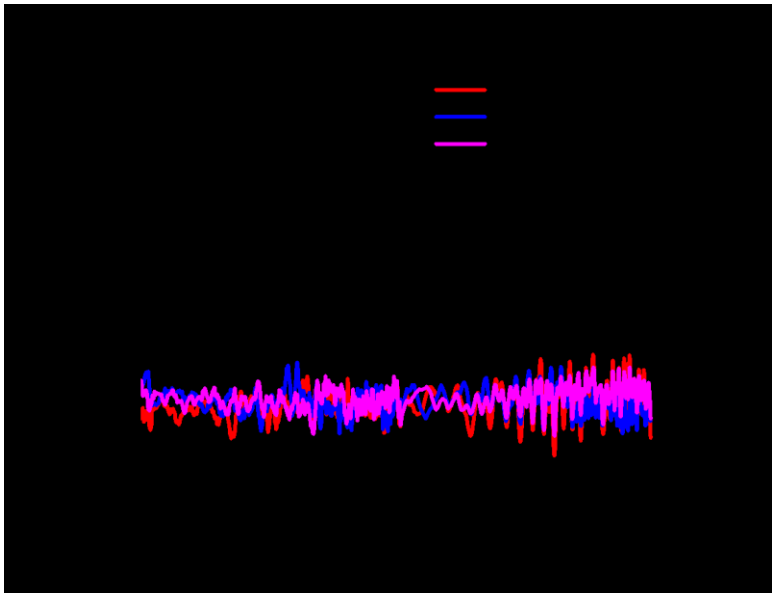

Figure 4-2-9. Transient absorption kinetics measured at 1,000 nm for $PEA_3Bi_2I_9$ thin films on different substrates and with different polymers. The signals were normalised by the absorption of the film at 450 nm, which is the excitation wavelength.

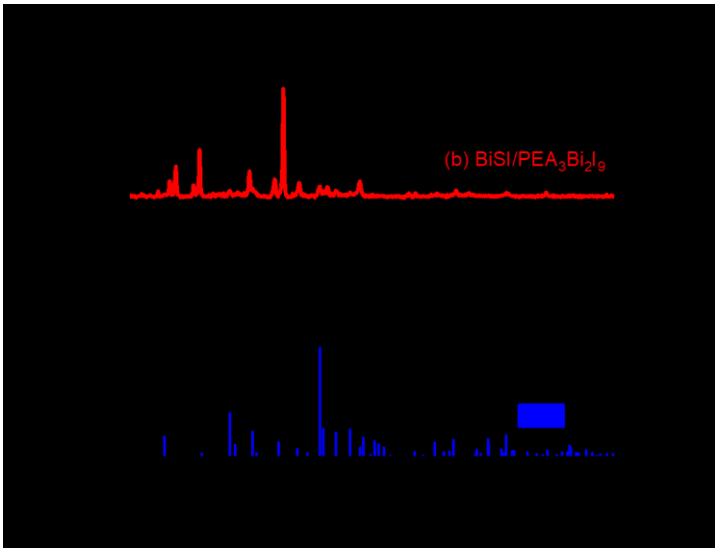

Figure 4-2-10. X-ray diffraction patterns of $PEA_3Bi_2I_9$ on (a) mp-Al_2O_3 and (b) mp-Al_2O_3/BiSI substrates and the reference of BiSI (blue, code: 01-073-1171).

Figure 4-2-10 shows the XRD patterns from the prepared $PEA_3Bi_2I_9$ thin films on mp-Al_2O_3 scaffold for thickness. Figure 4-2-10 (a) and (b), which are comparisons of $PEA_3Bi_2I_9$ with and without a BiSI layer, respectively, can be compared to confirm the formation of $PEA_3Bi_2I_9$ without reaction with BiSI. $PEA_3Bi_2I_9$ on BiSI shows both $PEA_3Bi_2I_9$ and BiSI peak without additional peaks where peaks from $PEA_3Bi_2I_9$ are the majority, meaning that the $PEA_3Bi_2I_9$ is thicker than BiSI.

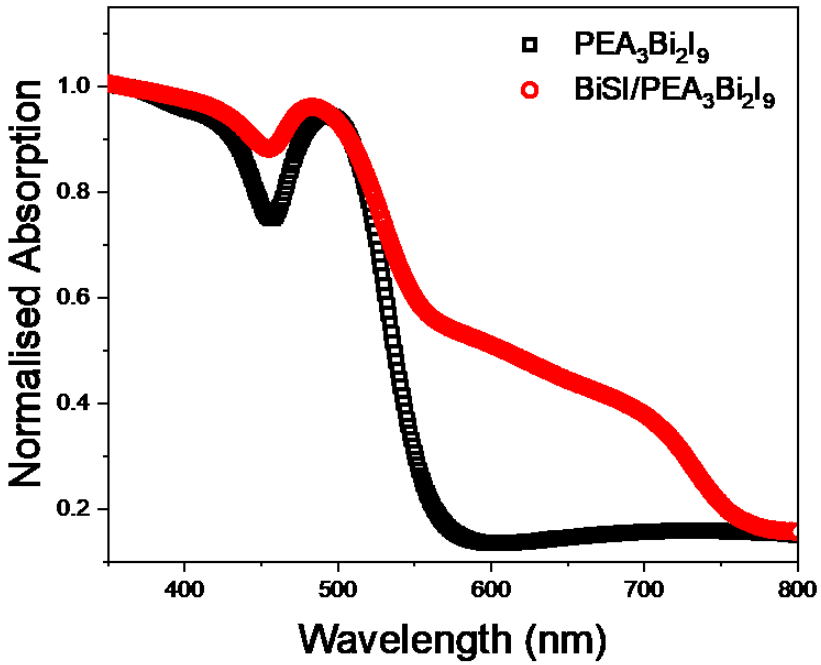

Figure 4-2-11. Normalised absorption spectra of $PEA_3Bi_2I_9$ on glass and glass/BiSI substrates.

Figure 4-2-11 shows the UV–Vis spectra of $PEA_3Bi_2I_9$ on glass (black symbols) and glass/BiSI (red symbols) substrates. For the $PEA_3Bi_2I_9$ film on glass, the absorption band starts at around 550 nm (2.25 eV), which matches well the obtained bandgap above. Meanwhile, $MA_3Bi_2I_9$ on

glass shows another absorption increase at around 750 nm (1.65 eV) which is similar to the BiSI Tauc plot above (Figure 3-6 (c)). From both the XRD and UV–Vis data, we can conclude that $PEA_3Bi_2I_9$ was formed on the BiSI interlayer without reacting with BiSI.

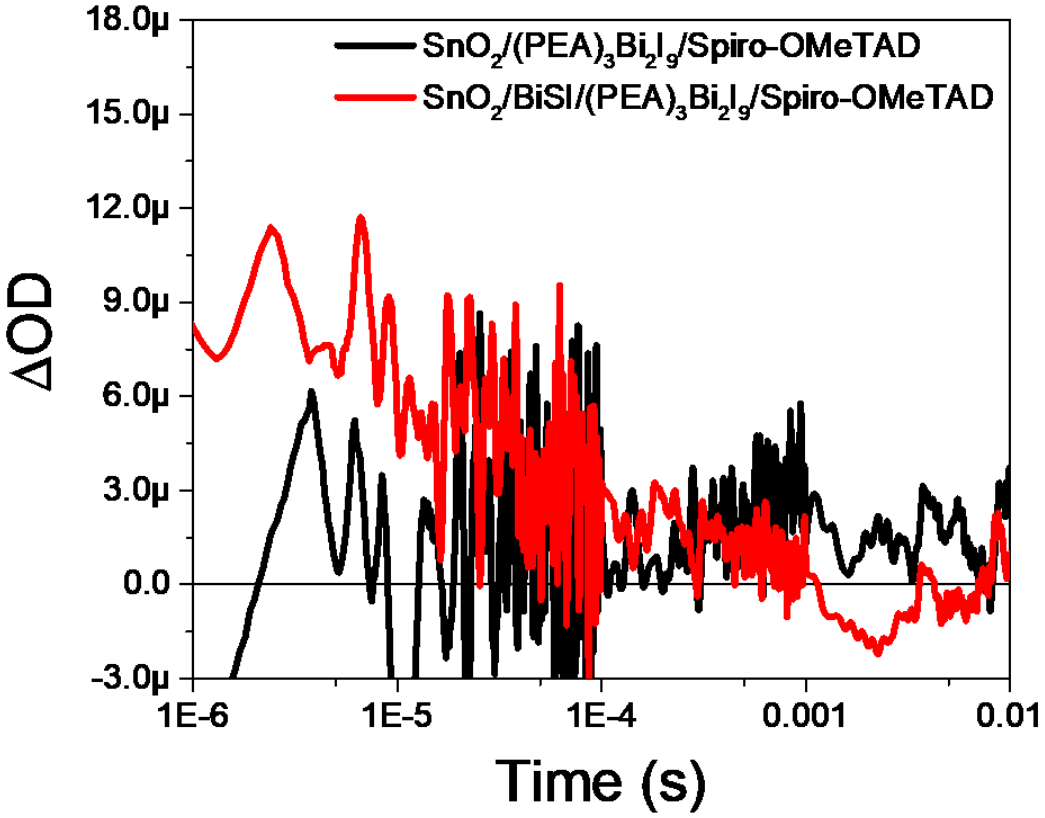

Figure 4-2-12. Transient absorption kinetics measured at 1,600 nm for $PEA_3Bi_2I_9$ thin films on c-SnO_2 with and without a BiSI interlayer. The signals were normalised by the absorption of the film at 450 nm, which is the excitation wavelength.

Figure 4-2-12 shows the transient absorption kinetics from $PEA_3Bi_2I_9$ thin film with and without a BiSI layer with spiro-OMeTAD. The signal was probed at 1,600 nm where the

polaron of spiro-OMeTAD could be easily observed. For the $PEA_3Bi_2I_9$ thin film without BiSI (the black trace in Figure 4-2-12), the signal is negligible, which means that while the charges were generated in $PEA_3Bi_2I_9$, the generated holes were short-lived due to the charge recombination between holes transferred to spiro-OMeTAD and electrons in the perovskite or that the generated holes were still not transferred to the HTM due to its high excitonic behaviour. When BiSI was employed (the red trace in Figure 4-2-12), the signal became clearer compared to that without the BiSI layer and it seems that the BiSI layer extracted the electrons more efficiently than the compact SnO_2 ETL; therefore, more holes could be transferred to spiro-OMeTAD because the exciton were split into the charges due to the high driving force from the BiSI.

Based on this knowledge, the solar cell devices were fabricated in the structure shown in Figure 4-2-13 (a). The solar cell without BiSI layer (red trace in Figure 4-2-13 (b)) was short-circuited. It might be because the high excitonic energy in $PEA_3Bi_2I_9$ did not allow the generated excitons to split into free charges and so the charge was not transferred to the ETM or HTM as observed in TAS (Figure 4-2-9). Meanwhile, the solar cell with BiSI layer worked even though its PCE was only 0.013%. Although BiSI helped split generated excitons with a larger driving force from the energy level difference, it seems that the charge transfer is still insufficient to have a high PCE.

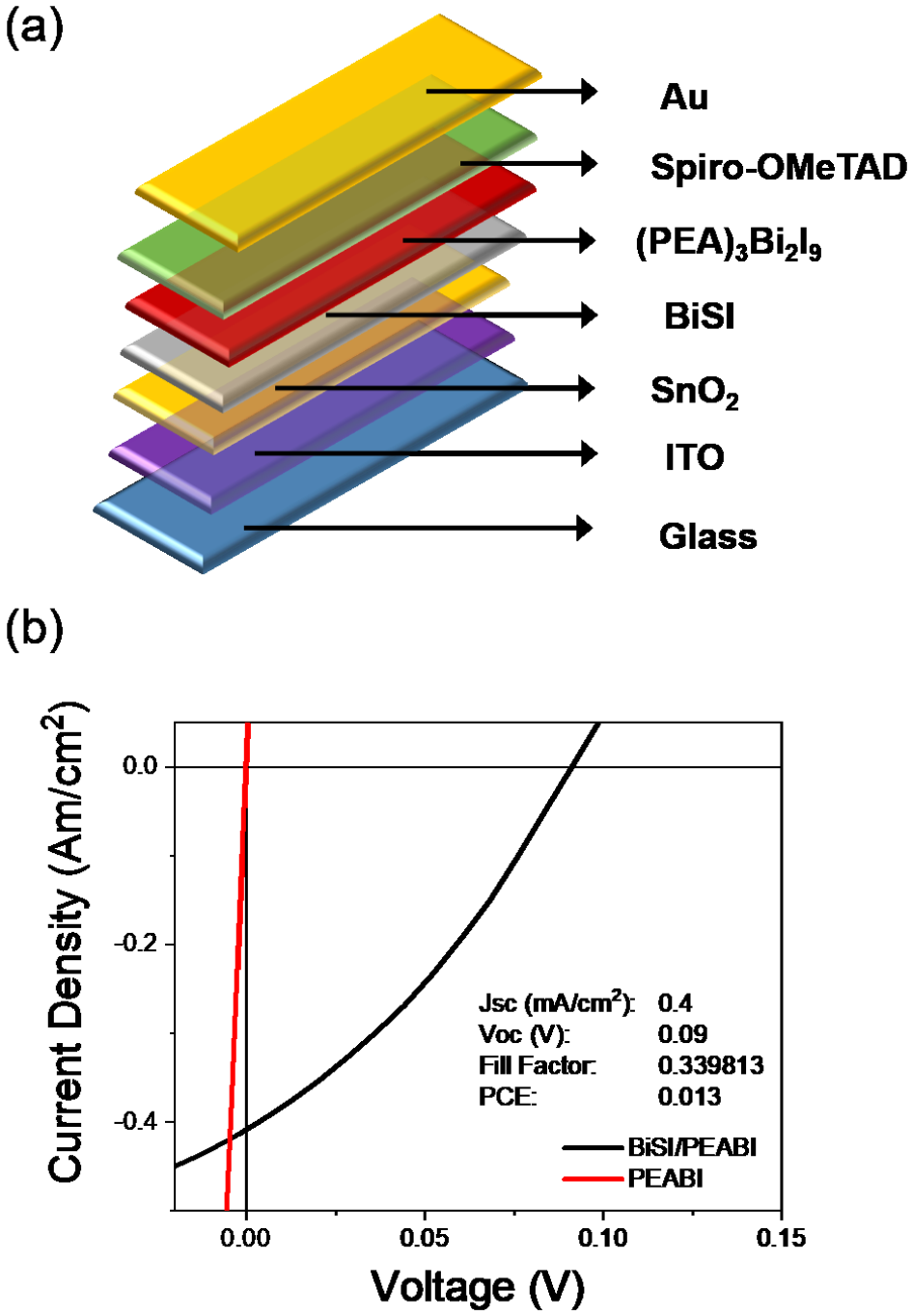

Figure 4-2-13. (a) Schematic device architecture of $PEA_3Bi_2I_9$-based solar cells fabricated with the BiSI interlayer and (b) JV traces of the assembled devices with and without the BiSI interlayer.

4-3. Conclusion

In this chapter, two ways to overcome the concerns of lead-free bismuth-based perovskites are suggested. To mix bismuth and antimony in a 0D perovskite structure ($MA_3(Bi_{1-x}Sb_x)_2I_9$) and to introduce phenylethylammonium (PEA^+) to the small cation position worked efficiently, improving the optical property of bismuth-based perovskites.

In the chapter regarding metal cation transmutation, the physical and opto-physical properties of bismuth-and-antimony mixed 0D perovskites were explored using a combined experimental and computational approach. This study has improved the fundamental understanding of these systems and suggested ways that such systems can be improved for their potential use in solar-cell applications. This investigation has revealed the following key results.

a) There is <1% change in the lattice parameters and a small shift in the XRD peaks with no impurities seen, which indicates that a solid solution would form.

b) The calculations indicate the complete disorder of configurations for mixed systems; this is supported from the reduction in PLQY seen in mixed systems.

c) Significant bandgap bowing is seen in the system. This effect is chemical in nature and is likely a result of a mismatch of energy levels between Bi and Sb p-orbitals. This effect would be beneficial for fine-tuning and reducing the bandgap for solar-cell applications.

d) Sb substitution for Bi leads to a lower effective mass, which is a major factor in the reduction of the calculated and observed binding energies. A lower binding energy leads to a reduced density of excitons and should increase the PCEs. However, further work is needed to evaluate

the PCEs of these materials by optimising the t device architecture.

The insights from this study are also applicable to other semiconductors, including silver bismuth or antimony double perovskites, Sb/Bi sulfide and Sb/Bi triiodide for various applications.

In the chapter regarding 2D-structured bismuth-based perovskite, $PEA_3Bi_2I_9$ was successfully synthesised and fabricated in thin films and they were compared to 0D bismuth-based perovskite. The 2D bismuth perovskite showed a blue shift in the UV–Vis and PL due to the quantum confinement, improved charge lifetime and improved PLQY; it seems to come from the increased excitonic behaviour and reduced defect density in the perovskite. Unfortunately, $PEA_3Bi_2I_9$ showed poor charge transfer to HTM, which is unbeneficial in a solar cell application and so the fabricated solar cell did not perform well. However, employing the BiSI interlayer meant that the solar cell started working. If the structure can be optimised, it is expected to have a higher PCE in the future. Replacing MA with PEA can be applied to antimony-based perovskite, which has a smaller binding energy compared to bismuth-based ones; it would be interesting to see how 2D antimony perovskites work.

4-4. References

1. B. W. Park, B. Philippe, X. Zhang, H. Rensmo, G. Boschloo and E. M. J. Johansson, *Adv. Mater.*, 2015, **27**, 6806-6813.

2. M. Scholz, O. Flender, K. Oum and T. Lenzer, *J. Phys. Chem. C*, 2017, **121**, 12110-12116.

3. M. Scholz, M. Morgenroth, K. Oum and T. Lenzer, *J. Phys. Chem. C*, 2018, **122**, 5854-5863.

4. G. Paul and A. J. Pal, *J. Phys. Chem. C*, 2019, **123**, 13500-13507.

5. X. Zhang, G. Wu, Z. Gu, B. Guo, W. Liu, S. Yang, T. Ye, C. Chen, W. Tu and H. Chen, *Nano Res.*, 2016, **9**, 2921-2930.

6. M. Lyu, J. H. Yun, M. Cai, Y. Jiao, P. V. Bernhardt, M. Zhang, Q. Wang, A. Du, H. Wang, G. Liu and L. Wang, *Nano Res.*, 2016, **9**, 692-702.

7. J. Shin, M. Kim, S. Jung, C. S. Kim, J. Park, A. Song, K. B. Chung, S. H. Jin, J. H. Lee and M. Song, *Nano Res.*, 2018, **11**, 6283-6293.

8. F. Bai, Y. H. Hu, Y. Q. Hu, T. Qiu, X. L. Miao and S. F. Zhang, *Sol. Energy Mater. Sol. Cells*, 2018, **184**, 15-21.

9. S. Oz, J. C. Hebig, E. W. Jung, T. Singh, A. Lepcha, S. Olthof, J. Flohre, Y. J. Gao, R. German, P. H. M. van Loosdrecht, K. Meerholz, T. Kirchartz and S. Mathur, *Sol. Energy Mater. Sol. Cells*, 2016, **158**, 195-201.

10. S. M. Jain, D. Phuyal, M. L. Davies, M. Li, B. Philippe, C. De Castro, Z. Qiu, J. Kim, T. Watson, W. C. Tsoi, O. Karis, H. Rensmo, G. Boschloo, T. Edvinsson and J. R. Durrant, *Nano Energy*, 2018, **49**, 614-624.

11. J. C. Hebig, I. Kuhn, J. Flohre and T. Kirchartz, *ACS Energy Lett.*, 2016, **1**, 309-314.

12. P. C. Harikesh, H. K. Mulmudi, B. Ghosh, T. W. Goh, Y. T. Teng, K. Thirumal, M. Lockrey, K. Weber, T. M. Koh, S. Li, S. Mhaisalkar and N. Mathews, *Chem. Mater.*, 2016, **28**, 7496-7504.

13. F. Y. Jiang, D. W. Yang, Y. Y. Jiang, T. F. Liu, X. G. Zhao, Y. Ming, B. W. Luo, F. Qin, J. C. Fan, H. W. Han, L. J. Zhang and Y. H. Zhou, *J. Am. Chem. Soc.*, 2018, **140**, 1019-1027.

14. P. Karuppuswamy, K. M. Boopathi, A. Mohapatra, H. C. Chen, K. T. Wong, P. C. Wang and C. W. Chu, *Nano Energy*, 2018, **45**, 330-336.

15. K. M. Boopathi, P. Karuppuswamy, A. Singh, C. Hanmandlu, L. Lin, S. A. Abbas, C. C. Chang, P. C. Wang, G. Li and C. W. Chu, *J. Mater. Chem. A*, 2017, **5**, 20843-20850.

16. P. Szklarz, A. Pietraszko, R. Jakubas, G. Bator, P. Zieliński and M. Gałazka, *J. Phys. Condens. Matter*, 2008, **20**, 255221.

17. R. Jakubas and L. Sobczyk, *Phase Transitions*, 1990, **20**, 163-193.

18. T. Kawai, A. Ishii, T. Kitamura, S. Shimanuki, M. Iwata and Y. Ishibashi, *J. Phys. Soc. Japan*, 1996, **65**, 1464-1468.

19. K. Eckhardt, V. Bon, J. Getzschmann, J. Grothe, F. M. Wisser and S. Kaskel, *Chem. Commun.*, 2016, **52**, 3058-3060.

20. B. Yang, Y. J. Li, Y. X. Tang, X. Mao, C. Luo, M. S. Wang, W. Q. Deng and K. L. Han, *J. Phys. Chem. Lett.*, 2018, **9**, 3087-3092.

21. L. S. Liang and P. Gao, *Adv. Sci*, 2018, **5**, 1700331.

22. F. Hao, C. C. Stoumpos, R. P. H. Chang and M. G. Kanatzidis, *J. Am. Chem. Soc.*, 2014, **136**, 8094-8099.

23. G. E. Eperon, T. Leijtens, K. A. Bush, R. Prasanna, T. Green, J. T. W. Wang, D. P. McMeekin, G. Volonakis, R. L. Milot, R. May, A. Palmstrom, D. J. Slotcavage, R. A. Belisle, J. B. Patel, E. S. Parrott, R. J. Sutton, W. Ma, F. Moghadam, B. Conings, A. Babayigit, H. G. Boyen, S. Bent, F. Giustino, L. M. Herz, M. B. Johnston, M. D. McGehee and H. J. Snaith, *Science*, 2016, **354**, 861-865.

24. J. Im, C. C. Stoumpos, H. Jin, A. J. Freeman and M. G. Kanatzidis, *J. Phys. Chem. Lett.*, 2015, **6**, 3503-3509.

25. A. Goyal, S. McKechnie, D. Pashov, W. Tumas, M. van Schilfgaarde and V. Stevanovic, *Chem. Mater.*, 2018, **30**, 3920-3928.

26. V. D'Innocenzo, G. Grancini, M. J. P. Alcocer, A. R. S. Kandada, S. D. Stranks, M. M. Lee, G. Lanzani, H. J. Snaith and A. Petrozza, *Nat. Commun.*, 2014, **5**.

27. M. Saba, M. Cadelano, D. Marongiu, F. Chen, V. Sarritzu, N. Sestu, C. Figus, M. Aresti, R. Piras, A. G. Lehmann, C. Cannas, A. Musinu, F. Quochi, A. Mura and G. Bongiovanni, *Nat. Commun.*, 2014, **5**.

28. F. Meillaud, A. Shah, C. Droz, E. Vallat-Sauvain and C. Miazza, *Sol. Energy Mater. Sol. Cells*, 2006, **90**, 2952-2959.

29. R. L. Z. Hoye, R. E. Brandt, A. Osherov, V. Stevanovic, S. D. Stranks, M. W. B. Wilson, H. Kim, A. J. Akey, J. D. Perkins, R. C. Kurchin, J. R. Poindexter, E. N. Wang, M. G. Bawendi, V. Bulovic and T. Buonassisi, *Chem. Eur. J.*, 2016, **22**, 2605-2610.

30. A. Miyata, A. Mitioglu, P. Plochocka, O. Portugall, J. T. W. Wang, S. D. Stranks, H. J. Snaith and R. J. Nicholas, *Nat. Phys.*, 2015, **11**, 582-U594.

31. X. H. Chen, H. P. Lu, Y. Yang and M. C. Beard, *J. Phys. Chem. Lett.*, 2018, **9**, 2595-2603.

32. M. G. Ju, J. Dai, L. Ma and X. C. Zeng, *J. Am. Chem. Soc.*, 2017, **139**, 8038-8043.

33. Q. Q. Lin, A. Armin, R. C. R. Nagiri, P. L. Burn and P. Meredith, *Nat. Photonics*, 2015, **9**, 106-112.

34. L. Protesescu, S. Yakunin, M. I. Bodnarchuk, F. Krieg, R. Caputo, C. H. Hendon, R. X. Yang, A. Walsh and M. V. Kovalenko, *Nano Lett.*, 2015, **15**, 3692-3696.

35. I. C. Smith, E. T. Hoke, D. Solis-Ibarra, M. D. McGehee and H. I. Karunadasa, *Angew. Chem. Int.*, 2014, **53**, 11232-11235.

36. S. Y. Shao, J. J. Dong, H. Duim, G. H. ten Brink, G. R. Blake, G. Portale and M. A. Loi, *Nano Energy*, 2019, **60**, 810-816.

37. L. Lanzetta, J. M. Marin-Beloqui, I. Sanchez-Molina, D. Ding and S. A. Haque, *ACS Energy Lett.*, 2017, **2**, 1662-1668.

38. D. H. Cao, C. C. Stoumpos, O. K. Farha, J. T. Hupp and M. G. Kanatzidis, *J. Am. Chem. Soc.*, 2015, **137**, 7843-7850.

39. H. Tsai, W. Nie, J.-C. Blancon, C. C. S. Toumpos, R. Asadpour, B. Harutyunyan, A. J. Neukirch, R. Verduzco, J. J. Crochet, S. Tretiak, L. Pedesseau, J. Even, M. A. Alam, G. Gupta, J. Lou, P. M. Ajayan, M. J. Bedzyk, M. G. Kanatzidis and A. D. Mohite, *Nature*, 2016, **536**, 312-316.

40. Z. Yuan, Y. Shu, Y. Xin and B. W. Ma, *Chem. Commun.*, 2016, **52**, 3887-3890.

41. B. Saparov, F. Hong, J. P. Sun, H. S. Duan, W. W. Meng, S. Cameron, I. G. Hill, Y. F. Yan and D. B. Mitzi, *Chem. Mater.*, 2015, **27**, 5622-5632.

42. A. J. Lehner, D. H. Fabini, H. A. Evans, C. A. Hebert, S. R. Smock, J. Hu, H. B. Wang, J. W. Zwanziger, M. L. Chabinyc and R. Seshadri, *Chem. Mater.*, 2015, **27**, 7137-7148.

43. Z. H. Liu, M. M. Chen, L. Wan, Y. Liu, Y. L. Wang, Y. S. Gan, Z. G. Guo, D. Eder and S. M. Wang, *Sn Applied Sciences*, 2019, **1**.

44. F. Hao, C. C. Stoumpos, D. H. Cao, R. P. H. Chang and M. G. Kanatzidis, *Nat. Photonics*, 2014, **8**, 489-494.

Chapter 5: Metal doping in Lead-free Blue-emitting Quantum Dots for Improved Optical Property

Abstract

Although lead halide perovskite nanocrystals with a tuneable bandgap and narrow-band emissions are very promising for modern lighting and display applications, they suffer from toxicity and instability problems. To overcome these concerns, lead-free tin-, bismuth- and antimony- perovskite NCs are being developed. In particular, 0D perovskites' high binding energy can be beneficial for high PLQY, opening routes towards the formation of a new generation of high-performance light-emitting materials, but much room yet remains for improvements. Recently, Pb and Sb mixed perovskites achieved high PLQY in NCs and these also seem applicable to bismuth- and antimony-based perovskites.

This chapter reports the synthesis and characterisation of $Cs_3(Bi_{1-x}Sb_x)_2X_9$ perovskite QDs. By doping and mixing bismuth and antimony in 0D perovskite, changes in the structure, absorption and emission wavelengths and charge-carrier lifetime were observed. These changes can be applied to further applications in light-emitting or photovoltaic devices.

5-1. Introduction

0D perovskites have high binding energies to meet the needs of high-performance solar cell fabrication. However, the intrinsic characteristics of 0D perovskites can be beneficial for high PLQY, opening routes towards the formation of a new generation of high-performance light-emitting materials.[1, 2] While 0D perovskites have low PLQY due to their high level of defects, their fabrication in nanocrystals (NCs) can be a good strategy to increase the PLQY. The PL emissions from 0D perovskites are excitonic due to their high binding energy, as mentioned above. The increased exciton binding energy in NCs compared to $Cs_3Bi_2Br_9$ single crystals brings the enhanced exciton stability and can lead to their increased potential in excitonic recombination. In addition, reducing their size to the nanometre scale brings fewer defects in NCs and excitons are more prone to radiative recombination.[3, 4]

Modern lead-based perovskite NCs are receiving broad attention due to their excellent optical and electronic properties like their high PL quantum yield (PLQY) (>90%), narrow full width at half maximum (FWHM; <25 nm) and tuneable PL emissions due to the quantum confinement.[5–8] Fully inorganic $CsPbX_3$ (X = Cl, Br, I) NCs are emerging as a class of metal halide perovskite QDs that are less susceptible to oxygen and moisture. To date, tremendous progress has been achieved in controlling the morphology, size and halide of CsPbX3 perovskite QDs with tuneable PL emissions from blue to red.[6, 9, 10] However, the toxicity of lead is a big hurdle to clear before their application. Additionally, while tin-based perovskite NCs ($CsSnX_3$ and Cs_2SnX_6) have been fabricated, they have both relatively low PLQY (<1%) and lower stability.[11, 12]

Bismuth- and antimony-based perovskites are another type of perovskite developed to avoid both problems from lead-based perovskites simultaneously. $(MA)_3Bi_2Br_9$ single-crystal and NCs have been synthesised and their NCs obtained a PLQY of 12%.[13] This has 2D crystal structure and consequently ≤2D electronic dimension, which leads to increased exciton binding energy and even the formation of trapped excitons, which is beneficial for high PLQY.[1, 2, 14] Recently, 26.4% PLQY for $Cs_3Bi_2Cl_9$ NCs and 19.4% PLQY for $Cs_3Bi_2Br_9$ were reported by Leng *et al*.[4] Alongside the higher PLQY, they achieved high stability, maintaining 80% of their original performance for 78 hours under UV light. Antimony-based perovskite NCs achieved 46% PLQY in the blue region with $Cs_3Sb_2Br_9$.[15]

There have also been several reports that mixed or doped perovskite QDs have improved optical properties.[16–18] In 2018, Vitoreti *et al*.[19] reported that PLQY was improved tenfold by mixing 7% tin into the perovskite in lead-based perovskite NCs. It looks like this is also applicable in bismuth- and antimony-based perovskites.

In this study, all inorganic bismuth- and antimony-based perovskite ($Cs_3B_2X_9$) NCs were fabricated and characterised. To improve their characteristics, bismuth- and antimony-based perovskites were doped with antimony and bismuth, respectively. Additionally, bismuth-and-antimony mixed perovskite NCs were fabricated and characterised.

5-2. Method

Materials

BiI_3, $BiBr_3$, $BiCl_3$, oleic acid (OA) and oleylamine (OlAm) were purchased from Sigma Aldrich; CsI, CsBr, CsCl and anhydrous dimethyl sulfoxide (DMSO) were purchased from ACROS Organics™; Absolute ethanol, acetone and isopropanol (IPA) were purchased from VWR; $SbBr_3$ was purchased from Alpha Acer. All products were used directly without any further purification.

Synthesis of NCs

The general principle for the fabrication of monodisperse colloidal nanocrystals needs a temporal separation of nucleation and the subsequent growth of particles on the nuclei generated. In heterogeneous nucleation conditions, the particle growth proceeds by deposition of material on already existing "seed" crystals in solution (region 3 in Figure 5-1). To achieve the nucleation burst, hot-injection method is generally used. The precursors decompose thermally and release monomers. By rapidly injecting the precursors into the hot solution above the precursors' decomposition temperature, the concentration of monomers suddenly increases above the nucleation threshold (region 1 in Figure 5-1), forming a super-saturation, driving the nucleation (region 2 in Figure 5-1). By a sudden decrease of reaction temperature during the nucleation period, the concentration of monomers falls below the nucleation threshold and the nucleation process stops (region 3 in Figure 5-1).

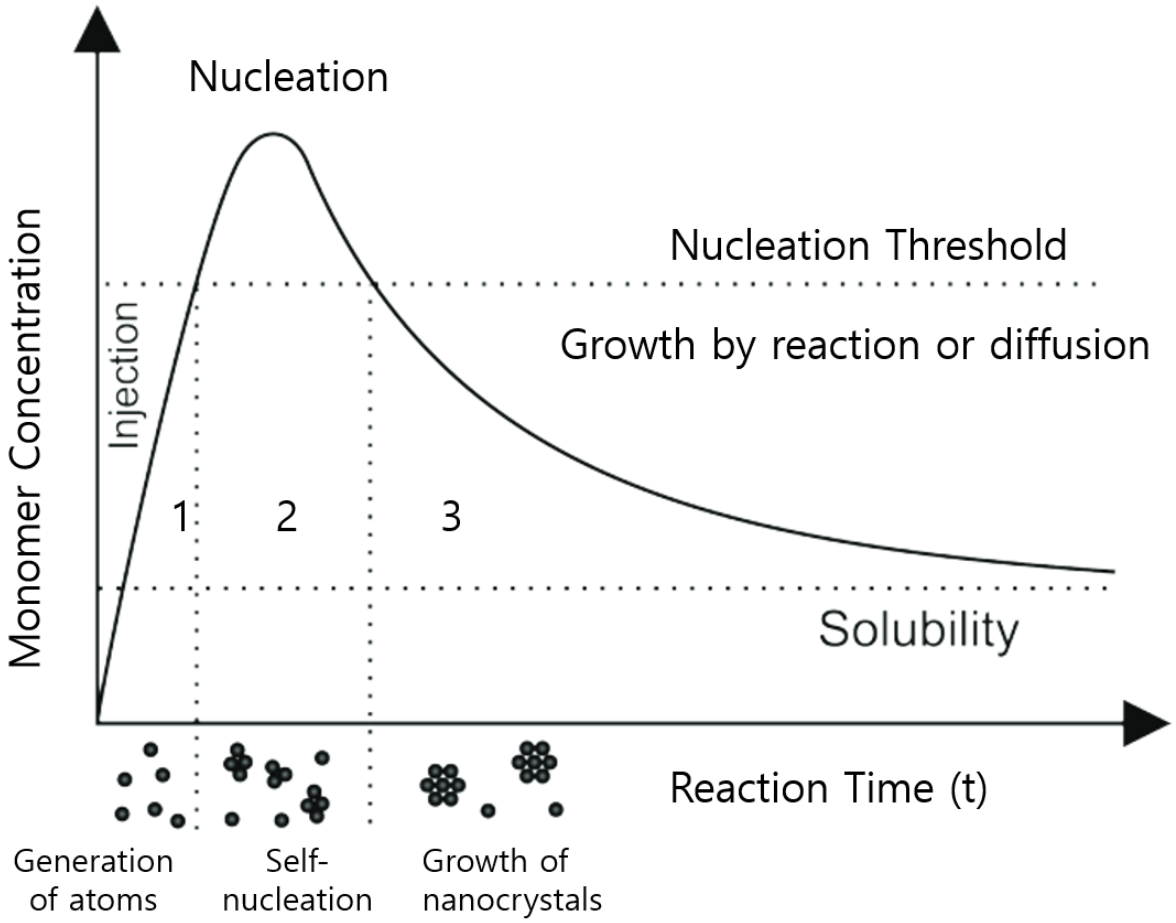

Figure 5-1. A LaMer plot showing the separation of nucleation and growth.

In the typical synthesis of $Cs_3Bi_2X_9$ (X= I, Br, Cl), NCs, 0.4 mmol of CsX, 0.268 mmol of BiX_3 and 66 µL of OLAm were dissolved in 6 mL of DMSO to form a clear precursor solution. One millilitre of this precursor solution was slowly dropped into a mixture of 10 mL ethanol and 1 mL OA with vigorous stirring at 80°C. A natural surfactant, OA was chosen as the surface-binding ligand for stabilising the nanocrystals and the cationic precursors. The precursor solution is with OLAm is not stable in ethanol and OA can stabilise the precursor solution and therefore, this stability difference can be a driving force to proceed. Ligands from OA keep the particles isolated, thus preventing nuclei agglomeration and facilitating homogeneous growth.

Nanocrystal size variations are reduced when ligands control the growth rate of particles. Ligands passivate the surface and bind to the surface during organometallic synthesis naturally provide surface passivation, which protects the surface from oxidation and minimizes the electronic trapping properties of surface defects. The reaction mixture was centrifuged at 8,000 rpm for 10 min to discard precipitates containing large particles. Afterwards, a clear colloidal suspension of $Cs_3Bi_2Br_9$ NCs was obtained. For Sb mixed and doped NCs ($Cs_3(Bi_{1-x}Sb_x)_2Br_9$, two solutions containing 0.4 mmol of CsBr, 66 μL of OLAm and 0.268 mmol of $BiBr_3$ or $SbBr_3$ respectively, were prepared and mixed into a precursor solution in accordance with the different ratios. The mixed precursor solution was slowly dropped into a mixture of 10 mL ethanol and 1 mL OA with vigorous stirring at 80°C and the reacted mixture was then centrifuged at 8,000 rpm for 10 min to discard the precipitates containing large particles as above. After that, a clear colloidal suspension of $Cs_3(Bi_{1-x}Sb_x)_2Br_9$ NCs was obtained; Figure 5-2 illustrates this process. For solid powders of $Cs_3(Bi_{1-x}Sb_x)_2Br_9$ NCs for XRD were obtained by centrifugation at 8,500 rpm for 20 min.

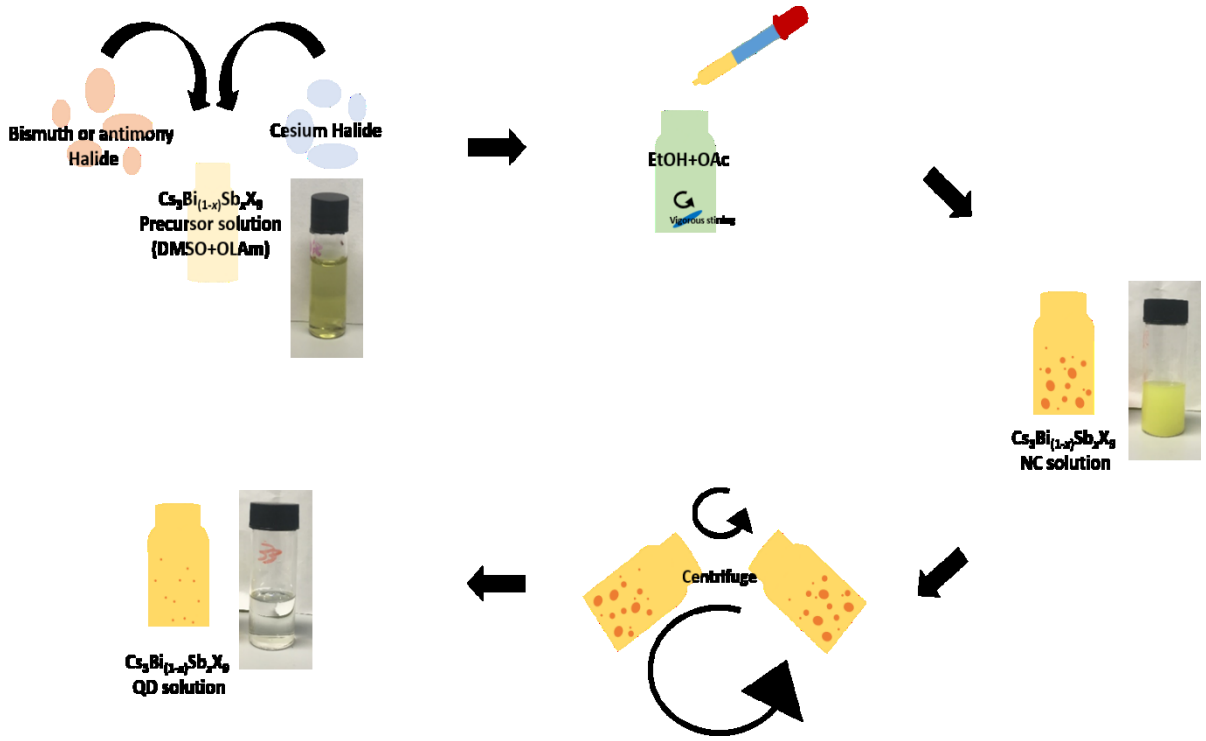

Figure 5-2. Preparation of bismuth-and-antimony mixed perovskite NCs.

Characterisation Techniques

XRD, steady-state PL, steady-state UV–Vis and time-resolved photoluminescence (TRPL) were carried out as described in Chapter 2. 2-9. For Transmission Electron Microscopy (TEM) images, TEM (JEM-2100F with FE (Field Emission) and analytical electron microscope at 200 kV) was applied to characterise the size of the QDs. TEM images were obtained by Dr. Mahmoud G. Ardakani, who is a technician in the Department of Materials. ImageJ was used to analyse the size distribution.

5-3. Results & Discussion

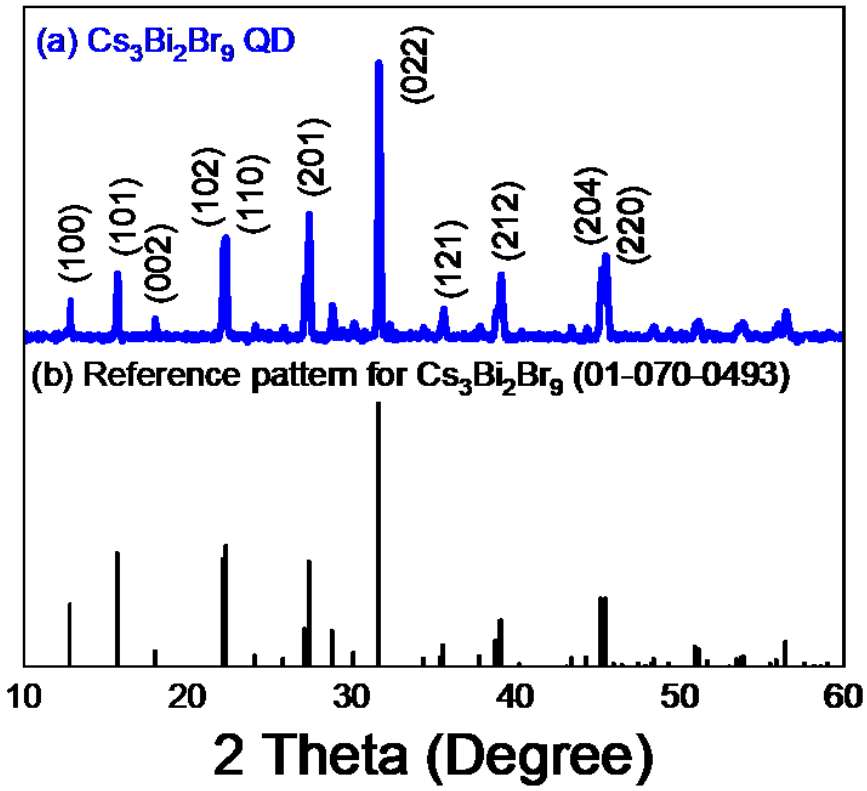

Figure 5-3. (a) X-ray diffraction pattern of prepared $Cs_3Bi_2Br_9$ powder and (b) a reference of $Cs_3Bi_2Br_9$ (code: 01-070-0493).

X-ray diffraction was employed to confirm whether the prepared NCs were bismuth perovskite. Figure 5-3 (a) shows the X-ray Diffraction (XRD) patterns from prepared $Cs_3Bi_2Br_9$ powder as described above. The peaks at 12.8°, 15.6°, 22.1°, 22.3°, 27.3° and 31.6° are attributed to the (100), (101), (102), (110), (201) and (022) planes. The obtained pattern was compared with the reference (01-070-0493) (Figure 5-3 (b)); it verifies that $Cs_3Bi_2Br_9$ NCs were successfully

fabricated through the above method.

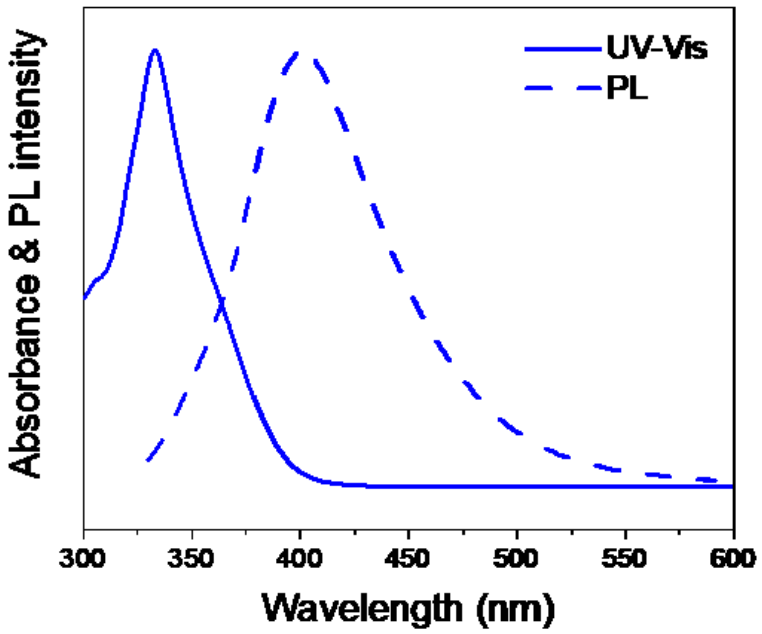

Figure 5-4. Absorbance spectrum (solid line) and normalized PL spectrum (dashed line) of prepared $Cs_3Bi_2Br_9$ NCs. The selected excitation wavelength was 280 nm for PL measurement.

The absorbance spectrum and PL spectrum were obtained to characterise the optical properties of the prepared bismuth perovskite NCs. Figure 5-4 (a) shows the normalised absorbance spectrum. From this spectrum, the absorption onset can be found near 395 nm (~ 3.09 eV). From the PL spectrum, the PL peak position was found at 401 nm with ~76 nm for the full width at half maximum (FWHM). When compared with values from the single crystal (absorption onset = 2.61 eV, PL peak = 473 nm and FWHM = 42 nm) reported by Leng *et al.*,[4] there is a notable blue-shift of 70 nm, which might have resulted from the strong quantum confinement effect. The FWHM in NC is wider than that in single crystal. This phenomenon

will be explained later with the diameter distribution of the synthesised NCs.

For further study of the exciton recombination dynamics, TRPL decay was measured and shown in Figure 5-5. The PL decay can be fitted by a tri-exponential function (Eq. 5-1))[20].

$$I(\mathrm{t}) = I_1 \exp\left(\frac{-t}{t_1}\right) + I_2 \exp\left(\frac{-t}{t_2}\right) + I_3 \exp\left(\frac{-t}{t_3}\right) \qquad \text{(Eq. 5-1)}$$

Here, the contribution of the ultralong-lived component is negligible with relative amplitudes (RAs) <10% while the lifetimes of the other two components deviated little with samples.

The PL decay curve (Figure 5-5) can be fitted with a short-lived PL lifetime (t_1) of 2.84 ns with a percentage of 43.3% and a long-lived PL lifetime (t_2) of 10.50 ns with a percentage of 56.4%. The photoluminescence of $Cs_3Bi_2Br_9$ NCs is driven by the exciton radiative recombination but also strongly limited by the presence of nonradiative defects.[21, 22] Although reducing the size to the nanometre scale can brings fewer defects in NCs,[3, 4] the surface defect recombination still dominates in bismuth perovskite NCs.

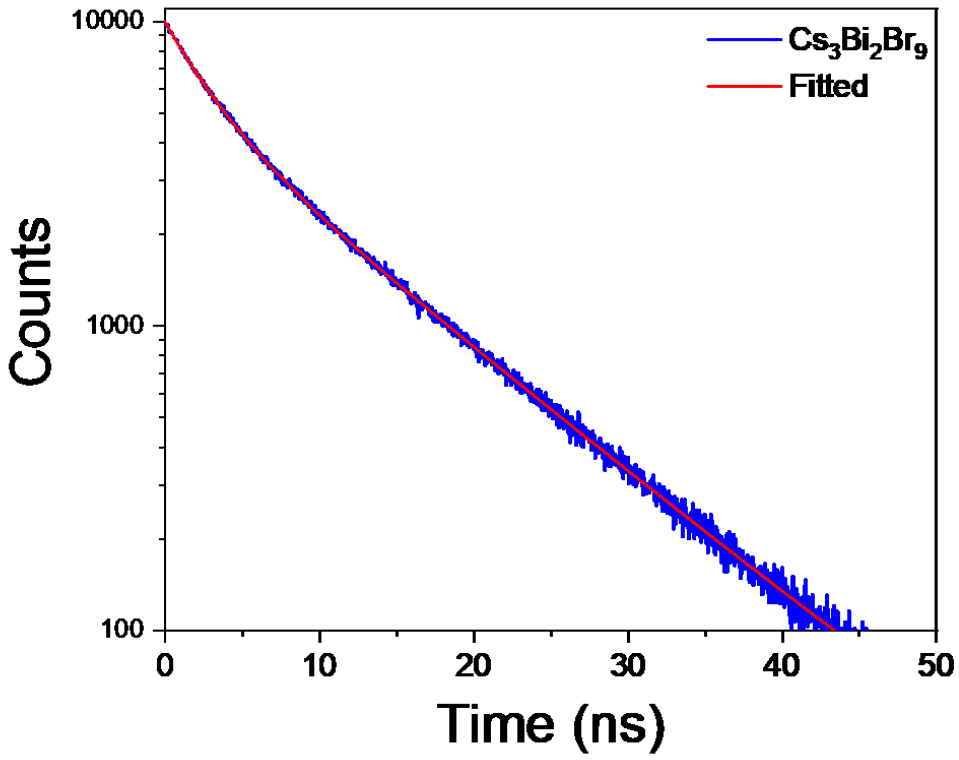

Figure 5-5. TRPL from $Cs_3Bi_2Br_9$ NCs (blue) and its the fitted line using eq. 5-1 (red). The selected excitation wavelength was 282 nm and probed at 400 nm.

Figure 5-6 (a) and (b) present the transmission electron microscopy (TEM) image of as-synthesised $Cs_3Bi_2Br_9$ NCs and the size distribution. Black dots can be found in the TEM image (Figure 5-6 (a)), which are synthesised bismuth perovskite NCs. The $Cs_3Bi_2Br_9$ NCs have average diameter 3.191 nm and size deviation ±0.802 nm (Figure 5-6 (b)), which may explain the wider FWHM (~76 nm) observed in the photoluminescence spectra compared to single crystal (42 nm).

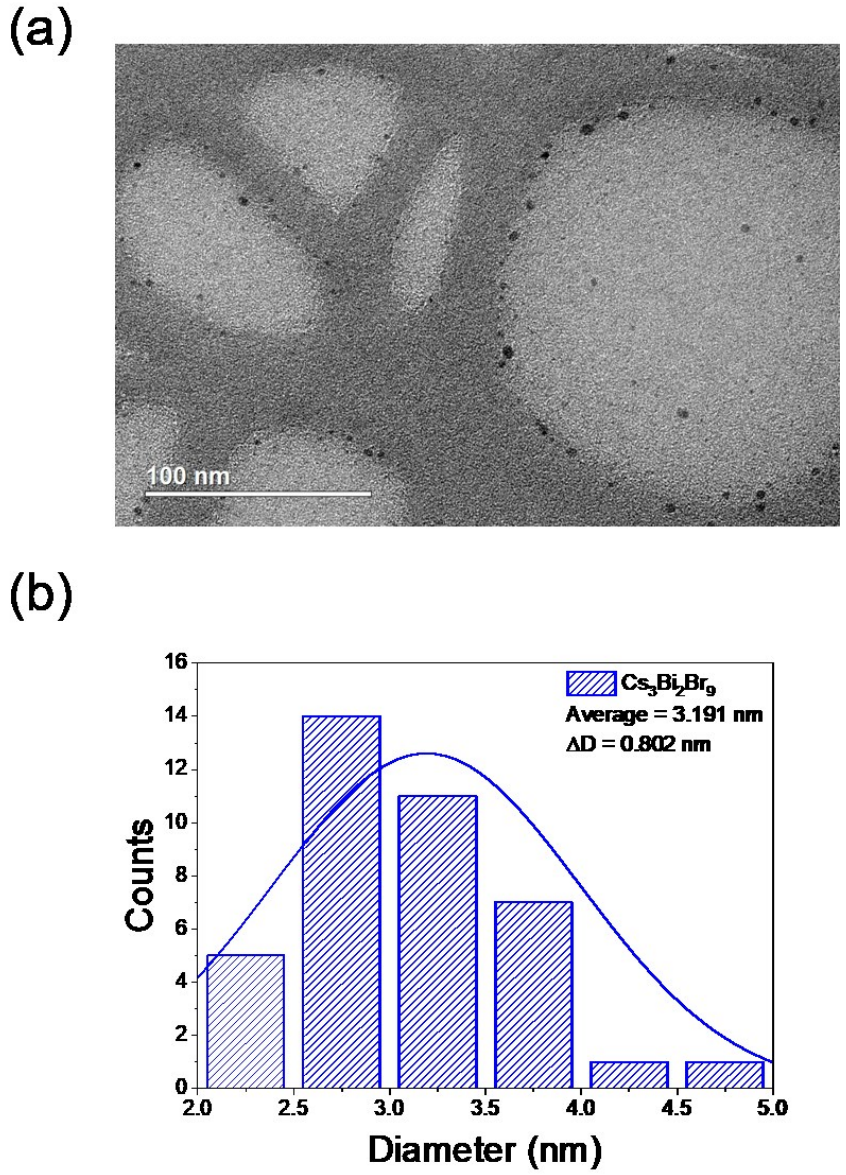

Figure 5-6. (a) TEM image of $Cs_3Bi_2Br_9$ NCs and (b) its analysis of the size distribution.

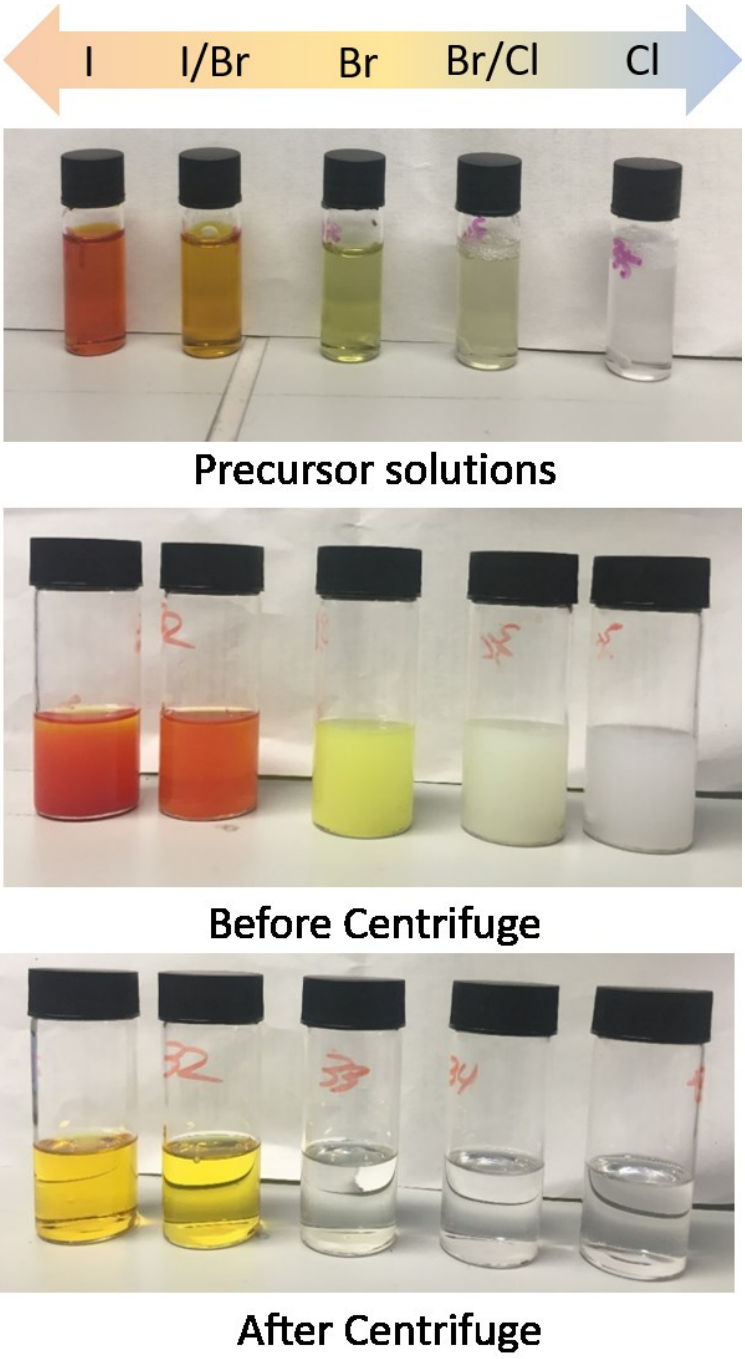

Figure 5-7. Photo of prepared $Cs_3Bi_2X_9$ (where X is I, Br or Cl) precursor solutions, NC solutions before and after centrifuge (from top to bottom).

Bismuth perovskite NCs with other halide composition $Cs_3Bi_2X_9$ (where X is halides) can be synthesised through the same method used for $Cs_3Bi_2Br_9$ NCs. Figure 5-7 shows the colour differences as the halide component changes. The precursor solutions with different halides show red-to-yellow and yellow-to-transparent colour changes as the bromide component increases and the chloride component increases, respectively. Then, after the precursor solution was dropped into the ethanol and oleic acid (OA) mixed solution, the bismuth perovskites precipitate, making the solution opaque due to particles in the solution. By centrifuging, the large particles can be discarded, leaving only nano-sized particles in the solution, resulting in a clear solution as shown in Figure 5-7. When the large particles are discarded, the solution's colour changes because the small particles have a quantum confinement effect and so there is a blue-shift to the absorption spectroscopy, as found in Figure 5-4.

Figure 5-8 shows X-ray Diffraction (XRD) patterns from prepared $Cs_3Bi_2X_9$ powder as described above. In Figure 5-8 (a) and (b), the obtained patterns from $Cs_3Bi_2I_9$ and $Cs_3Bi_2Cl_9$ powder were compared with references (01-073-0707) and (01-084-1037), respectively. They verify that $Cs_3Bi_2I_9$ and $Cs_3Bi_2Cl_9$ NCs were successfully fabricated through the above method. Regarding $Cs_3Bi_2I_9$, the peaks at 14.7°, 16.7°, 25.2° and 51.8° are attributed to the (104), (004), (006) and (0012) planes. It seems $Cs_3Bi_2I_9$ has a preferred orientation which is along the c-axis. Regarding $Cs_3Bi_2Cl_9$, the peaks at 11.2°, 20.0°, 21.9° and 31.2° are attributed to the (111), (600), (511) and (712) planes. Figure 5-8 (c) shows the XRD patterns from the $Cs_3Bi_2X_9$ powder including Br/I and Cl/Br mixed perovskites. When the patterns from the mixed perovskites were compared with patterns from pure perovskites, the patterns from mixed perovskites did not contain peaks from the pure perovskites. This means that the halide mixed perovskites have

their own phase rather than the two separate perovskites exist together.

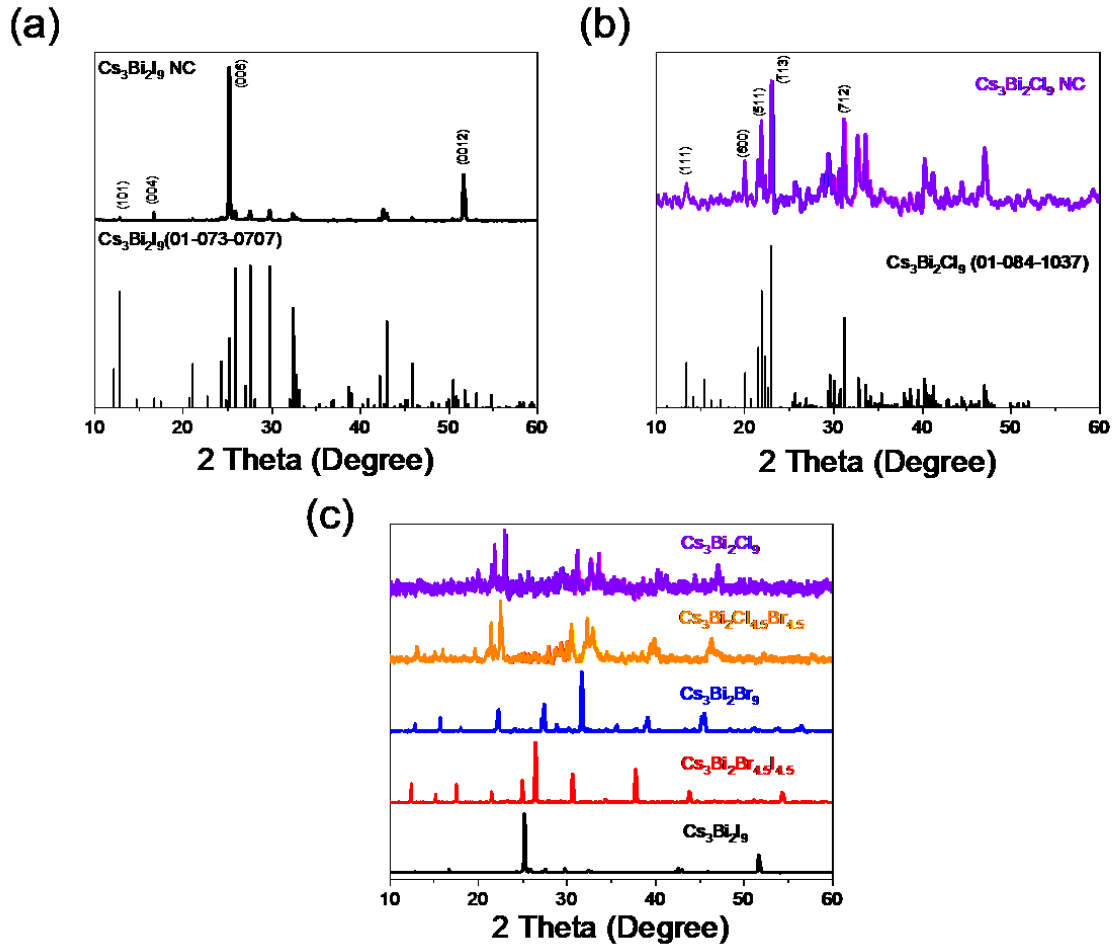

Figure 5-8. X-ray diffraction pattern of (a) prepared $Cs_3Bi_2I_9$ powder and a reference of $Cs_3Bi_2I_9$ (code: 01-073-0707), (b) prepared $Cs_3Bi_2Cl_9$ powder and a reference of $Cs_3Bi_2Cl_9$ (code: 01-084-1037) and (c) prepared $Cs_3Bi_2X_9$ powders (where X = I, Br, Cl).

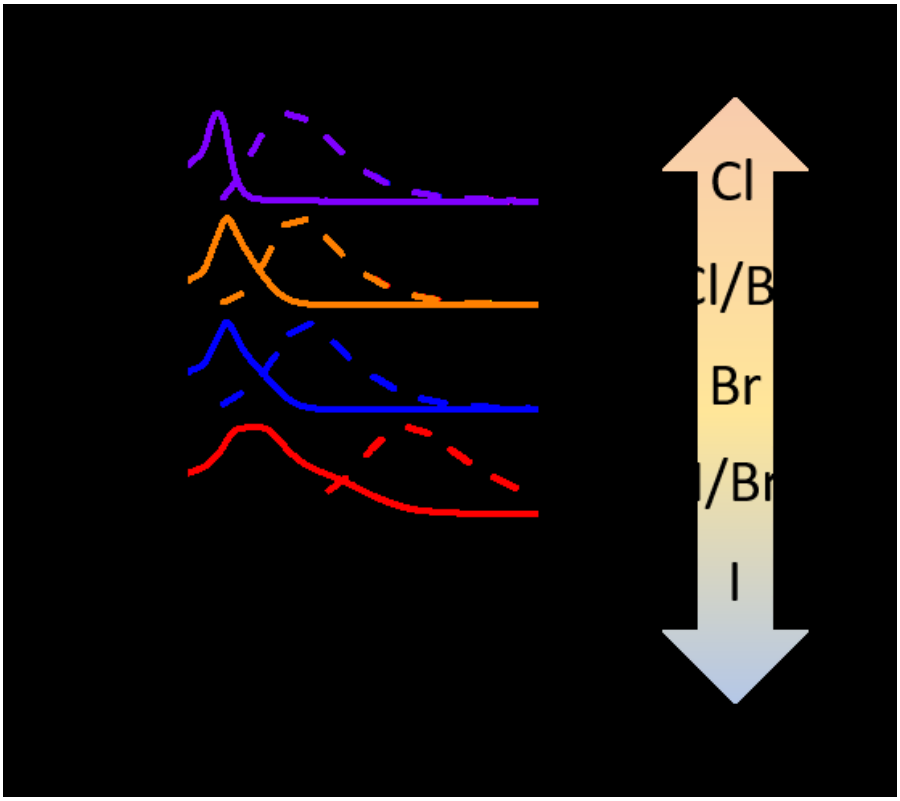

Figure 5-9. UV-Vis (solid lines) and PL (dashed lines) spectra of $Cs_3Bi_2I_9$ (black), $Cs_3Bi_2Br_{4.5}I_{4.5}$ (red), $Cs_3Bi_2Br_9$ (blue), $Cs_3Bi_2Cl_{4.5}Br_{4.5}$ (orange) and $Cs_3Bi_2Cl_9$ (purple) NCs.

As shown in Figure 5-9, the absorbance and PL spectra of various $Cs_3Bi_2X_9$ (X = Br, Cl, and I) NCs can be easily tuned from 385 nm (from $Cs_3Bi_2Cl_9$) to 497 nm (from $Cs_3Bi_2I_9$) by varying the halides. When Br atoms were partially replaced with Cl or I, the bandgaps increased or decreased, respectively, leading to composition-dependent photoluminescence. From the reports by Leng *et al*., Cl-containing bismuth perovskite has a higher photo luminescent quantum yield (PLQY) than Br-containing bismuth perovskite and Br-containing bismuth perovskite has a higher PLQY than I-containing bismuth perovskite.[4, 13] From Figure 5-9, it can be found that the peak shift by the I-to-Br halide change (497 nm (2.52 eV) to 401 nm (3.09 eV), shift = 96 nm (0.57 eV)) is more dramatic than that by the Br-to-Cl halide change (401

nm (3.09 eV) to 385 nm (3.22 eV), shift = 16 nm (0.13 eV)). This difference can be explained by the NC size differences.

Figure 5-10 shows TEM images of synthesised $Cs_3Bi_2X_9$ NCs and the size distributions. In the TEM image (Figure 5-10 (a)–(d)), the black dots are the synthesised bismuth perovskite NCs as seen in Figure 5-6 (a). The $Cs_3Bi_2I_9$ NCs have average diameter 5.473 nm with a size deviation of ± 1.611 nm (Figure 5-10 (e)) while $Cs_3Bi_2Br_9$ NCs have an average diameter of 3.191 nm with a size deviation of ± 0.802 nm (Figure 5-6 (b)). Because the centrifuge speed was the same for the all solutions, smaller size of particles can remain in colloidal solution for heavier compositions and bigger size of particles can remain in the colloidal solution for lighter composition. The trend of the sizes is going down from 4.167 nm (I only) to 3.191 nm (Br only) then going up to 5.473 nm (Cl only). The size increase for Br/Cl mixed and Cl only perovskites might be related to this. There is a size difference of about 2 nm between I-containing perovskites and Br-containing perovskites. This might have brought the dramatic peak shift due to the increased quantum confinement effect. However, $Cs_3Bi_2Cl_9$ NCs have an average diameter of 4.167 nm with a size deviation of ± 1.066 nm (Figure 5-9 (h)). The Cl-containing perovskite has a larger size than the Br-containing perovskite and the size difference between the Br-containing perovskite and Cl-containing perovskite is approximately 1 nm. This might have reduced the quantum confinement effect and so the shift is smaller, as seen in the figure.

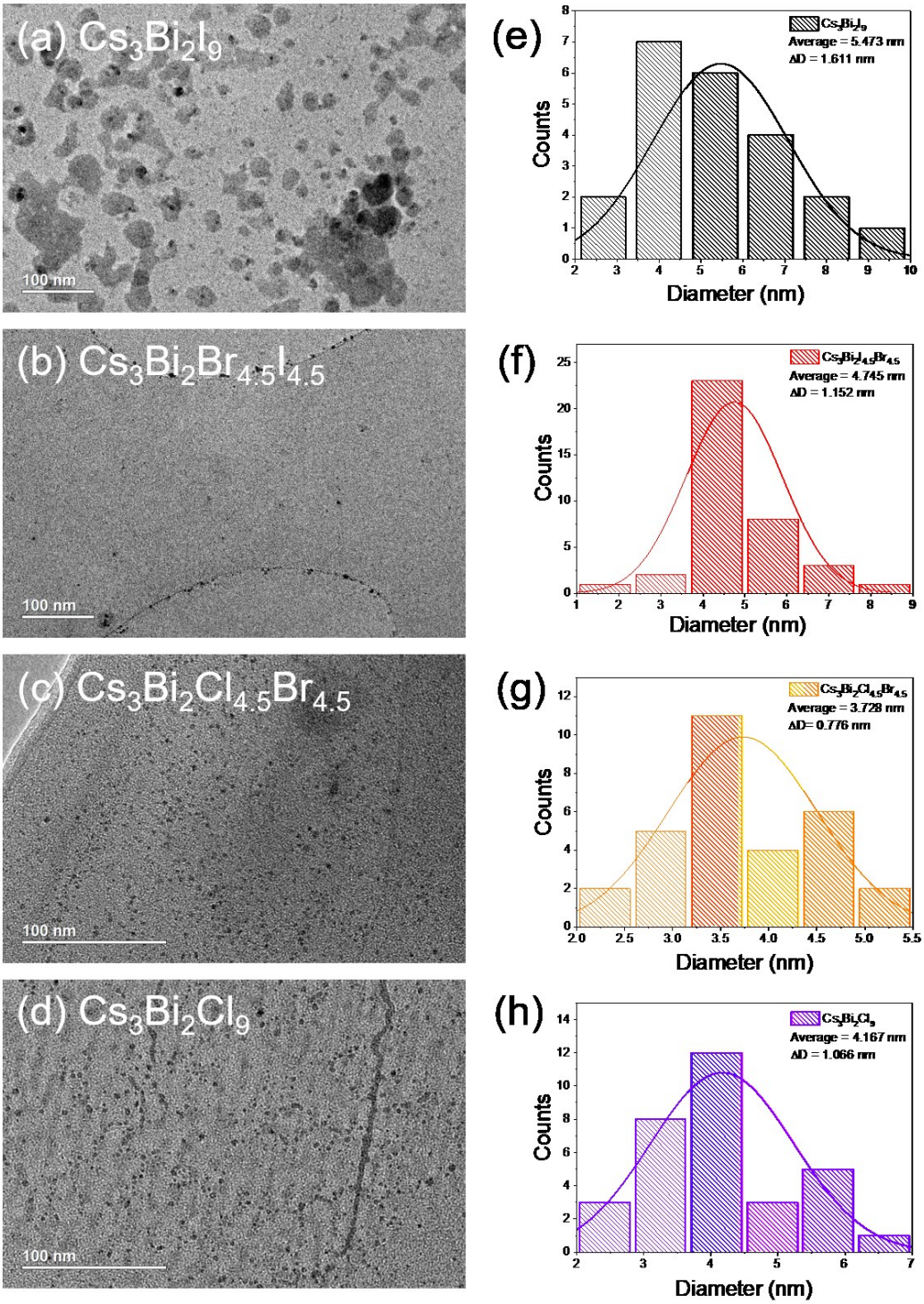

Figure 5-10. (a), (b), (c) and (d) TEM images of $Cs_3Bi_2X_9$ NCs and (e), (f), (g) and (h) their analysis of the size distribution.

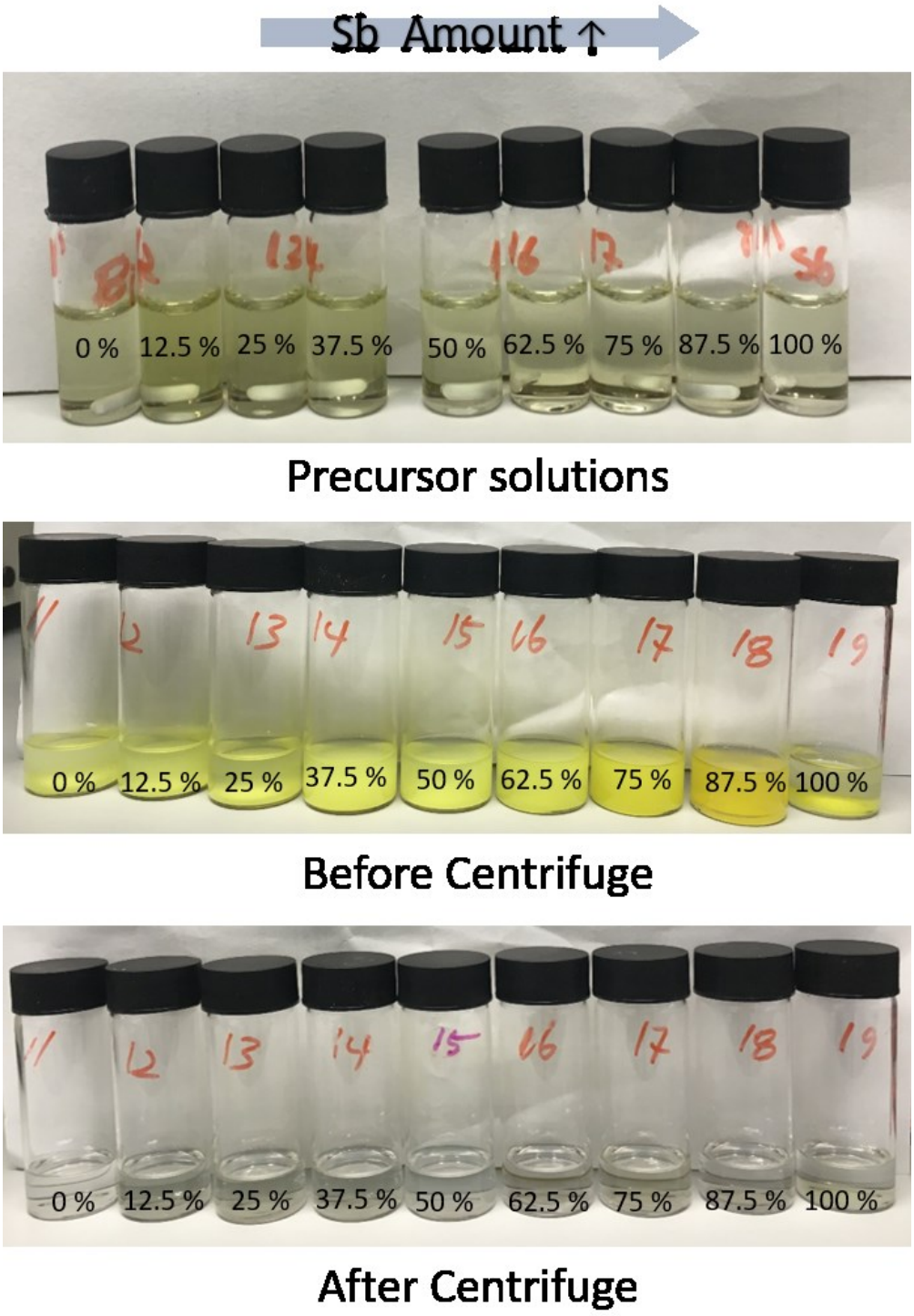

Figure 5-11. Photo of prepared $Cs_3(Bi_{1-x}Sb_x)_2Br_9$ precursor solutions, NC solutions before and after centrifuge (from top to bottom).

From Chapter 4-1, bandgap bowing, energy level disorder and changes in binding energy were observed by antimony replacement. Expecting a similar effect as that found in Chapter 4-1, bismuth was replaced with antimony in the perovskite. The bismuth/antimony mixed perovskite NCs ($Cs_3(Bi_{1-x}Sb_x)_2Br_9$) were synthesised using the same method as that for $Cs_3Bi_2Br_9$ NCs.

Figure 5-11 shows the colour differences as the antimony component increases. The precursor solutions with different ratios of Bi/Sb show similar colour; however, the saturation increases until reaching a 1:1 ratio mixture and then decreases to the end members. After the precursor solution is dropped into the ethanol and OA mixed solution, the perovskites precipitated and the solution became opaque due to particles in the solution. By centrifuging, large particles were discarded and only nano-sized small particles remained in the solution, resulting in a clear and transparent solution. When large particles were discarded, the colour of the solution changed because the small particles have a quantum confinement effect and so there is a blue shift. The transparent colouration came from the absorption onset in the ultra-violet region.

Figure 5-12 shows the XRD patterns of the prepared $Cs_3(Bi_{1-x}Sb_x)_2Br_9$ powders. As Bi is replaced by Sb, there are no impurity peaks, only a shift of the peaks to higher angles. This confirms the absence of any large change in lattice parameters, suggesting that the solid solution would readily mix. This agrees with the experimental work on end members (Figure 5-3).[4, 15] For the Bi end member phase, diffraction peaks are seen at 22.17°, 31.61° and 39.05° and increase to 22.50°, 32.10° and 39.55°, respectively, for the Sb end member phase. This small change in the peak position indicates a small change in the lattice parameters and suggests the complete mixing of the solid solution as found in Chapter 4-1.

To investigate the optical property changes after Sb substitution, steady-state UV–Vis and PL were employed.

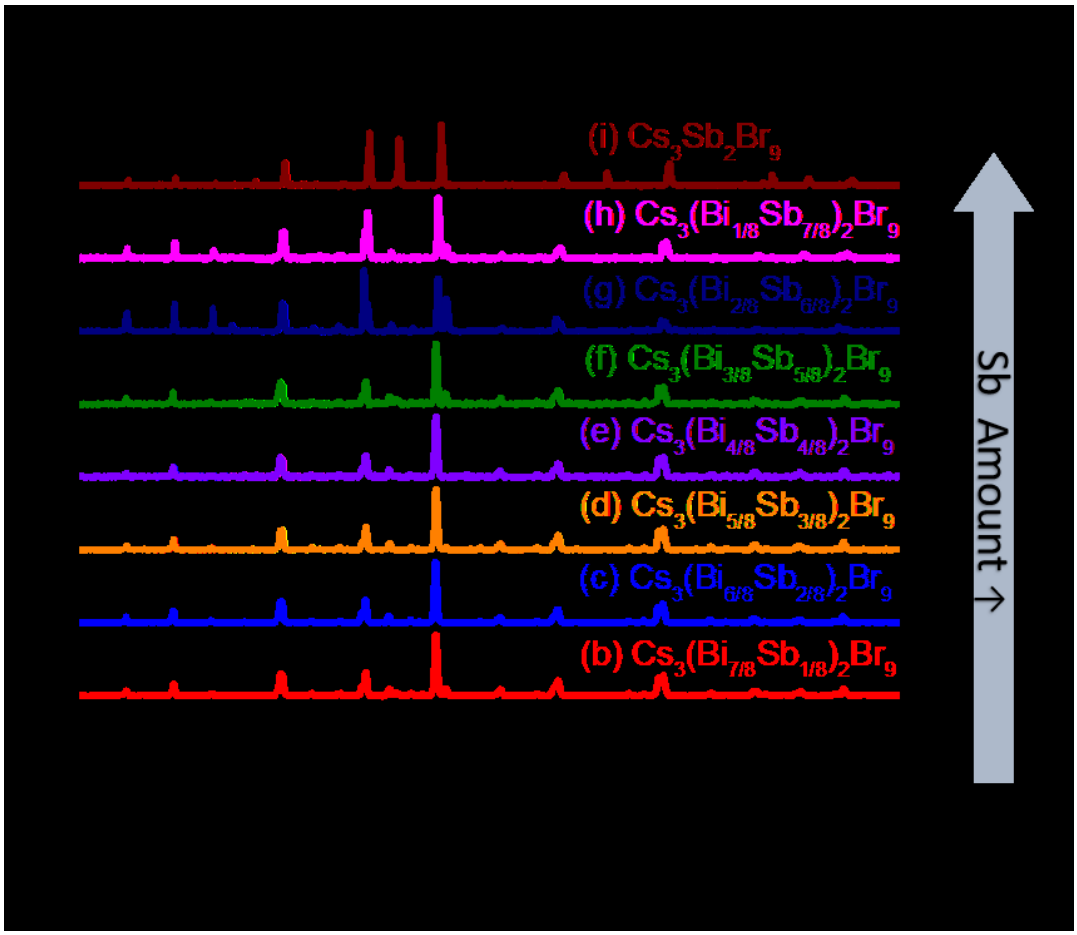

Figure 5-12. X-ray diffraction patterns of prepared $Cs_3(Bi_{1-x}Sb_x)_2Br_9$ powders.

Figure 5-13 (a) shows the normalised UV–Vis spectra from the pure and mixed perovskites. As can be seen in this figure, the absorption onset red-shifts until a 1:1 ratio mixture and then blue-shifts to the end members. The PL spectra have similar behaviour to the absorbance spectra. The emission peak shifts towards the lower energy direction until reaching the 50/50 mixed perovskite and then returns to the higher energy. As described in Chapter 4-1 with

$MA_3(Bi_{1-x}Sb_x)_2I_9$, this behaviour is called the bandgap bowing effect and comes from the energy level mismatch between Bi and Sb orbitals. While the bandgap can be considered tuneable with Sb substitution, the effect is less than halide control.

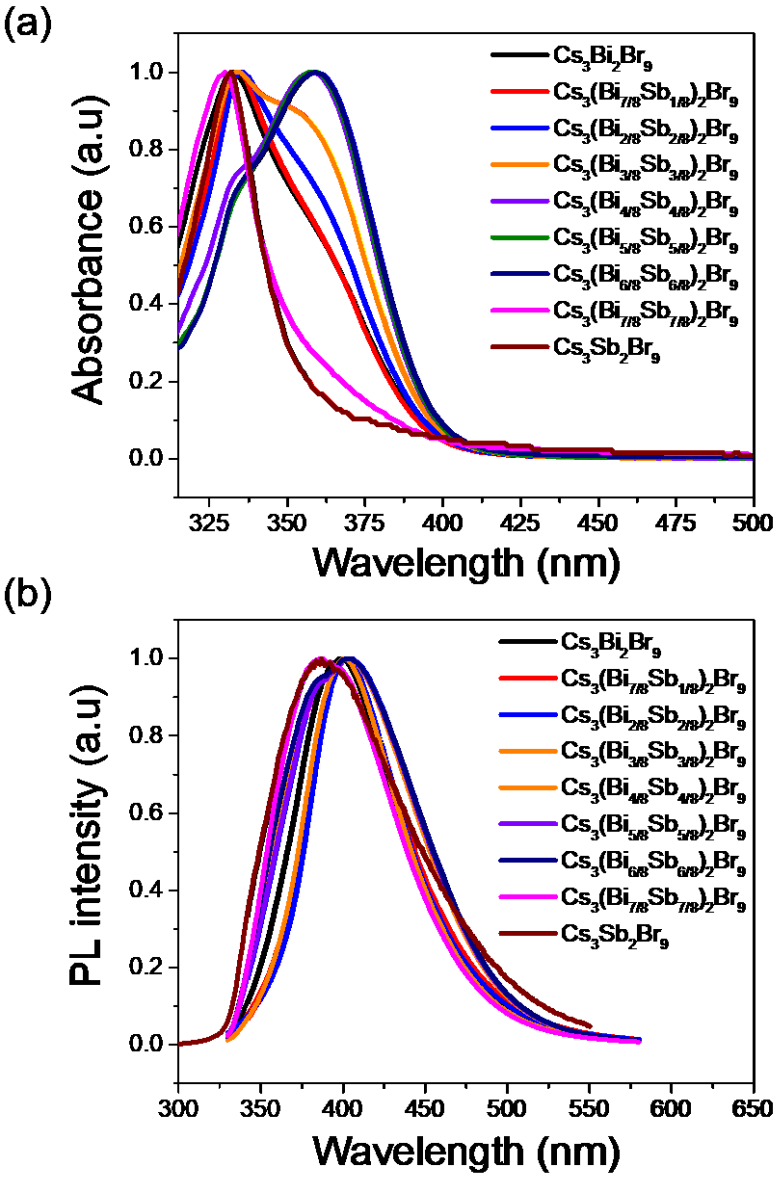

Figure 5-13. Normalised (a) UV-Vis and (b) PL spectra of $Cs_3(Bi_{1-x}Sb_x)_2Br_9$ NCs. The selected excitation wavelength was 282 nm for PL measurement.

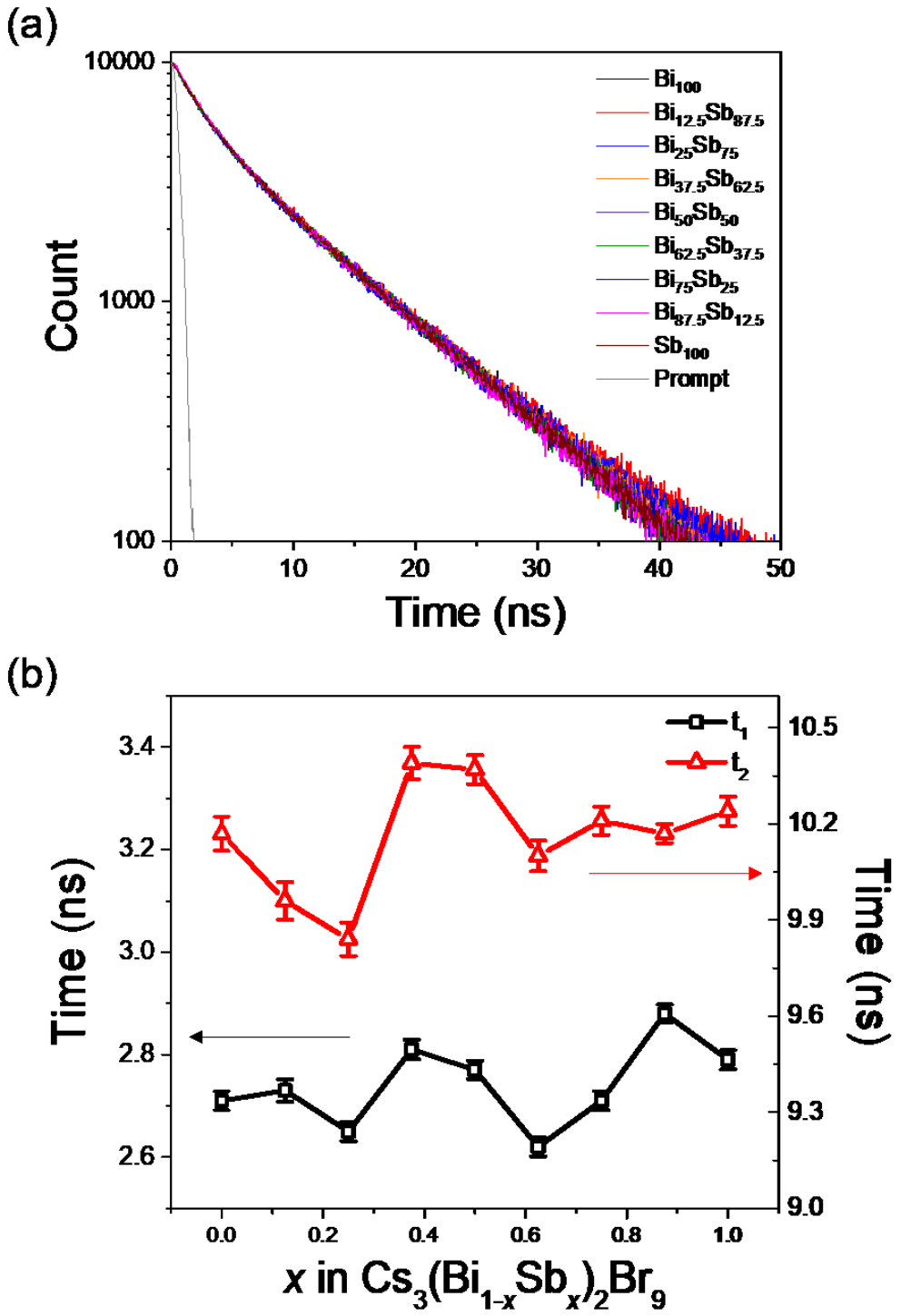

Figure 5-14. (a) TRPL from $Cs_3(Bi_{1-x}Sb_x)_2Br_9$ NCs and (b) the t_1 and t_2 values from the fitting. The selected excitation wavelength was 282 nm and probed at 400 nm.

Table 5-1. Fitting parameters of PL decays in Figure 5-14. Tri-exponential functions (Eq. 5-1) were employed.

x in $Cs_3(Bi_{1-x}Sb_x)_2Br_9$	I_1	t_1 (ns)	I_2	t_2 (ns)	I_3	t_3 (ns)	R^2
0	4318 ± 31	2.71 ± 0.02	5757 ± 27	10.17 ± 0.05	28 ± 9	72.66 ± 22.07	0.99972
0.125	4406 ± 37	2.73 ± 0.02	5771 ± 34	9.96 ± 0.06	77 ± 8	89.58 ± 11.51	0.99961
0.25	4357 ± 33	2.65 ± 0.02	5746 ± 30	9.84 ± 0.05	77 ± 8	81.27 ± 8.99	0.99968
0.375	4528 ±31	2.81 ±0.02	5613 ± 30	10.39 ±0.05	15 ± 5	202.53 ±175.96	0.99967
0.5	4444 ± 29	2.77 ± 0.02	5756 ± 28	10.37 ± 0.05	5 ± 5	244.55 ± 618.52	0.9997
0.625	4231 ± 29	2.62 ± 0.02	5884 ± 28	10.10 ± 0.05	9 ± 6	111.05 ± 112.75	0.99967
0.75	4404 ± 29	2.71 ± 0.02	5775 ± 28	10.21 ± 0.04	5 ± 4	566.69 ± 3365.15	0.99966
0.875	4607 ± 26	2.86 ± 0.02	5705 ± 28	10.19 ± 0.03	5 ± 1	1.2E133	0.99965
1	4385 ± 30	2.79 ± 0.02	5769 ± 29	10.24 ± 0.05	5 ± 6	243.57 ± 648.80	0.9997

To see the changes in the recombination dynamics, time-resolved PL (TRPL) decays of $Cs_3(Bi_{1-x}Sb_x)_2Br_9$ were measured as shown in Figure 5-14 (a). The PL decays were fitted with Eq. 5-1, which is the tri-exponential function. The t_1 and t_2 values in Figure 5-14 (b) and Table 5-1 were obtained by fitting with Eq. 5-1. As with $Cs_3Bi_2Br_9$ NCs, the contribution of the ultralong-lived

component is negligible with relative amplitudes (RAs) <10%, while the lifetimes of the other two components deviated slightly between samples.

When the decay (Figure 5-14 (a)) and carrier lifetimes (Table 5-1) were compared, some trends were revealed. Figure 5-14 (b) shows the trend of the carrier lifetimes for the Sb substituted into the bismuth perovskite NCs. Both t_1, which is related to the exciton recombination, and t_2, which is related to the surface defect recombination, have the tendency to drop until 25% Sb mixing and then increase at 37.5% Sb mixing. They decrease until 62.5% mixing, t_1 then increases up to 87.5% mixing and then drops in the Sb pure perovskite with t_1, for t_2, the Sb pure perovskite increases in the case of t_2. It seems that a specific ratio of the mixed perovskite has a longer carrier lifetime than Bi or Sb pure perovskite.

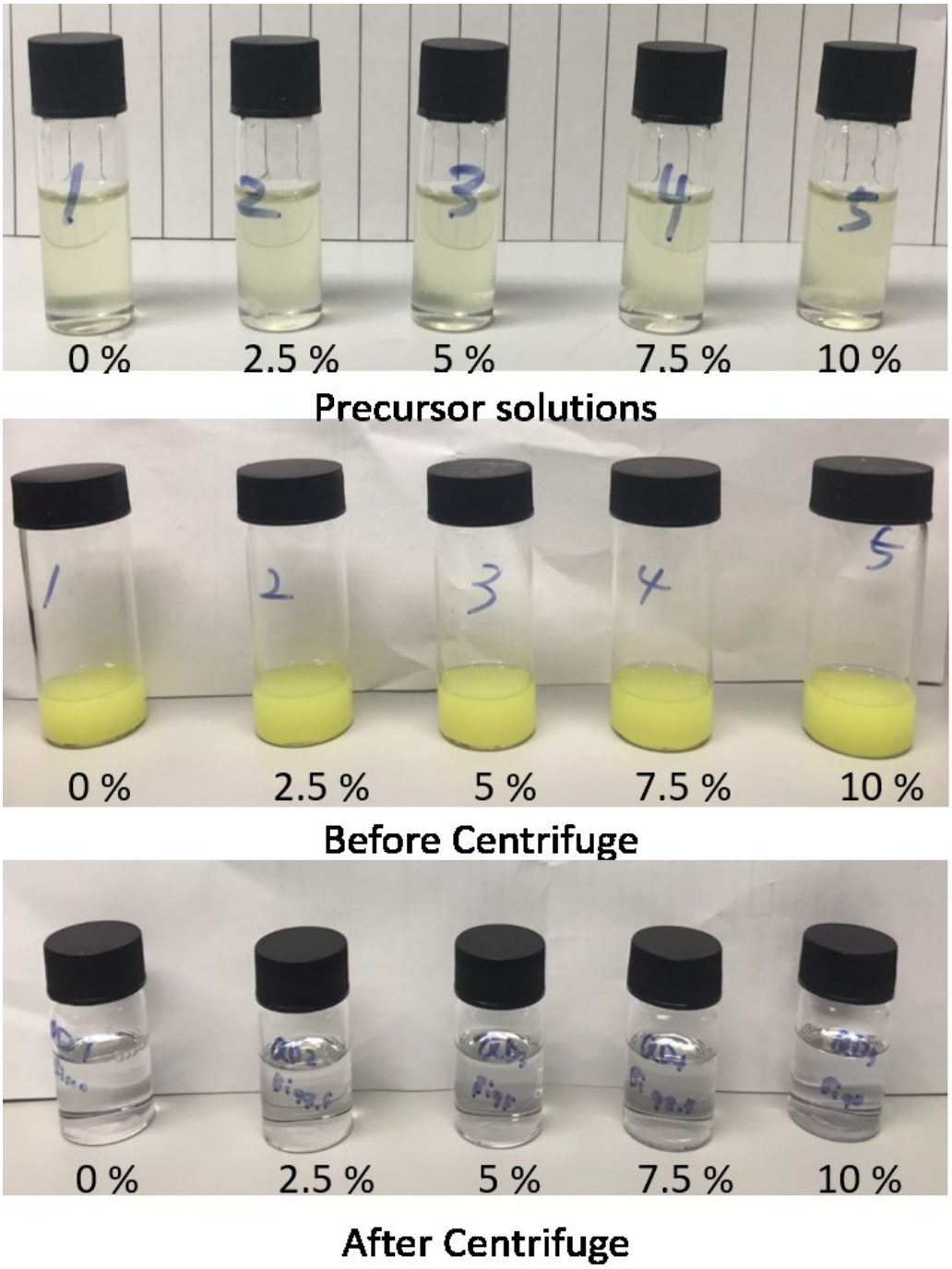

Figure 5-15. Photo of prepared $Cs_3(Bi_{1-x}Sb_x)_2Br_9$ (where the Sb amount is small) precursor solutions, NC solutions before and after centrifuging (from top to bottom).

To investigate the effect of a small amount of Sb doping, Sb doped (≤10%) bismuth perovskite NCs were prepared. Figure 5-15 shows the solutions obtained while preparing the Sb-doped bismuth perovskite NCs. They were synthesised through the same method used for $Cs_3Bi_2Br_9$ NCs. The precursor solutions with different Bi/Sb ratios show similar colours; the ethanol and OA mixed solution with the precursor solution dropped in also looks similar. The solution became opaque because the perovskites precipitated. After centrifugation, large particles were discarded and only nano-sized small particles remained in the solution, resulting in a clear and transparent solution. All solutions had the same transparent colour.

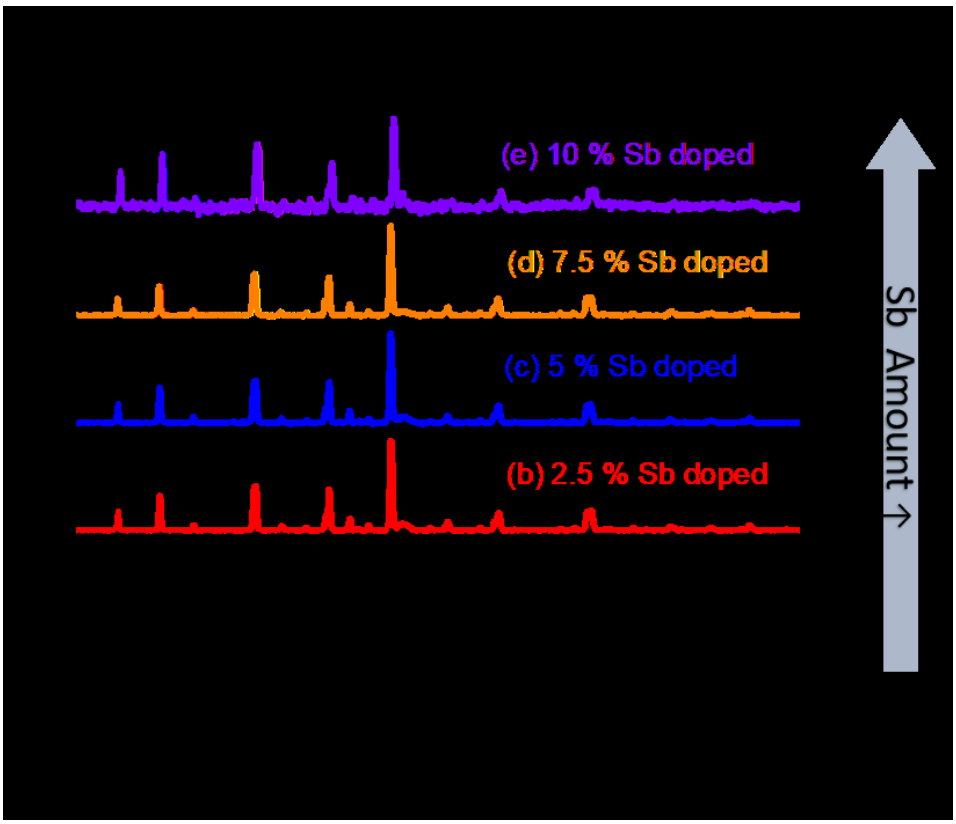

Figure 5-16. X-ray diffraction patterns of the prepared $Cs_3(Bi_{1-x}Sb_x)_2Br_9$ (where the Sb amount is small) powders.

Figure 5-16 shows the XRD patterns of the prepared Sb-doped bismuth perovskite powders. As Bi is replaced by Sb, there are no impurity peaks, only a shift in the peaks to higher angles as seen in Figure 5-12. This confirms the absence of any large change in the lattice parameters, which suggests that the solid solution would readily mix as expected. The diffraction peaks that can be seen at 22.17°, 27.33° and 31.68° for the Bi end member phase increased to 22.37°, 27.54° and 31.92°, respectively, for the 10% Sb-doped bismuth perovskite. This small change in the peak position indicates a small change in the lattice parameters and suggests the complete mixing of the solid solution as found in Chapter 4-1 and above.

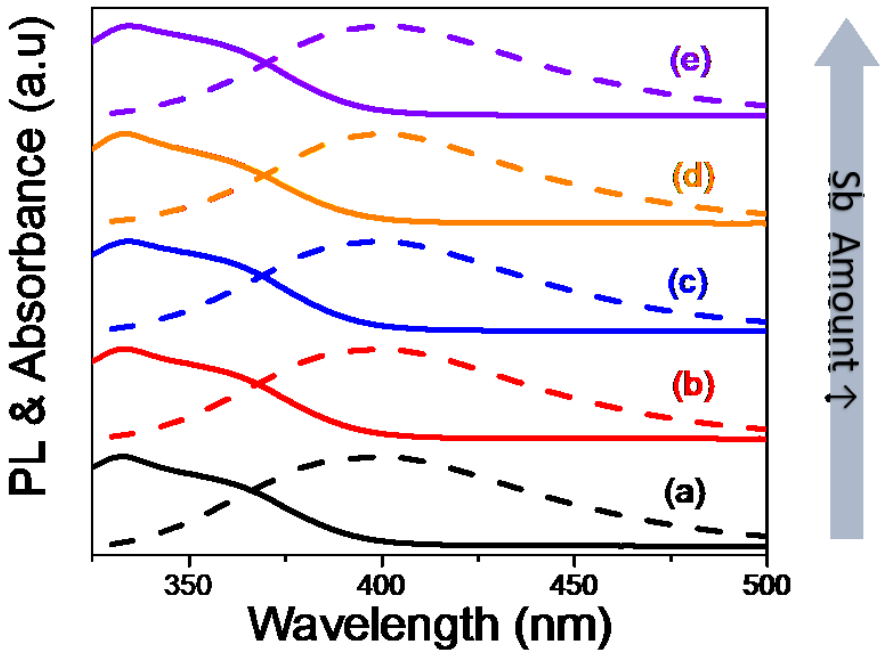

Figure 5-17. Normalised UV–Vis and PL spectra of $Cs_3Bi_2Br_9$ NCs with (a) 0%, (b) 2.5%, (c) 5%, (d) 7.5% and (e) 10% Sb doping. The selected excitation wavelength was 280 nm for PL measurement.

Figure 5-17 shows the normalised UV–Vis spectra and PL spectra from the pure and doped perovskites. Only a small shift was observed in the lower energy direction within 1 nm both in the absorption onset and PL emission peak. Doping with a small amount of Sb seems to have a negligible effect on the steady-state results.

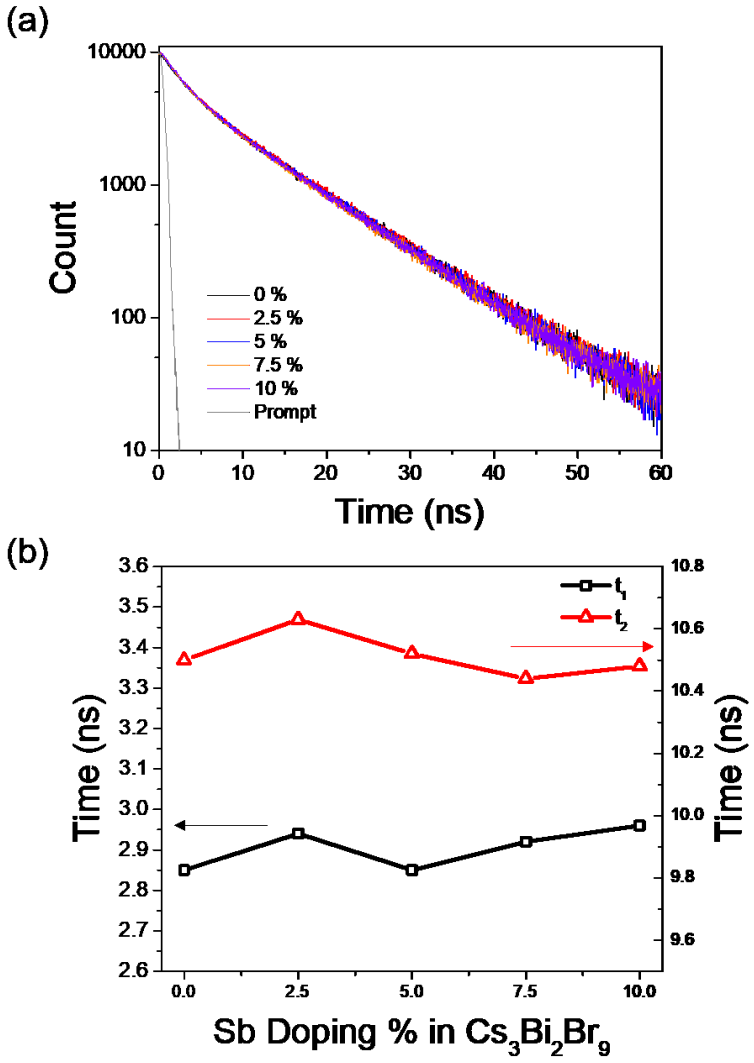

Figure 5-18. TRPL from $Cs_3(Bi_{1-x}Sb_x)_2Br_9$ (where the Sb amount is small) NCs and (b) the t_1 and t_2 values from the fitting. The selected excitation wavelength was 282 nm and probed at 400 nm.

To see the effect of Sb doping in the recombination dynamics, TRPL decays of $Cs_3(Bi_{1-x}Sb_x)_2Br_9$ were measured and shown in Figure 5-18 (a). The PL decays were fitted with eq. 5-1 which is the tri-exponential function. The t_1 and t_2 values in Figure 5-18 (b) were obtained by fitting with Eq. 5-1. The contribution of the ultralong-lived component is negligible with RAs <10%, while the lifetimes of the other two components deviated little with samples. However, upon comparing the charge decays and lifetimes, it seems that the small amount of Sb doping was not notable.

Regarding the effect of Sb mixing, when Sb is mixed into bismuth perovskite NCs, there is a small effect on the lattice parameter, bandgap and charge carrier lifetime. However, the effect is negligible when the amount of Sb is small unlike for the lead perovskite, which achieved a tenfold PLQY increase with only 7% Sn doping.[19]

5-4. Conclusion

In summary, colloidal $Cs_3Bi_2Br_9$ NCs were successfully synthesised by employing a hot injection method, which can be expected to bring fewer defects and higher excitonic behaviour. It seems that the prepared NCs could reduce the surface defect recombination and improve the excitonic behaviour, but the surface defect recombination still dominates in bismuth perovskite NCs. To improve this, colloidal NCs of $Cs_3(Bi_{1-x}Sb_x)_2Br_9$ alloys were prepared with $0 \leq x \leq 1$. As with the result in Chapter 4-1, they showed small changes in the lattice parameter due to the bandgap bowing effect. TRPL showed some improvement over its lifetime by mixing 37.5% Sb into the bismuth perovskite NCs. Further study on small amounts of Sb doping was conducted but no significant effect was found in either steady-state or time-correlated spectroscopic views.

5-5. References

1. Z. W. Xiao, W. W. Meng, J. B. Wang, D. B. Mitzi and Y. F. Yan, *Mater. Horiz.*, 2017, **4**, 206-216.

2. C. K. Zhou, H. R. Lin, Y. Tian, Z. Yuan, R. Clark, B. H. Chen, L. J. van de Burgt, J. C. Wang, Y. Zhou, K. Hanson, Q. J. Meisner, J. Neu, T. Besara, T. Siegrist, E. Lambers, P. Djurovich and B. W. Ma, *Chem. Sci.*, 2018, **9**, 586-593.

3. H. Huang, M. I. Bodnarchuk, S. V. Kershaw, M. V. Kovalenko and A. L. Rogach, *ACS Energy Lett.*, 2017, **2**, 2071-2083.

4. M. Y. Leng, Y. Yang, K. Zeng, Z. W. Chen, Z. F. Tan, S. R. Li, J. H. Li, B. Xu, D. B. Li, M. P. Hautzinger, Y. P. Fu, T. Y. Zhai, L. Xu, G. D. Niu, S. Jin and J. Tang, *Adv. Funct. Mater.*, 2018, **28**.

5. L. Protesescu, S. Yakunin, M. I. Bodnarchuk, F. Krieg, R. Caputo, C. H. Hendon, R. X. Yang, A. Walsh and M. V. Kovalenko, *Nano Lett.*, 2015, **15**, 3692-3696.

6. Q. A. Akkerman, V. D'Innocenzo, S. Accornero, A. Scarpellini, A. Petrozza, M. Prato and L. Manna, *J. Am. Chem. Soc.*, 2015, **137**, 10276-10281.

7. A. Swarnkar, R. Chulliyil, V. K. Ravi, M. Irfanullah, A. Chowdhury and A. Nag, *Angew. Chem. Int.,* 2015, **54**, 15424-15428.

8. F. Zhang, H. Z. Zhong, C. Chen, X. G. Wu, X. M. Hu, H. L. Huang, J. B. Han, B. S. Zou and Y. P. Dong, *ACS Nano*, 2015, **9**, 4533-4542.

9. X. M. Li, F. Cao, D. J. Yu, J. Chen, Z. G. Sun, Y. L. Shen, Y. Zhu, L. Wang, Y. Wei, Y. Wu and H. B. Zeng, *Small*, 2017, **13**.

10. A. Z. Pan, B. He, X. Y. Fan, Z. K. Liu, J. J. Urban, A. P. Alivisatos, L. He and Y. Liu, *ACS Nano*, 2016, **10**, 7943-7954.

11. T. C. Jellicoe, J. M. Richter, H. F. J. Glass, M. Tabachnyk, R. Brady, S. E. Dutton, A. Rao, R. H. Friend, D. Credgington, N. C. Greenham and M. L. Boehm, *J. Am. Chem. Soc.*, 2016, **138**, 2941-2944.

12. A. F. Wang, X. X. Yan, M. Zhang, S. B. Sun, M. Yang, W. Shen, X. Q. Pan, P. Wang and Z. T. Deng, *Chem. Mater.*, 2016, **28**, 8132-8140.

13. M. Y. Leng, Z. W. Chen, Y. Yang, Z. Li, K. Zeng, K. H. Li, G. D. Niu, Y. S. He, Q. C. Zhou and J. Tang, *Angew. Chem. Int.,* 2016, **55**, 15012-15016.

14. K. M. McCall, C. C. Stoumpos, S. S. Kostina, M. G. Kanatzidis and B. W. Wessels, *Chem. Mater.*, 2017, **29**, 4129-4145.

15. J. Zhang, Y. Yang, H. Deng, U. Farooq, X. K. Yang, J. Khan, J. Tang and H. S. Song, *ACS Nano*, 2017, **11**, 9294-9302.

16. B. Yang, F. Hong, J. S. Chen, Y. X. Tang, L. Yang, Y. B. Sang, X. S. Xia, J. W. Guo, H. X. He, S. Q. Yang, W. Q. Deng and K. L. Han, *Angew. Chem. Int.*, 2019, **58**, 2278-2283.

17. A. Mehta, J. Im, B. H. Kim, H. Min, R. Nie and S. I. Seok, *ACS Nano*, 2018, **12**, 12129-12139.

18. N. Chen, T. Cai, W. H. Li, K. Hills-Kimball, H. J. Yang, M. D. Que, Y. Nagaoka, Z. Y. Liu, D. Yang, A. G. Dong, C. Y. Xu, R. Zia and O. Chen, *ACS Appl. Mater. Interfaces*, 2019, **11**, 16855-16863.

19. A. B. F. Vitoreti, S. Agouram, M. S. de la Fuente, V. Munoz-Sanjose, M. A. Schiavon and I. Mora-Sero, *J. Phys. Chem. C*, 2018, **122**, 14222-14231.

20. B. Yang, J. Chen, F. Hong, X. Mao, K. Zheng, S. Yang, Y. Li, T. Pullerits, W. Deng and K. Han, *Angew. Chem. Int. Ed.*, 2017, **56**, 12471-12475.

21. M. Sykora, A. Y. Koposov, J. A. McGuire, R. K. Schulze, O. Tretiak, J. M. Pietryga and V. I. Klimov, *ACS Nano*, 2010, **4**, 2021-2034.

22. M. V. Kovalenko, L. Manna, A. Cabot, Z. Hens, D. V. Talapin, C. R. Kagan, V. I. Klimov, A. L. Rogach, P. Reiss, D. J. Milliron, P. Guyot-Sionnnest, G. Konstantatos, W. J. Parak, T. Hyeon, B. A. Korgel, C. B. Murray and W. Heiss, *ACS Nano*, 2015, **9**, 1012-1057.

Chapter 6: Conclusions & Future Work

6-1. Conclusions

Bismuth iodide and bismuth/antimony-based perovskites were investigated as new materials to overcome the intrinsic problems of lead-based perovskites. Now, the efficiency of these materials has been improved by optimising the device structure, metal cation transmutation or controlling the dimensionality or size. In addition, the understanding of those materials has been deepened by characterising the materials. This thesis has made critical steps towards promoting the cell performance and provided an outlook for lead-free materials for use in photovoltaics.

The first results chapter (Chapter 3) was about the application of BiI_3 in a solar-cell device with an *in situ* fabricated BiSI interlayer. The interlayer efficiently extracted charges from BiI_3, which has a short charge-carrier lifetime, and so the device efficiency could be improved. When the same structure was applied to $MA_3Bi_2I_9$, the device efficiency was also improved.

The second result chapter (Chapter 4) described improving bismuth-based perovskite ($MA_3Bi_2I_9$) through metal cation transmutation or a quasi-2D perovskite approach. First, metal transmutation brought changes in the physical and opto-physical properties. In particular, there were changes in the bandgap, PLQY and binding energy. The binding energy reduction by Sb substitution seems to have a major effect on the device performance. The 2D bismuth-based perovskite was successfully fabricated and characterised. Its devices did not work due to the too-high binding energy, so a BiSI interlayer was employed to overcome this. The device

worked with the interlayer; it can be expected to have a higher performance after optimisation.

The last results chapter (Chapter 5) presented the fabrication of bismuth/antimony-based perovskite nanocrystals and their characterisation. The photoluminescence of bismuth perovskite NCs was dominated by the surface defect recombination, although the nano-sized particles reduced the defect density. To overcome this, metal cation transmutation was applied, and this showed some improvement. A small amount of Sb doping was unable to change the properties.

In summary, the work presented in this thesis has demonstrated the great potential of bismuth iodide and bismuth/antimony-based perovskites to work as a light-absorbing material and has provided a fundamental understanding of these systems. Furthermore, it suggests ways to improve their usage in solar cells or light-emitting devices.

6-2. Future Work

Regarding the BiSI interlayer, its thickness was not optimised here. The thickness of the BiSI could be the key to further improvements. The energy level of the BiSI interlayer is such that only SnO_2 can be used as its ETM; fabricating a smooth and compact mesoporous SnO_2 layer was attempted but failed. If a high-quality mesoporous SnO_2 layer can be fabricated, it can be expected to greatly improve the efficiency.

In Chapter 4, the study focused on the characterisation of new materials rather than on the device performance. There is much room for improving the device performance including the optimising the thickness of the layers including the active layer. The perovskite layer was about 200 nm thick; however, thinner is recommended for bismuth/antimony-based perovskite due to the short charge-carrier length.

In terms of nanocrystals, Sb mixing is expected to lead to a higher PLQY because 37.5% mixing showed a longer carrier lifetime. In this study, the PLQY was not obtained due to a lack of time. It would be helpful to measure the PLQYs of the mixed perovskite nanocrystals to understand them in greater depth. In addition, further passivation of harmful defects could help achieve a higher PLQY.

Furthermore, the current transient absorption spectroscopy measurement is limited by the instrument response timescale of microsecond; therefore, if faster timescale TAS such as picosecond and femtosecond could be applied to monitor the charge transfer processes, particularly the electron injection from perovskites to the interlayer or ETL, it will lead to a deeper understanding of the key factors that influence the electron transfer process and provide

guidance for the device design and optimisation.